

# Non-polar InGaN quantum dots: polarisation-controlled semiconductor single-photon sources at on-chip temperatures



WANG Tong  
St Catherine's College  
Department of Physics

*Thesis submitted for the degree of  
Doctor of Philosophy*

Trinity Term 2019

---

**Non-polar InGaN quantum dots: polarisation-controlled semiconductor  
single-photon sources at on-chip temperatures**

WANG Tong

St Catherine's College

Thesis submitted for the degree of Doctor of Philosophy

Trinity Term 2019

**Abstract**

Polarisation-controlled single-photon sources are at the heart of quantum information applications, e.g. truly secure communication with polarisation-based quantum key distribution protocols, and all-optical quantum computation with logic gates defined by the polarisation states of photons. Non-polar (11 $\bar{2}$ 0) *a*-plane InGaN/GaN quantum dots are one of the strongest candidates due to their ability to operate at temperatures similar to those in on-chip conditions, and intrinsic polarisation properties built into the material.

Time-integrated, time-resolved, polarisation-resolved micro-photoluminescence, and Hanbury Brown and Twiss studies are conducted on *a*-plane QDs fabricated by two different methods, yielding results that are not only a significant step forward in nitride-based single-photon research, but also open up the underexplored field of high-temperature semiconductor quantum dot photophysics. In particular, the first demonstration of ultrafast polarisation-controlled single-photon generation from a semiconductor quantum dot platform at 220 K ( $-53^\circ\text{C}$ ) is achieved, along with an unexpected observation of temperature-dependent fine-structure splitting previously unseen in other systems.

Radiative recombination lifetime and slow-timescale spectral diffusion have been investigated with statistical significance, producing mean values that are on par with state-of-the-art nitride developments in the literature. Combined with efforts from theory collaborators, the insensitivity of radiative lifetime and optical polarisation to differences in the physical dimension, geometry and material composition of the quantum dots has been demonstrated. In particular, *a*-plane InGaN quantum dots have been shown both theoretically and experimentally to exhibit high polarisation degrees with deterministic axes along nitride crystal directions, from cryogenic to temperatures above 200 K. These developments advance the field of single-photon science and bring the current platform a step closer to on-chip quantum information applications.

Meanwhile, other temperature-dependent optical properties, such as emission intensity quenching, exciton linewidth broadening and phonon-assisted redshift, have been investigated in detail. Parameters relevant to thermally assisted processes in the *a*-plane platform, including acoustic phonon scattering strengths, typical activation energies of local potential depths and Huang-Rhys factors, have also been evaluated for the first time, thereby facilitating further development of the platform and fundamental research of related photophysics.

# Publications

## First Author

- *Non-polar nitride single-photon sources.* (Invited Review)  
Tong Wang, Rachel A. Oliver, and Robert A. Taylor, **Journal of Optics**, under review (2019).
- *Polarisation-controlled single photon emission at high temperatures from InGaN quantum dots*  
Tong Wang, Tim J. Puchtler, Tongtong Zhu, J. C. Jarman, L. P. Nuttall, R. A. Oliver, and R. A. Taylor, **Nanoscale** 9, 9421 (2017).
- *Direct generation of linearly polarized single photons with a deterministic axis in quantum dots*  
Tong Wang, Tim J. Puchtler, Saroj K. Patra, Tongtong Zhu, Muhammad Ali, Tom J. Badcock, Tao Ding, R. A. Oliver, Stefan Schulz, and R. A. Taylor, **Nanophotonics** 6, 1175 (2017).
- *Deterministic optical polarisation in nitride quantum dots at thermoelectrically cooled temperatures*  
Tong Wang, Tim J. Puchtler, Saroj K. Patra, Tongtong Zhu, John C. Jarman, R. A. Oliver, Stefan Schulz, and R. A. Taylor, **Scientific Reports** 7, 12067 (2017).
- *Temperature-dependent fine structure splitting in InGaN quantum dots*  
Tong Wang, Tim J. Puchtler, Tongtong Zhu, John C. Jarman, Claudius C. Kocher, R. A. Oliver, Stefan Schulz, and R. A. Taylor, **Applied Physics Letters** 111, 053101 (2017).
- *High-temperature performance of non-polar (11 $\bar{2}$ 0) InGaN quantum dots grown by a quasi-two-temperature method*  
Tong Wang, Tim J. Puchtler, Tongtong Zhu, John C. Jarman, R. A. Oliver, Stefan Schulz, and R. A. Taylor, **Physica Status Solidi B** 254, 1600724 (2017).

- 
- *Reduction of radiative lifetime and slow-timescale spectral diffusion in InGaN polarized single-photon sources.*

**Tong Wang**, Tongtong Zhu, Tim J. Puchtler, Claudius C. Kocher, Helen P. Springbett, John C. Jarman, Luke P. Nuttall, Rachel A. Oliver, and Robert A. Taylor, **Physical Review Applied**, under review (2019).

## Second (Main) Author

- *Ultrafast, polarized, single-photon emission from m-plane InGaN quantum dots on GaN nanowires*

Tim J. Puchtler, **Tong Wang**, Christopher X. Ren, Fengzai Tang, Rachel A. Oliver, Robert A. Taylor, and Tongtong Zhu, **Nano Letters**, 16, 7779 (2016).

- *Theoretical and experimental analysis of radiative recombination lifetimes in nonpolar InGaN/GaN quantum dots*

Saroj K. Patra, **Tong Wang**, Tim J. Puchtler, Tongtong Zhu, R. A. Oliver, R. A. Taylor, and Stefan Schulz, **Physica Status Solidi B** 254, 1600675 (2017).

- *Whispering gallery mode lasing from a monolithic InGaN/GaN nanoporous micropillar*

Tim J. Puchtler, **Tong Wang**, Huixin Xiu, Yingjun Liu, John Jarman, Rachel A. Oliver, Robert A. Taylor, Tongtong Zhu, **Applied Physics Letters**, under review (2019).

## Contributing Author

- *Highly polarized electrically driven single photon emission from a non-polar InGaN quantum dot*

Claudius C. Kocher, Tim J. Puchtler, John C. Jarman, Tongtong Zhu, **Tong Wang**, Rachel A. Oliver, and Robert A. Taylor, **Applied Physics Letters**, 111, 251108 (2017).

- *Structureactivity correlations for Brønsted acid, Lewis acid, and photocatalyzed reactions of exfoliated crystalline niobium oxides*

Yusuke Koito, Gregory J. Rees, John V. Hanna, Molly M. J. Li, Yung-Kang Peng, Tim J. Puchtler, Robert A. Taylor, **Tong Wang**, Hisayoshi Kobayashi, Ivo F. Teixeira, M. Abdullah Khan, Hannah T. Kreissl, and S. C. Edman Tsang **ChemCatChem**, 9, 144–154 (2017).

# Acknowledgement

Without the help and support from all those mentioned below, I would not have come anywhere close to completing my DPhil work. Words, especially under the command of a non-native speaker like myself, could hardly convey how grateful I am to their invaluable contribution to this journey.

First and foremost, I would like to express my sincerest gratitude to my supervisor Robert. His experience in the lab and breadth of scientific knowledge have always been my most reliable source of help throughout the years. The way he magically solves all experimental problems dispels any confusion or doubt, and brings about the knowledge and positive energy that are so desperately needed in this challenging course.

The work presented in this thesis would be non-existent without the amazing samples grown by Rachel and Tongtong, and such useful nanopillars processed by John. I could not be more thankful for the provision of myriads of samples, which became the cornerstone of literally all my research.

To our amazing theory collaborators Stefan and Saroj, I am very grateful to have known and worked with you. Your command of theoretical knowledge has cleared so many of my doubts and provided insights that I would not have had without your help.

Tim, your arrival in the lab has made such a difference in my DPhil studies that I could not imagine how much less I would achieve without your patient guidance. You taught me skills and knowledge without holding back, and guided an initially confused apprentice until he became your competent comrade in the lab. If I were a good sample, you would be the right excitation photon to trigger maximum photoluminescence. My DPhil research over the years is mostly the journey that we undertook together every day, and I am eternally grateful for all that you have done.

Special thanks to Luke for your computer programming skills, without which my experiments would have been so much less efficient. And to Claudius, whose exactitude in doing science has been truly helpful in the scientific discussions, and whose Matlab scripts helped me tremendously in analysing large sets of data.

I would also like to express my gratefulness to Singapore's Agency for Science, Technology and Research for providing me with the financial means to embark on this journey.

---

Part of the journey is the end, and the beginning to a new one in which I am willing to use my newly acquired knowledge and skills to contribute back to you.

Last but not least, thank you to my family for your years' of support. To my parents who willingly sent their only child half a globe away to pursue his studies, I could not visit you easily, but your presence, however physically far away, gives me moral support all the same. To my wife Jixuan, meeting you has been one of the luckiest things that happened to me during the years of my DPhil. The family and life support that you have been giving me for the past years are what allowed me to complete the final and most challenging stage of this journey. To beloved my parents and wife, my successful DPhil completion is as much mine as it is yours.

# Contents

<b>Publications</b>	<b>i</b>
<b>Acknowledgement</b>	<b>iii</b>
<b>Contents</b>	<b>v</b>
<b>1 Introduction</b>	<b>1</b>
1.1 Motivation and thesis layout . . . . .	1
1.2 Polarised single-photon sources . . . . .	4
1.2.1 Non-classical sub-Poissonian light sources . . . . .	4
1.2.2 Importance in quantum information sciences . . . . .	6
1.2.3 High-temperature polarised single-photon sources . . . . .	7
1.3 Semiconductor quantum dots . . . . .	8
1.4 Non-polar InGaN . . . . .	9
1.4.1 Nitride semiconductors and QDs . . . . .	9
1.4.2 Polar InGaN QDs and current challenges . . . . .	10
1.4.3 Non-polar $m$ - and $a$ -plane InGaN QDs . . . . .	13
<b>2 Experimental techniques</b>	<b>16</b>
2.1 Chapter introduction . . . . .	16
2.2 Growth of $a$ -plane InGaN QDs . . . . .	17
2.2.1 Development of epitaxial fabrication methods . . . . .	17
2.2.2 Key growth differences . . . . .	18
2.2.3 Nanopillar fabrication . . . . .	21
2.3 Micro-photoluminescence . . . . .	23

2.3.1	Two-photon pulsed excitation . . . . .	23
2.3.2	Closed-cycle cryostat . . . . .	26
2.3.3	Time-integrated and polarisation-resolved $\mu$ PL . . . . .	28
2.3.4	HBT and time-resolved $\mu$ PL . . . . .	31
<b>3</b>	<b>Cryogenic quantum light sources</b>	<b>36</b>
3.1	Chapter introduction . . . . .	36
3.2	Elucidation of polarisation properties . . . . .	37
3.2.1	Polarisation and its control in polar nitride QDs . . . . .	37
3.2.2	Origin and theoretical foundation . . . . .	38
3.2.3	Observation of linear polarisation . . . . .	44
3.2.4	Statistical significance and contrast to QW . . . . .	47
3.2.5	Angle of polarisation . . . . .	50
3.3	Ultrafast radiative lifetime . . . . .	52
3.3.1	Reduction of exciton radiative recombination rate . . . . .	52
3.3.2	Non-polar and polar nitride QD lifetimes . . . . .	56
3.3.3	Effect of QD sizes . . . . .	60
3.4	Emission of single photons . . . . .	63
3.4.1	First evidence of antibunching . . . . .	63
3.4.2	Background estimation . . . . .	65
3.4.3	Conventional background correction and limitations . . . . .	66
3.4.4	An alternative background correction method . . . . .	68
3.5	Chapter summary . . . . .	71
<b>4</b>	<b>Impact of growth on optical properties</b>	<b>73</b>
4.1	Chapter introduction . . . . .	73
4.2	QD emission and polarised antibunching . . . . .	74
4.2.1	QD and background QW . . . . .	74
4.2.2	Polarisation degree and angle . . . . .	75
4.2.3	Antibunching and single-photon purity . . . . .	77
4.3	Spectral diffusion . . . . .	81
4.3.1	Linewidth and fast-timescale spectral diffusion . . . . .	81

4.3.2	Carrier traps and slow-timescale spectral diffusion . . . . .	84
4.4	Faster radiative lifetime . . . . .	87
4.4.1	Carrier traps and oscillator strength . . . . .	87
4.4.2	Further reduction of <i>a</i> -plane QD lifetime . . . . .	88
4.5	Temperature stability . . . . .	92
4.5.1	Comparable pair of dots . . . . .	93
4.5.2	Integrated intensity and linewidth . . . . .	95
4.6	Chapter summary . . . . .	99
<b>5</b>	<b>Ultrafast polarised single-photon sources beyond 200 K</b>	<b>101</b>
5.1	Chapter introduction . . . . .	101
5.2	Observation of QD emission up to 250 K . . . . .	102
5.3	Quenching of emission intensity . . . . .	106
5.3.1	Non-radiative decay pathways . . . . .	106
5.3.2	Temperature evolution of emission intensity . . . . .	107
5.4	Redshift of emission energy . . . . .	109
5.4.1	Temperature dependence of band gap . . . . .	109
5.4.2	Temperature evolution of emission energy . . . . .	110
5.5	Broadening of emission linewidth . . . . .	112
5.5.1	Linewidth and Heisenberg's uncertainty principle . . . . .	112
5.5.2	Slow broadening of linewidth . . . . .	113
5.6	Single-photon generation at 220 K . . . . .	116
5.6.1	Filtered spectra and single-photon antibunching . . . . .	116
5.6.2	Rate of single-photon emission . . . . .	120
5.6.3	Non-classical light emission at 250 K . . . . .	123
5.7	Stability of polarisation properties . . . . .	125
5.7.1	Single-photon emission with polarisation control . . . . .	125
5.7.2	Confirmation of high-temperature polarisation . . . . .	127
5.7.3	Theoretical support . . . . .	132
5.8	Temperature-dependent fine-structure splitting . . . . .	134
5.8.1	Probing exchange interactions in nitrides . . . . .	134

5.8.2	Constancy and change of FSS with temperature . . . . .	135
5.8.3	Statistical significance and phonon scattering . . . . .	138
5.9	Chapter summary . . . . .	140
<b>6</b>	<b>Concluding remarks and outlook</b>	<b>142</b>
	<b>Bibliography</b>	<b>145</b>

# 1

## Introduction

### 1.1 Motivation and thesis layout

The exploitation of the quantum nature of light-matter interaction often relies on the presence of extreme conditions that cannot be easily applied outside the laboratory setting. In the context of polarised single-photon sources [1, 2, 3], most of contemporary developments rely on defect-based platforms [4, 5, 6, 7, 8, 9] to achieve the emission of single photons at high temperatures, with [6, 7, 8] or without [4, 5, 9] deterministic polarisation properties. These systems suffer from challenges in achieving electrical contacts, device integration, and scalable development in realistic optoelectronic platforms. On the other hand, while the physical properties of semiconductor quantum dots (QDs) [10, 11, 12] can be much more easily manipulated and controlled in the solid state, most of current QD single-photon sources [13, 14, 15, 16, 17, 18, 19, 20, 21] have operation temperatures limited to cryogenic conditions and do not possess deterministic optical polarisation properties that are necessary for their quantum information applications.

In this thesis, non-polar  $(11\bar{2}0)$  *a*-plane InGa<sub>N</sub>/Ga<sub>N</sub> QDs [22] will be investigated in detail so as to assess their ability in removing the bottleneck in polarised single-photon source development caused by the reliance on material defects, low operation temperatures, and lack of deterministic polarisation properties. The zero dimensional nature of the QDs [10] creates the necessary two-level system for the generation of single photons, while the large band gaps of nitride materials [23] produce much stronger quantum confinement than con-

ventional arsenide-based QDs, allowing for operation at higher temperatures. The use of the non-polar crystal plane also breaks the nitride valence band degeneracy, thereby introducing linearly polarised emission [24]. The threshold for on-chip temperature regulation is determined by Peltier cooling. Commercial thermoelectric coolers can currently achieve a stable temperature differential of  $\sim 100$  K, making on-chip devices operable at  $\sim 190$  K. As such, the ability of the non-polar InGaN system to generate polarised single photons at  $T > 190$  K will be examined [25, 26, 27]. In the process, investigations will also be made into the underexplored area of high-temperature solid-state QD photophysics, revealing results [28] that are of fundamental interest.

The remainder of **Chapter 1** will provide a brief introduction to the key concepts of single-photon sources, photon autocorrelation studies, and their potential applications in quantum information sciences. In these discussions, the limitations of current systems will be highlighted, leading to an introduction of wide band gap nitride QDs. The differences between crystal planes of nitride and their impact on the optical properties of QDs will be discussed.

**Chapter 2** continues to explain experimental methods that enable the optical investigations in this thesis. An overview of the detailed growth routines developed by our collaborators in the University of Cambridge will be made, highlighting the differences between the original [22] and a newly developed [27] fabrication method. The complete setup of micro-photoluminescence ( $\mu$ PL) used for optical investigations of the samples will be explained in detail, with the choice, capability and precautions of important setup components discussed.

As a semiconductor QD single-photon emitting system, its optical properties are best manifested at cryogenic temperatures due to the suppression of undesired thermally assisted processes. **Chapter 3** provides an investigation of the ability of non-polar *a*-plane InGaN QDs to emit ultrafast single photons with deterministic optical polarisation properties at cryogenic conditions [24]. The first evidence of single-photon generation is shown for this platform, along with theoretically rigorous data and statistically significant experimental results to elucidate the fast radiative lifetimes and high polarisation degrees with predefined axes.

**Chapter 4** demonstrates how two of the fabrication methods explained in Chapter 2 have impacted on the optical properties of the QDs. The effects of the reduced carrier trapping sites around QDs of the newer growth method will be addressed, and the ability of the QDs to emit ultrafast antibunched photons confirmed. While a drop in single-photon purity is observed, a further increase of the radiative recombination rate is also recorded. The potential repetition rate of these antibunched light sources are thus one of the fastest in the literature. With detailed investigation and discussion of spectral diffusion, a marked reduction in the slow timescale has been found with the new QDs, which are again on par with state-of-the-art systems. A significant increase of temperature stability has also been identified, and the potential causes and usefulness have been explained in detail. A discussion of how QDs grown with both the old and new methods should be used in conjunction for the further development of the platform is also presented.

The temperature-dependent properties of the QDs have been covered comprehensively in **Chapter 5**. The ability of *a*-plane InGaN QDs to generate ultrafast polarisation-controlled single photons is confirmed up to 220 K [25], which is also the first such evidence for any semiconductor QD system. The photophysics of thermally assisted radiative intensity quenching, homogeneous exciton transition linewidth broadening, and phonon-assisted emission energy redshift are also discussed in the context of this QD platform. As the key differentiating factor, the persistence of high polarisation degrees at elevated temperatures will again be elucidated with theoretical results and statistically significant experimental data [26]. An unusual and unexpected temperature dependence of the fine-structure splitting energy [28] has been found for the first time in a semiconductor QD system, and its possible correlation with the strength of phonon scattering has been investigated.

Conclusion of the thesis is presented in **Chapter 6**, with an overview of the current achievements in this non-polar platform, and a bright outlook of the potential for further development of *a*-plane InGaN QD-based single-photon sources and elucidation of their high-temperature photophysics.

## 1.2 Polarised single-photon sources

### 1.2.1 Non-classical sub-Poissonian light sources

By definition, a single-photon emitter is a light source that strictly emits only one photon at a time. When a laser is heavily attenuated, the light output can be treated as a close approximation for a single-photon source [29]. However, the probability of multiple photon emission is still non-zero in such a setting. For a true single-photon emitter, a two-level quantum system would be required. There are abundant resources [2, 3, 10, 30] that comprehensively cover the basic science of single-photon generation and detection. The key concepts, which revolves around photon statistics and Hanbury Brown and Twiss (HBT) experimentations [31], will be highlighted in this section.

In general, a light source can be categorised as Poissonian, super-Poissonian, or sub-Poissonian, depending on the nature of the statistical distribution of its emitted photons. An HBT experiment is designed to study the photon statistics of light sources, by investigating the second-order autocorrelation function  $g^{(2)}(\tau)$  [30] shown by,

$$g^{(2)}(\tau) = \frac{\langle I(t)I(t+\tau) \rangle}{\langle I(t) \rangle \langle I(t+\tau) \rangle}. \quad (1.1)$$

Here,  $I(t)$  is the time-dependent light intensity, and  $\tau$  is the time delay introduced into one of the detection branches of the HBT setup, as illustrated in Figure 1.1. Each time both detectors register incident light simultaneously, an event is recorded. The  $g^{(2)}(\tau)$  function can then be described by the variation of the number of events with delay  $\tau$ . The determination of the type of light source can be made in the case of zero time delay, i.e. when  $\tau = 0$ . Equation 1.1 thus becomes

$$g^{(2)}(0) = \frac{\langle I(t)^2 \rangle}{\langle I(t) \rangle^2}. \quad (1.2)$$

If the light source is a perfectly coherent one with a constant intensity, e.g. a laser, the average of the intensity squared and the square of the average intensity would be the same, giving a  $g^{(2)}(0)$  of 1. These coherent light sources are Poissonian, as their probability

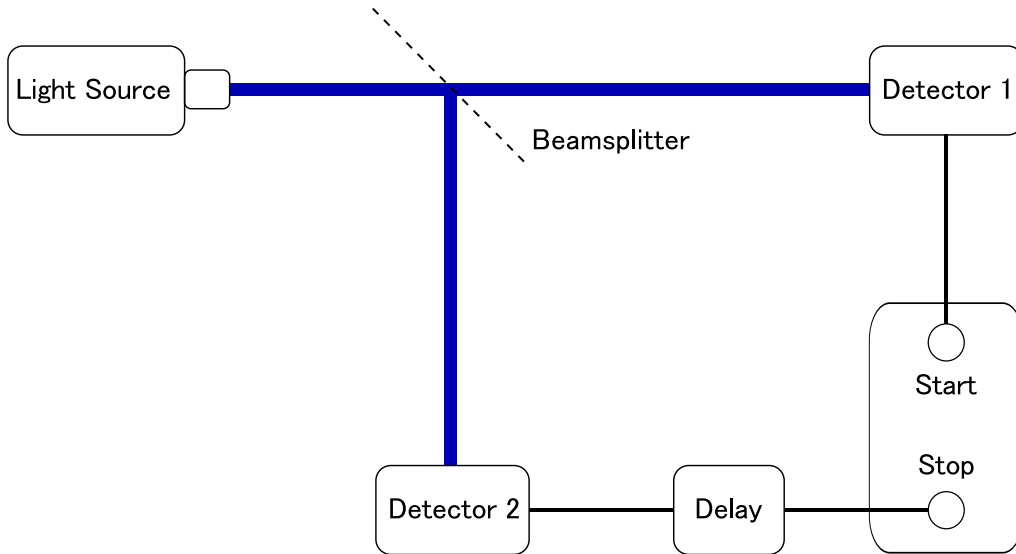


**Figure 1.1: Typical setup for a Hanbury Brown and Twiss experiment.** Photons from the light source are incident onto the 50 : 50 beamsplitter and directed towards two identical photon detectors. A signal delay can be introduced, physically or digitally, into one of the detection arms. An event is recorded when the start and stop “switches” in the photon counting device are triggered simultaneously.

distribution of photon detection follows Poisson statistics, where the standard deviation  $\Delta n$  and mean  $\bar{n}$  follow  $\Delta n = \bar{n}$  [30].

For most common light sources, the emission is not coherent and the intensity fluctuates with time. In this case, it can be mathematically shown that  $g^{(2)}(0) > 1$  is always the case [30]. Intuitively, the squaring process of  $\langle I(t)^2 \rangle$  exaggerates the difference of  $I(t) - \langle I(t) \rangle$  more at  $I(t) > \langle I(t) \rangle$  than at  $I(t) < \langle I(t) \rangle$ , giving a greater numerator and a  $g^{(2)}(0)$  larger than unity. The photons are emitted in groups together, producing “bunched” light with a super-Poissonian distribution ( $\Delta n > \bar{n}$ ).

For an ideal single-photon source, the one photon incident on the beamsplitter can only reach one of the two detectors at a given time, but never both simultaneously. Therefore, it is not possible to register any events at  $\tau = 0$ , resulting in  $g^{(2)}(0) = 0$ . In reality, if there are any other sources of photons present in the HBT experiment, the probability of recording events at  $\tau = 0$  will increase, and the  $g^{(2)}(0)$  value will be greater than 0. For the development of a single-photon platform, a lower  $g^{(2)}(0)$  is always desirable

as it shows the purity of the quantum emitter that is essential for its applications. For a greater probability of single- than multiple-photon detection, the number of events at  $\tau = 0$  should hence be less than half of those at  $\tau \neq 0$ , i.e.  $g^{(2)}(0) < 0.5$ . A quantum mechanical treatment [10] of the second-order autocorrelation function could also yield a minimum  $g^{(2)}(0)$  of 0.5 for the presence of a two-photon state. However, such treatment assumes all photon states to be in the same basis, originating from the light source alone. In realistic systems, the degradation of single-photon purity is often more significantly affected by the contamination from other undesired and unavoidable light sources, e.g. underlying quantum wells (QWs) emitting in the same spectral range for nitrides. The photons from these light sources cannot be considered in the same basis as those from the single-photon emitter, making the quantum mechanical result less relevant and useful than the intuitive understanding in realistic settings. It is also worth noting that the concept of single-photon sources requires the quantum nature of light. Without considering light as photons (i.e.  $I(t) = n(t)$ ), the value of  $g^{(2)}(0)$  will always be greater or equal to 1. Light sources with  $g^{(2)}(0) < 1$  follow sub-Poissonian statistics ( $\Delta n < \bar{n}$ ), and produce “antibunched” photons.

### 1.2.2 Importance in quantum information sciences

One of the most important applications of polarised single-photon sources are in secure quantum communication [32, 33, 34, 35, 36, 37, 38, 39]. Bits of information can be stored as polarisation states of each of the emitted single photons. In the case of eavesdropping, measurements have to be performed on existing photons, thereby altering their states and revealing the act of information stealth. If a multiple-photon source is used, the same information will be stored in more than one photon at a given time. The eavesdropper could in theory utilise the additional photons to access contents of the communication, without the risk of being found. As such, a highly pure ( $g^{(2)}(0)$  very close to 0) polarised single-photon source would be the key component for fundamentally secure communications. Such proof-of-concept free-space quantum communication has now been demonstrated in daylight over a distance of  $> 50$  km [39]. With single-photon devices cryogenically cooled and embedded in satellites, these developments provide a potential pathway towards the

demonstration of satellite-satellite and satellite-ground quantum network key distributions.

Another important application of polarised single-photon sources is in all-optical quantum computation [40, 41, 42, 43, 44]. With the beginning of the failure of Moores law and the increasing bottleneck of copper interconnects, the performance of classical computers has been approaching its fundamental limit. The vast performance leaps with qubit-based computers would require the generation of indistinguishable [45, 46] single photons, and benefit from the ability to manipulate their polarisation states. At the moment, quantum computers with complexity comparable to that of earlier classical computers have been demonstrated using arsenide quantum dots [44].

### 1.2.3 High-temperature polarised single-photon sources

In the latest developments for both aforementioned applications, the single-photon devices need to be cryogenically cooled, and the control of polarisation can only be achieved externally at a cost of 50% external quantum efficiency. The highest reported temperature at which an arsenide-based QD still generates single photons with a  $g^{(2)}(0)$  of  $< 0.5$  is 120 K [47]. Typically, their intensity would decrease by more than two orders of magnitude before the temperature increases beyond 100 K. Furthermore, it is also non-trivial to engineer and effectively control optical polarisation in InAs nanostructures [48, 49, 50, 51, 52, 53], particularly due to their relative insensitivity to shape anisotropies. Therefore, arsenide QDs are less suitable for the generation of polarised single photons at on-chip thermal conditions.

On the other hand, deeply confined trap states in the defects of various materials have been shown to demonstrate photon antibunching without the need for cryogenic cooling. Fluorescent point defects have been found in the colour centres of both nanocrystals and compound semiconductors, such as nitrogen and silicon vacancy (NV and SiV) centres in diamonds [4, 54, 55, 56], and colour centres in SiC [7, 57] and ZnO [9, 58, 59]. These systems have all been reported to manifest room temperature single-photon generation. Oxygen-based defects in carbon nanotubes [5, 60] have been shown to exhibit single-photon emission at ambient conditions at the telecommunication wavelength of  $1.55 \mu\text{m}$ . Studies

reveal that QD-like nanostructures based on perovskites can also emit single photons at room temperatures [61]. More recently, defects embedded in GaN wafers [8, 62, 63] and 2D hexagonal boron nitride (hBN) [6, 64] have also demonstrated similar non-classical light emission operating at high temperatures. In particular, the single-photon characteristics of hBN defects remain even at a temperature of 800 K [64].

However, the challenge of defect-based systems lies in their reproducibility, controllability, and scalability. They cannot be easily integrated into existing semiconductor platforms for further development, thereby significantly limiting their prospect for future applications in quantum information sciences. For this reason, semiconductor QDs, especially those with band gaps wider than arsenides, such as phosphides [65, 66, 67, 68], selenides [69, 70, 71], and nitrides [72, 73, 74, 75], remain one of the most relevant and important branches of single-photon research.

### 1.3 Semiconductor quantum dots

Thanks to developments in advanced material fabrication techniques, the dimensions of conventional bulk semiconductors can be controlled and reduced to the order of  $\sim 10$  nm, comparable to the *de Broglie* wavelength of the carriers. By surrounding these small-scale nanostructures in a matrix material with a different band gap, quantum confinement is realised with their band offset as the confinement potential [10]. Depending on the number of confined dimensions, these nanostructures can be categorised into quantum wells with one, nanowires with two, and QDs with all three spatial dimensions confined. In the case of QDs, quantisation of the carrier kinetic energy in all directions leads to delta-function-like density of states and atom-like discrete energy levels. Therefore, although QDs are physically more than  $10^3$  times larger than a single atom, they exhibit similar optical properties that were once considered exclusive to atoms [76, 77, 78] and molecules [79] only, e.g. single-photon generation. Furthermore, the composition, dimension, geometry, and electrical contacts of semiconductor QDs can be manipulated in the solid state much more easily than single atoms or defects. It is also relatively more straightforward to investigate the deterministically fabricated wafers in characterisation studies, leading to more efficient and better understanding of the properties of semiconductor QDs.

## 1.4 Non-polar InGaN

### 1.4.1 Nitride semiconductors and QDs

Previous sections have highlighted the need for wide band gap semiconductors, which combine the benefits of solid-state QDs with deep confinement energies similar to those of defect-based systems. The band gaps of GaN, InN, and AlN are 3.4 [80, 81], 0.7–0.8 [23, 82], and 6.1 eV [23] respectively. Through binary (e.g. GaN in AlN matrix) and ternary (e.g. InGaN in GaN or AlGaN matrix) compound semiconductors, very large band offsets and high quantum confinement energies could be achieved using nitrides.

However, unlike other III-V semiconductors such as InAs, the development of nitrides has been slow and the properties of nitrides are much less well understood. One of the key reasons was due to poor material quality. For instance, very high threading dislocation densities could induce the formation of carrier traps, which facilitate undesired non-radiative carrier recombination [74]. A breakthrough in nitride research only happened in 1994 when Nakamura *et al.* developed blue light-emitting diodes (LEDs) using InGaN [83]. Even so, the high emissivity of these LEDs in samples with significant threading dislocation was not fully understood. One of the explanations suggests the probable formation of metallic rich QD-like fluorescent centres under the influence of strain fields caused by the threading dislocations. These unintentionally grown ensembles of nitride QDs could significantly increase the brightness of the LEDs [74, 84].

Till now, there have been various methods for the intentional fabrication of nitride QDs [22, 75, 85, 86, 87, 88, 89, 90, 91, 92, 93, 94, 95, 96]. One of the most successful developments has been in site-controlled dot-in-nanowire systems, where a very thin (2–5 nm) layer of GaN with a diameter of  $\sim 20$  nm is embedded at the apex of a GaN/AlGaN core-shell nanowire [72, 97, 98, 99]. The strong confinement allows this system to operate as a single-photon source up to 350 K and show detectable photoluminescence up to 400 K, which are both the highest in all reported semiconductor QD literature. Each nanowire structure is separated from their adjacent neighbours by  $\sim 20 \mu\text{m}$ , allowing excellent scalability and ease of re-investigation.

However, this development is limited by the non-trivial challenge of adding electrical contacts, and till now still requires optical pumping for operation. Another problem lies in the emission wavelength of GaN QDs, which is in the UV range and less useful in realistic single-photon applications. On the other hand, by adding indium to GaN and creating the ternary nitride alloy of InGaN, their emission energy can be tuned to the blue end of the visible spectrum. While the exciton energies are still not near telecommunication wavelengths, blue light is useful in short-distance free-space data transmission and detection [100]. However, the fabrication of InGaN QDs itself has proven to be a more involving task than that of their GaN counterparts, particularly due to the difficulty in indium incorporation, dot formation, and the achievement of good material qualities [27]. As a result, InGaN systems comparable to the aforementioned site-controlled GaN dot-in-nanowire platform have not yet been developed. Without similar ultra-small QDs in ultra-clean environments, the undesired physical effects of the nitride material, which will be explained in the following section, dominate in the QDs' operation as polarised single-photon sources.

#### 1.4.2 Polar InGaN QDs and current challenges

Two possible crystal symmetries exist in nitride materials—hexagonal wurtzite and cubic zinc-blende [101, 102]. In particular, zinc-blende nitride nanostructures have been much less researched due to their thermodynamic instability at ambient conditions. The current growth methods of these cubic QDs require plasma-assisted molecular beam epitaxy [103], which was not available for the research period of this thesis. Therefore, only wurtzite nitrides are considered here. An illustration of the relevant crystallographic planes of the hexagonal symmetry is presented in Figure 1.2(a). With Miller-Bravais indices denoting the (0001) *c*-plane, (1 $\bar{1}$ 00) *m*-plane, and (11 $\bar{2}$ 0) *a*-plane, a set of 3 mutually orthogonal crystal axes is defined and will be used throughout the discussion of this thesis.

The (0001) *c*-plane is also called the polar plane, due to the internal electric fields built into the wurtzite nitride material along this direction. These internal fields are comprised of two components. The first component arises from the non-zero electronegativity offset caused by the asymmetric spread cationic and anionic charges, resulting in a permanent

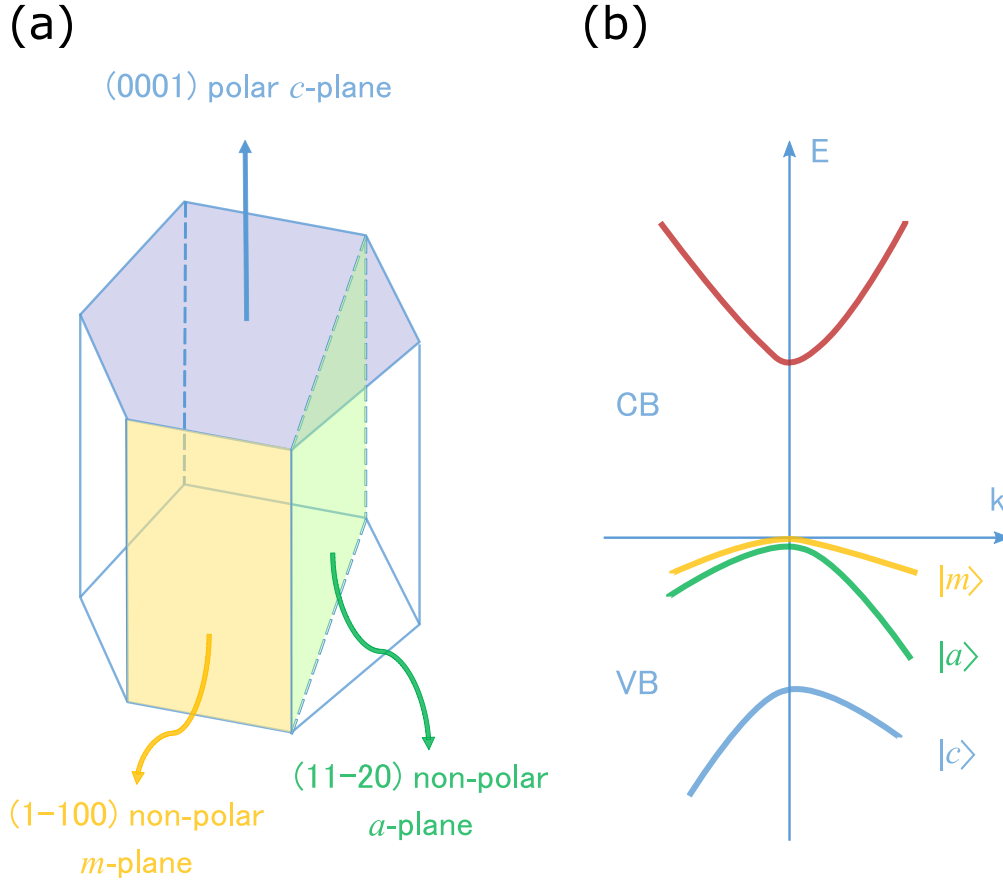


**Figure 1.2: Wurtzite nitride crystallographic planes and band structure.** (a) A set of mutually orthogonal basis for the wurtzite nitride structure. The polar  $c$ -plane and non-polar  $m$ - and  $a$ -planes are also denoted by Miller-Bravais indices. (b) Band structure of a (0001) polar  $c$ -plane bulk GaN. Each valence band has orbital characteristics of the  $|m\rangle$ -,  $|a\rangle$ - and  $|c\rangle$ -like states respectively. With a small contribution of spin-orbit interaction, the first two valence bands are nearly degenerate at the  $\Gamma$  point. The illustration is not drawn to scale.

dipole along the crystal  $c$ -direction. However, in the context of an InGaN/GaN QD, the magnitude of this spontaneous polarisation is small compared to the second component, which is caused by piezoelectricity. The lack of inversion symmetry of the wurtzite crystal structure gives rise to non-zero piezoelectric constants. Strain caused by the lattice mismatch between InGaN and GaN induces an electric field along the crystal  $c$ -axis, adding to the internal spontaneous polarisation in the same direction [73].

The built-in fields cause quantum-confined Stark effect (QCSE) [104], which shifts the

energy of the QDs ground state transition by  $\delta E$  as described by

$$\delta E = -\mu F + \alpha F^2. \quad (1.3)$$

In Equation 1.3,  $F$  is the magnitude of the built-in fields, and  $\mu$  and  $\alpha$  are constants such that the linear term is always greater than the quadratic term [105, 106, 107]. Furthermore, the electron and hole states are moved further away from each other, with a decreased spatial overlap of their wavefunctions [108]. As a result, the oscillator strength of the exciton is reduced and the rate of radiative recombination is slowed down. Measurement of polar InGaN QDs shows that their radiative lifetimes are around 1 to 10 ns (see Section 3.3.2), which are an order of magnitude slower than situations where QCSE is minimised. Detailed analyses of the radiative recombination lifetimes can be found in Sections 3.3 and 4.4.

Another challenge of polar  $c$ -plane nitride is in the lack of desirable optical polarisation properties. Figure 1.2(b) illustrates the band structure of bulk  $c$ -plane GaN [26]. The valence band degeneracy is first lifted by the positive crystal field splitting energy, pushing the state with  $|c\rangle$ -like orbital characters away from the  $|m\rangle$ - and  $|a\rangle$ -like states. The spin-orbit interaction breaks the degeneracy of the top two valence band states. However, due to the weak and negligible spin-orbit coupling, these two bands are still very close to each other near the  $k = 0$  point, giving rise to band mixing effects [24]. As a result, the hole wavefunctions have a combination of  $|m\rangle$ - and  $|c\rangle$ -like states, and are thus expected to be circularly, rather than linearly, polarised. However, due to the difference in hole effective masses in the first two valence band states, any shape anisotropy of the nanostructure would break their degeneracy [24, 109] and cause a change in the degree of valence band mixing. Depending on the extent of anisotropy, the  $|a\rangle$ -like state could be shifted to a relatively lower energy, as shown in Figure 1.3. Thus, the contribution of  $|a\rangle$ -type characteristics will be reduced, increasing the degree of optical linear polarisation. In a self-assembled system where the anisotropy of each individual QD is random, the degree and direction of optical polarisation will also be random, making it difficult for the development of single-photon sources with deterministic polarisation properties. The sensitivity of optical polarisation properties to shape anisotropies can also be used as a direction for the

engineering of nanostructures, thereby controlling the direction and degree of polarisation. Further discussion of these attempts can be found in Section 3.2.1.

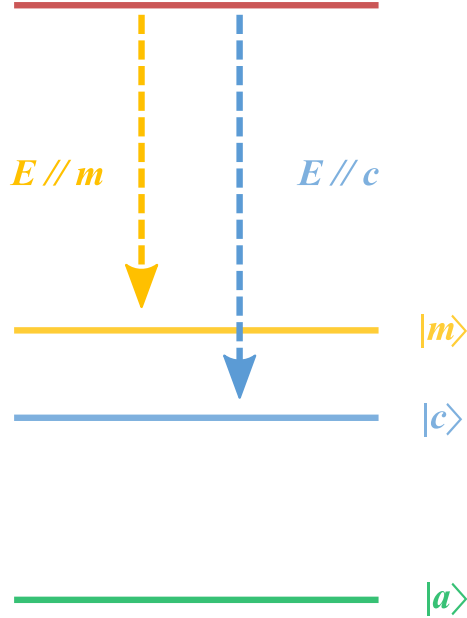


**Figure 1.3: Order of energy levels of a wurtzite nitride system with a strong symmetry breaking of the first two valence bands.** A large anisotropy could in principle push the  $|a\rangle$ -like state away, resulting linearly polarised emission from the first two states. Such a situation can also be achieved with quantum confinement along the crystal  $a$ -direction, e.g. in  $a$ -plane QWs or QDs with a stronger confinement along the  $a$ -direction.

### 1.4.3 Non-polar $m$ - and $a$ -plane InGaN QDs

Solutions to combat the problem of QCSE and optical polarisation in nitride QDs are not straightforward. As mentioned previously, the use of cubic zinc-blende nitride could circumvent the issue of QCSE, which is only intrinsic to the hexagonal wurtzite symmetry. Single-photon sources based on cubic GaN have been demonstrated in one report from the literature, which indeed shows fast radiative lifetime of 360 ps [103]. However, aside from the difficulty of fabrication and lack of thermodynamic stability, cubic nitride does not have intrinsic optical polarisation properties.

On the other hand, if the QDs are grown along one of the non-polar planes of wurtzite nitride [22, 89, 110, 111, 112, 113] as shown in Figure 1.2(a), the internal fields along the

crystal  $c$ -direction could be minimised. This is especially so for lens-shaped QDs with a base of  $\sim 30$  nm in diameter and a height of  $< 5$  nm. The polarisation discontinuity at the material interface is greatly reduced, and only limited to the side facets with a small component contributing to the total internal field. Furthermore, the stronger confinement along the crystal  $a$ -direction breaks the valence band degeneracy, and creates a situation similar to that presented in Figure 1.3. Both theoretical and experimental work has been done to demonstrate linearly polarised emission from non-polar nitride nanostructures [24, 26, 114, 115, 116]. A comprehensive investigation of the optical polarisation properties of  $a$ -plane InGaN QDs is presented in Section 3.2, and their temperature dependence in Section 5.7.

However, one of the key challenges in the development of non-polar InGaN QDs lies in their fabrication—a suitable substrate needs to be identified to enable their growth. The obvious choices of non-polar bulk GaN substrates, including high-quality ammonothermal  $a$ - and  $m$ -plane ones, fail to result in dot formation in our investigations. For non-polar  $a$ -plane, the  $r$ -plane of sapphire serves as a useful substrate. The details of two available  $a$ -plane QD fabrication routines [22, 110] will be explained in 2.2. In the case of non-polar  $m$ -plane QDs, there are no useful substrates for planar epitaxial fabrication that could result in dot formation. As a workaround, a method has been designed to allow QD growth on the sidewalls [117] of InGaN nanowires [112]. Back to Figure 1.2(a), these sidewalls are parallel to the crystal  $m$ -direction, and the resultant nanostructures should be non-polar  $m$ -plane QDs. More details of this method can be found in our publication [112]. Ultrafast radiative lifetimes with a  $< 300$  ps average and statistically high optical polarisation degrees have both been verified, which are signatures of reduced QCSE and valence band symmetry breaking.

Although this novel growth routine makes the fabrication of  $m$ -plane QDs possible, it falls into the same category as GaN/AlGaIn dot-in-nanowire systems, whereby further development of electrical contacting is much more challenging than a planar epitaxy-grown platform. Furthermore, the restricted geometry of nanowires makes local heat dissipation inefficient. As a result, the single-photon generation is limited to a sample temperature of 100 K. Since these  $m$ -plane QDs does not meet the criteria of  $> 190$  K operation as

explained previously, this particular development of ours will not be discussed in detail in this thesis. Due to the similarity of  $m$ -plane QDs optical properties to their  $a$ -plane counterparts, this thesis will focus on the thorough investigation of  $a$ -plane QDs, with minute differences to  $m$ -plane ones noted when necessary. The studies will hence form a holistic understanding of the characteristics of non-polar InGaN/GaN QDs in general.

## 2

# Experimental techniques

## 2.1 Chapter introduction

In this chapter, an overview of the experimental techniques involved in the fabrication and optical characterisation of non-polar  $a$ -plane InGaN QDs is provided. The growth of all relevant QD samples has been carried out by our collaborators in the centre of gallium nitride of the University of Cambridge. The details of the original epitaxial growth routine [22, 110] and a recent successful attempt [27] in improving the method are explained here. The key differences in their resultant nanostructures are also discussed, leading to further elucidation of their impact on optical properties in Chapter 4. The setup for micro-photoluminescence used for all relevant experiments in the thesis is introduced, which is capable of time-integrated, time-resolved, polarisation-resolved, and HBT measurements at temperatures between 4 to 320 K. Important optical components are explained in detail. In particular, the use of two-photon pulsed excitation, closed-cycle rather than continuous-flow cryostat, precautions in polarisation-resolved studies, and the necessity of tuneable bandpass filters and position optimisation in autocorrelation studies are closely examined.

## 2.2 Growth of *a*-plane InGaN QDs

### 2.2.1 Development of epitaxial fabrication methods

There are currently two available methods for the fabrication of *a*-plane InGaN QDs, both of which are metal-organic vapour phase epitaxy (MOVPE) routines. The modified droplet epitaxy (MDE) [22, 110] routine was the original successful attempt, the exact processing details of which can be found in the publications and are briefly outlined in the next section. This method is adapted from previous routines [118, 119] used for the growth of polar nitride QDs. Using MDE, InGaN QDs with either GaN [22] or AlGaIn [120] barriers can be fabricated. However, due to the relatively poorer material quality of QDs with AlGaIn matrix, it is difficult to elucidate their optical properties, and a study is not included in this work. In MDE, a thermal annealing step [118] of the wafer is used to induce decomposition of the InGaIn epilayer and the subsequent formation of metallic droplets, which are crucial for dot formation upon capping. However, this indispensable fabrication step also introduces a multitude of local carrier trapping sites during the breaking of the InGaIn epilayer. Thus, several optical properties of the resultant QDs, such as brightness, temperature performance, and spectral diffusion, could be adversely affected.

In order to resolve this issue and improve upon the quality of the QDs, modifications to the original MDE routine have been attempted so as to replace the annealing step with a process that does not involve the InGaIn epilayer decomposition. A two-temperature (2T) method [121] was proposed and developed a year after the development of the MDE routine. Using a temperature ramp after epilayer deposition and before capping, this method aims to induce Stranski-Krastanov (SK) type island formation during the gradual thermal variation of the environment. While weakly emitting QDs with sub-500 ps lifetimes have been observed [121], it has not been possible to study more complex optical properties such as polarisation and single-photon emission with these 2T QDs, due to their much lower sample emissivity, dot density, and brightness.

In the meantime, a quasi-two-temperature (Q2T) routine [27] was developed, and drastically improved the sample qualities grown with the previous 2T method. In optical investigations, these Q2T QDs also exhibit several improved characteristics compared to

the original MDE ones. The key change is the use of a thin low-temperature capping, along with other optimisations of growth temperatures for better material incorporation. In the following section, the details of the Q2T method and its key growth differences from MDE will be explained. Chapter 4 will provide a comprehensive investigation comparing the radiative lifetime, temperature stability, spectral diffusion, polarisation, and single-photon emission of QDs grown by these two methods. At the end of that chapter, whether the new Q2T method should replace MDE for future development of the *a*-plane platform will also be discussed.

### 2.2.2 Key growth differences

In both MOVPE methods, a  $6 \times 2$  in *Thomas Swan* close-coupled showerhead reactor is used with *r*-plane sapphire as substrate.  $(11\bar{2}0)$  *a*-plane GaN is then grown as the pseudo-substrate, before the deposition of InGaN epilayer with trimethylgallium, trimethylindium and ammonia as precursor gases.

#### Growth temperature

The first difference is the temperature at which the epilayer deposition occurs. For more indium incorporation, a lower temperature is required. Due to projected loss of indium in the annealing-induced epilayer decomposition in MDE, a greater amount of indium is needed during the deposition than in the Q2T method. As such, temperatures of 690 and 675 °C are used for Q2T and MDE respectively [27]. It is important to note that the *a*-plane InGaN material is highly sensitive to growth temperature changes, and a difference of 15 °C has a significant impact on both the incorporation of indium and the sample quality. Defects are more likely to form at lower temperatures. In this case, the MDE epilayer could possess a higher defect density, potentially hindering the formation of dots, leading to greater numbers of local carrier traps, and opening more pathways of non-radiative recombination.

Furthermore, due to the higher epilayer deposition temperature, there is greater room to alter the amount of indium in these Q2T nanostructures. As such, the wavelength of a Q2T sample can be more easily tuned towards the redder or bluer end of the spectrum

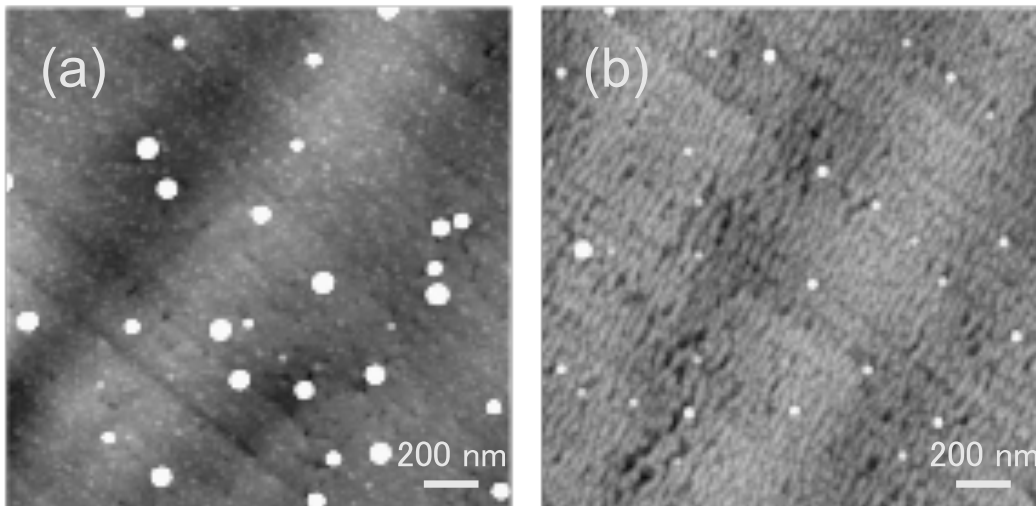


**Figure 2.1: Atomic force microscope images of uncapped *a*-plane InGaN QD samples.** Metal-rich regions are indicated by bright spots. (a) Q2T metallic islands formed on top of a relatively smooth InGaN epilayer, exhibiting a two-size bimodal “dot” distribution. (b) MDE metallic droplets formed on top of a significantly disrupted epilayer made of fragmented InGaN QW. The AFM images are obtained by our collaborators in the University of Cambridge.

during growth. In  $\mu$ PL experiments, the emission energies of Q2T QDs range from 410 to 560 nm, larger than the typical range of 440 to 520 nm observed in MDE samples. The more flexible and easier control of QD emission energy allows for more attainable wavelengths of these potential single-photon emitters.

### Annealing vs. temperature ramping

The second difference lies in the use of a thin capping and a temperature ramping step in the Q2T routine. In the original MDE method, an annealing process [118] lasting for 30 s in nitrogen atmosphere is immediately carried out after InGaN epilayer deposition at the same temperature of 675 °C. During this stage, the epilayer decomposes and induces the formation of metallic droplets. For dot formation, a 10 nm thick GaN cap is grown at the same temperature, during which ammonia and the metallic droplets are thought to re-react forming QDs. The temperature is finally increased to 1050 °C, when another 10 nm GaN cap is grown in hydrogen atmosphere.

The Q2T routine aims to circumvent the annealing process at low temperature, by em-

ploying a similar indium-clustering effect without the need for epilayer decomposition. Immediately following the deposition of InGaN epilayer, a first GaN capping layer with a thickness of 2 nm is grown at the same temperature in the Q2T routine. After this initial capping, the temperature is ramped from 690 °C until it stabilises at 860 °C in a period of 90 s. It is important to note that the very thin 2 nm cap—introduced specifically to improve material quality [122]—is unlikely to cover the larger 3D nanostructures. As such, the sample is mostly uncapped during this 90 s ramping process, similar to annealing but without the requirement of a much lower temperature or the decomposition of the InGaN epilayer. During this ramping process, SK-like indium-rich islands are thought to form on top of a much less disrupted InGaN epilayer, which is likely preserved by the thin cap. As shown in the atomic force microscope (AFM) images in Figure 2.1(a) and (b), the underlying InGaN QW is much smoother for the Q2T sample, compared to the heavily fragmented morphology of its MDE counterpart. Most possibly due to in-plane strains in the annealing and decomposition process, these fragmented quantum wells (fQWs) are parallel to the [0001] crystal  $c$ -axis [22]. As such, the Q2T routine is able to produce metal-rich regions like MDE without requiring a low-temperature anneal, thereby retaining the undisrupted InGaN epilayer morphology for a potentially decreased number of carrier trapping sites [123].

The final capping for Q2T dot formation happens after the temperature ramp, and is carried out at the same high temperature of 860 °C. Similar to the MDE case, the SK-like metallic islands are thought to re-react with ammonia during the growth of an 8 nm GaN layer. Again, the higher dot formation temperature (860 vs 675 °C) also allows Q2T samples to have fewer defects and carrier traps.

### Nanostructure dimensions

The third significant difference is the resultant QD size and underlying QW thickness. It can be observed that in Figure 2.1(a), there are generally two different sizes of metal-rich clusters. A more detailed investigation revealed that these uncapped Q2T QDs exhibit a bimodal size distribution. As shown in Figure 2.2(a), Gaussian distribution fittings yield mean diameters of 1.5 and 15 nm. Further AFM analyses also give estimated heights of  $< 2$

and  $> 10$  nm for these two categories respectively. In contrast, uncapped MDE QDs have an average height of  $< 5$  nm and diameter of  $\sim 30$  nm, without any observable non-Normal size distributions. While it is non-trivial to confirm the exact QD sizes after capping, the results presented above do predict that there are large variations in the dimensions of Q2T QDs. The effect of size differences on the optical properties of MDE QDs, such as polarisation and radiative recombination lifetimes, will be examined in Chapter 3. The findings will then be re-confirmed with Q2T QDs with even larger size variations in Chapter 4, when all other relevant optical properties of MDE and Q2T samples are also compared. Another physical dimension difference is caused by the amount of material needed for the InGaN epilayer. To achieve the highest sample emissivity, the MDE routine requires an epilayer thickness of 10 monolayers (ML), while that in Q2T's recipe is optimised at 16 ML. Although carrier generation in QWs differs from bulk materials, a thicker QW does have a higher capacity to produce more carriers for recombination. Furthermore, the 10 ML thick fQWs in MDE samples might not be emitting as strongly as QWs that are undisrupted. As such, it would be more likely to observe generally stronger QW emission from Q2T samples. For purer single-photon emission, it is undesirable to for the QD signal to be contaminated by the background QWs. Therefore, Q2T samples might have worse single-photon performance than MDE ones—another prediction which will be tested in Chapter 4.

### 2.2.3 Nanopillar fabrication

To isolate QDs and increase photon extraction efficiencies, nanopillars were post-processed for both Q2T and MDE samples. Silica nanospheres [124] with a diameter of 180 nm are drop-casted onto the sample wafer, and act as process masks. After dry-etching to a depth of  $\sim 350$  nm (deeper than the active InGaN region), ultra-sonication and buffered-oxide etch are performed on the samples to remove the residual nanospheres. A complete description of the processing steps can be found in the publication [24]. Examples of the resultant nanostructures for both Q2T and MDE samples are shown in Figure 2.2(b) and (c). With the same masking and etching processes, the dimensions of the resultant nanopillars are

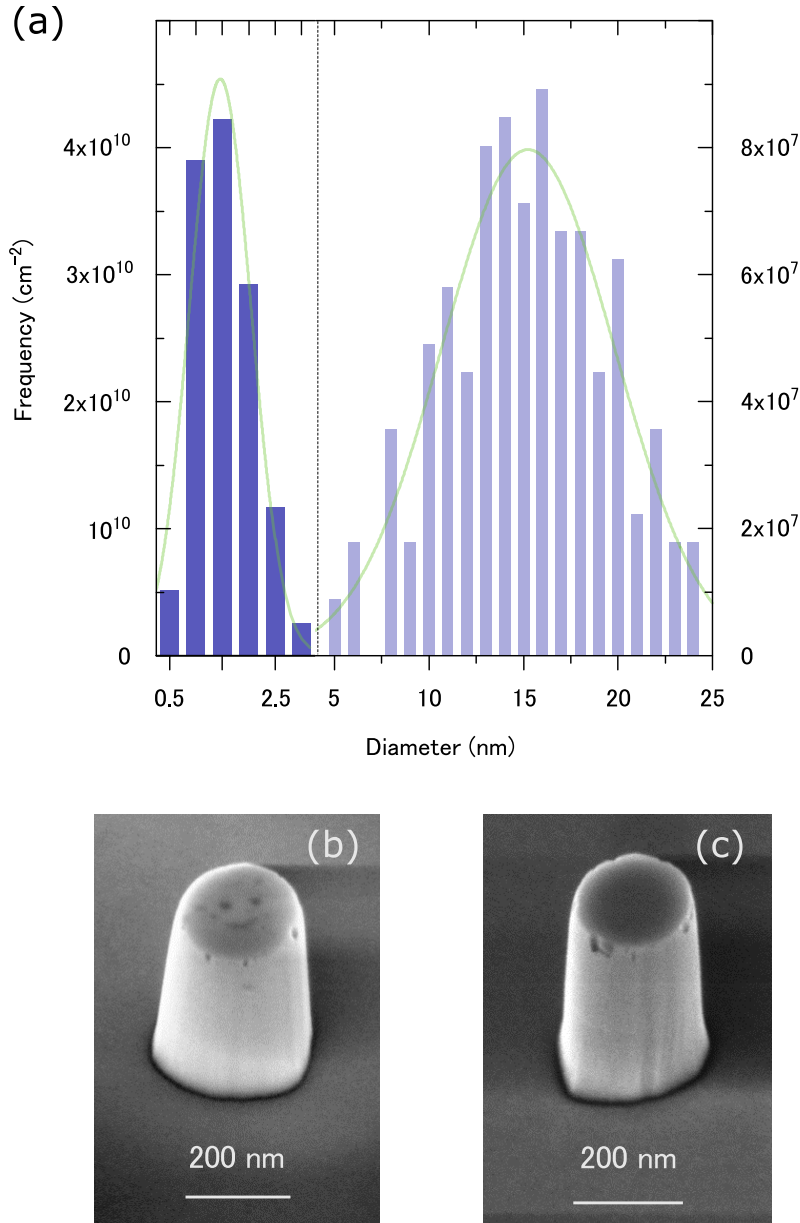


**Figure 2.2: Uncapped QD size distribution of Q2T samples and nanopillars for both MDE and Q2T QDs.** (a) Bimodal distribution of the uncapped Q2T QD size, where both components are fitted with Gaussian profiles. (b) A typical nanopillar post-processed for the Q2T sample for isolation of QDs and increase of photon extraction efficiencies. (c) A typical nanopillar for the MDE sample, which is very similar to the Q2T counterpart under the same processing recipe. The QD size data and SEM images are obtained by our collaborators in the University of Cambridge.

highly reproducible for both samples and should expedite optical investigations to similar extents.

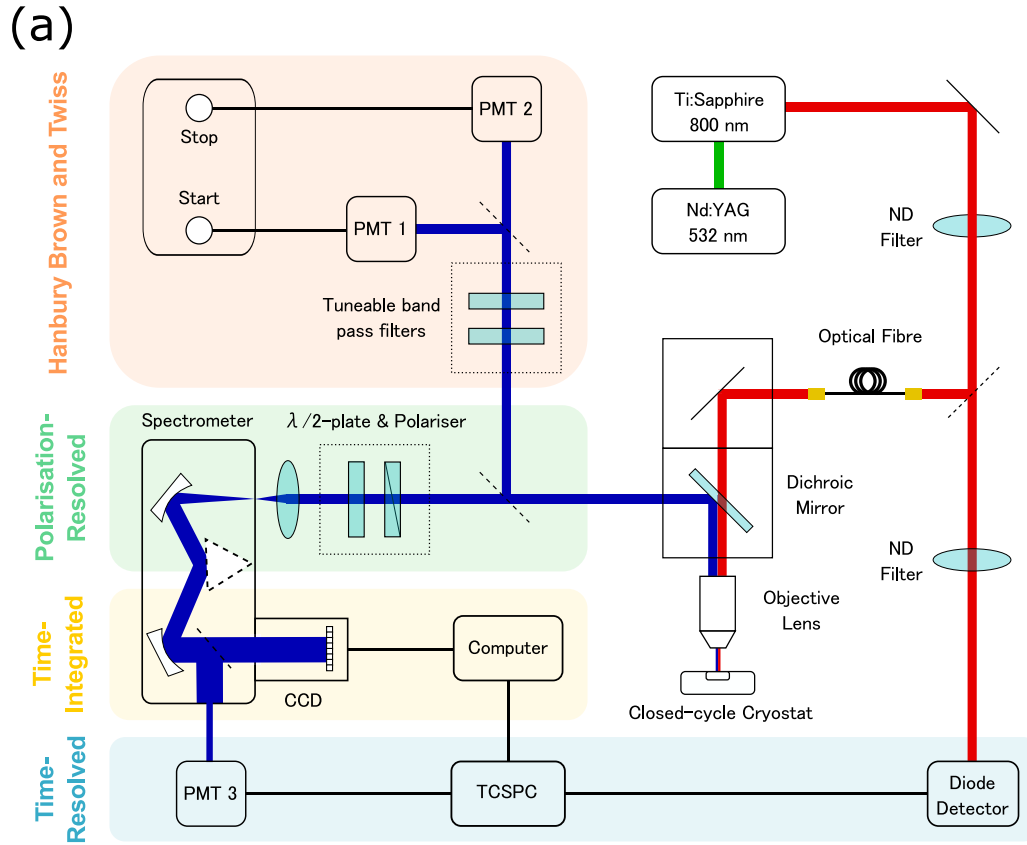
It is worth noting that for experiments detailed in this thesis, no additional distributed Bragg reflector [125, 126, 127] structures are included in the samples. As such, the nanopillars do not produce quantum electrodynamic [128, 129] enhancements, and only improve the efficiency of light extraction. As the diameter of the nanopillars are much smaller than the laser spot, a significant portion of undesired background emission will be removed, resulting in better signal-to-background ratio of the QDs in the case of a single nanopillar excitation. However, unlike previously mentioned dot-in-nanowire GaN systems [97, 99, 130], the diameter of the  $a$ -plane QDs are much smaller than the pillars themselves, and several single QDs could be present in each nanopillar. In optical studies, it is still necessary to spectrally isolate the QD of interest, with methods explained in the following sections.

### 2.3 Micro-photoluminescence

Micro-photoluminescence refers to the process of photon generation triggered by the optical excitation of an emitting medium at micron scales. The optical setup used in the  $\mu$ PL investigation of non-polar  $a$ -plane InGaN QDs is shown in Figure 2.3. All optical characterisation data in this thesis have been obtained using relevant sections of this setup.

#### 2.3.1 Two-photon pulsed excitation

The source of excitation is a *Coherent Mira 900* Ti:Sapphire laser, which can produce pulsed excitations with a repetition rate of 76 MHz ( $\sim 13$  ns between pulses) across a tuneable range of 700 to 1000 nm. A *Coherent Verdi V8* laser uses the second harmonic generation of a 1064 nm Nd:YVO<sub>4</sub> crystal to provide 532 nm pumping of the Ti:Sapphire with a power of 8 W. The use of pulsed excitation not only provides sufficient instantaneous power to trigger optical emission in the QDs, but also makes time-resolved lifetime measurements possible. The Ti:Sapphire laser can operate either in a picosecond mode with a pulse duration of 1 ps and energy resolution of 1.3 meV, or in a femtosecond mode



(b)

Figure 2.3:  $\mu$ PL setup used for the optical characterisation of non-polar  $a$ -plane InGaN QDs. (a) A schematic showing a Ti:Sapphire laser system, whose output is transmitted by a single-mode fibre and directed towards a dichroic mirror. A  $100\times$  objective focuses the beam to a  $1\mu\text{m}$  spot on the sample housed in a closed-cycle cryostat. The PL from the sample is directed to setups for time-integrated, time-resolved, polarisation-resolved, or HBT measurements. (b) A photograph of the actual setup.

where the pulse duration is 100 fs and the energy uncertainty increases to 13 meV due to Heisenberg's uncertainty principle. For QD-focused investigations detailed in this thesis, the narrower laser bandwidth of picosecond mode is preferred and used for all experiments. The output power of the Ti:Sapphire laser is usually around 1 W, which is then reduced to 150–200 mW by ND filters before entering a single-mode fibre with a core of 4  $\mu\text{m}$ . With a coupling efficiency of  $\sim 50\%$ , the output power is 60–90 mW. The fibre also acts a spatial filter and provides a smooth near-Gaussian beam output, thus forgoing the need of a conventional pinhole setup.

Usually, a laser operation wavelength with photon energy greater than the expected QD exciton ground state transition (410 to 560 nm) should be chosen, e.g. 405 nm. However, in this case, instead of passing the pulsed excitation through a frequency doubler, a laser wavelength of  $\sim 795$  nm is used directly for two-photon excitation. It has been shown both theoretically and experimentally that multi-photon excitation results in higher relative absorption cross section of nanostructures with greater degrees of quantum confinement [105, 131, 132, 133]. Therefore, the use of 795 nm excitation allows relatively stronger QD emission intensity than the underlying QWs that generate photons in the same spectral range, resulting in higher dot-to-background ratios and facilitating the investigation of QDs' optical properties. For this reason, all results from this thesis are obtained with pulsed 795 nm two-photon excitation. Compared to the one-photon case, the power of two-photon excitation varies with the square of its intensity. Due to the much lower absolute two-photon absorption cross section, the full extent of the fibre output power mentioned above (60–90 mW) is used, which is 3 orders of magnitude higher than typical one-photon excitation powers [62]. It should be noted that the optical injection power in this particular setting is just enough to saturate the emission of *a*-plane InGaN QDs. Based on separate experiments performed without an optical fibre, the intensity of the QDs do not increase further as the two-photon power is increased beyond 100 mW.

The laser pulses out of the fibre is transmitted through a long-pass dichroic mirror, and focused by a *Mitutoyo* near-infrared 100 $\times$  objective with a numerical aperture of 0.5, resulting in a 1  $\mu\text{m}$  spot onto the sample. The transmission of the objective at 800 nm is  $\sim 70\%$ . With further losses of mirror reflection and restricted beam entrance into the

objective accounted for, the power output is about a third (20 to 30 mW) of the fibre output.

### 2.3.2 Closed-cycle cryostat

The sample is housed in a closed-cycle *attoDRY 800* cryogenic system, the schematic of which is shown in Figure 2.4. The sample is placed on a holder and fixed to a stack of piezo-controllers responsible for movements in the  $x$ -,  $y$ - and  $z$ -directions. A shroud provides vacuum sealing and thermal isolation, while an actively cooled radiation shield prevents thermal radiation from the vacuum shroud itself due to its exposure to room temperature. A stable sample temperature of  $\sim 4.7$  and  $8.9$  K with laser incident can be achieved with and without the radiation shield respectively. Cooling is performed on the expander (cold-head) by the compressor, which itself is cooled by continuous supply of cold water. Before the compressor starts and cooling commences, an internal vacuum pump is turned on to extract air and lower the pressure to  $< 10^{-3}$  bar. Over a course of  $\sim 5$  hours, the internal pressure reaches  $< 10^{-5}$  bar and the temperature of the sample  $< 5$  K. Along with temperature and pressure sensors, a proportional integral derivative (PID) controller allows accurate and efficient tuning of the target temperature. Thus, the sample temperature can be regulated up to 320 K within an accuracy of 15 mK. As set out in the introduction, part of the work in this thesis aims to investigate the ability of  $a$ -plane InGaN QDs to operate as polarised single-photon sources at  $T > 190$  K. For these investigations, a temperature resolution of 1 K would be sufficient. Therefore, the *attoDRY 800* system is more than capable for the needs of the relevant studies. The setup is built into a floating optical table, which significantly damps any sources of vibration such as that generated by the compressor. The  $N_2$  supply in Figure 2.4 is used fill the chamber during vacuum breaking and sample exchange, minimising undesired water condensation. The use of a closed-cycle dry cryostat, instead of a conventional continuous flow wet version, is essential for the intended investigations. Firstly, the absolute brightness of current  $a$ -plane samples, especially under two-photon excitation, is much weaker compared to conventional arsenide ones. The expected time for an HBT experiment is on the order of hours instead of seconds. Furthermore, as the samples have been enhanced by nanopillar

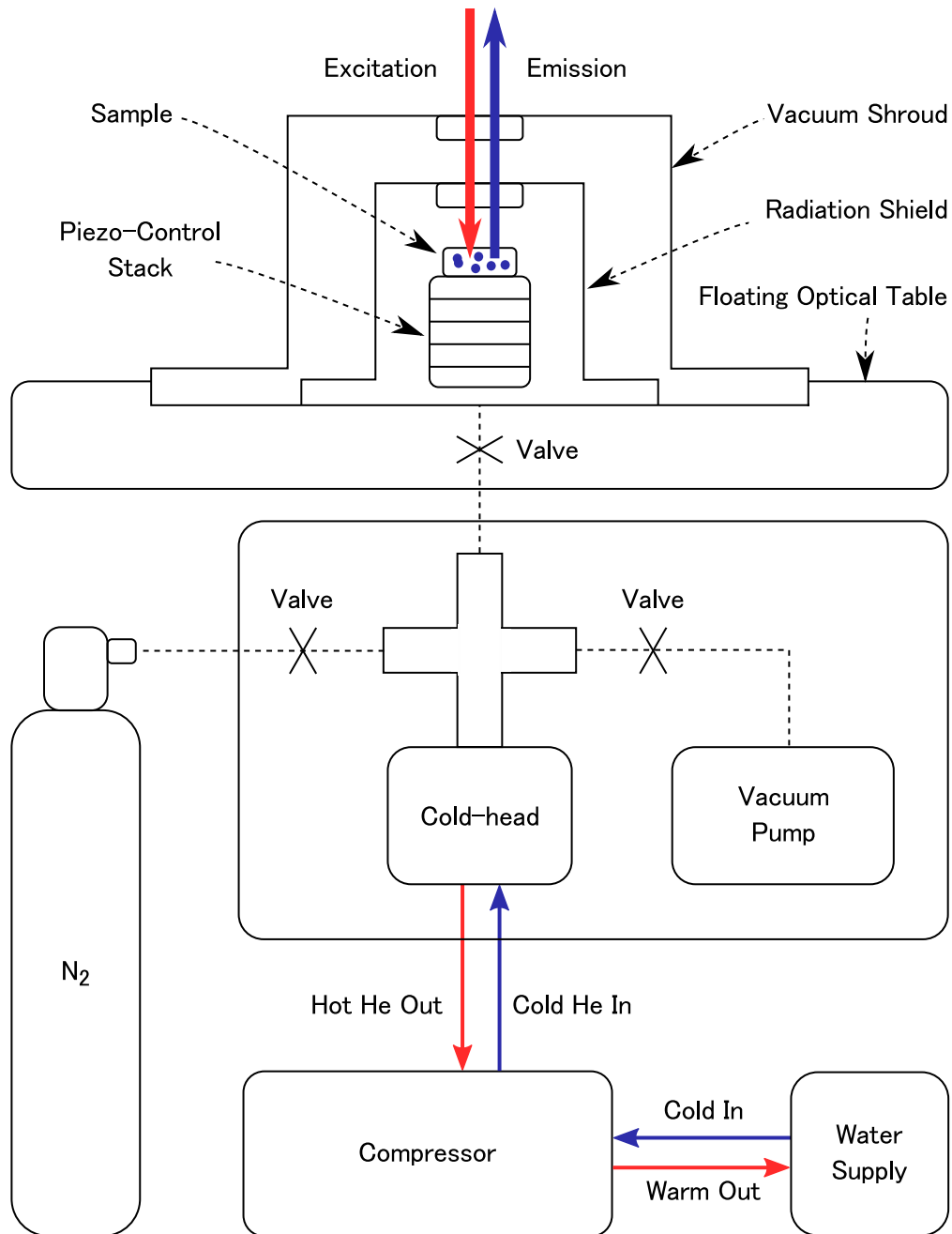


**Figure 2.4:** Schematic of the version of attoDRY 800 closed-cycle cryogenic system used for sample cooling in all experiments of the thesis. A stable sample temperature of  $< 5\text{ K}$  can be obtained with the setup, and regulated up to  $320\text{ K}$  within an accuracy of  $< 15\text{ mK}$ . The closed-cycle nature of the system in-principle allows the cooling to be retained for as long as necessary. The components are not illustrated to scale.

structures, it is less feasible to apply a patterned mask for sample identification. As such, in these self-assembled systems, all measurements need to be performed once a QD candidate is chosen. These include polarisation, lifetime and autocorrelation studies, from low to high temperatures. For instance, the experiment that produced data for high-temperature polarisation-controlled single-photon emission up to 220 K [25], which will be discussed in Chapter 5 in detail, took a single experiment session of 4.5 days to complete. It is unlikely for a conventional liquid He continuous flow cryostat for keep stable temperatures for such extended periods of time. On the other hand, the closed-cycle system should in theory be able to operate for as long as necessary, given a stable power supply and good working conditions of all components.

### 2.3.3 Time-integrated and polarisation-resolved $\mu$ PL

The PL triggered from the sample is then collected by the same objective, reflected by the dichroic mirror, and directed towards a *Shamrock 500i* half-metre spectrograph. The slit of the spectrometer can be controlled between 10  $\mu$ m to 2.5 mm. Two of the triple turret gratings, 300 and 1200 l/mm, are blazed at 500 nm with a maximum efficiency of  $\sim 80\%$ . The photoelectric detection of the dispersed light occurs in an *Andor iDus 420* Si-based charge-coupled device (CCD), which has an array of  $1024 \times 255$  pixels. The pixel size of the CCD is 26  $\mu$ m, providing a maximum pixel resolution of  $\sim 38$  pm for the time-integrated  $\mu$ PL setup. The CCD is Peltier-cooled to 50  $^{\circ}$ C, reducing thermal fluctuation noise to 3–5 cts/s.

An example of the typical emission spectrum observed in time-integrated  $\mu$ PL is displayed in Figure 2.5. All sharp emission features come from nanostructures with 3 spatial dimensions confined. Due to the stochastic self-assembly process, the physical attributes of these nanostructures could differ tremendously within the 1  $\mu$ m laser excitation spot. These properties, such as size, shape and indium content, could affect the strength of quantum confinement, intensity, emission energy and exciton transition linewidth significantly, resulting in the observed variety of sharp peaks in Figure 2.5 spectrally overlapping with  $\sim 50$  cts/s background InGaN QW emission. Four particularly strong QD-like emissions can be seen at 461, 463, 472, and 475 nm, which are near the centre of the experimentally

observed *a*-plane InGaN QD emission range of 410–560 nm. These QDs are often chosen for temperature-dependent and HBT studies, where high absolute emission intensities are desired. However, in unbiased statistical investigations of optical polarisation (Section 3.2.4), exciton transition linewidth (Section 4.3.1), and radiative recombination lifetime (Section 4.4.2), other sharp QD-like peaks such as those between 465 and 470 nm are also included.

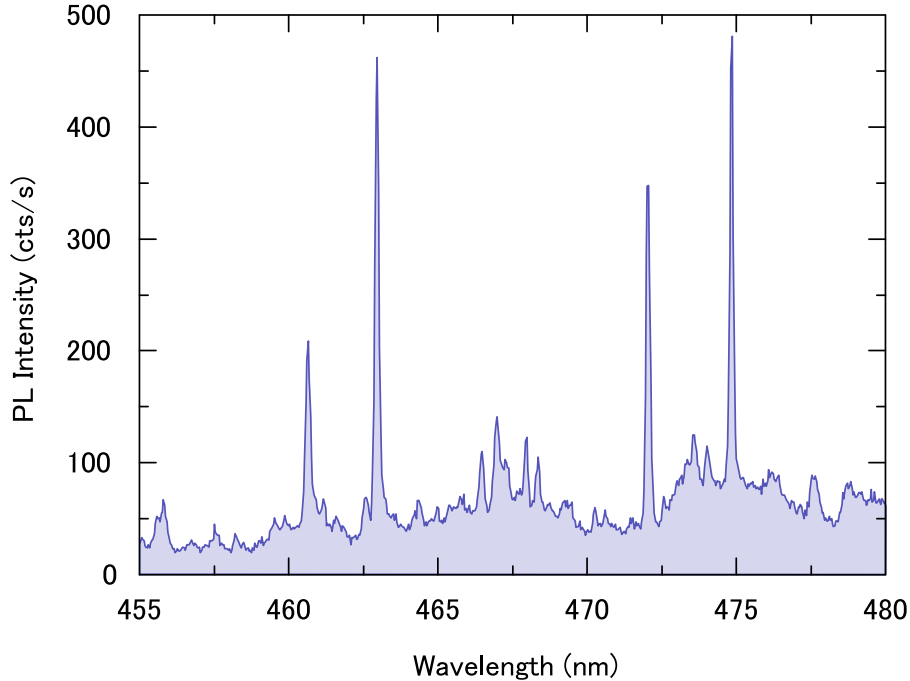


**Figure 2.5:** Typical  $\mu$ PL spectrum containing several self-assembled single *a*-plane InGaN/GaN QDs. Across the 25 nm spectral range, a number of sharp emission features characteristic of QDs can be seen on top of fluctuating (average  $\sim 50$  cts/s) QWs. Four of the relatively stronger QD-like emissions at 461, 463, 472, and 475 nm are usually chosen for further studies due to higher intensities and narrower linewidths, which are indicative of good quantum confinement.

The linewidths of the QD emission profile is broadened by the uncertainty of the exciton transition, which is related to its radiative lifetime by  $\hbar/2$  according to Heisenberg’s uncertainty principle. However, in the context of nitride QDs, carriers present in the vicinity of the single quantum emitter can induce an instantaneous electric field, causing QCSE and a small change of its exciton energy. This energy fluctuation is called spectral diffusion, and could occur at both fast- and slow-timescales [134, 135]. Further discussion and mea-

surement of these two types of spectral diffusion can be found in Sections 4.3.1 and 4.3.2 respectively. A linewidth study with consideration of other temperature-dependent broadening processes is included in Section 5.5. Due to these reasons, the measured linewidth is a random accumulation of Lorentzian peaks. Therefore, a Voigt profile, which is a convolution of Gaussian and Lorentzian functions, should provide the most accurate description [136]. In the case of current *a*-plane InGaN QDs, the measured linewidth ( $\sim 1$  meV) is much larger than the expected Lorentzian linewidth ( $\sim 1$   $\mu$ eV for a recombination lifetime of 309 ps, see Section 4.4.2). As such, fitting with Gaussian functions alone should provide an accurate estimation of the observed linewidth, and is therefore used throughout the thesis. For instance, the four strongly emitting QDs in Figure 2.5 have Gaussian linewidths of  $918 \pm 57$ ,  $696 \pm 18$ ,  $775 \pm 26$ , and  $552 \pm 17$   $\mu$ eV from low to high wavelengths respectively. A pair of polariser and half-wave plate can be introduced to or removed from the optical collection path, allowing for optical polarisation studies. There are several challenges in realising sufficient accuracy for these studies, particularly due to imperfect optical components, physical position drift of the sample, QD intensities fluctuations, and data acquisition of the weaker fine-structure PL component. Therefore, three measures have been taken to maximise the precision of the recorded data:

1. For each angle rotated by the polariser, the half-wave plate is rotated by half the angle in the opposite direction, thereby maintaining the axis of polarisation for the PL at all angles. This is done to avoid a  $\sim 10\%$  difference in the detected intensity caused by different polarisation angles.
2. The tolerance of optical alignment of components is not sufficient to account for the changes caused by the manual rotation of the cubic polariser. As a result, the PL slightly moves around the slit while the polariser angle is changed. Thus, the slit is opened wide enough such that all PL can enter the spectrometer during a polariser rotation, as the maximum spectral resolution is not a necessity in optical polarisation measurements. Alternatively, this can also be achieved by placing the half-wave plate before the polariser, fixing the polariser angle, and rotating the half-wave plate instead.

3. Due to unpredictable random sample position drifts, the maximum PL intensity of the QD is immediately recorded as a reference after data at each polariser angle is taken. The final results are then normalised with respect to the reference measurements.

Several other precautions in the analysis of polarisation data have also been used—these are explained in detail in Section 3.2.3 of the next Chapter, together with experimental results and their discussions.

### 2.3.4 HBT and time-resolved $\mu$ PL

The HBT setup follows the standard model introduced in Figure 1.1 of the previous chapter. As the accurate measurement of  $g^{(2)}(0)$  is paramount, spectral isolation of the QD signal is of central importance. This can be achieved directly and accurately with the second exit (the first exit being connected to the CCD) of spectrometer, where the slit opening can be controlled for a desired number of pixels of light output. However, such an arrangement results in intensity losses that are less ideal for autocorrelation studies of relatively weakly emitting  $a$ -plane InGaN QDs. In an HBT experiment, an event is recorded when both detectors register a photon simultaneously, indicating a quadratic dependence of the histogram data count with PL intensity. To ensure the highest possible experimental accuracy, it is desirable to maximise the intensity of PL that reaches the detectors. For this reason, a pair of *Semrock VersaChrome* tuneable bandpass filters are used to spectrally select the desirable wavelength range of PL transmission, before passing it to the HBT setup directly (see Figure 2.3(b)). Each Semrock filter allows  $> 90\%$  transmission over a spectral range of  $\sim 15$  nm. With a rotation of up to  $60^\circ$ , this transmission window can be tuned towards the bluer end of the spectrum up to a change of  $-55$  nm. An example of the transmission of a *Semrock* 501/15 filter is shown in Figure 2.6. Therefore, with an identical pair of these filters, a narrow (a few nm) transmission range can be defined and tuned between 455 to 495 nm. Since the emission of  $a$ -plane QDs are expected to be between 410 to 560 nm, four different pairs (449/15, 487/15, 501/15, and 547/15) are prepared and used according to the QD of interest.

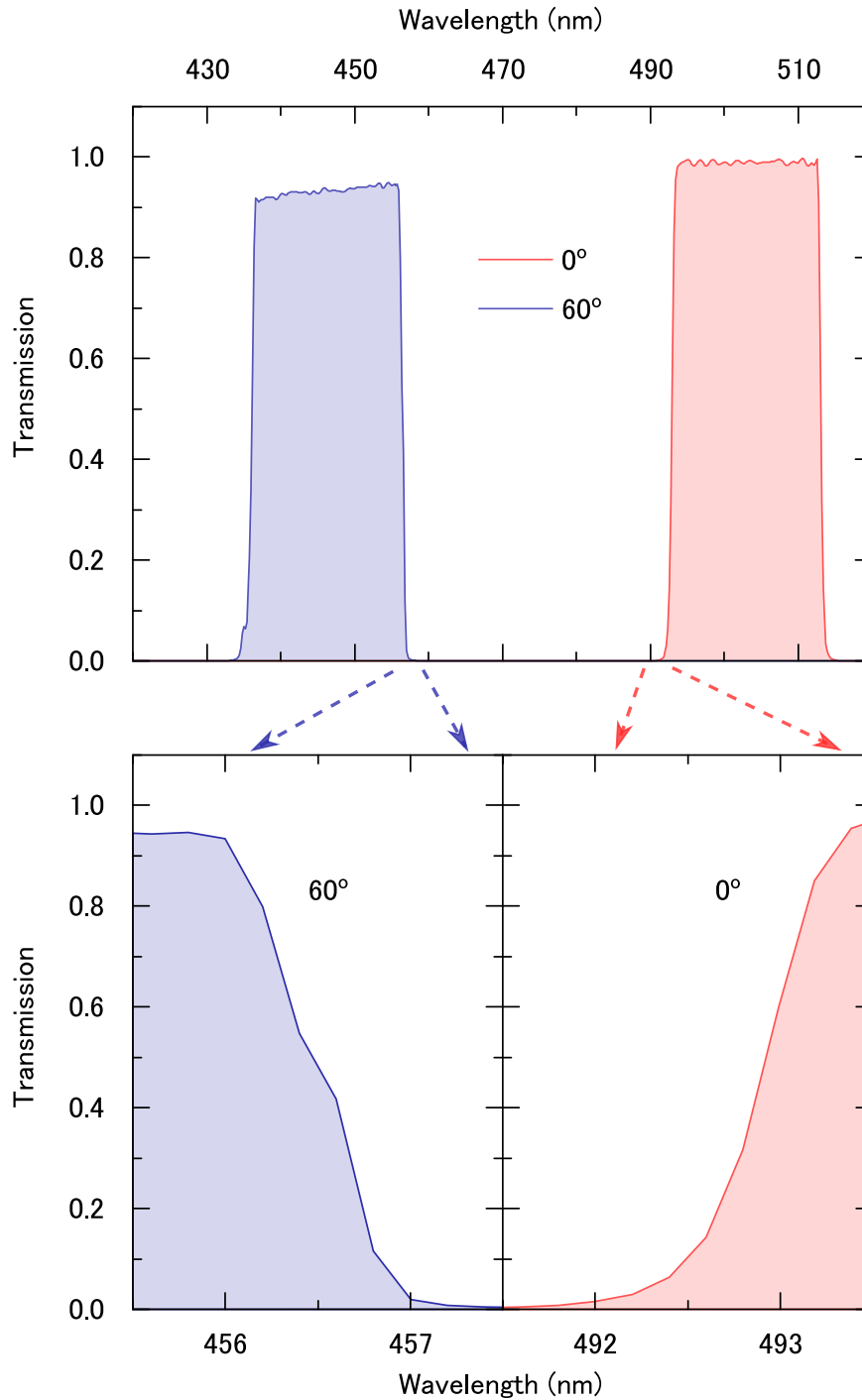


**Figure 2.6: Transmission of a Semrock 501/15 VersaChrome tuneable bandpass filter.** A 15 nm spectral window of transmission can be tuned by  $> 50$  nm with a rotation of  $60^\circ$ , maintaining a  $> 90\%$  transmission. Using a pair of these filters, QDs in the range of 455 to 495 nm can be spectrally isolated. Also shown is the non-perfect boxcar-like spectral bandpass edges with finite slopes, which could reduce the PL intensity of the studied QDs.

### 2.3. MICRO-PHOTOLUMINESCENCE

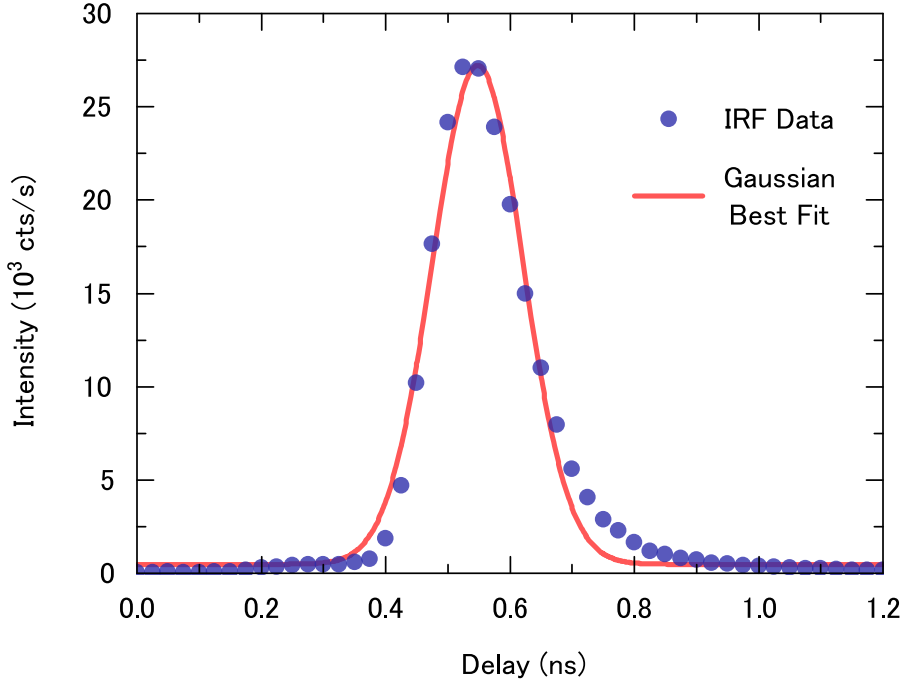
---

Figure 2.6 also shows that the edges of the transmission are not perfect boxcar functions with infinite slopes. The gradual transmission change over  $\sim 2$  nm would partially and undesirably reduce the transmission of a QD's PL, especially when it has a narrow ( $\sim$ nm) exciton transition linewidth. In these situations, a judgement is made in balancing the amount of unwanted signal reduction and QD signal retention. Given the high sensitivity of these *Semrock* filters to the angle of rotation, obtaining an optimal trade-off is a significant challenge. Due to this reason, it is also much harder to provide an accurate estimation of the dot-to-background ratio with the bandpass filters in place. A method to minimise this estimation error is explained in Section 3.4.2.

The spectrally selected PL is then incident on a non-polarising 50 : 50 beamsplitter, which directs the beam to two *Hamamatsu H10720* photomultiplier tubes (PMTs) [100] for detection. The electric signals from the PMTs are passed on to a *PicoQuant TimeHarp 260* time-correlated single-photon counting (TCSPC) card. The TCSPC module is connected to a computer via a PICE channel, allowing for parameter control, such as digital delay, bin width, and real-time histogram visualisation. The smallest bin width of the TCSPC card is 25 ps, and the maximum acquisition time is 100 hours. With the 25 ps time resolution, a digital delay of up to  $\pm 100$  ns can be introduced in either of the detection arm. In the actual HBT experiments, the highest bin resolution is not required due to the 13 ns interval between each laser pulse. In order to increase the data count per bin, the resolution has been changed to 100 ps. Autocorrelation data for *a*-plane InGaN QDs and their discussion can be found in Sections 3.4 and 5.6.

During the course of data acquisition, random position drifts of the QD could occur. As such, the position of the sample needs to be optimised using the piezo-controllers at least every minute to allow maximum QD PL intensity. In order to achieve this without having to re-direct the PL back to the spectrometer, a position optimisation computer programme has been developed by Dr. Luke P. Nuttall in the optical characterisation lab. Over a user-defined time interval, the programme moves the sample in  $\pm x$  and  $\pm y$  directions by one single position step and records four different count rates from the TCSPC card. It then compares these to the count rate without any position movement, and selects the highest reading of the five. The position of the sample is then adjusted accordingly or

kept unchanged. The programme can be set to run several times in order to reach a fixed sample position. With the optimisation script, the TCSPC card and the closed-cycle cryostat, a single set of autocorrelation data can be collected for up to four days.



**Figure 2.7: Measurement of the instrument response function of the PMTs.** Using sample surface reflection of the second harmonic generation of 795 nm excitation pulses, the IRF data of the detector are recorded. A Gaussian profile is fitted to the data, yielding a width of  $137 \pm 4$  ps.

For radiative lifetime measurements, the same HBT setup can be used with the signals from only one of the two PMT detectors as the source input. A small fraction of the laser pulses is attenuated and directed to a diode detector, the signal of which is passed on to the sync input channel of the TCSPC module. Alternatively, the spectrometer exit slit can be used to select the desired range of PL wavelength, and a third PMT can be used for detection as shown in Figure 2.3(b). This would be more efficient especially when simultaneous HBT measurements are not required. Such an arrangement is possible because the rate of event recording in this case is directly related to the PL intensity, instead of the square of intensity in the HBT case. The instrument response function (IRF) of the PMTs has been measured using the second harmonic generation of the Ti:Sapphire laser reflected off the sample surface. An example of the IRF measurement of the PMTs used is shown in

Figure 2.7. According to the results of Gaussian fitting, the IRF has a width of  $137 \pm 4$  ps. As the expected radiative lifetimes of *a*-plane InGaN QDs are  $< 500$  ps, the relatively large IRF could cause inaccuracies in the analysis of exponential decay. A method to resolve this issue is discussed in Section 3.3 where the recombination lifetimes of the QDs are investigated in detail.

# 3

## Cryogenic quantum light sources

### 3.1 Chapter introduction

As explained in Chapter 1, the potential of *a*-plane InGaN QDs to act as ultrafast single-photon sources with deterministic polarisation properties is the key feature that makes this platform stand out from other nitride contenders. In this chapter, the low-temperature optical polarisation properties, radiative lifetime, and single-photon generation of *a*-plane QDs will be examined in detail. Firstly, the situation and challenges in the conventional polar *c*-plane nitride will be highlighted, and contrasted to how the *a*-plane system attempts to resolve these challenges. For the investigation on optical polarisation and radiative recombination rate, statistically significant experimental data are combined with possible theoretical foundations to elucidate the origin of these desirable advantages.

Although nitride QDs are able to operate at elevated temperatures—a key motivation for the work set out in this thesis—their optical properties are still best manifested at cryogenic conditions. For this reason, the results in this chapter are solely from  $\mu$ PL experiments performed at  $\sim 5$  K. A comprehensive temperature-dependent study will be detailed in Chapter 5. Currently, MDE QDs still have better signal-to-background ratios and higher average emission intensities than the newer Q2T samples. For low-temperature investigations in this chapter, all data were taken with MDE QDs.

## 3.2 Elucidation of polarisation properties

### 3.2.1 Polarisation and its control in polar nitride QDs

It has been well established both theoretically and experimentally that in a symmetric polar [0001]  $c$ -plane nitride QD, the in-plane polarisation of emitted photons is a circular one [137, 138, 139]. However, due to the uncertain nature of the self-assembly process, the epilayer strain and local environment cause random QD size, geometry, and composition variations. These differences in turn affect the polarisation properties of the self-formed QDs. In the nitride case, the impact of shape anisotropies on the polarisation properties is especially pronounced compared to other materials [138, 140]. As such, although individual QDs from several  $c$ -plane nitride systems [96, 113, 130] have been able to achieve high degrees of optical linear polarisation (DOLP), statistical analyses reveal random distributions of DOLP and polarisation angles [139]. In these cases, prior measurements would be needed to determine specific QDs with high DOLPs, and external half-wave plates would be required to alter the polarisation angle. Hence, the ability to achieve reproducible intrinsic polarisation control would be more desirable for the potential implementation of quantum key distribution protocols, such as BB84 [141, 142].

Several solutions to artificially create nanostructure anisotropies for light guiding have been used to control the polarisation properties of  $c$ -plane nitride QDs. The most common among these are nanowire structures [112, 130, 143, 144, 145, 146]. Although QDs formed in nanowires do not have intrinsic polarisation control *per se*, the dipole of the QD exciton is preferentially confined by the nanowire geometry when the structure is lying horizontally, orthogonal to the crystal  $c$ -direction of PL emission. Due to the small diameter of the nanowire and the large contrast in its length, horizontally aligned nanowires can almost always produce near-unity DOLP, with polarisation angles along its long axis. However, it is challenging to achieve further electrical contacting on these nanowires. The only current solution [143] have complex structures and would be difficult to implement at larger scales. The limited physical geometry also confines heat more strongly than a planar epitaxial system, thereby creating higher local temperatures. This lack of proper heat dissipation is

thought to be the culprit that undermines some systems [112, 113] for higher-temperature operation.

Another approach aims to control the output shapes of the nitride photonic nanostructures. QDs embedded in pyramids [140, 147, 148, 149] with elongated tops [140] and in elliptical nanocolumns [150, 151] have both consistently produced high degrees of DOLP with predefined polarisation axes. Due to the limit in controlling ellipticity, the statistical DOLP of the asymmetric nitride nanocolumns is currently limited at  $\sim 0.7$  [150]. On the other hand, the larger diameters of the elliptical nanocolumns make electrical contacting easier than nanowires. The use of elongated pyramids can achieve a larger aspect ratio and thus higher average DOLP at  $\sim 0.9$  [140], but poses a more involving task to make electrical contacts. In both cases, the issue of heat dissipation makes high-temperature operation difficult, and there have been no report of single-photon operation above cryogenic temperatures yet for these systems.

### 3.2.2 Origin and theoretical foundation

#### Basics and motivation

Bypassing the difficulties in nanostructure fabrication and electrical contacting, the  $a$ -plane system lowers the wurtzite crystal symmetry and breaks the valence band degeneracy at the material level. As explained in Chapter 1, the changed degree of band mixing effect introduces a system-wide polarisation anisotropy. This effect has been well studied non-polar (both  $a$ - and  $m$ -plane) QWs [115, 116, 152, 153, 154, 155, 156, 157, 158]. However, in the case of self-assembled QDs, the expected optical polarisation properties still need to be quantified, particularly due to the following two reasons.

1. A lens-shaped  $a$ -plane QD nanostructure with stronger vertical (growth direction) than lateral quantum confinement has different degrees of energy level shifting, and thus polarisation properties, comparing to that in an  $a$ -plane QW system where confinement is only present in the growth direction.
2. Similar to most  $c$ -plane systems,  $a$ -plane QDs grown by the current methods still have random differences in dimension, geometry, and material composition due to

### 3.2. ELUCIDATION OF POLARISATION PROPERTIES

---

the stochastic self-assembly process. These variations have a non-zero and unknown impact on the polarisation properties, which needs to be quantified and compared to that caused by the use of the  $a$ -plane material alone.

In order to answer these two questions, our collaborators in Tyndall National Institute used  $\mathbf{k}\cdot\mathbf{p}$  theory [159, 160, 161, 162] to elucidate the polarisation properties of self-assembled  $a$ -plane InGaN QDs. The final results of these theoretical studies are quoted here in support of the physics discussion and experimental findings, without elaborations on their finer details.

#### **Lens-shaped QD with symmetrical base and typical indium content**

It is non-trivial to obtain experimental data on  $a$ -plane InGaN QD geometry, dimension, or indium content after capping. In other nitride and non-nitride QD systems, it has been widely assumed that a typical QD would have a lens-shaped geometry [163, 164]. As such, this assumption is also followed here. According to results from earlier AFM analysis [22], the typical base diameter and height of the nanostructure have been chosen to be 30 and 2.5 nm respectively. An indium content of 20% is set as the starting point, which is usually the target in growth. The  $\mathbf{k}\cdot\mathbf{p}$  simulations were performed on a  $50 \times 50 \times 30 \text{ nm}^3$  supercell with periodic boundary conditions. More detailed information on the theoretical work, such as built-in fields and electronic structures, can be found in our joint publication [24]. The QD ground state emission energies resulting from these simulations were between 2.7 and 2.9 eV, which are close to typical experimental observations and those published in the literature [25, 26, 27, 28, 114, 134, 165]. As such, the assumptions made for the QD geometry, dimension, and material composition are reasonable ones, and were used for further calculations of the DOLP.

The in-plane polarisation properties of the ground state emission can be determined by the relative contributions of  $|m\rangle$  and  $|c\rangle$  in the hole wavefunction. The  $\mathbf{k}\cdot\mathbf{p}$  simulation shows that a hole ground state should be 97%  $|m\rangle$ -like and 2%  $|c\rangle$ -like. In  $\mu\text{PL}$  experiments, these should directly translate into a maximum intensity parallel to the  $m$ -direction, and a minimum intensity perpendicular to it, with an intensity ratio of 97 : 2. According to the formula to calculate the DOLP  $P$ ,

$$P = \frac{I_{\max} - I_{\min}}{I_{\max} + I_{\min}}, \quad (3.1)$$

where  $I_{\max}$  and  $I_{\min}$  are the maximum and minimum intensities measured in PL, a typical  $a$ -plane InGaN QD without shape anisotropies should have a  $P$  of 0.96. This first result is already very different from  $c$ -plane InGaN systems, where the DOLP is 0 for a QD with no in-plane anisotropies [138, 139].

A currently unaddressed effect is the possible mixing of contributions from single-particle excited states with the ground state, due to Coulomb effects. Our collaborators in Tyndall has calculated that for  $a$ -plane InGaN QDs, the first few excited hole states also have close to 100% contributions from  $|m\rangle$ -like states, indicating that Coulomb-induced excited state mixing with the ground state does not affect the results obtained at cryogenic temperatures. However, at elevated temperatures, the effect of excited states becomes much more significant. The temperature evolution of the DOLP of self-assembled  $a$ -plane InGaN QDs will be discussed in Section 5.7.

#### **QDs with differences in shape and indium content**

On the other hand, a different issue needs to be addressed regardless of the operation temperature. As explained previously, self-assembled QDs are highly unlikely to be all symmetric in shape, or have uniform size and material composition. Work on other systems, such as arsenide [48, 49, 50, 51, 52, 53] and  $c$ -plane nitride [138, 139], has shown that shape anisotropy alone can already drastically change their polarisation properties. In the  $a$ -plane InGaN case, the random variations of physical and material properties could introduce relative shifts of the  $|m\rangle$ -,  $|c\rangle$ -, and  $|a\rangle$ -like states. These changes in turn contribute to differences in the hole ground state, and thus the polarisation of emission. Hence, it is important to quantify the extent of the possible optical polarisation changes caused by these differences, and to determine the impact they have on the DOLP of  $a$ -plane QDs.

For instance, if the QD is “squeezed” such that its dimension along the  $c$ -direction becomes smaller, the energetic separation between the  $|m\rangle$ - and  $|c\rangle$ -like states would increase the DOLP of the QD further. Coupled with the lower effective mass of the  $|c\rangle$ -like states

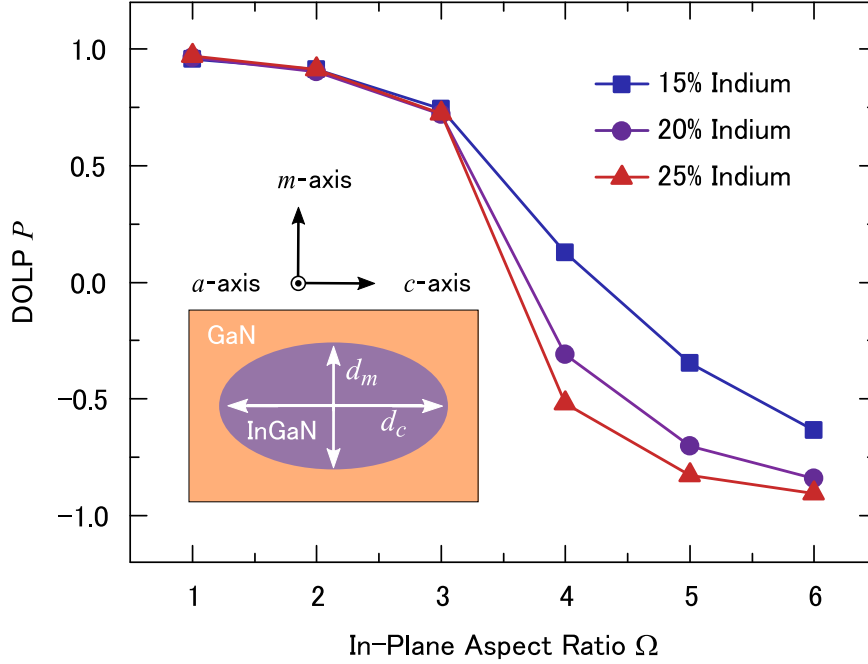


**Figure 3.1: DOLP variation with in-plane aspect ratio and indium contents for non-polar  $a$ -plane InGaN QDs.** The inset defines the coordinate system used in the simulation, and the in-plane dimensions of  $d_c$  and  $d_m$ . The in-plane aspect ratio  $\Omega$  is defined as  $\Omega = d_c/d_m$ . The study has been conducted for an indium composition between 15% and 25%, and for  $\Omega$  between 1 and 6. Final results of this theoretical investigation are obtained by our collaborators in Tyndall National Institute.

along the  $c$ -direction, the hole ground state would have a smaller relative contribution from these states. In other words, a compression (elongation) along the  $c(m)$ -direction would further increase the high DOLP of  $a$ -plane InGaN QDs until it reaches unity. The more interesting situation is when the anisotropy works “against” the built-in polarisation of the  $a$ -plane material. Opposite to the situation explained above, a compression along the  $m$ -direction would reduce the relative contribution of the  $|m\rangle$ -like states to the hole ground state, owing to the lower effective mass of these states along the  $m$ -direction. As such, anisotropy would be acting against the high built-in  $a$ -plane DOLP. A quantitative investigation of this situation would provide two important insights:

1. The extent of deformation needed for shape anisotropy to overcome the intrinsic polarisation of the  $a$ -plane material, and

2. how useful this self-assembled  $a$ -plane system is producing high DOLPs with realistic anisotropies.

As shown in the inset of Figure 3.1, the in-plane dimensions of the base of the lens-shaped QD are defined as  $d_c$  and  $d_m$ , which are along the crystal  $c$ - and  $m$ -axis respectively. The starting point of the simulation is the same as the previous section, i.e.  $d_c = d_m = 30$  nm. This coordinate system is represented slightly differently from our publication [24], in order to reflect their associations with the crystal axes more directly. To simulate anisotropy, the in-plane aspect ratio, defined as  $\Omega = d_c/d_m$ , is varied between integer values of 1 to 6, with  $d_m = 30, 15, 10, 7, 6,$  and  $5$  nm. Additionally, an increased (decreased) band offset caused by higher (lower) indium contents would make confinement effects stronger (weaker), thereby making effects of shape anisotropy greater (weaker). As such, a  $\pm 5\%$  variation from the indium content of 20% has also been included to reflect the outcome of the self-assembly process more accurately. In Figure 3.1, the DOLP remains mostly constant for  $\Omega = 1$  and  $2$ , with a small decrease for  $\Omega = 3$ . It is important to note that  $\Omega = 3$  already indicates a very drastic shape anisotropy ( $d_c = 30$  nm,  $d_m = 10$  nm). As such, to answer the two questions proposed previously:

1. In order to completely overcome (reversing the directions of  $I_{\max}$  and  $I_{\min}$ , so that the numerator in Equation 3.1 becomes negative in the simulation)  $a$ -plane's built-in polarisation along the  $m$ -direction, a very high aspect ratio of at least  $\Omega = 4$ , coupled with a high indium content, would be required.
2. With a realistic in-plane anisotropy of  $\Omega < 3$ , the intrinsic polarisation overrides the impact of shape anisotropies and indium content variations. Hence, the DOLP of  $a$ -plane InGaN QDs should be consistently high with very small variations caused by in-plane dimension differences and indium content fluctuations.

#### **QDs with differences in size, shape, and geometry**

In this case, the size and geometry of these QDs are also varied, in the context of varying in-plane anisotropy. For the starting point of the size dependence investigation, the dimension the lens-shaped QD's base is decreased such that  $d_c = d_m = 24$  nm. In order to keep the

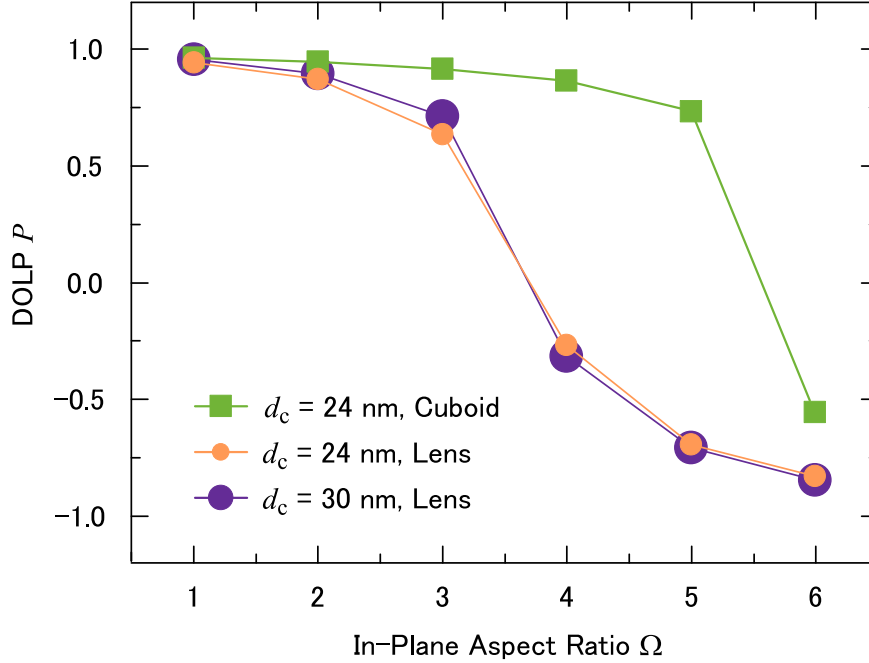


**Figure 3.2:** DOLP variation with in-plane aspect ratio, size, and geometry of non-polar  $a$ -plane InGaN QDs. An additional two sets of data for lens-shaped QDs with  $d_c = 24$  nm and for cuboid-shape QDs with  $d_c = 24$  nm have been included in the study. Final results of this theoretical investigation are obtained by our collaborators in Tyndall National Institute.

same range of  $\Omega$  values for a compression along the  $m$ -direction,  $d_m$  has been decreased to 12, 8, 6, 5, and 4 nm. In this investigation, the indium content has been fixed a 20%. As shown in Figure 3.2 (small yellow circles), the DOLPs for  $\Omega = 3$  to 6 coincide almost completely with the data obtained for the original size, indicating that a 20% decrease in size have a very small effect on the DOLP of  $a$ -plane InGaN QDs.

In order to study the impact of non-lens geometry on anisotropy-varied QDs, a cuboid-shaped QD is adopted with a length and width of 24 nm, and a height of 2.5 nm. In Figure 3.2 (green squares), the DOLPs of the QDs with this geometry are even more insensitive to variations of anisotropy, with very high values for  $\Omega = 1$ –5. A very extreme  $\Omega$  value of 6 would be needed to reverse the polarisation. As such, a drastic change of QD shape from lens to cuboid would make the polarisation properties even more insensitive to anisotropy variations.

All in all, the theoretical results obtained from our collaborators in Tyndall National Institute have shown that the polarisation properties intrinsic to the  $a$ -plane material are not significantly affected by size, geometry, anisotropy, or indium content fluctuations. Therefore, self-assembled non-polar  $a$ -plane InGaN QDs are predicted to have consistently high DOLPs of  $P > 0.9$  and a polarisation axis along the  $m$ -direction, with very small variations.

### 3.2.3 Observation of linear polarisation

With these theoretical foundations, polarisation-resolved  $\mu$ PL experiments were conducted at 5 K. The  $m$ - and  $c$ -components of the emission of a representative single  $a$ -plane InGaN QD are shown in the spectra of Figure 3.3. It can already be seen that the peak intensity of the  $m$ -component (blue) is much stronger than that of the  $c$ -component (red). In polarisation-resolved  $\mu$ PL measurements, the peak QD intensities from  $0^\circ$  to  $360^\circ$  at  $10^\circ$  intervals were recorded and shown in the polar plot in the inset of Figure 3.3.

#### Peak vs. integrated intensities in polarisation measurements

Although integrated QD intensities should produce more accurate results theoretically, their calculations are prone to several sources of error in practice in the context of polarisation studies.

1. In obtaining the polarisation results of this thesis, the polariser and half-wave plate were manually adjusted. In between each adjustment and PL spectrum acquisition, there were at least a period of 10 seconds, during which sample position drift, laser power fluctuation, and slow-timescale spectral diffusion could occur. These factors, especially spectral diffusion, could cause the fitting of data at different angles to be different and inaccurate.
2. Except for angles at which maximum and minimum intensities occur, the PL spectra of a QD should always be a superposition of two cross-polarised components. Due to non-zero emission energy differences between these components, i.e. fine-structure splitting (FSS), most of the QD PL spectra would be a combination of two different

### 3.2. ELUCIDATION OF POLARISATION PROPERTIES

Gaussian profiles. The resultant shape peaks, especially those close to the weaker fine-structure component, would be much harder to fit accurately. A multi-peak fitting routine with consideration of the FSS is not always possible. Due to the small FSS and spectral diffusion, such a fitting does not always converge.

3. The profile of the background QW emission cannot always be determined accurately, to make the fitting of the QD more precise.

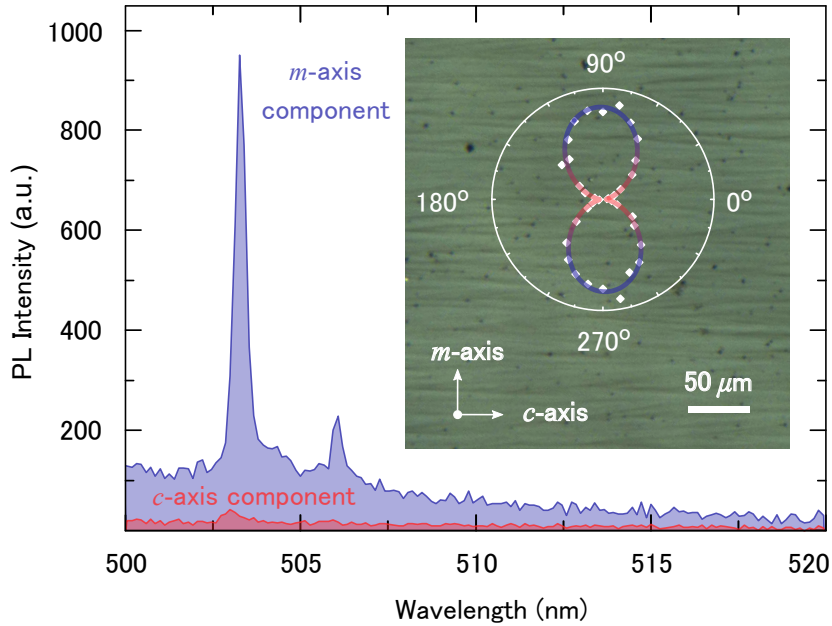


**Figure 3.3: Polarisation-resolved  $\mu$ PL measurement for a non-polar  $\alpha$ -plane InGaN QD.** Maximum PL intensity of the QD at 503 nm is more than 20 times stronger than the minimum, indicating highly polarised emission. Inset: Polar plot demonstrating Malus's law-type intensity variation of the studied QD. The background optical microscope image shows  $c$ -aligned striations naturally formed during growth, orthogonal to the polarisation axis along the crystal  $m$ -direction.

Due to these reasons, the results obtained by analysing the integrated intensities are not necessarily more accurate than the peak intensities of the QDs. As such, for polarisation measurements only, peak intensities with a linear background approximation should provide a reasonable estimate. Integrated intensities will be used again when difficulties specific to polarisation studies are not present, e.g. for temperature-dependent intensity

evolutions in Section 5.3.

#### Accurate use of Malus's law

Malus's law describes the sinusoidal intensity variation with polariser angles for a linearly polarised light source. For most QD platforms, including this  $a$ -plane system, the average polarisation degree is less than exactly 1. As such, it is important to note that both of these two components should exhibit sinusoidal intensity variations in accordance with Malus's law, with a phase difference of exactly  $90^\circ$ . As such, the intensity data in the inset of Figure 3.3 were fitted with

$$I(\theta) = I_{\max} \cos^2(\theta - \varphi) + I_{\min} \sin^2(\theta - \varphi), \quad (3.2)$$

where  $I_{\max}$  and  $I_{\min}$  are still the maximum and minimum PL intensities as introduced in Equation 3.1, and  $\theta$  is the polariser angle. For this study,  $\theta = 0^\circ$  is defined to be along the crystal  $c$ -axis, within a  $10^\circ$  error due to the manual placement of the sample in the cryostat. A separate parameter  $\varphi$  is introduced to indicate the angle at which the maximum PL intensity occurs relative to the  $c$ -axis, i.e.  $\theta = 0^\circ$ . Equation 3.2 is equivalent to the Malus's law form of

$$I(\theta) = (I_{\max} - I_{\min}) \cos^2(\theta - \varphi) + I_{\min}, \quad (3.3)$$

which is a function with a maximum of  $I_{\max}$  and minimum of  $I_{\min}$ . If the  $90^\circ$  out of phase sinusoidal variation of the weaker fine-structure component is ignored, the fitting function becomes

$$I(\theta) = I_{\max} \cos^2(\theta - \varphi) + I_{\min}, \quad (3.4)$$

with a maximum intensity of  $(I_{\max} + I_{\min})$  [112, 166, 167, 168]. Unless the minimum intensity is  $> 2$  orders of magnitude smaller, in which case the error in  $P$  is  $< 0.01$ , the polarisation analysis would be highly inaccurate. In reality, no systems have been reported to exhibit such high average DOLPs. Even for the highly polarised  $a$ -plane QD in Figure

## 3.2. ELUCIDATION OF POLARISATION PROPERTIES

---

3.2 where the maximum intensity is 20 times stronger than the minimum, an error as large as 0.05 in the DOLP would be introduced if Equation 3.4 were used. Therefore, Equation 3.2 or 3.3 should always be used in the study of QD polarisation.

The close fit with Malus's law, as indicated in the polar plot, demonstrates that the studied QD is emitting as a polarised light source. Using Equation 3.1 and 3.2, a  $P$  of  $0.92 \pm 0.05$  and  $\varphi$  of  $92^\circ \pm 1^\circ$  are found, showing that the studied  $a$ -plane QD is highly polarised with an axis along the crystal  $m$ -axis (orthogonal to the  $c$ -axis). The value of DOLP also coincides with our theoretical findings for a QD with in-plane anisotropy of  $< 2$ .

Also shown in the inset of Figure 3.3 is an optical image of the sample used. As explained in Section 2.2.2, physical striations visible to the naked eye are naturally formed during the fabrication of the sample. These striations are always parallel to the crystal  $c$ -axis, and are useful features to identify the orientation of the sample. The polar plot overlaid on top, in which  $\theta = 0^\circ$  is intentionally aligned parallel to these striations during sample placement in the cryostat, further demonstrates that the axis of polarisation is perpendicular to the crystal  $c$ -axis.

### 3.2.4 Statistical significance and contrast to QW

Although the single QD studied in Figure 3.3 is a representative one, current  $a$ -plane (MDE) samples contain QDs emitting from 440 to 520 nm, with varied optical properties such as intensities, linewidths, and dot-to-background ratios. In order to show that the  $a$ -plane platform can consistently produce highly polarised photon emission experimentally, DOLP calculations on 180 individual single QDs were performed. In an attempt to minimise selection bias, every QD-like shape emission in the PL spectra was studied. However, an exception was made in the selection: If a QD has an intensity of  $< 50$  cts/s, it was not included in the study. This is because intensities near the weaker fine-structure component of these weakly emitting QDs are smaller than the noise of the CCD, making accurate polarisation measurements impossible. It is also worth noting that in an experimental study, the maximum intensity is always greater than the minimum one, i.e.  $P \geq 0$ . The special case where the numerator in Equation 3.1 becomes negative is purely caused by the fixed and predefined polarisation axes (where the maximum intensity is attributed to

### 3.2. ELUCIDATION OF POLARISATION PROPERTIES

---

the intensity along the  $m$ -axis) in extreme situations of the theoretical simulation. The experimental investigation of polarisation angle will be presented separately in the next section.

All 180 DOLPs are plotted against their emission energies in Figure 3.4(a), with histograms and a Gaussian fit indicating their statistical distribution. All data are in the range of 0.6 to 1, and can be separated in 3 categories as follows.

1. Out of the 180 QDs investigated, there are 23 cases in which the weaker fine-structure emission is within the 5 cts/s fluctuation noise of the CCD and cannot be detected, resulting in a  $P$  of 1. In the theoretical discussion presented earlier, the presence of these QDs indicate an elongation (compression) along the crystal  $m(c)$ -axis, which adds to the built-in polarisation of the  $a$ -plane material.
2. There are 6 QDs with lower DOLPs between 0.6 and 0.75. According to the results of simulations, these 6 QDs have more extreme in-plane aspect ratios of  $> 3$ . The  $\sim 3\%$  occurrence of these QDs is in agreement with our expectation that drastic QD deformations with  $\Omega > 3$  are unlikely to occur frequently.
3. The remaining 84% of the QDs have DOLP between 0.75 and 1, with small differences possibly caused by in-plane anisotropies, size and geometry differences, and indium content variations. The  $\Omega$  (with a compression along the  $m$ -axis) for these QDs should be between 1 and 2, as previously expected for most of the self-formed QDs.

All the QDs investigated have DOLP values between 0.6 and 1. The Gaussian distribution fit yields a mean and standard deviation of  $0.90 \pm 0.08$ . The very small standard deviation again demonstrates that the built-in polarisation of the  $a$ -plane material is able to effectively overcome random variations of QD shape and composition introduced in the stochastic self-assembly process. In this investigation, no correlation with the emission energy has been found, indicating that  $a$ -plane InGaN QDs should be able to operate as reliable polarised photon sources across their available range of emission wavelength.

As explained in Section 2.2.2, the MDE growth routine requires an InGaN QW epilayer to be deposited before its fragmentation and the subsequent metallic droplet formation.

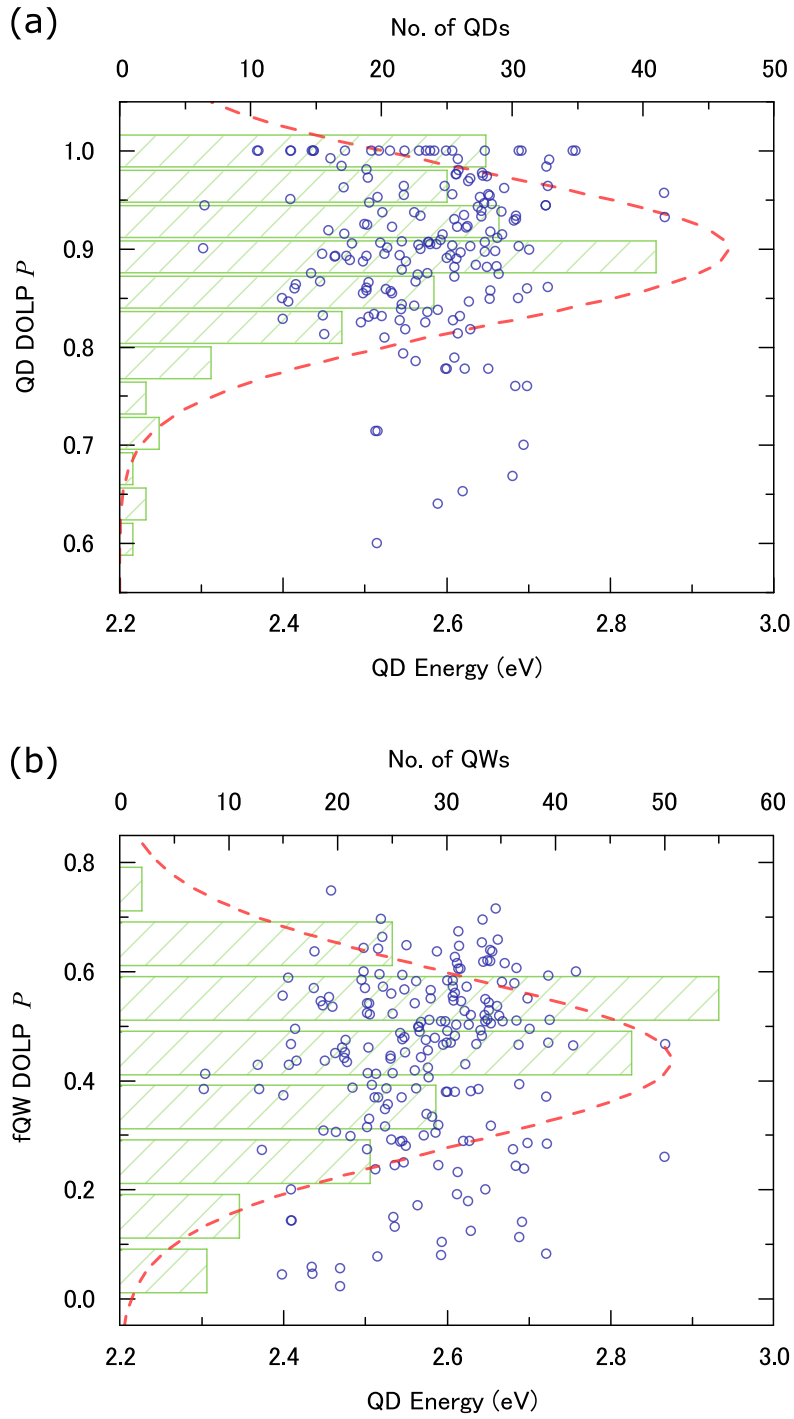


**Figure 3.4: Statistical investigations of the DOLP of  $a$ -plane InGaN QDs and their respective fQWs.** (a) A selection of 180 QDs with minimum selection bias. Histograms are fitted with a Gaussian distribution, yielding a mean and standard deviation of  $0.90 \pm 0.08$ . (b) The same calculations and statistical fitting for the fQW in the spectral proximity of each QD. The mean and standard deviations are  $0.46 \pm 0.14$ .

Hence, all QDs studied in this statistical investigation are emitting together with their underlying fQWs in similar wavelength ranges, such as the two QDs and their shared fQW in Figure 3.2. In conducting  $\mu$ PL experiments, it has been observed that these fQWs are also similarly polarised with an axis along the crystal  $m$ -direction. Hence, for each of the 180 QDs, the DOLP of the fQW in their spectral proximity was also analysed. These are presented in Figure 3.4(b) using identical statistical analysis tools as those used for the investigation of QDs in Figure 3.4(a).

Similar to QDs, there are no observable correlations between the QD energies and the DOLP of fQWs in their proximity. However, in contrast to the high DOLPs obtained for QDs, the results for the fQWs are between 0 and 0.8, with an average and standard deviation of  $0.46 \pm 0.14$ . This is an unexpected result, as  $a$ -plane QWs should have DOLPs close to unity with near-zero standard deviations. Across similar thickness of the same epilayer, QWs do not have a known polarisation-altering parameter equivalent to shape anisotropies of QDs. Work in the literature has also found very high theoretical DOLPs, but much lower experimental observations [116, 153, 154] as this investigation has discovered. Fundamentally, there should exist factors that either affect band mixing and energy level separation, or act as a source to introduce  $|c\rangle$ -like orbital contributions to the hole ground state. As QWs are not the focus of this thesis, these hypotheses are not pursued further. However, the observation itself is intriguing—for various  $a$ -plane nanostructures, high DOLPs can only be obtained with QDs.

#### 3.2.5 Angle of polarisation

For an  $a$ -plane QD with no in-plane shape anisotropy, the axis of polarisation should be parallel to the crystal  $m$ -axis of the material, corresponding completely to the  $|m\rangle$ -like states contribution to the hole ground state, such as that shown in the inset of Figure 3.3. However, similar to rationale behind the work on  $c$ -plane polarisation control with geometry engineering [140, 150], the angle of polarisation will also be further affected by the random QD shape anisotropies introduced during growth. Again, a competition exists between the intrinsic polarisation direction along the material's  $m$ -axis and the in-plane geometry of specific QDs.

### 3.2. ELUCIDATION OF POLARISATION PROPERTIES

---

To minimise selection bias, the polariser was initially set to  $45^\circ$ . As such, QDs with all polarisation angles (regardless of their PL intensity at this angle), except those with an alignment of exactly  $-45^\circ$ , can be observed. The polariser has also been rotated slightly back and forth to see if these exceptions do exist. In order to determine the polarisation angle of a QD, the polariser has been rotated such that both a maximum and a minimum intensity can be observed from the PL spectrum. The judgment by eye and manual rotation of the polariser are within a  $10^\circ$  error. Out of  $\sim 80$  additional QDs observable in a number of PL spectra, 91% have a polarisation axis along the crystal  $m$ -axis, in agreement with our expectations from both theoretical and experimental polarisation results discussed above. A very intriguing 9% of the studied QDs exhibited a polarisation axis along the crystal  $c$ -axis, exactly opposite the majority of data obtained. Back to the  $\mathbf{k}\cdot\mathbf{p}$  results (Figures 3.1 and 3.2), in order to produce a hole ground state with a very high contribution from  $|c\rangle$ -like states, a combination of at least  $\Omega > 4$  and high indium composition would be required. In the previous section, it has already been found that QDs with  $3 < \Omega < 4$  occur only 3% of the time. As such, the more extreme case of  $\Omega > 4$  is unlikely to happen 9% of the time. A more probable cause could be alloy fluctuation [169] effects, which have been reported to result in similar observations in other platforms.

A demonstration of this 9% exception is shown in Figure 3.5. While the fQW is polarised along the crystal  $m$ -axis as expected, the QD emitting at  $\sim 505$  nm was recorded to have a maximum intensity when the polariser was aligned to the  $c$ -direction. Based on the intensities measured, this QD and its fQW have DOLPs of 1 and 0.27 respectively. Both of these values agree with the statistical studies presented in Figure 3.4(a) and (b). For these 9% QDs, the effect of anisotropy should be exactly opposite to the  $m$ -aligned QDs discussed above. The 0 detectable intensity of the studied QD along the crystal  $m$ -axis hence implies that the QD should be slightly elongated along the  $c$ -direction. These 9% QDs also have the potential to produce purer polarised single-photon sources than  $m$ -aligned ones. As the QW background intensity is suppressed at the maximum intensity of the QD, the  $g^{(2)}(0)$  values should be closer to 0. However, a good single-photon source also requires, on top of many other criteria, an intrinsically high dot-to-background ratio (before the background suppression by polarisation) and an intrinsically high emission

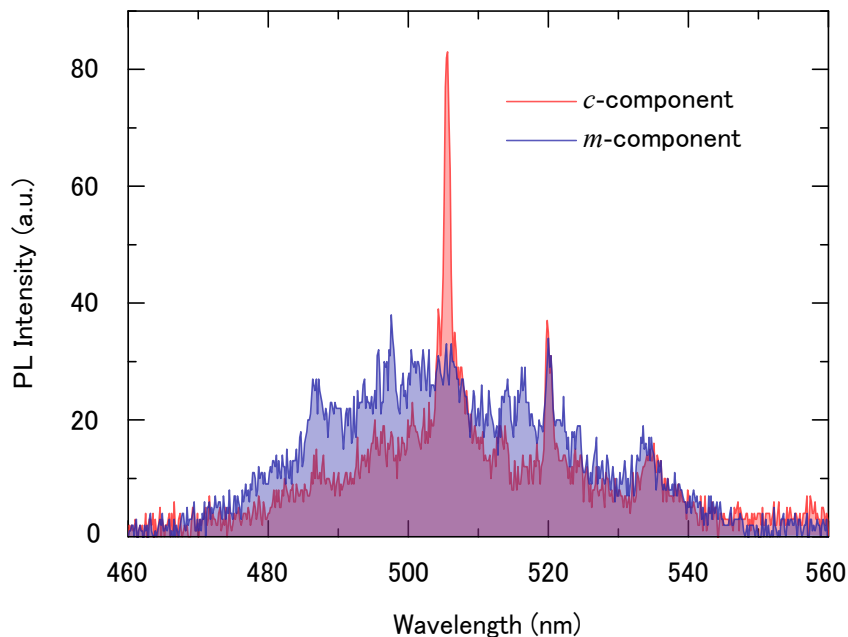


**Figure 3.5: Cross-polarised QD and QW in the  $a$ -plane InGaN system.**  $\mu$ PL spectra showing a QD at 505 nm polarised along the  $c$ -direction, while its underlying fQW is polarised along the  $m$ -direction. This situation occurs  $\sim 9\%$  of the time, and is possibly due to random alloy fluctuation effects.

intensity. Therefore, the rarity of these 9% exceptions does make the identification of these high-quality QDs more difficult.

### 3.3 Ultrafast radiative lifetime

#### 3.3.1 Reduction of exciton radiative recombination rate

One of the key disadvantages of using conventional polar nitride-based QDs for the development of quantum light sources is the slow radiative lifetime, often in the range of 1 to 10 ns [104, 105, 143]. These slow radiative recombination rates thus limit the repetition rate and efficiency of the potential single-photon sources. As explained in Section 1.4.2, built-in fields along the polar direction introduces undesired quantum confined Stark effects, reducing electron and hole wavefunction overlap. The oscillator strength of the QD exciton is thus significantly weakened, thereby slowing down the rate of radiative

recombination [104].

The radiative lifetime  $\tau$  of a semiconductor exciton is related to the oscillator strength  $f$  by the equation [170, 171]

$$\tau = \frac{2\pi\epsilon_0 m_0 c^2 \hbar^2 v}{e^2 E_{\text{exc}}^2 f} = \frac{C_0}{E_{\text{exc}}^2 f}, \quad (3.5)$$

where all fundamental constants and phase velocity  $v$  (inversely proportional to the material's refractive index) can be expressed as a single constant of  $C_0$  for the same system. Hence, the only two factors affecting the radiative recombination efficiency is the exciton transition energy  $E_{\text{exc}}$ , and the oscillator strength  $f$ . In order to achieve faster radiative lifetime at a fixed emission energy,  $f$  needs to be increased as far as possible.

The analytical expression for oscillator strength  $f$  has been widely used in the literature [171, 172, 173, 174] for theoretical researches, but is less meaningful to include in this discussion. Qualitatively,  $f$  measures the extent of electron and hole wavefunction overlap. In the design of a QD platform, there are several ways in which this overlap can be increased.

1. Physically, the size of the QD directly affects the oscillator strength of the exciton. In nitride systems, the strength of the built-in field decreases with smaller QD volume [175]. The weaker fields thus separate the electron and hole wavefunction less significantly, resulting in faster radiative lifetime at the same emission energy. This effect is evident in state-of-the-art dot-in-nanowire GaN systems [176], where the QDs are  $\sim 2$  nm in height and  $\sim 10$  nm in width. Being a few times smaller than typical nitride systems, these ultra-small polar GaN QDs have radiative lifetimes around 300 ps, which is an order of magnitude smaller than typical polar ones.
2. An external electric field can then be applied against the direction of the built-in fields, to partially compensate for the internal quantum confined Stark effect. This has been successfully demonstrated on polar InGaN QDs [104, 177], but is only able to reduce the lifetime by a factor of 2 before significant quenching of the intensity ensues.

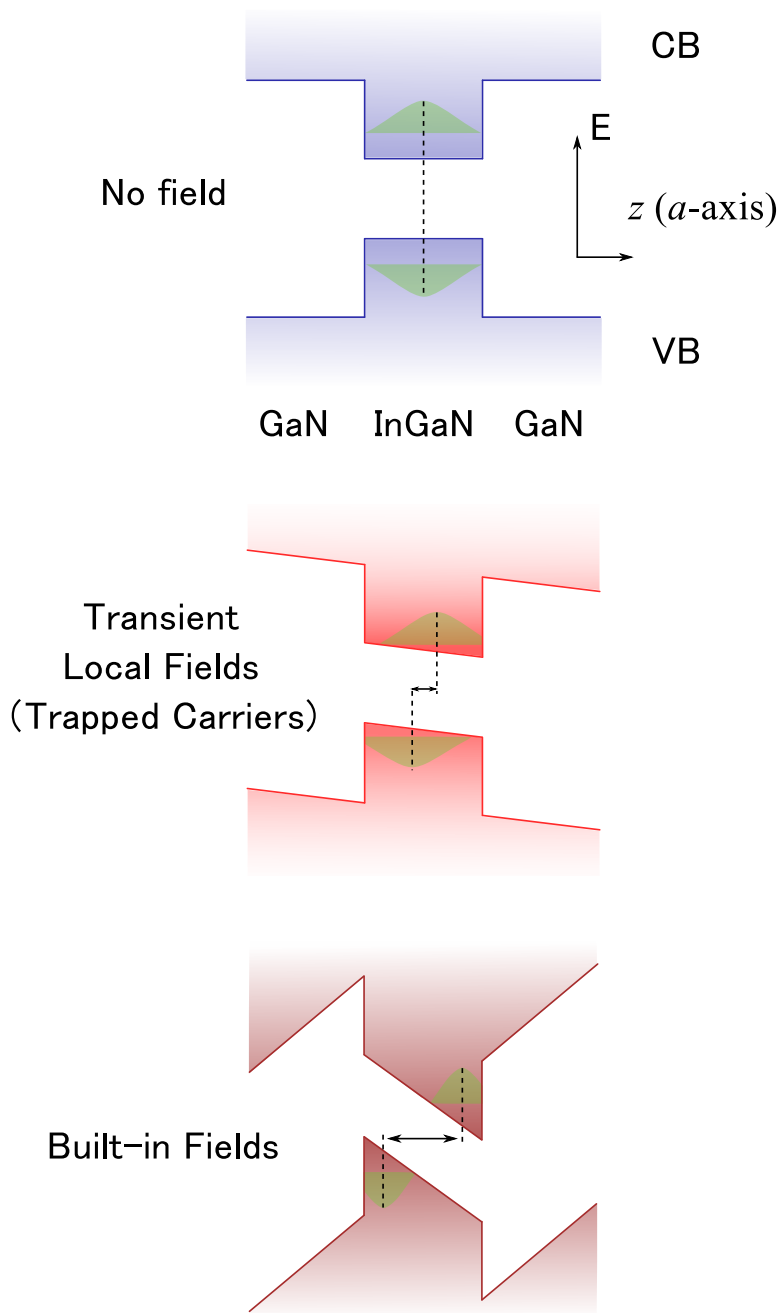


**Figure 3.6: Illustration of InGaN energy profile with and without the effect of electric fields.** With the presence of an electric field, there will be changes to the gradient of energy profiles, and in turn the spatial separation of the electron and hole wavefunction overlap, causing a decrease in the exciton oscillator strength and increasing radiative lifetime. Due to the much weaker instantaneous fields caused by nearby carriers, the amount of wavefunction separation and lifetime increase is much less than in the case of built-in fields. The degrees of energy level change and wavefunction separation are not illustrated to scale.

3. Another method to resolve the effect of built-in fields is to find similar alternative materials without the intrinsic built-in fields. In the context of polar nitrides, QDs can be grown on the two non-polar planes [22, 112], or on a zinc-blende substrate[103]. With lens-shaped QDs, the residual fields are much smaller than in the polar case. An order of magnitude reduction of radiative lifetime has been achieved in all three cases, making this method more effective than method 2. The challenge lies in the availability of suitable substrates, dot formation mechanisms, and material quality improvement.
4. The local environment of a QD, such as the presence of carrier trapping sites, also indirectly affects the oscillator strength of the exciton through quantum confined Stark effect [165, 178]. The instantaneous electric fields caused by carriers trapped in the vicinity of a QD not only cause Stark shifts of the emission energy, but also reduces the spatial separation of the electron and hole wavefunctions. As a result, the radiative lifetime would be slightly longer. However, due to the random nature of these transient fields and the uncertain local environment of individual QDs, especially in a self-assembled system, this effect should cause a large spread of the lifetime values. The strength of these fields should also be much smaller and the extent of lifetime changes should be less significant than method 3. As such, maintaining a smaller number of carrier trapping sites in the fabrication of the sample would potentially increase the radiative recombination rate of the QDs. In conjunction with method 1, this is another reason for the aforementioned dot-in-nanowire GaN system to achieve ultrafast lifetimes of  $\sim 300$  ps.

All methods 1–4 rely on the minimisation of any sources of electric fields in the QDs that could potentially weaken the oscillator strength  $f$ . In the context of InGaN/GaN QDs, as illustrated in Figure 3.6, any field present would change the slope of the energy levels and thus the spatial separation of the electron and hole wavefunctions. It is easy to ignore method 4—the reduction of carrier traps around QDs could potentially reduce the extent of electron and hole wavefunction separation and increase the rate of radiative recombination. The practical implementation of this method, however, would require a revised fabrication routine that significantly improves the local environment of the QDs. This

will be explained in greater detail in the next chapter, where the use of the Q2T growth method and its impact on radiative lifetime and other optical properties are assessed.

While method 2 has been achieved in *c*-plane InGaN systems, the development of an *a*-plane device with external vertical electric field has not yet been achieved at the time of the composition of this thesis, and is beyond the current scope. Nonetheless, such a device could potentially reduce the residual fields in lens-shaped *a*-plane QDs even further, achieving faster radiative lifetimes. For this section, method 3—the effect of using the non-polar *a*-plane alone in reducing the exciton radiative lifetime—will be assessed, and method 1—the usefulness of QD size reduction in the context of *a*-plane InGaN QDs—will be examined.

#### 3.3.2 Non-polar and polar nitride QD lifetimes

Similar to achieving intrinsic polarisation, the use of *a*-plane reduces the problem of weakened oscillator strength at a material level, without requiring sophisticated nanostructure engineering to create an ultra-small and ultra-clean system. For a typical *a*-plane InGaN QD, the result of the time-resolved  $\mu$ PL measurement is shown in Figure 3.7. Unlike measurement of systems with much slower radiative decay rates, the raw TCSPC data would be significantly affected by the instrument response time of the detector. As explained in Section 2.3.4, the PMT used for time-resolved  $\mu$ PL experiments in this thesis has an IRF with a width of  $\sim 140$  ps. As the TCSPC data is a convolution of the IRF Gaussian and the actual exponential decay of the sample, a function  $F(t)$  that includes the contribution from both components, in the form of

$$F(t) = F_0 + (F_{\text{Gauss}} \otimes F_{\text{exp}})(t), \quad (3.6)$$

should be used so as to obtain accurate results. In Equation 3.6,  $F_0$  is the background counts,  $F_{\text{Gauss}}$  is the IRF of the PMT with a measured and predefined width of 137 ps (see Section 2.3.4), and  $F_{\text{exp}}$  is an exponential decay with its time constant representing the measured radiative lifetime. Depending on the situation, the exponential function could be a single or multiple component decay.

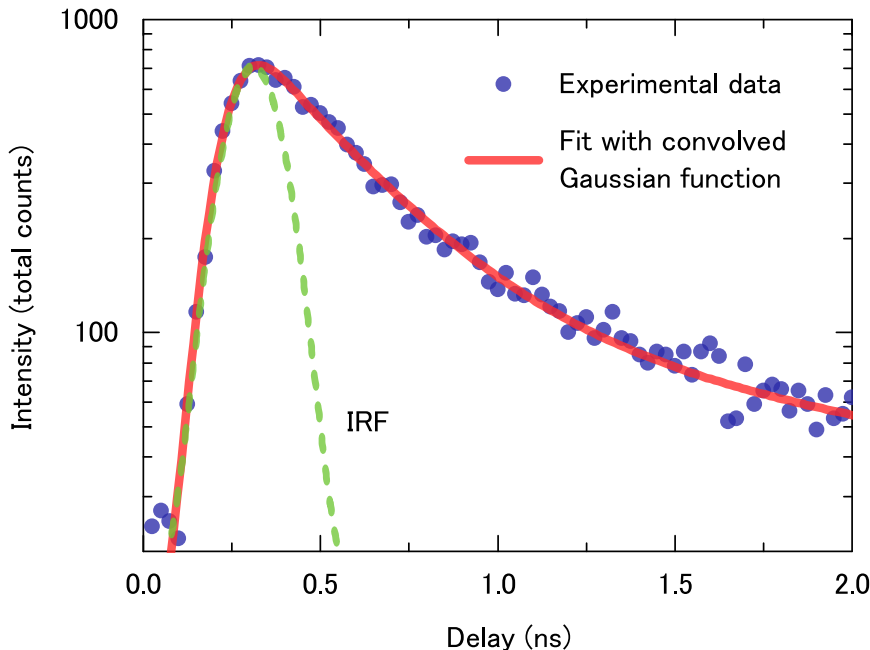


**Figure 3.7: Time-resolved  $\mu$ PL measurement of an  $a$ -plane InGaN/GaN QD with two exponential components.** Also shown is the Gaussian of the PMT’s IRF, with a width close to the radiative lifetime of the QD exciton. A Gaussian function convolved with a bi-exponential decay is used for fitting in order to more accurately measure the radiative lifetime of the studied QD, which is found to be  $\sim 300$  ps.

With a bi-exponential decay [179] convolved with a Gaussian, the data in Figure 3.7 has been fitted very closely, yielding a time constant of  $296 \pm 6$  ps for the main decay component. Another component with a  $\sim 5$ -fold lower contribution has a time constant of  $1.93 \pm 0.09$  ns. In the measurement of self-assembled  $a$ -plane InGaN QD radiative lifetimes, there will always be non-zero contributions from the underlying QWs. While the decay time for QW exciton is mostly similar to QDs, there are sometimes longer components observable in the lifetime measurements. This could be attributed to a small fraction of bound carriers in localised traps [180, 181]. Some of these carriers eventually decay non-radiatively, but others still undergo radiative recombination. However, depending on the specific local environment, these components may not contribute significantly in the time-resolved measurement of a QD, where most of the photons selected by the spectrometer originate from QD itself. In these cases, the underlying QW already has a very small contribution to the photons that reach the detectors, and thus the longer and even weaker

decay component caused by trapped carriers are not always visible.

The example in Figure 3.7 is one in which the long component is indeed visible, but contributes much less strongly than the main component of the QD emission as expected. However, TCSPC data of the *a*-plane QD in Figure 3.8(a) represents the more commonly observed case in which the weaker and longer component has a contribution much smaller (more than an order of magnitude) than that of the main QD, and thus does not affect the measurement of the QD lifetime significantly. It is worth noting that although the data in Figure 3.8(a) can be fitted with a single exponential, attempts to fit the data of Figure 3.7 with a conventional bi-exponential alone have been unsuccessful. The failure to reach convergence in the fitting routine could be attributed to the non-negligible Gaussian component. As such, for accurate measurement of *a*-plane QDs' lifetimes with the current PMT, the use of Equation 3.6 is necessary.

For the *a*-plane QD studied in Figure 3.8(a), a radiative recombination time constant of  $301 \pm 7$  ps has been found after fitting with Equation 3.6. This result is very similar to that obtained for the QD investigated in Figure 3.7. In contrast, the *c*-plane QD in Figure 3.8(a) has a radiative lifetime of  $2.64 \pm 0.01$  ns, which is an order of magnitude slower than both of the *a*-plane QDs investigate so far. Although not necessary, Equation 3.6, instead of an exponential decay, has also been used for the fitting of the *c*-plane data for consistency. The much faster radiative lifetimes of *a*-plane QDs are expected due to the minimised quantum confined Stark effect, and in agreement with the discussion in 3.3.2. In order to examine the exciton lifetime reduction in *a*-plane QDs further, an additional 10 *a*-plane and 10 *c*-plane InGaN QDs have been investigated, and their measured lifetimes shown in Figure 3.8(b). Although the emission energy plays a part in determining the radiative recombination rate according to Equation 3.5, the range of emission energies between 2.4 and 3.0 eV should only cause a maximum lifetime difference of  $\sim 50\%$ . Therefore, the much larger distribution should be attributed to the difference in exciton oscillator strength. The range of 200 to 600 ps for *a*-plane QDs is indeed an order of magnitude faster than the range of 1 to 10 ns for their *c*-plane counterparts.

According to Equation 3.5, the lifetimes should be decreasing with increasing emission energies. However, such a downward trend is very vague and can hardly be seen with the

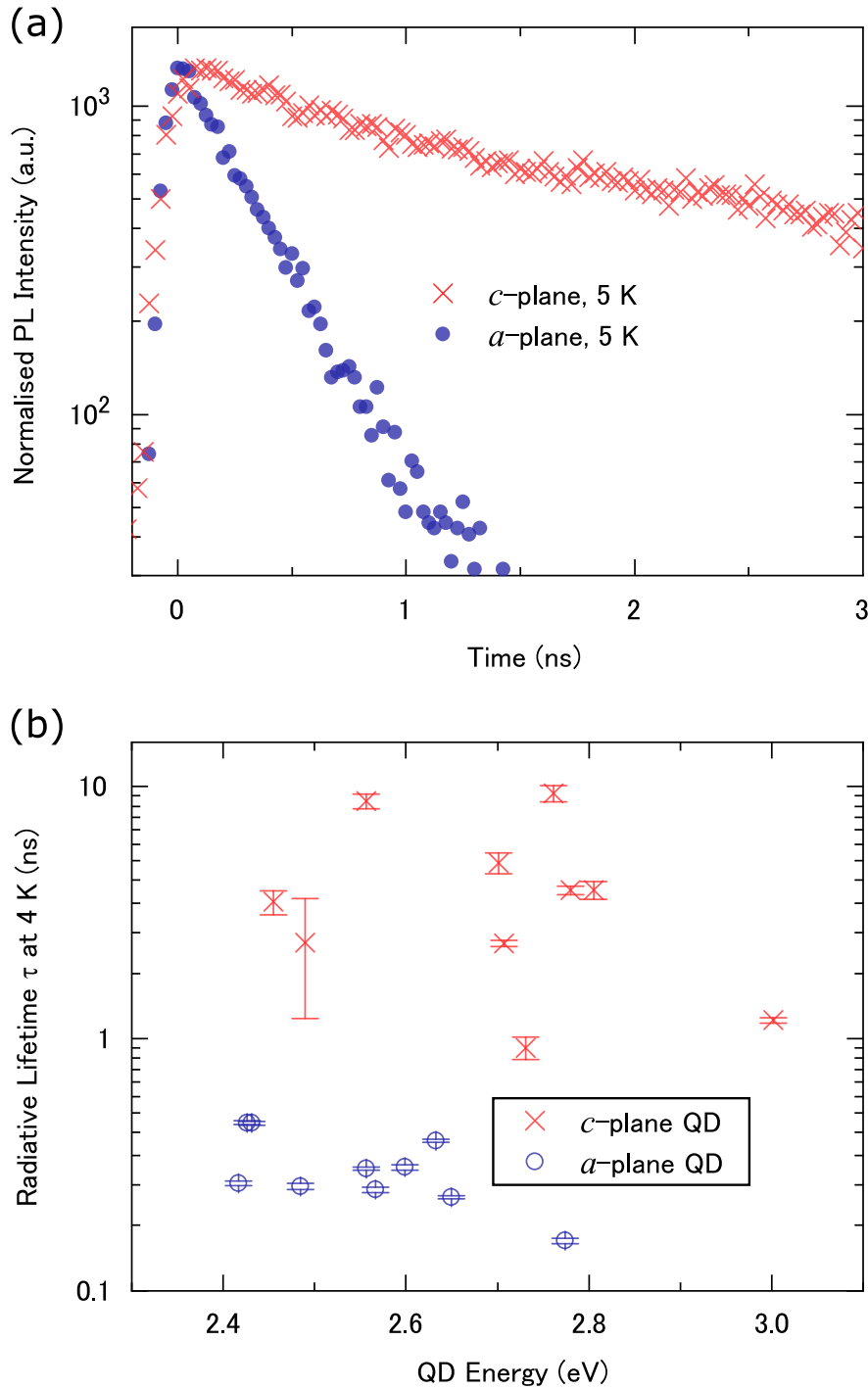


**Figure 3.8: Comparison between the radiative lifetimes of  $a$ -plane and  $c$ -plane InGaN/GaN QDs.** (a) Time-resolved  $\mu$ PL measurement of another typical  $a$ -plane QD and a typical  $c$ -plane one at a temperature of 5 K. (b) Measurement of the radiative lifetimes of 10  $c$ -plane and 10  $a$ -plane InGaN QDs. An order of magnitude faster radiative decay time can be seen in the  $a$ -plane system.

data in Figure 3.8(b). As explained previously, other factors such as the QD size, shape, and interaction with locally trapped carriers could all cause fluctuations of the oscillator strength and thus the radiative recombination rate. However, since  $a$ -plane and  $c$ -plane QDs are both self-assembled, there should be a similar degree of size and local environment fluctuations. Nonetheless, the variation of lifetimes in  $c$ -plane QDs is much larger than that of the  $a$ -plane case. It is possible that similar to the case of optical polarisation, the radiative lifetime of this  $a$ -plane system also has a different sensitivity to its physical properties. In the next section, the effect of QD sizes in altering the lifetime of  $a$ -plane QDs will be discussed.

#### 3.3.3 Effect of QD sizes

As explained in the discussion of optical polarisation properties, it is non-trivial to obtain accurate information about the size of QDs. As such, a comparison of time-resolved  $\mu$ PL measurement of lifetime on QD with different sizes is not currently possible on a self-assembled QD system. However, the results from the previous section has indirectly shown that the radiative lifetime of  $a$ -plane QDs could be less sensitive to changes in their sizes. Theoretically, the built-in field of a nitride QD should increase with a greater volume of material. As such, the stronger fields in a larger QD would result in a slower radiative lifetime. Although the built-in fields of non-polar  $a$ -plane InGa<sub>N</sub> QDs have been minimised, there are still facets of the lens-shaped QD that could generate residual fields. These residual fields should scale similarly with QD sizes as polar QDs do.

In order to shed light into this question, our collaborators in Tyndall National Institute performed  $\mathbf{k}\cdot\mathbf{p}$  calculations with consideration of Coulomb interactions [163, 164] between the electrons and holes. Adopting the same model as that explained in the polarisation section of 3.2.2, the oscillator strengths and radiative lifetimes of both polar  $c$ -plane and non-polar  $a$ -plane InGa<sub>N</sub> QDs can also be calculated. Our joint publication [173] has a more detailed description of the theoretical framework.

A lens-shaped QD with a symmetrical base has been used as the QD model. The height and base diameter of the QD are varied separately, simulating the variation of QD sizes. A height of 2.5 nm, base diameter of 24 nm, and indium content of 15% have been chosen as

### 3.3. ULTRAFAST RADIATIVE LIFETIME

---

the starting point, as these parameters produce results most similar to the experimental findings in the previous section, i.e. lifetimes of 3 ns for  $c$ -plane and 0.5 ns for  $a$ -plane. At a constant height of 2.5 nm, radiative lifetime calculations for base diameters of 6, 12, 18, and 24 nm have been performed, and the results for both  $c$ - and  $a$ -plane are displayed in Figure 3.9(a). Although the height is constant, there are still more materials in the top and bottom of the QD with larger base diameters, and thus stronger field in the normal direction. As expected, the lifetime of the  $c$ -plane QD increases proportionately with larger base diameters. However, our collaborators have found that due to the minimisation of internal field in the  $a$ -plane case, the attractive Coulomb interaction between the electron and hole has been able to significantly counteract the increased strength of the residual fields. As a result, although the residual fields have also scaled up due to increased base diameters, their impact on the radiative lifetime is minimised by the dominating Coulomb effects. Therefore, while the lifetime of the  $c$ -plane QD increases more than 4-fold (from 708 ps to 2.92 ns) with a 4-time increase of base diameter, the lifetime of the  $a$ -plane QD only increased by  $\sim 7\%$  (from 435 to 466 ps).

For the effect of height variation, the base diameter has now been fixed at 24 nm. QDs with a height of 2, 3, 4, and 5 nm have been investigated and their lifetimes shown in Figure 3.9(b). Although the radiative lifetime of the  $c$ -plane QD increases with height as expected, the changes are much more drastic. The exponential increase of radiative lifetime could be attributed to the much greater change in material along the normal  $c$ -direction. As the height of the QD increases, the built-in fields are much stronger, thereby decreasing the oscillator strength more drastically. However, in the  $a$ -plane case, the increase is limited to residual fields, which again has been mostly counteracted by the Coulomb interactions between the electrons and holes. As such, even though the lifetime of the  $c$ -plane QD increases by more than 2 orders of magnitude (from 1.60 to 237 ns) with height increased by 2.5 times, the lifetime of its  $a$ -plane counterpart only increases by 12% (from 449 to 502 ps).

It is important to note that other factors such as QD geometry and indium content could also affect the radiative recombination lifetime of the QD. However, unlike optical polarisation, QD size should be the most significant factor in determining the changing strength

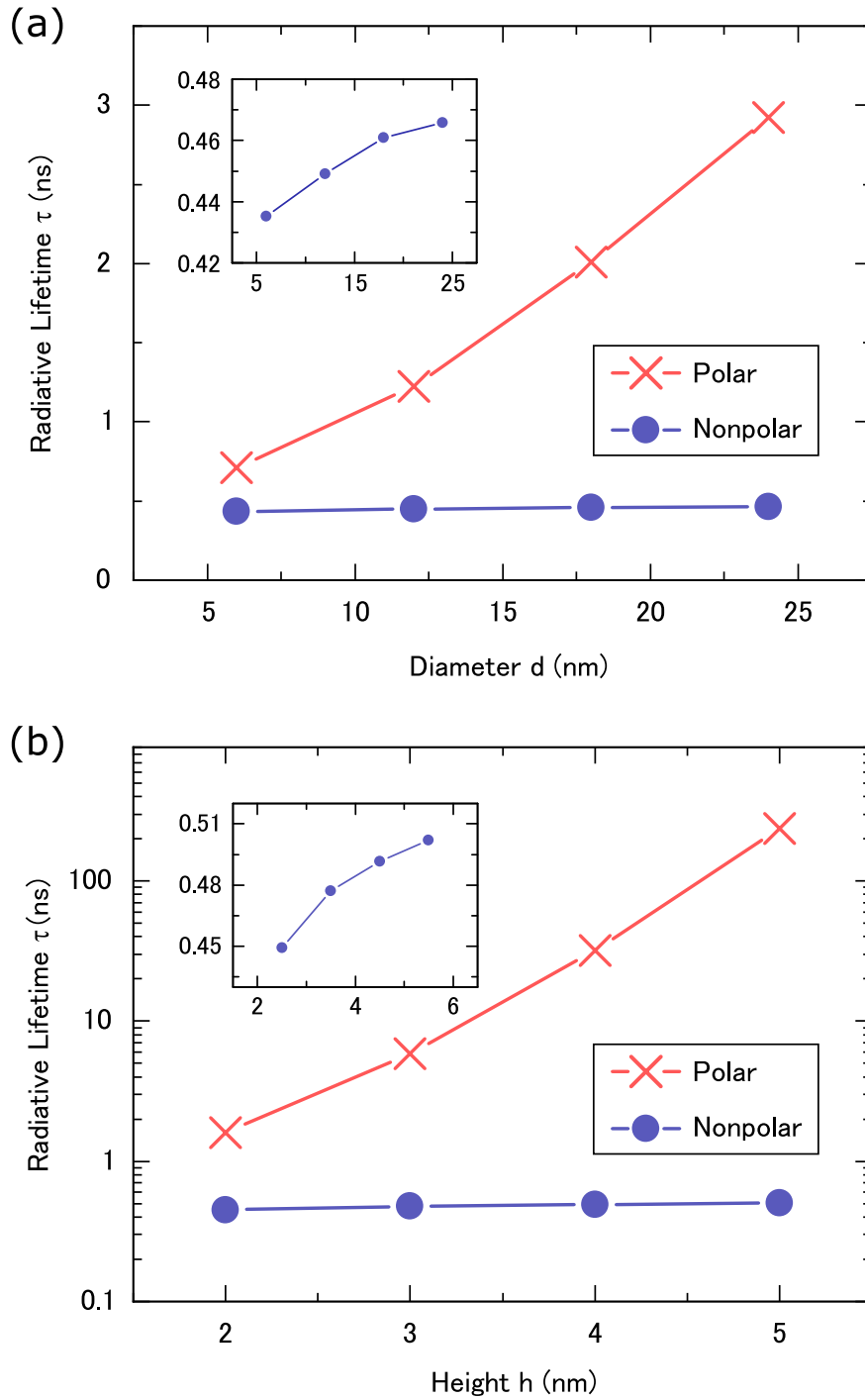


**Figure 3.9: Effect of QD sizes on radiative lifetimes for lens-shaped  $c$ -plane and  $a$ -plane InGaN QDs.** (a) Lifetimes with varying base diameter. The height of the QD is fixed at 2.5 nm. (b) Lifetimes with varying height. The base diameter is fixed at 24 nm. Both insets show the smaller changes of lifetimes in the  $a$ -plane case. The final results of this theoretical investigation are obtained by our collaborators in Tyndall National Institute.

of the built-in fields and their effect in reducing the exciton oscillator strength. Moreover, while the local environment does not affect optical polarisation significantly, the extent of fluctuating electric fields around a QD does alter its radiative lifetime (see Figure 3.6). Since these are factors which cannot be easily quantified experimentally, a corresponding theoretical investigation is not performed. As such, the most important factor of varying QD size is the only investigation carried out in the collaborative work with Tyndall National Institute.

The results of this investigation provides both good and bad news for the development of the *a*-plane platform in achieving faster radiative recombination lifetimes. Thanks to the minimisation of the internal fields, the attractive Coulomb effects between the electrons and holes dominate over the residual fields. Although these fields change with QD sizes, their effect on the radiative recombination rate is minimal. Therefore, while the lifetime of self-assembled *c*-plane InGaN QDs vary between 1 to 10 ns, it is possible to achieve consistently fast sub-nanosecond lifetimes with *a*-plane QDs. The non-zero fluctuation of *a*-plane lifetimes should be caused by both the minimised residual fields and the difference in their local environments. However, this finding does mean that the fabrication of ultra-small *a*-plane QD via future development of nanoscale engineering would be less useful to reduce the lifetime further, although it could bring about other advantages such as greater confinement and emission intensity. The only other options to achieve even faster lifetimes would be the introduction of external fields or fabrication of samples with fewer carrier trapping sites, the latter of which will be explained in detail in the next chapter.

## 3.4 Emission of single photons

### 3.4.1 First evidence of antibunching

The basic theory of HBT measurements and the detail setup used has been explained in Sections 1.2.1 and 2.3.4 respectively. With all the guidelines described, the sharp peak in Figure 3.10 should be an ideal candidate for HBT autocorrelation experiments. A pair of bandpass filters have been used to select a spectral window that contains the highest perceivable QD-to-QW ratio, while retaining the strong emission intensity as much as

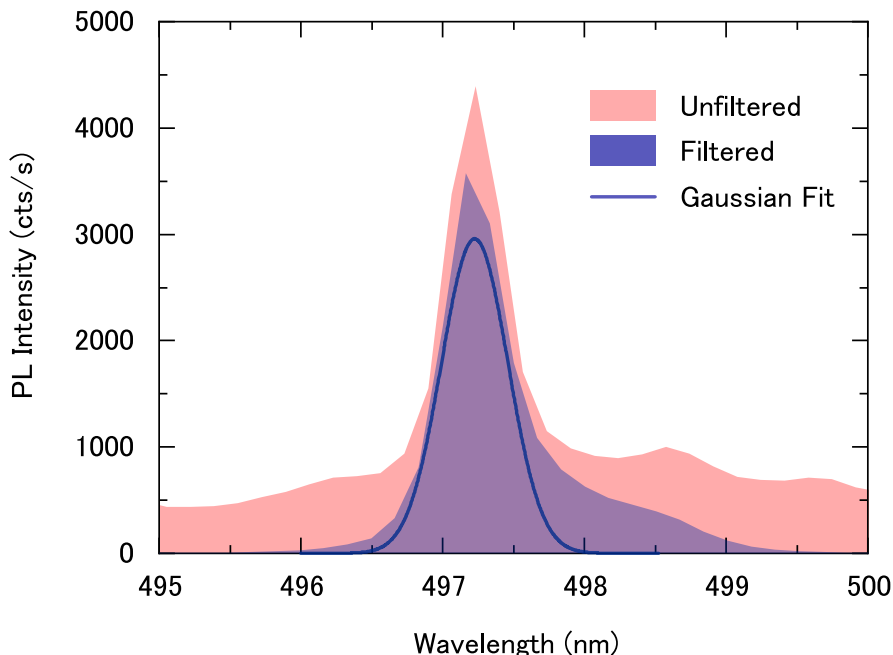


**Figure 3.10: A high-intensity single *a*-plane InGaN QD used for HBT experimentation.** Both the original and filtered spectra are shown for a comparison of their intensity and contribution of background QW. A Gaussian best fit of the filtered spectrum is also displayed to show the likely contribution of QD emission. Due to imperfect bandpass filter profiles, there is greater QW contribution at the longer wavelength side of the filtered spectrum.

possible. As shown in filtered spectrum in Figure 3.10, the peak intensity of the PL decreased by  $\sim 20\%$ , but most of the QW emission outside the QD's emission wavelength range has been blocked. Nonetheless, as the profiles of the bandpass filters are not exact boxcar functions (see Figure 2.6 in Chapter 2), the emission from those wavelengths cannot be blocked completely. Furthermore, the slope of the filter profile is steeper in the shorter wavelength end, but less so as the wavelength increases. This results in a greater amount of QW emission at the longer wavelength tail of the QD, as shown by the Gaussian fit for the filtered spectrum in the figure. However, the sharp emission is still dominating the filtered spectrum, and should therefore produce a  $g^{(2)}(0)$  of less than 1 in the photon statistics.

The filtered signal was directed to the HBT setup for a data acquisition period of 1 hour, and the photon statistics results are shown in Figure 3.11. All peak coincidences occur at multiples of  $\sim 13$  ns, which is the excitation pulse interval of the 76 MHz repetition-

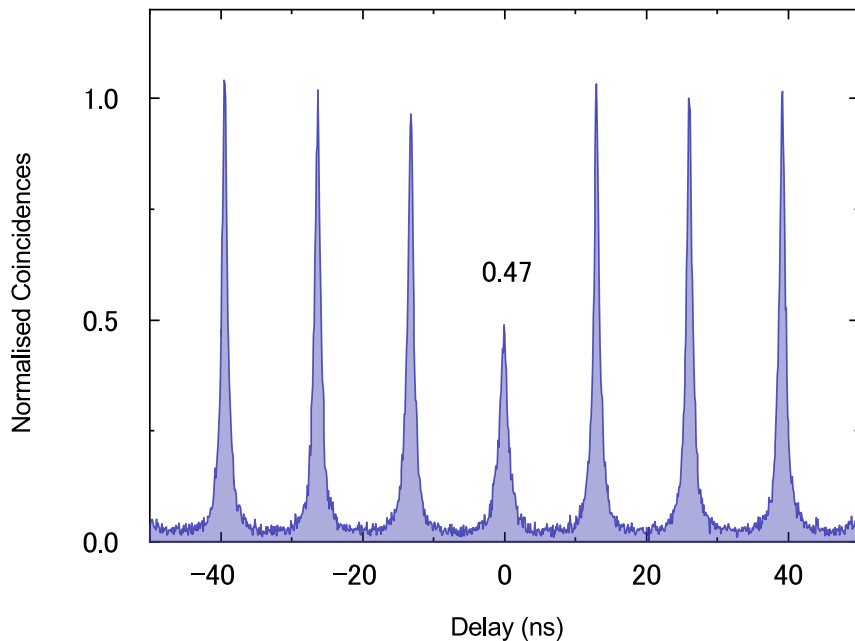


**Figure 3.11: Photo autocorrelation data from a single *a*-plane InGaN QD.** Raw HBT data of the filtered sharp peak in Figure 3.10, without any form of background reduction or correction. All 7 peaks have been normalised by a factor of 516.3, which is the mean of all recorded peak coincidence counts away from time zero. A raw  $g^{(2)}(0)$  of 0.47 ( $< 0.5$ ) confirms that the sharp peak in Figure 3.10 is emitting as a single-photon source.

rate Ti:Sapphire laser. The average count of all peaks with non-zero delays is 516.3, and the peak coincidence at time zero is 244, giving a raw  $g^{(2)}(0)$  of 0.47 without any form of background correction. As explained in Section 1.2.1, since this  $g^{(2)}(0)$  is  $< 0.5$ , antibunching with a greater probability of single- than multi-photon generation is achieved. The HBT result in Figure 3.11 thus confirms the ability of *a*-plane InGaN QDs to generate single photons. With direct evidence of the presence of a single quantum emitter, there is also much greater confidence in claiming that the nanostructure producing the sharp peak in the spectrum of Figure 3.10 originates from a single InGaN QD.

### 3.4.2 Background estimation

It is non-trivial to directly analyse the wavelength-dependent profile of the bandpass filters, and quantify its effect on the QD spectrum. In this case, a workaround is used to estimate the proportion of QW and QD intensities. Firstly, a Gaussian best fit is performed on the

unfiltered QD spectrum, and a background level of 753 cts/s is obtained. After filtering, the peak intensity of the QD decreased from 4400 to 3585 cts/s. Therefore, the QW intensity at the same wavelength (i.e. near the centre wavelength of the QD) should be decreased proportionately, to 614 cts/s. In this case, if the count rate registered by a particular CCD pixel is greater than 614 cts/s, their difference would have originated from the QD. For instance, the peak QD count rate is 3578 cts/s, indicating that approximately 2964 photons per second should arise from the QD emission at this pixel. If the count rate is lower than 614, the photons should arise from the QW.

With this method, a total of 9003 cts/s is estimated to have originated from the QD. The total count rate across the filtered spectrum, which is also the total PL intensity directed to the HBT setup, is 16766 cts/s. Therefore, the dot-to-total-intensity ratio  $\rho$  is 54%. Other methods, which involve the calculation of the area under a fitted Gaussian and estimation of the area of the background QW, have also been attempted and a similar result can be obtained. However, it is still important to note that the several assumptions have been made in this estimation, such as the level of background QW, and the proportion of QW intensity decrease after filtering. While useful, a more precise background estimation cannot be obtained in this setting. Nonetheless, the estimated  $\rho$  of 54% for the QD emission should be accurate enough for understanding the approximate contribution of single and non-single photons in the experiment.

#### 3.4.3 Conventional background correction and limitations

Since sources of unwanted background are often present in most single-photon experiments, researchers have proposed a commonly used method [54, 99, 112, 113] to correct the effect of the background and to obtain a true  $g^{(2)}(0)$  value. The corrected result should therefore be useful to understand the performance of the single-photon source itself. In the following equation,

$$\frac{1 - g_{\text{raw}}^{(2)}(0)}{1 - g_{\text{cor}}^{(2)}(0)} = \rho^2, \quad (3.7)$$

the value of  $g_{\text{raw}}^{(2)}(0)$  is used in conjunction with  $\rho$ , which again is the ratio between the intensity of the QD and the total intensity, to estimate a corrected  $g_{\text{cor}}^{(2)}(0)$ . The rationale

of Equation 3.7 is a phenomenological one. The HBT dip of an imperfect single-photon source with background signal is given by  $1 - g_{\text{raw}}^{(2)}(0)$ , and the equivalent of this imperfect quantum light source without background is  $1 - g_{\text{cor}}^{(2)}(0)$ . It was proposed that the ratio of the two dips, both of which are caused by the presence of the single photons, should be proportional to the square of the ratio between the intensity of the single quantum emitter to the total intensity. In other words, the  $g_{\text{raw}}^{(2)}(0)$  should approach  $g_{\text{cor}}^{(2)}(0)$  as  $\rho$  approaches 1.

While Equation 3.7 is frequently used in the literature [54, 99, 112, 113], researchers do not tend to use the obtained  $g_{\text{cor}}^{(2)}(0)$  values to indicate the true performance of single-photon sources. Rather, it should only be used as a guideline to understand the approximate contribution of the background in the HBT experiments. The reasons are as follows:

1. The correction formula does not have a strong quantitative basis. Although the qualitative trend of the HBT dip change with  $\rho$  is correct, the amount of change has not been rigorously derived for Equation 3.7.
2. Drastic changes in  $g_{\text{cor}}^{(2)}(0)$  are produced with small changes in  $\rho$ . In estimating the single-photon intensity ratio, there will most likely be sources of error that cannot be minimised further. However, in many cases, a 10% change in  $\rho$  could result in a 50% difference in  $g_{\text{cor}}^{(2)}(0)$ , which is clearly not physical. As such, it is easy to introduce a small source of imprecision in the estimation of  $\rho$  and produce a much higher/lower  $g_{\text{cor}}^{(2)}(0)$ . Hence,  $g_{\text{cor}}^{(2)}(0)$  calculated from Equation 3.7 should not be used as a reliable benchmark for the purity of the single-photon source.
3. In numerous cases, including the analysis of HBT results of *a*- and *m*-plane InGaN QDs, a negative  $g_{\text{cor}}^{(2)}(0)$  value is obtained with Equation 3.7, even when  $\rho$  has been estimated within reasonable accuracies. For example, with  $\rho$  estimated as 54% for the QD in Figure 3.10 and a  $g_{\text{raw}}^{(2)}(0)$  of 0.47, a  $g_{\text{cor}}^{(2)}(0)$  of  $-0.84$  is produced. Even if a  $\pm 10\%$  error is considered for the estimated  $\rho$ , the  $g_{\text{cor}}^{(2)}(0)$  still ranges between  $-1.7$  and  $-0.29$ . Although  $\rho$  is obtained with some degrees of imprecision, as noted in the previous section, it should still be a reasonably close estimate for the studied QD. The results produced by Equation 3.7 is thus highly unphysical in this situation.

Similar situations also occurred for the analyses of several other sets of HBT results, for both  $a$ - and  $m$ -plane InGaN/GaN QDs.

#### 3.4.4 An alternative background correction method

The main source of error in Equation 3.7 originates from the treatment of the HBT dip. In an autocorrelation experiment, the dip is not directly recorded. Instead, it is the coincidence events that are directly accumulated at each delay time. As explained previously, the recording of an event in the HBT setup is proportional to the square of the detected intensity. An experimental  $g^{(2)}(0)$  measurement is not a direct measurement of the dip, but of the peak at time zero. Empirically, the relationship of

$$g^{(2)}(0) \approx \frac{I_{\text{non-single}}^2}{(I_{\text{single}} + I_{\text{non-single}})^2} \quad (3.8)$$

should be a correct estimation. Again, this is not an analytical expression of the second-order autocorrelation function, but a semi-empirical model of the function's value at zero delay. The value of  $I_{\text{non-single}}$  contains both the emission from the background, and from the imperfect single quantum light source itself when it does not to emit single photons. Therefore, the expression  $1 - g_{\text{raw}}^{(2)}(0)$  in Equation 3.7 does not have a clear physical meaning, and cannot be used to represent the extent of an HBT dip or relative intensity of the single-photon source. In this case, I propose a modification of Equation 3.7 to the form of

$$\frac{1 - \sqrt{g_{\text{raw}}^{(2)}(0)}}{1 - \sqrt{g_{\text{cor}}^{(2)}(0)}} = \rho. \quad (3.9)$$

In Equation 3.9, the expression  $1 - \sqrt{g_{\text{raw}}^{(2)}(0)}$  should now represent the normalised intensity of the emitted single photons (see Equation 3.8). Following the same rationale as Equation 3.7, the ratio is thus a better indication of the comparison of HBT dips. In order to prove the validity of Equation 3.9 as an estimation of  $g_{\text{cor}}^{(2)}(0)$ , I provide the following derivation. The intensity of non-single-photon emission should have contribution from both the imperfect single-photon source,  $I_{\text{non-single,SPS}}$ , and the background (e.g. QW in the case of

### 3.4. EMISSION OF SINGLE PHOTONS

---

nitride QDs),  $I_{\text{BG}}$ . Together, they should be responsible for the non-zero peak at time zero in a photon statistics measurement. As such,  $g_{\text{raw}}^{(2)}(0)$  can be expressed as

$$g_{\text{raw}}^{(2)}(0) = \frac{I_{\text{non-single}}^2}{I_{\text{total}}^2} = \frac{(I_{\text{non-single,SPS}} + I_{\text{BG}})^2}{(I_{\text{non-single,SPS}} + I_{\text{single,SPS}} + I_{\text{BG}})^2}. \quad (3.10)$$

On the other hand, the  $g_{\text{cor}}^{(2)}(0)$  value should be a measurement of the purity of the imperfect single-photon source itself, without the contamination of background, as indicated by

$$g_{\text{cor}}^{(2)}(0) = \frac{I_{\text{non-single,SPS}}^2}{I_{\text{SPS}}^2} = \frac{I_{\text{non-single,SPS}}^2}{(I_{\text{non-single,SPS}} + I_{\text{single,SPS}})^2}. \quad (3.11)$$

At this stage, it is worth noting that the signal-to-total-intensity ratio  $\rho$  cannot incorporate  $I_{\text{non-single,SPS}}$ . It can only distinguish intensities between the single-photon source and the background, as shown in

$$\rho = \frac{I_{\text{SPS}}}{I_{\text{total}}} = \frac{I_{\text{non-single,SPS}} + I_{\text{single,SPS}}}{I_{\text{non-single,SPS}} + I_{\text{single,SPS}} + I_{\text{BG}}}. \quad (3.12)$$

The subtle differences in the subscripts between these intensities should be noted, especially in the numerators in Equation 3.10 and 3.12. Rearrangement of Equation 3.12 for  $I_{\text{BG}}$  and substitution into Equation 3.10 yield

$$\sqrt{g_{\text{raw}}^{(2)}(0)} = \frac{I_{\text{non-single,SPS}}}{I_{\text{non-single,SPS}} + I_{\text{single,SPS}}} \rho + 1 - \rho. \quad (3.13)$$

Combined with Equation 3.11, the following relationship between  $g_{\text{raw}}^{(2)}(0)$ ,  $g_{\text{cor}}^{(2)}(0)$ , and  $\rho$  is obtained.

$$\rho \sqrt{g_{\text{raw}}^{(2)}(0)} = \sqrt{g_{\text{raw}}^{(2)}(0)} + \rho - 1 \Rightarrow \frac{1 - \sqrt{g_{\text{raw}}^{(2)}(0)}}{1 - \sqrt{g_{\text{cor}}^{(2)}(0)}} = \rho \quad (3.14)$$

An arrangement of Equation 3.14 leads to the originally proposed Equation 3.9, demonstrating its theoretical foundation.

This new formula is hence used to analyse the HBT results presented in Section 3.4.1. With  $\rho$  estimated as 54% and a  $g_{\text{raw}}^{(2)}(0)$  of 0.47, a  $g_{\text{cor}}^{(2)}(0)$  value of 0.17 is obtained. Assuming a  $\pm 10\%$  ( $\rho$  values of 44% and 64%) error, the  $g_{\text{cor}}^{(2)}(0)$  values are also between 0.08 and 0.26.

Hence, these corrected results are much more physical than the negative values obtained with the conventional method.

By analysing from the origin of recording coincidences in an HBT setup, an improved background correction method is obtained. In this case, the corrected values do have stronger scientific backgrounds. However, in the interest of developing a single-photon platform, the  $g_{\text{raw}}^{(2)}(0)$  values are still the most important benchmarks. After all, the corrected result is not directly generated from the system, and is thus less meaningful as a performance metric. Theoretically and ideally, all single-photon sources recorded with absolutely zero background contamination, resonantly excited with the most optimal parameters should have a  $g^{(2)}(0)$  of 0. Nonetheless, the new  $g_{\text{cor}}^{(2)}(0)$  values can be used to more accurately analyse the impure signals from a single-photon emitter. In the  $a$ -plane InGaN QD investigated here, the corrected  $g^{(2)}(0)$  is 0.17 and still not very close to 0. As investigated in Section 3.3.2, the radiative lifetimes of  $a$ -plane QDs are around 300 ps, similar to those reported in ultra-small dot-in-nanowire GaN systems [97]. With such a fast radiative recombination rate, repopulation of a dot-related continuum of states has a higher probability to occur. The subsequent emission from these states contaminates the generation of single photons, resulting in higher  $g^{(2)}(0)$  values measured [25, 97, 112]. This could also be the reason why no  $g_{\text{raw}}^{(2)}(0)$  values of  $< 0.3$  have been measured in  $a$ -plane QDs yet, even with much weaker background QW emissions. This issue could be minimised by resonant excitation, which has not been successfully developed yet at the time of writing. It is also worth noting that although the reason above might have caused a non-zero  $g_{\text{cor}}^{(2)}(0)$  of 0.17, the presence of QW emission is still mainly responsible for the much higher raw  $g_{\text{raw}}^{(2)}(0)$  of 0.47. Reports in the literature has shown that by using weaker powers of excitation, fewer QW states will be excited, resulting in cleaner single-photon emission [127]. Due to the limited brightness of the QDs and feasibility of HBT experiments, saturation power has been used in all autocorrelation studies. As the brightness of the QD depends on the quality of the sample, it is important to develop QD samples with both higher dot density and emission intensity. In this way, there would be a greater probability to identify QDs that are both spectrally isolated and strongly emitting, thereby allowing

weaker excitation powers to be used, and potentially producing in  $g^{(2)}(0)$  values closer to zero.

### 3.5 Chapter summary

At the present stage, only self-assembled growth of  $a$ -plane InGaN QDs can be achieved. The stochastic process introduces random variations of QD size, geometry, and material composition, which could cause different orbital contributions to the hole ground state, thus affecting the polarisation of emission. These variations could also result in different amounts of residual fields, affecting the radiative recombination rate of the QDs. Combined with theoretical work from Tyndall National Institute, our experimental results have demonstrated that the intrinsic polarisation of the  $a$ -plane material is able to overcome the polarisation changes caused by these physical and compositional fluctuations, and the attractive Coulomb interactions mitigate most of the differences in oscillator strength caused by variations in size and residual fields. As a result, the  $a$ -plane QD system is not only able to produce a statistical average polarisation degree of 0.90, with a deterministic axis along either the crystal  $c$ - or  $m$ -direction, but also radiative lifetimes ranging from 200 to 600 ps.

Having fast lifetimes is an indication of an order of magnitude reduction in the built-in fields from conventional  $c$ -plane platforms. Nonetheless, it is still beneficial to aim for even faster radiative lifetimes, so as to achieve higher repetition rate of these polarised single-photon sources. Given the insensitivity of  $a$ -plane QD exciton oscillator strength to physical size differences, the development of ultra-small QDs might not be able to increase its radiative decay rate further. On the other hand, the growth of QD within a cleaner local environment—with minimised number of carrier trapping sites as Q2T samples—does have the potential to reduce the residual fields even further. The effectiveness of the Q2T routine in reducing the exciton radiative lifetime will be examined in great detail in the next chapter.

For the first time, direct evidence of single-photon generation in  $a$ -plane QDs has been achieved via HBT experiments. A recorded raw  $g^{(2)}(0)$  of less than 0.5 without any background correction indicates a greater probability of single- than multi-photon emission.

The positive result of the HBT experiment has confirmed that the identity of the sharp emission peak in the spectrum is indeed the signature of a single-photon emitting QD, and is a major milestone in the collaborative development of *a*-plane InGaN QD platform. The limitations of a background correction technique in the literature have also been evaluated, and an improved method has been proposed to produce more physical and realistic estimations of the true  $g^{(2)}(0)$  values.

# 4

## Impact of growth on optical properties

### 4.1 Chapter introduction

After the discussion of low-temperature optical characteristics of *a*-plane InGaN/GaN QDs, this chapter provides a review of the differences in their optical properties caused by two of the major growth methods. The details of these methods—modified droplet epitaxy and quasi-two-temperature routine—have been discussed in detail in Section 2.2. As explained multiple times so far in this work, advances in growth have been the key factor from making the first single-photon emitting *a*-plane InGaN QDs to alleviating current issues of their optical performance. This chapter first investigates the characteristics of PL emission and polarisation-controlled antibunching of the Q2T QDs, and contrasts them to their MDE counterparts, highlighting the trade-off made in introducing a heavier QW reliance of dot formation. Subsequently, the benefits of the resultant InGaN epilayer are quantified in areas of slow-timescale spectral diffusion, radiative recombination lifetime, and high-temperature operation stability. Lastly, the importance of using both MDE and Q2T QDs for the development of the *a*-plane platform is discussed.

## 4.2 QD emission and polarised antibunching

### 4.2.1 QD and background QW

Two typical QDs are chosen from the Q2T and MDE samples respectively for  $\mu$ PL studies, and their spectra are shown in Figure 4.1. Unlike the previous 2T development [121] mentioned in Section 2.2.1, the best of the improved Q2T samples contains QDs that emit almost as strongly as average MDE ones, albeit with lower dot densities. Gaussian profiles have been used in the figure to model both studied QDs and their QW backgrounds, as guides to the possible contributions of the full  $\mu$ PL spectra. Without a rigorous calculation, it is already clear that the Q2T QD is spectrally sitting on top of a much stronger QW emission than the MDE one. Estimations using count rates per CCD pixel—same as the method used in Section 3.4.2—across the QD spectral window yield dot-to-total-intensity ratios of 42.8% and 77.7% for the Q2T and MDE QDs respectively. The additional quantity of carrier-generating material and the undisrupted morphology result in stronger QW emission in the Q2T sample. This is especially pronounced in  $\mu$ PL experiments, because the same  $1\ \mu\text{m}$  laser spot is more likely to excite more optically active InGaN material in the Q2T sample (see Figure 2.1 in Section 2.2.2).

Spectral separation the QD and QW is highly desirable in both the study and development of a nitride QD platform. Although the formation of dots for both growth methods is reliant on the underlying QWs, the differences in their mechanisms make it more difficult to identify spectrally isolated QDs in Q2T samples. There are two possible reasons:

1. Ideally, a spatially standalone QD should emit without any contamination from background QWs. The SK-like island formation in the Q2T routine requires presence of underlying QW, whereas the metallic droplet formation in MDE relies more on decomposed QW and strain fields in the epilayer. Therefore, while the possibility of standalone MDE QDs is low in both cases, it would be highly unlikely to have Q2T QDs spatially separated from its underlying QW.
2. Due to the heavily disrupted epilayer in MDE samples, not all pieces of fragmented QWs captured by the  $1\ \mu\text{m}$  laser spot are emitting. For those that are emitting,

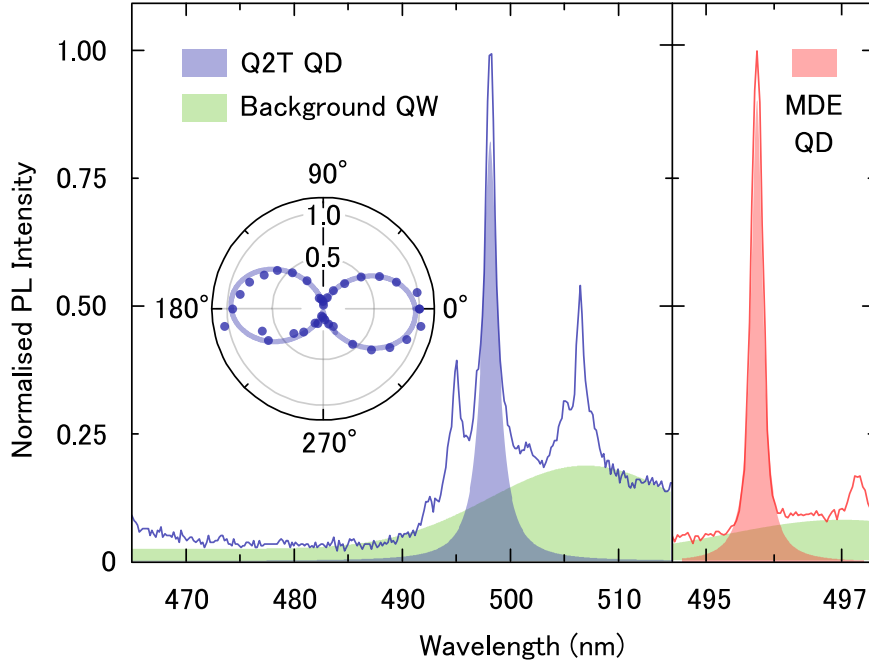


**Figure 4.1:**  $\mu$ PL spectra for polarised QD emitters in Q2T and MDE samples. The emission of QDs and their underlying QWs are fitted with Gaussian distributions as guides to the eye, demonstrating stronger QW emission in the Q2T samples. Inset: normalised QD intensity with polariser angle, fitted with Malus's law described in Equation 3.2.

their strengths should be weaker. As such, it is more likely to see a continuous spectrum of QW emission that spans over a large wavelength range in a Q2T sample. Under a broader background emission, it is thus more difficult to observe spectrally isolated QDs. Therefore, while the new growth routine provides potential benefits in optical performance with fewer carrier trapping sites, Q2T QDs have lower dot-to-background ratios than the original MDE ones. The stronger background QW emission will adversely affect the purity of single-photon emission more severely, as will be discussed in greater detail in the following sections.

#### 4.2.2 Polarisation degree and angle

Polarisation-resolved  $\mu$ PL experiment was conducted on the studied Q2T QD in Figure 4.1, with the  $0^\circ$  marking of the polariser parallel to the  $m$ -axis. Gradual intensity decreases were observed as the polariser was rotated away from  $0^\circ$ . The measured peak intensities

## 4.2. QD EMISSION AND POLARISED ANTIBUNCHING

---

at  $10^\circ$  intervals over a full  $360^\circ$  cycle have been recorded and normalised as described in Section 3.2.3, and shown in the inset of Figure 4.1. These data have also been fitted with Equation 3.2, confirming their agreement with Malus's law of polarisation. The main axis of the polar plot is also aligned to  $0^\circ$ , with  $\varphi < 5^\circ$ , due to errors of manual placement of the sample in the cryostat. Calculation of the polarisation degree yields a  $P$  of  $0.92 \pm 0.05$ , which is coincidentally the same as result at that obtained for the MDE QD previously. Therefore, the studied Q2T QD exhibits an MDE-like high polarisation degree with a fixed axis along the crystal  $m$ -direction.

However, as previously explained, Q2T QDs exhibit a bimodal size distribution (see Figure 2.2) and therefore much larger dimension variation than MDE ones. In the last chapter, we have concluded that  $a$ -plane InGaN QDs are highly insensitive to these differences in geometry and size, as the effect of the polarisation anisotropy built into the  $a$ -plane material itself is much more dominant. As such, this conclusion is expected to be re-confirmed with Q2T QDs, despite their greater size variations.

Based on the DOLP calculation of 50 QDs from each sample shown in Figure 4.2, Gaussian distributions with means of  $0.88 \pm 0.08$  and  $0.87 \pm 0.09$  have been obtained for Q2T and MDE QDs respectively. First of all, the MDE polarisation results agree very well with our investigations detailed in Section 3.2.4, where a mean of  $0.90 \pm 0.08$  has been found with 180 randomly selected MDE QDs. In the Q2T case, although much larger variations in QD size exist due to its bimodal distribution, the polarisation degrees are not significantly affected, yielding similarly high average DOLPs across the sample. This finding again re-confirms that the polarisation anisotropy built into the  $a$ -plane material itself is able to overcome the effects of size variations, even in the more drastic case of a bimodal distribution with potentially 10-fold different physical dimensions.

Within a  $10^\circ$  error, there is no significant difference in polarisation angle either. Most QDs are polarised along the crystal  $m$ -direction, with  $< 10\%$  exception along the  $c$ -direction as expected. Further experiments with exact calculations of the polarisation angle would be needed to ascertain if there is a difference between the two types of QDs. Such experimentations would require a fully automated polarisation data acquisition system, in order to be more feasibly and efficiently carried out. Due to time constraints and the unavailability

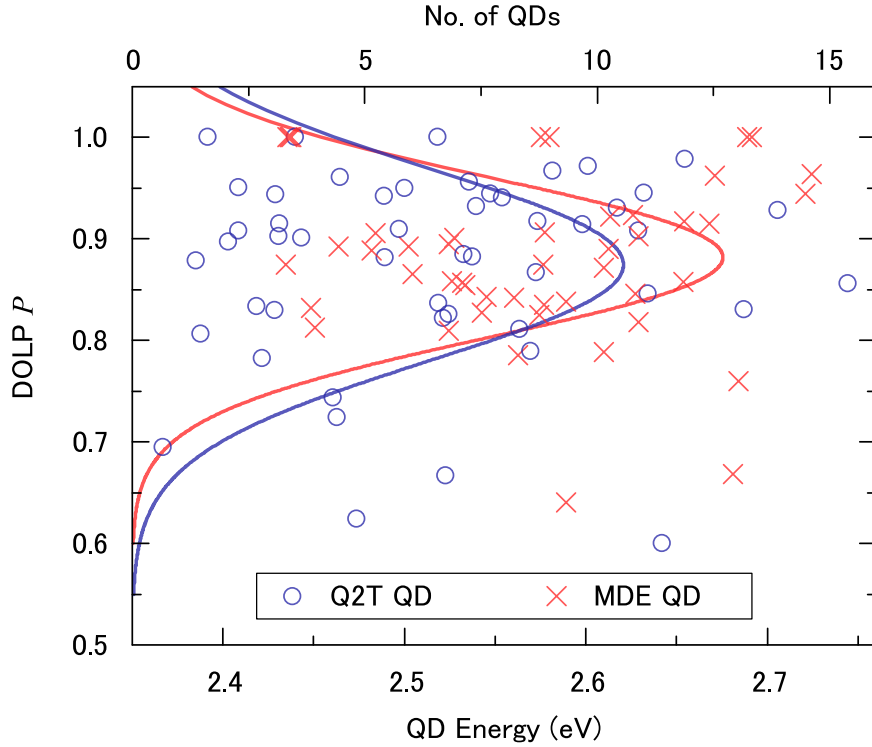


**Figure 4.2: Comparison of polarisation degrees of Q2T and MDE  $a$ -plane InGaN QDs with statistical significance.** A random selection of 50 Q2T and 50 MDE QDs has been made, and their DOLPs measured and shown in the scatter plot. Gaussian distributions have been fitted to both results, yielding near identical means and standard deviations. This statistical study indicates that there are no differences in optical polarisation properties for QDs grown by both methods.

of the said automatic system at the time, these experiments were not performed. While such investigations would be interesting for clarifying minute ( $< 10^\circ$ ) differences in the polarisation angles between these growth methods, the current results are sufficient to demonstrate that Q2T QDs are equally good quantum emitters with high average DOLPs mostly aligned along the crystal  $m$ -axis, and are thus useful for the development of the  $a$ -plane InGaN QD platform.

### 4.2.3 Antibunching and single-photon purity

As one of the most important goals in developing the  $a$ -plane platform, the ability to emit single photons has been tested against the newly developed Q2T QDs. Although Q2T samples with nanopillar enhancement have much stronger emission than the original 2T

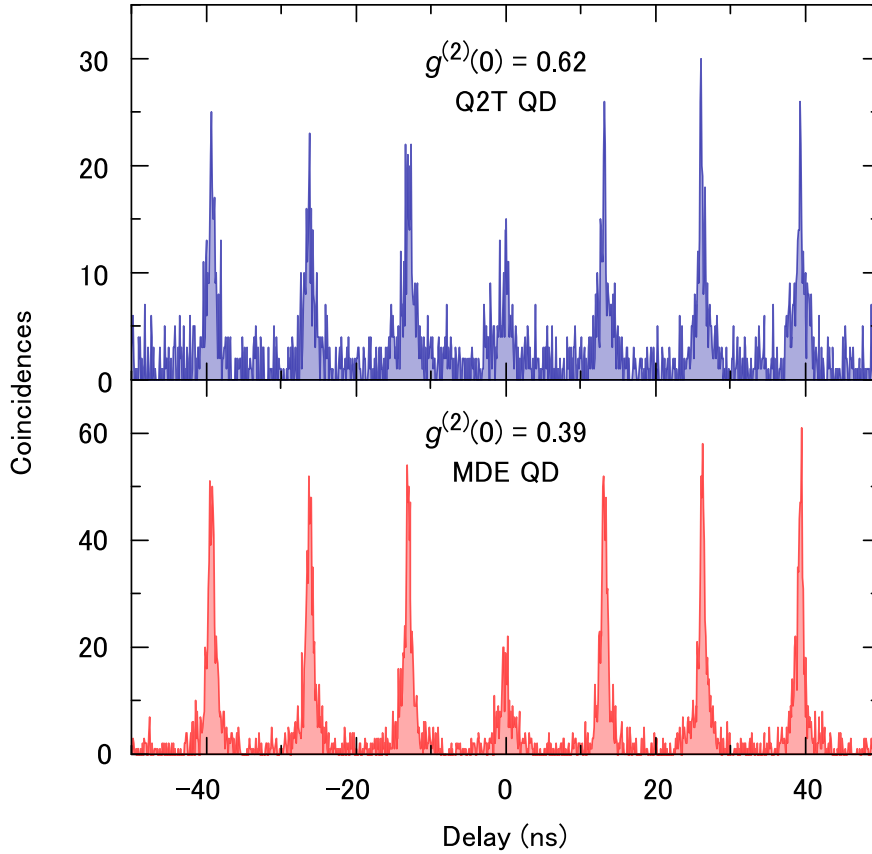


**Figure 4.3:** Comparison of single-photon antibunching from the pair of Q2T (top) and MDE (bottom) *a*-plane InGaN QDs shown in Figure 4.1. The uncorrected raw  $g^{(2)}(0)$  values demonstrate greater amount of undesired QW emission in the Q2T sample. The smaller number of total coincidences for the Q2T QD is due to the relatively weaker emission.

ones, their dot density and brightness are still not comparable to typical MDE ones, as explained previously. Therefore, it is relatively less challenging in the MDE sample to find QDs with  $> 1000$  cts/s in the same  $\mu$ PL system, which would expedite HBT experiments. While autocorrelation measurements have been performed on several candidates across a few Q2T samples, the QD shown in Figure 4.1 produced the lowest raw  $g^{(2)}(0)$  of 0.62. The studied MDE QD in Figure 4.1 yielded a raw  $g^{(2)}(0)$  of 0.39, similar values of which can be consistently obtained in MDE samples, such as that in Section 3.4.1. The HBT autocorrelation results of both QDs are shown in Figure 4.3.

Even with tuneable bandpass filters restricting the range of emission energies across the spectra, the stronger background QW emission in the same wavelength range as the Q2T

QD introduces more undesired signals in the HBT experiments. Having an intrinsically poorer dot-to-background ratio, the  $g^{(2)}(0)$  of the Q2T QD is significantly higher than the MDE one. With  $\rho$  of 42.8% and 77.7% and Equation 3.9 proposed in the last chapter, the corrected  $g^{(2)}(0)$  becomes 0.25 and 0.27 for the Q2T and MDE QDs respectively. These values are very similar, implying that the QDs are indeed emitting as imperfect single-photon sources with signals from their underlying QW. As explained in Section 3.4.4, the reason for the high non-zero corrected  $g^{(2)}(0)$  should be attributed to the rapid repopulation of dot-relation states, and the subsequent re-emission from them. The larger corrected values than that of the QD evaluated in Section 3.4.4 could be caused by the use of even higher laser excitation powers [127]. Since both of the QDs shown in Figure 4.1 are less strongly emitting than that in Figure 3.10, a power slightly larger than their perceived saturation level was used so as to improve the feasibility of the HBT experiments. Nonetheless, a comparison of the raw and corrected  $g^{(2)}(0)$  results confirms the adverse effects in achieving purer single-photon emission with Q2T QDs. At the moment, under pulsed laser excitation, no raw  $g^{(2)}(0)$  of  $< 0.5$  has been achieved in a Q2T sample, while  $g^{(2)}(0)$  between 0.3 and 0.5 can be obtained with MDE QDs.

In order to attempt reducing the dot-to-background ratio in Q2T samples, the thickness of the underlying QW epilayer could be reduced so as to decrease the total number of available carrier-generating material. However, a reduction of epilayer thickness from the optimal 16 monolayers also adversely affect the dot formation. Several Q2T samples with an epilayer thickness of 0.5, 2, 4, and 6 ML have been fabricated in Cambridge, and their optical performance tested in the same optical system. At 0.5 and 2 ML, the resultant nanostructures were not able to show characteristic QD emission under the same excitation conditions. The thinnest QW with which QD emission can still be observed is 4 ML. However, with a 75% reduction of the epilayer thickness, the probability of metallic island formation has also decreased significantly. As a result, there is approximately an order of magnitude drop of dot density compared to the original Q2T samples with 16 ML InGaN epilayers, which already have lower dot densities than MDE ones. Further compounding the problem is the reduction of emission intensity across the sample. Optical activity depends on the quality of the resultant nanostructures. The InGaN material quality for

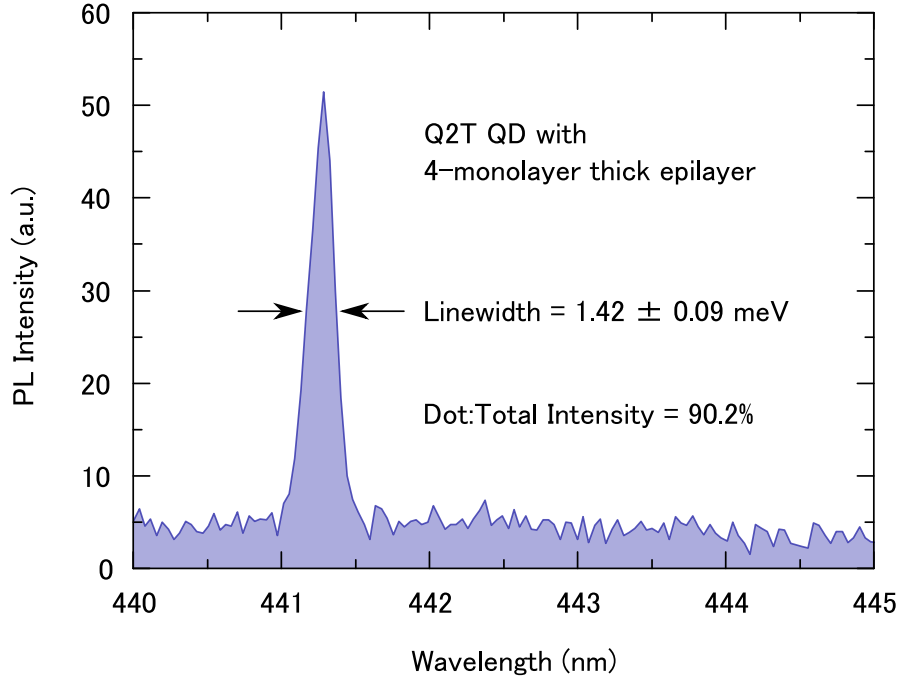


**Figure 4.4:**  $\mu$ PL from a Q2T QD with 75% reduced epilayer thickness. Dot-to-background ratio has been significantly improved, while the QD intensity has decreased drastically compared to previous Q2T QDs with 16-monolayer InGa<sub>N</sub> QW. There is no observed narrowing of linewidth after epilayer thickness reduction.

the Q2T routine is optimal at 16 ML, and thus the sample emissivity (both QD and QW) is much lower 4 ML. These problems make finding characteristic sharp emission peaks much more difficult.

However, when a QD is found, its dot-to-background ratio is indeed improved significantly compared to 16 ML Q2T ones. An example of a Q2T QD with a 4 ML underlying QW is shown in Figure 4.4, with a ratio of 90.2% between the dot signal and total intensity. This value is representative of the several QDs identified in the 4 ML sample, and is indeed much higher compared to the 42.8% and 77.7% of the Q2T and MDE QDs in Figure 4.1. In terms of brightness, the QD only has a peak intensity of  $< 50$  cts/s under the same excitation power, thus making autocorrelation experiments less feasible to perform.

As such, further improvement of the Q2T method would still be required to induce more effective island formation on a 4 ML epilayer. Nonetheless, it is important to realise that single-photon emission is not the only purpose of the development of the  $a$ -plane QD plat-

form. Investigations of high-temperature QD photophysics, elucidation and improvement of other QD optical properties are equally important. These could benefit much more from the development of the Q2T method, and will be explained in the following sections. At the moment, the 16ML samples are still the best balance of emission brightness, dot density, and signal-to-noise ratio for the investigation of these topics.

For instance, even with significantly reduced background QW carriers, the linewidth of the studied QD in Figure 4.4 ( $1.42 \pm 0.09$  meV) is still not small, noting that the average InGaN QD linewidth is  $\sim 1$  meV [28, 182] and that of typical *a*-plane ones can often be  $< 1$  meV (see Figure 2.5 and Section 2.3.3). As linewidth is a measure of the fast-timescale spectral diffusion caused by carriers in the QW, the development of Q2T QDs thus opens up the need for further discussion and elucidation of the nature of linewidth measurement in a  $\mu$ PL experiment.

## 4.3 Spectral diffusion

### 4.3.1 Linewidth and fast-timescale spectral diffusion

As explained in Section 2.3.3, the true linewidth of a QD exciton transition is Fourier-limited by its radiative lifetime. However, due to carriers in the vicinity of a QD, the instantaneous electric fields cause the QD exciton transition energy to undergo fluctuations. These spectral diffusions can happen at a slow ( $\sim$ ms to s) or a fast ( $\sim$ ns) rate [134]. The spectra recorded with an acquisition time of 0.5 to 1 s would thus not be able to determine the energy shifts of the fast-timescale spectral diffusion, resulting in a dataset accumulated with many nanosecond-scale ones at fluctuating energies [136, 183, 184]. Therefore, the observed linewidth of a 1 s QD spectrum is a measure of the degree of its fast-timescale spectral diffusion.

The origin of spectral diffusion of this type is the itinerant carriers in the nearby material [134]. In the case of both Q2T and MDE QDs, the laser excitation is below the GaN band gap, and directly into the InGaN QW. As mentioned earlier, the underlying QW in Q2T samples are less disrupted and contain more carriers than MDE ones. It would *prima facie*

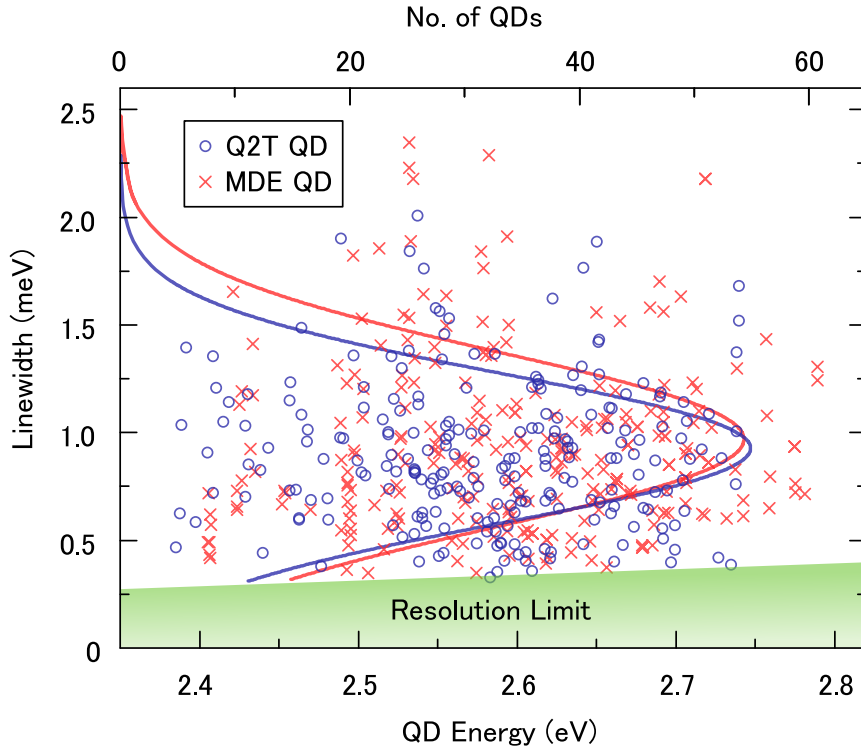


**Figure 4.5: Comparison of exciton linewidth of Q2T and MDE  $a$ -plane InGaN QDs with statistical significance.** A random selection of 229 Q2T and 265 MDE QDs has been made, and their linewidths measured and shown in the scatter plot. Gaussian distributions have been fitted to both results, yielding near identical means and standard deviations. This statistical study indicates that there are no significant differences in linewidth, and thus fast-timescale spectral diffusion, for QDs grown by either methods.

suggest that the linewidth of Q2T QDs might be narrower. However, this should not be the case for the following two reasons:

1. Due to the reliance on QW in dot formation in both methods, itinerant carriers will always be present in the vicinity of both Q2T and MDE QDs. The difference should be in the frequency of presence of these itinerant carriers in the QW at a nanosecond scale. According to the QW spectra in Figure 4.1, the frequency (also manifested in the QW intensity) could be at most a few times higher in a Q2T sample, but not a few orders of magnitude higher.
2. With an acquisition time of 1 s, there should be an accumulation of  $10^7$  to  $10^9$  number of nanosecond-scale dataset affected by fast-timescale spectral diffusion. The

extent of each individual nanosecond-scale energy change caused by the itinerant carriers is limited and has a finite range of possibilities. This range should be fully covered by  $10^7$  accumulations, and the linewidth should not increase infinitely (neglecting slow-timescale spectral diffusion and other variables) with a greater number of accumulations. Thus, even though itinerant carriers are appearing with frequencies a few times different between Q2T and MDE samples, the final result should be similar due to the much larger numbers of accumulations.

In order to confirm this argument, another statistical investigation of the linewidths of QDs grown with both Q2T and MDE methods has been conducted. From a total of 100  $\mu$ PL spectra obtained at random locations of each sample, all QDs contained in the spectra were studied without selection bias. As a result, the linewidths of 229 Q2T and 265 MDE QDs have been measured and the results displayed in Figure 4.5. The slightly larger number of MDE QDs is due to the greater dot density of the sample. All results were obtained at the same temperature of 4.7 K under the same excitation power.

The linewidths for both Q2T and MDE QDs lie in the range of  $\sim 0.3$  to 3 meV. It is important to note that the intrinsic differences in size, shape, and material contents not only affect the inhomogeneous broadening of the QDs, but also the extent of interaction with the instantaneous electric fields caused by itinerant QW carriers, i.e. the degree of fast-timescale spectral diffusion. As such, due to the stochastic self-assembly process, these physical differences result in the span of linewidth values. Statistical calculations yield means with standard errors of  $892 \pm 16 \mu\text{eV}$  for the Q2T QDs' linewidths, and  $932 \pm 15 \mu\text{eV}$  for their MDE counterparts. These results are very similar, and a Student's *t*-test further determines that their small difference should be within the statistical error of variation. Therefore, despite having greater numbers of carriers in the QW, the linewidths of Q2T QDs do not differ significantly from those of MDE ones.

However, although the extent of each instance of fast-timescale spectral diffusion has been combined over  $> 10^7$  accumulations in a 1 s  $\mu$ PL spectrum, it is still crucial to understand the actual characteristic spectral diffusion time and attempt to suppress the degree of fast-timescale spectral diffusion. The only successful method so far has been the use of photon autocorrelation measurements to calculate the characteristic rate of fast-timescale

spectral diffusion in high-intensity GaN [135] and CdSe [185, 186, 187] systems. Such measurements have not yet been successful in the *a*-plane InGaN system, due to the limited emission brightness. With further improvement of brightness beyond current MDE and Q2T samples, it would be important to conduct such investigations to better understand the nature of the challenge in reducing fast-timescale spectral diffusion of *a*-plane InGaN QDs.

#### 4.3.2 Carrier traps and slow-timescale spectral diffusion

Unlike itinerant carriers in the QWs, the cause of slow-timescale spectral diffusion is mostly attributed to charges trapped in sites near the QDs [134]. These trapped carriers have much longer presence at a timescale of ms to s, before going through non-radiative recombination. Therefore, unlike fast-timescale spectral diffusion, these much slower Stark shifts are observable in  $\mu$ PL studies [188] with comparable durations of data acquisition.

While the use of Q2T QDs does not suppress the extent of exciton linewidth broadening induced by fast-timescale spectral diffusion, the much less disrupted epilayer morphology has a more positive effect in reducing such spectral drifts at a much slower timescale. As previously discussed, the disruptions to the MDE InGaN epilayer potentially result in a greater number of carrier trapping sites, which under optical excitation increase the strength of a locally fluctuating electric field. As such, the strength of the spectral drifts of MDE QDs at a ms to s timescale should be greater than the Q2T sample.

The pair of QDs studied in Figure 4.1 would be less ideal for an investigation of spectral diffusion. Although both emitting strongly enough for HBT experiments, they have dissimilar linewidths and thus potentially different degrees of fast-timescale spectral diffusion. As the relationship between fast- and slow-timescale spectral diffusion is unknown and non-trivial to establish in a self-assembled system, a new pair of QDs from the Q2T and MDE samples with similar linewidth should be used to minimise the influence of fast-timescale spectral diffusion. As shown in Figure 4.6, these two QDs have very similar linewidths of 1.18 (Q2T) and 1.17 meV (MDE). They both have a peak intensity of  $\sim 300$  cts/s in the same  $\mu$ PL system, emitting at 2.59 (Q2T) and 2.51 eV (MDE) respectively. Over a period of 100 s, the Q2T PL has much smaller drifts across a 1 nm spectral

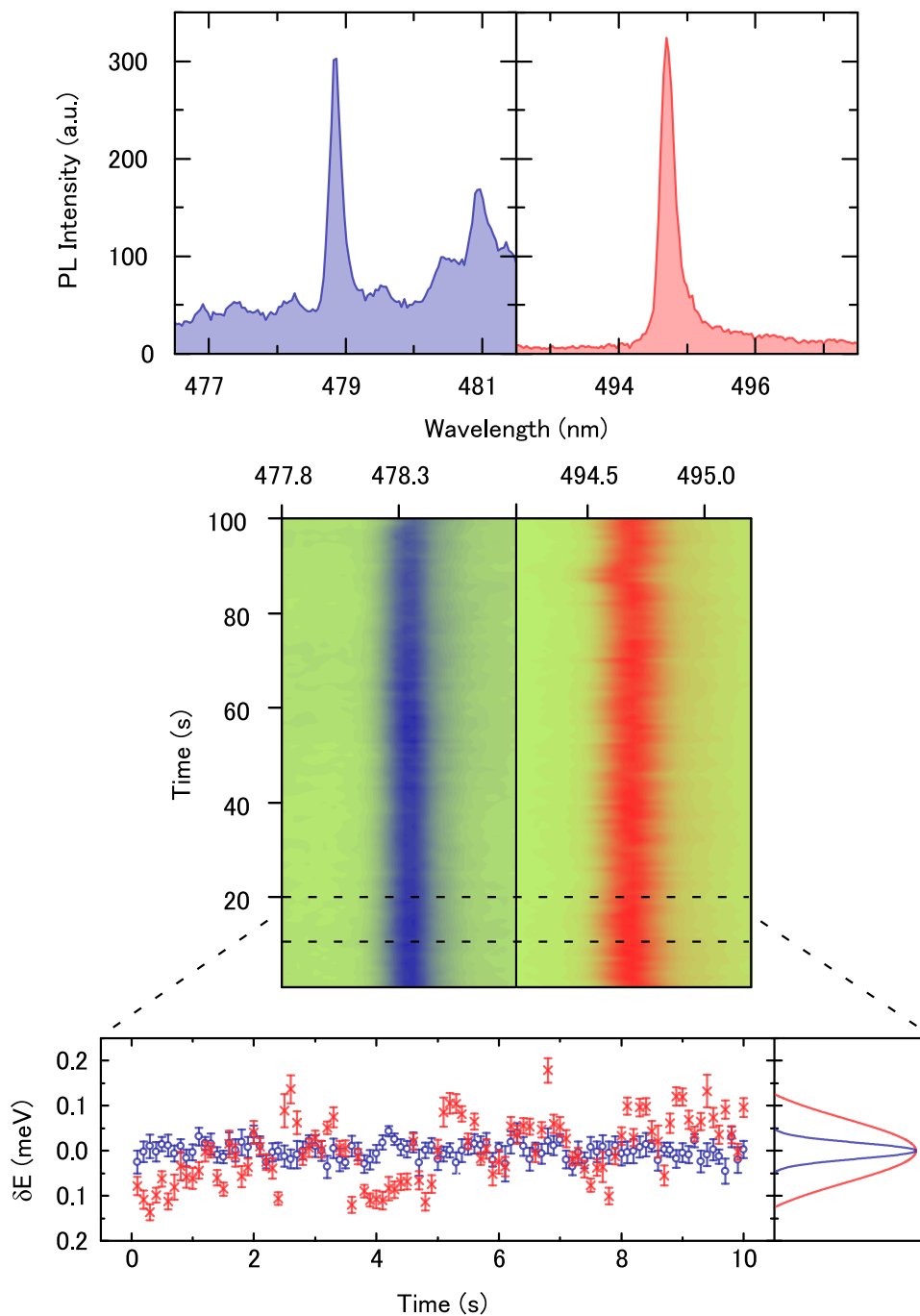


**Figure 4.6:** Comparison of slow-timescale spectral diffusion of a comparable pair of Q2T and MDE *a*-plane InGaN QDs. A 100 s  $\mu$ PL mapping with 1 s resolution is displayed together with evolution of QD emission energies over a 10 s period at steps of 100 ms. There is a significant reduction in the extent of slow-timescale spectral diffusion for the studied Q2T QD.

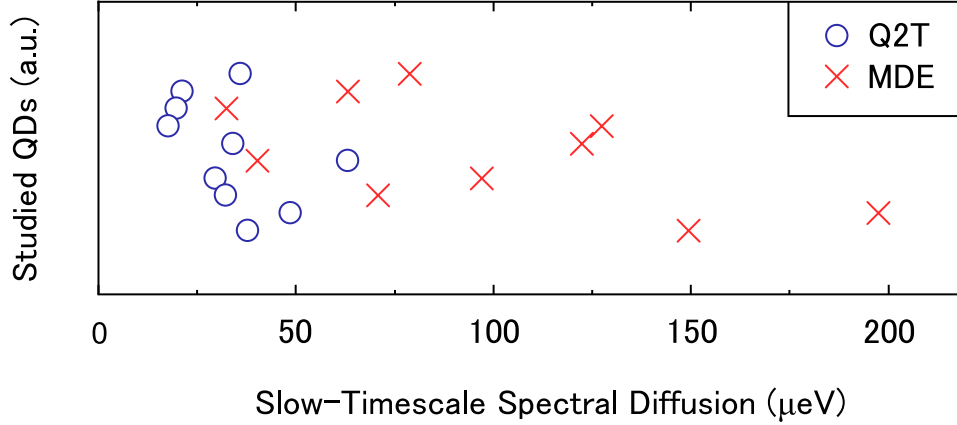


**Figure 4.7: Statistical comparison of slow-timescale spectral diffusion of Q2T and MDE *a*-plane InGaN QDs.** The emission energy standard deviations of 10 Q2T and 10 MDE QDs are calculated in the same manner as Figure 4.6, demonstrating that the Q2T QDs have a smaller average slow-timescale spectral diffusion with a narrower spread of drift values.

window as displayed in the maps of Figure 4.6. In order to quantify the extent of slow-timescale spectral diffusion,  $\mu\text{PL}$  spectra with an acquisition time of 100 ms over a total period of 10 s have been fitted with Gaussian profiles, yielding standard deviations of 17.5 and  $70.8 \mu\text{eV}$  for the Q2T and MDE QDs respectively. From the bottom part of Figure 4.6, it can be seen that the degree of Stark drifts in the studied MDE QD is indeed much greater.

In order to confirm this finding, a study of slow-timescale spectral diffusion of 10 Q2T and 10 MDE QDs has been carried out to gain more insights into the general behaviour of the two systems. The calculation of standard deviation follows the same method as that used in Figure 4.6, and the results are displayed in Figure 4.7. It can be seen that the standard deviations of Q2T QDs' mission energies are not only smaller, but also cover a much narrower range. Means of  $33.8 \pm 13.9$  and  $97.9 \pm 51.6 \mu\text{eV}$  have been found for the studied Q2T and MDE QDs respectively. The larger spread of the MDE data could be attributed to the more varied local environment, due to the random disruptions to the InGaN epilayer. The 65% reduction thus confirms that these Stark shifts occurring at slow timescales have indeed been minimised with the development of the Q2T fabrication method.

At this stage, it is worth noting that both Q2T and MDE QDs, as InGaN QDs grown along the non-polar  $a$ -plane, have smaller degrees of slow-timescale spectral diffusion compared to their  $c$ -plane counterparts. Literature reports indicate spectral drifts in the range of 120 to 260  $\mu\text{eV}$  in  $c$ -plane systems [134] with similar MOCVD fabrication methods. This is due to the minimisation of the built-in fields and the quantum confined Stark effect. Having greater electron and hole wavefunction overlap, carriers generated have much shorter radiative lifetimes, as established in Section 3.3. Therefore, given the same total number of carriers, their presence in trapping sites would decrease due to the increased rate of radiative recombination. Combined with the development of the Q2T method and the reduction of carrier traps, a 10-fold decrease in slow-timescale spectral diffusion has now been achieved, and is the smallest value reported in the InGaN QD literature. Furthermore, the Q2T emission energy drifts in both Figure 4.6 and 4.7 are now comparable to state-of-the-art GaN system reported in the literature (16.4  $\mu\text{eV}$ ) [189]. This is in spite of the fact that an InGaN platform has a greater inclination to form carrier-trapping sites during the indium incorporation stage. In the current  $a$ -plane InGaN system with an average linewidth of  $\sim 1$  meV, a slow-timescale spectral diffusion of  $\sim 30$   $\mu\text{eV}$  (3% of 1 s linewidth) rather than  $\sim 200$   $\mu\text{eV}$  (20% of 1 s linewidth), studies of bandpass filter-restricted single-photon generation, power-dependent energy shifts, fine-structure splitting, external field-induced Stark shifts, and other low-temperature optical and electro-optical properties could be conducted much more accurately and efficiently.

## 4.4 Faster radiative lifetime

### 4.4.1 Carrier traps and oscillator strength

In Section 3.3, the radiative lifetime of MDE  $a$ -plane QDs have been compared to  $c$ -plane ones, confirming the ability of the  $a$ -plane platform to generate photons with sub-nanosecond radiative lifetimes. The discussion also concluded that  $a$ -plane QDs are highly insensitive to variations in its QD sizes, due to the minimisation of built-in fields and dominance of electron-hole Coulomb interaction over the residual fields. As a result, the only other method to reduce the lifetime further without using an external electric field

would be the fabrication of a new sample with significantly decreased number of carrier traps.

As Figure 3.6 in Chapter 3 shows, the effect of carriers trapped in sites near a QD is similar to that of the internal fields in polar nitride. These instantaneously trapped charges generate transient electric fields that spatially separate the electron and hole wavefunctions, causing a reduction in oscillator strength and radiative recombination rate. Although the effect of their lifetime changes should be much smaller than that of the built-in fields, a significant reduction of carrier trapping sites across the sample should result in an observable decrease of the exciton lifetimes. As explained in the previous section, the much less disrupted epilayer in Q2T samples have fewer local carrier traps, which have already been shown to result in a reduction in slow-timescale spectral diffusion compared to MDE QDs. In this section, the radiative lifetime of Q2T QDs will be measured and the difference to MDE QDs will be quantified. Furthermore, with statistically significant measurement of the Q2T lifetime, the insensitivity of *a*-plane QDs to varying physical sizes will also be tested against the bimodal size distribution of Q2T QDs.

#### 4.4.2 Further reduction of *a*-plane QD lifetime

Using the same method described in Section 3.3.2, the radiative lifetime of Q2T QDs are assessed with time-resolved  $\mu$ PL. The TCSPC data of a typical single Q2T QD is shown in Figure 4.8(a). With a reduction of carrier traps in the vicinity of the QD, its radiative recombination lifetime is expected to be even shorter than the range of 200–600 ps for MDE QDs shown in Figure 3.8. Therefore, the width of the IRF ( $\sim 140$  ps) would have an even stronger influence on the raw exponential decay data originated from the QD emission. As such, the use of Equation 3.6—a convolution of the IRF Gaussian with an exponential decay—is paramount in performing accurate measurement of the radiative lifetime of Q2T *a*-plane InGaN QDs. The fitting yields a time constant of  $150 \pm 1$  ps, which is one of the lowest lifetimes measured in the *a*-plane system, and indeed smaller than the MDE range of 200–600 ps.

In order to ascertain that this single measurement is not merely an outlier data point, statistically significant investigation of the lifetime of Q2T QDs has been performed. Since

it is highly non-trivial to quantify the number of carrier traps around each individual QD, such a statistical study is necessary in determining the average behaviour of QD lifetimes across the sample. In this case, although the range of MDE QD lifetime has already been determined in Section 3.3.2, only 10 QDs were included in that investigation. These 10 QDs are indeed sufficient to determine the order of magnitude lifetime difference between *c*-plane and *a*-plane QDs, but might not be enough to quantify the potentially much smaller difference between MDE and Q2T QDs. As such, other than 36 Q2T QDs, another 46 MDE QDs have also been selected and their lifetime measured as the method described above. Similar to polarisation studies, these QDs are chosen with minimal selection bias. However, in order to obtain an accurate TCSPC dataset within a reasonable timeframe, only QDs with a peak intensity of  $> 100$  cts/s in our  $\mu$ PL system have been included. Otherwise the sample might either drift out of the laser excitation due to prolonged acquisition periods (e.g.  $> 5$  min) or produce TCSPC data with too much noise for accurate analysis.

The mean of the Q2T QDs shown in Figure 4.8(b) with standard error is  $173 \pm 12$  ps, which confirms that the single measurement in Figure 4.8(a) is indeed representative of QDs in a Q2T sample. Compared to the MDE mean of  $309 \pm 25$  ps, there is a  $\sim 45\%$  decrease in the radiative lifetime. As such, the reduced number of carriers trapped around Q2T QDs does indeed generate weaker transient fields, thereby doubling the oscillator strength of the exciton transitions. It is also interesting to note that with the larger statistics, the MDE lifetimes range from 100 to 900 ps, with a majority of the results between 200 to 500 ps. This is in agreement of the finding presented in Section 3.3.2, where a range of 200 to 600 ps is found based on 10 MDE QDs. The spread of the values should be attributed to the varying local environment of individual QDs. With a heavily disrupted InGaN epilayer, there could be large deviations of the number of trapping sites around different QDs, as explained in the previous spectral diffusion section. It is also worth noting that there are indeed MDE QDs with lifetimes faster than 200 ps, which should be a result of relatively fewer carrier traps around the particular QDs. However, this fast lifetime cannot be consistently reproduced due to the large and uncontrollable local environment variations. On the other hand, the smooth underlying QW in the Q2T sample not only contains fewer carrier traps, but also results in a smaller deviation in the local environment

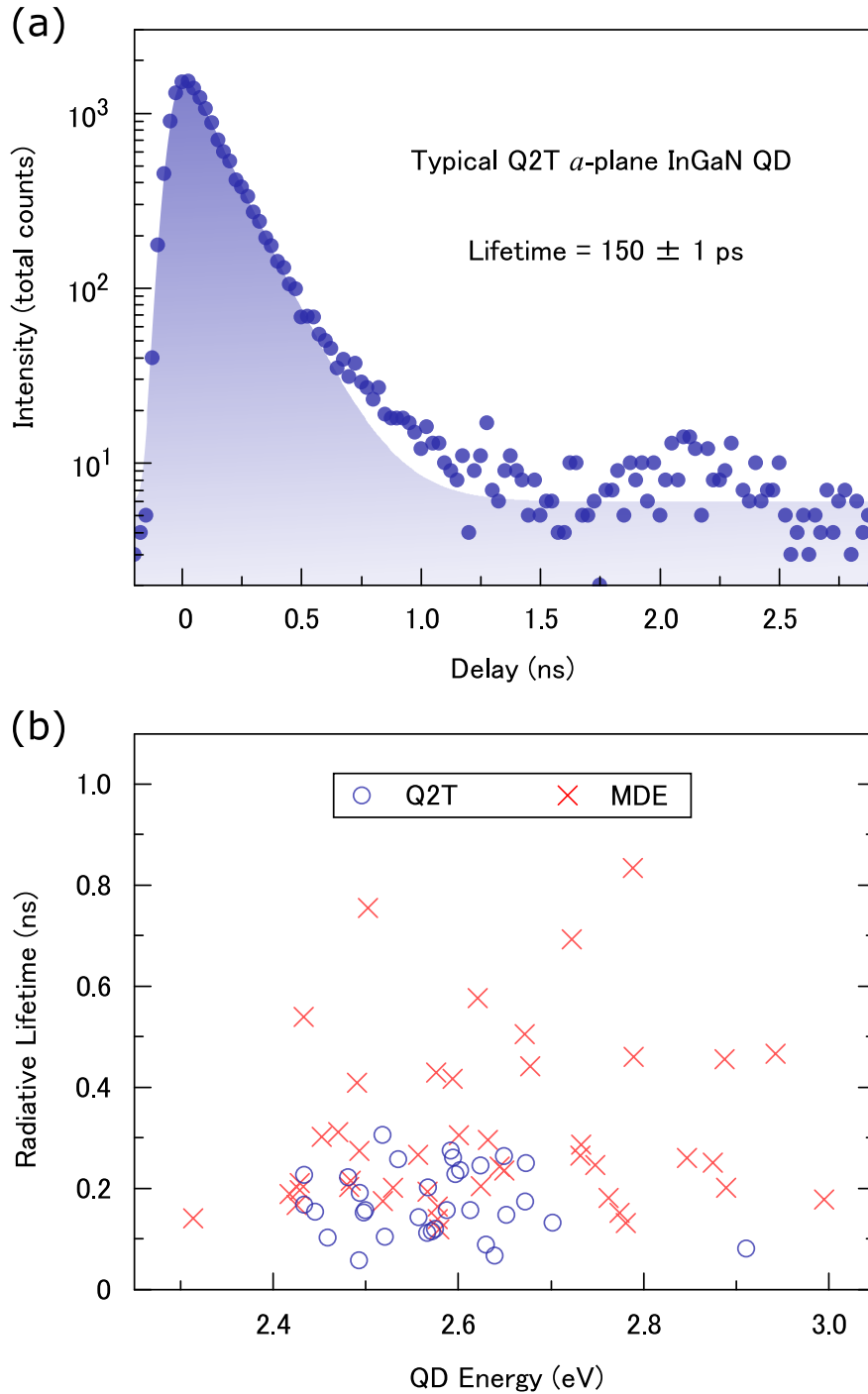


**Figure 4.8: Measurement of the radiative recombination lifetime of Q2T  $a$ -plane InGaN QDs.** (a) TCSPC data of a typical Q2T QD, fitted with a Gaussian convolved with an exponential decay. (b) Statistically significant measurement of the radiative lifetime of both Q2T and MDE QDs. A total of 36 Q2T and 46 MDE QDs have been selected with minimal bias. The studied Q2T QDs exhibit a reduction in both mean lifetime and its standard deviation.

of a QD. This is evident in the much smaller lifetime range of 50 to 300 ps produced by the Q2T data.

The insensitivity of *a*-plane lifetime with varying QD sizes has also been re-confirmed with this statistical study. The bimodal size distribution of Q2T QDs (see Figure 2.2 in Chapter 2) indicates very large variations of the QD diameter, which has two Gaussian components with means an order of magnitude different. Based on the results presented in Figure 3.9(a) and discussions therein, these variations would cause an order of magnitude variation in the radiative lifetimes of *c*-plane QDs, where the recombination rate decreases quasi-linearly with increasing QD diameter. For *a*-plane QDs, an order of magnitude difference of QD diameter could only result in a  $\sim 15\%$  difference in radiative lifetime, based on a linear extrapolation of the simulation result. Given that other properties, such as the small variation of local environment, QD geometry and indium content, could also affect the lifetime of a QD, the small fluctuation in Figure 4.8(b) is an indication that the order-of-magnitude difference in Q2T QD sizes does not affect its radiative lifetime significantly.

The development of the Q2T method has thus managed to decrease the lifetime of *a*-plane InGaN QDs even further. The average radiative lifetime of 170 ps is now faster than the state-of-the-art dot-in-nanowire *c*-plane GaN platform, where the small size and clean environment allow the QD excitons to have a  $\sim 300$  ps radiative recombination lifetime [97]. Furthermore, the much cleaner local environment of Q2T *a*-plane QDs reached lifetimes faster than 260 ps, which is the average obtained in our *m*-plane InGaN system with theoretically weaker residual fields [112]. It is also interesting to note that the radiative lifetime of Q2T *a*-plane InGaN QDs is now as fast as self-assembled *a*-plane GaN QD system [190], in spite of the 50% smaller emission energy ( $\tau \propto E_{\text{exc}}^2$ , see Equation 3.5) of InGaN. The lifetime of Q2T could be close to the lowest achievable limit of realistic self-assembled nitride QD systems.

To create an even cleaner local environment, a site-controlled dot-in-nanowire system needs to be used in place of the current self-assembled system. In such a situation, the fabrication of an ultra-small QD at the apex of a thin nanowire would have very little surrounding material, thus very few carrier trapping sites, resulting in potentially even

faster radiative lifetimes. Alternatively, according to discussions in Section 3.3, a device with external electric field injection could also be developed on top of the current self-assembled system. By tuning the strength of the external field, any fields still present in the QD could be further minimised. However, the fabrication or characterisation of either of these two methods would require several years of development, and are thus well beyond the scope of this thesis. The current progress of the Q2T routine has reached a sweet spot in balancing the challenge in fabrication and reduction of radiative lifetime, and should be a good starting point for several directions of further development in exciton lifetime engineering.

The reduction in local carrier trapping sites have already resulted in an improvement of both slow-timescale spectral diffusion and radiative recombination lifetime, so that their performances are among the state-of-the-art in the nitride QD community. However, the most evident change should be in the thermal stability of emission brightness, which will be explained in detail in the following section.

### 4.5 Temperature stability

Thermally assisted carrier escape from QDs and recombination through non-radiative recombination pathways are the primary reasons for the quenching of QD emission intensity at elevated temperatures. As discussed in Chapter 1, the primary incentive for developing a nitride QD system is the possibility to exploit its large band offsets, which result in much stronger quantum confinement and more stable operation as temperature increases. While nitride QDs can generally reach higher operation temperatures than arsenide ones, there have only been a small number of reports for InGaN [25, 144, 191] or GaN [87, 99] QD systems operating beyond 200 K. The activation of non-radiative recombination routes in nitride platforms have undermined their potential to achieve more stable high-temperature operations. As such, the minimisation of these undesirable carrier escape pathways is the key in the development of a nitride QD platform.

In the case of MDE *a*-plane InGaN QDs, while it is easy to observe QD emission at 100 K, the number of emitting QDs drops drastically as the temperature is increased further.

It is possible that the disrupted epilayer and increased number of carrier trapping sites have opened up a significant number of non-radiative recombination pathways, which are activated upon the introduction of greater amounts of thermal energy. Based on this analysis, the smooth InGaN epilayer in Q2T samples should contain a markedly decreased number of non-radiative carrier escape routes. Therefore, it would be more likely for a Q2T QD to reach higher operation temperatures.

### 4.5.1 Comparable pair of dots

In order to compare their temperature performance as fairly and accurately as possible, the two pairs of QDs used in Figure 4.1 and 4.6 are less ideal. For operation at higher temperatures, a strong quantum confinement is needed. Although this property of a self-assembled QD cannot be evaluated directly, a strong carrier confinement is usually manifested in a high emission intensity at low temperatures. Moreover, QDs with greater intensities also allow smaller uncertainties in the data analysis, as they are less affected by the fluctuating noise signals of the CCD, especially at higher operation temperatures. However, as both Q2T and MDE QDs are self-assembled ones, their physical and compositional properties cannot be controlled during growth. As such, an experiment is first conducted with a strongly emitting Q2T QD. Afterwards, the identification of a closely comparable MDE QD with similar low-temperature intensity, emission energy, dot-to-background ratio, and linewidth is attempted before an identical experiment is carried out.

The pair of QDs shown in Figure 4.9 has peak intensities of  $\sim 900$  cts/s (excluding background QW signals) at 5 K, and very similar linewidths of  $2.59 \pm 0.22$  (Q2T) and  $2.35 \pm 0.20$  meV (MDE) respectively. As such, these QDs have a similar low-temperature integrated intensity, which serves as a good starting point for the investigation of temperature-induced intensity quenching. The linewidths are also similar within their errors, and lie in the typical range of 0.3 to 3 meV as discussed in Section 4.3.1. With comparable linewidths, the degrees of fast-timescale spectral diffusion are also very close, providing a good starting point for the comparison of thermally assisted linewidth broadening. In terms of emission energy, both QDs are spectrally located at the shorter wavelength tail of their respective QWs. The Q2T QD is emitting at 489 nm and its underlying QW

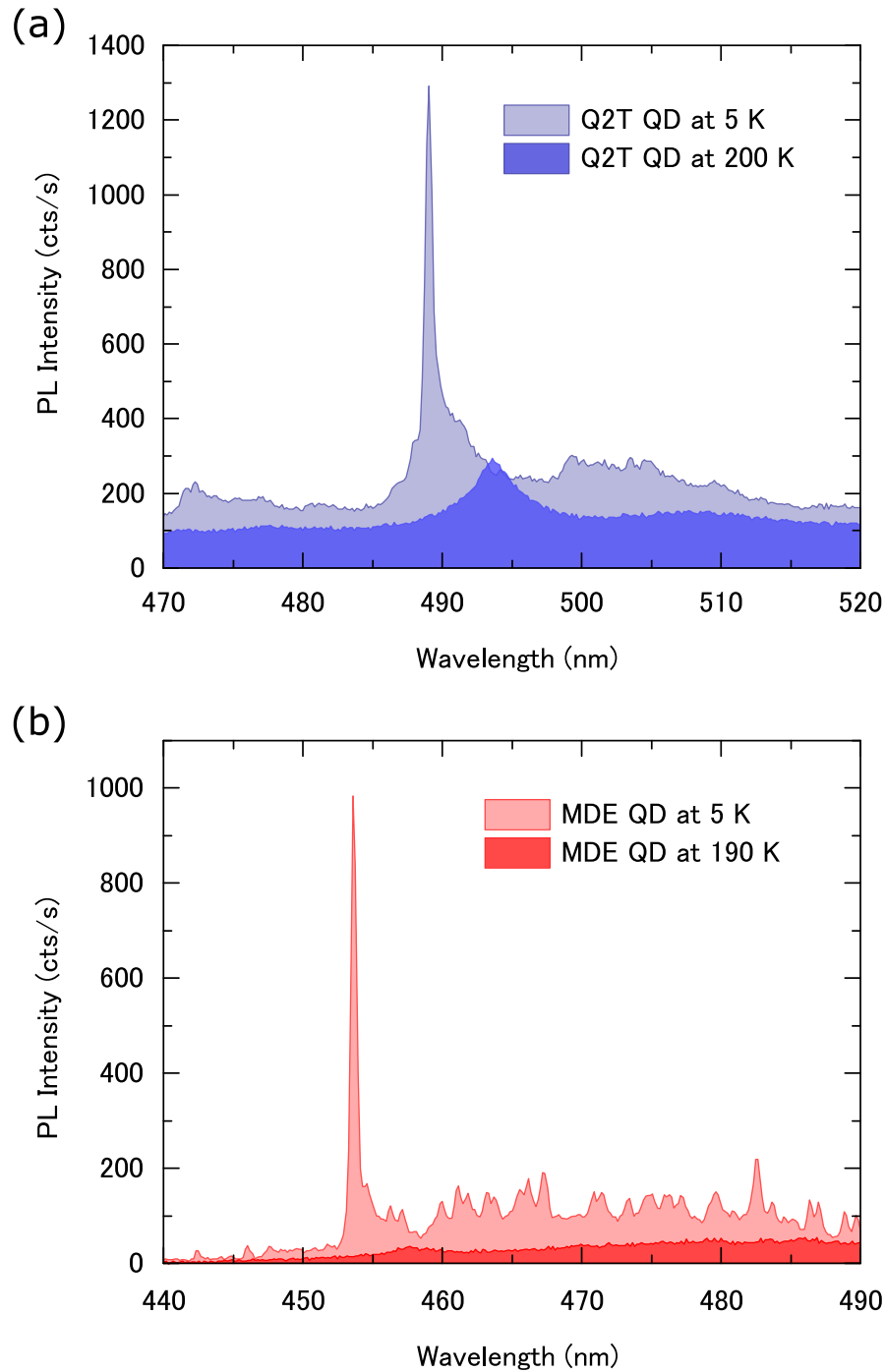


**Figure 4.9: Comparison of high temperature operation of a comparable pair of Q2T and MDE *a*-plane InGaN QDs.** (a)  $\mu$ PL spectra of a Q2T QD at 5 and 200 K, showing QD and QW intensities without normalisation. The Q2T peak at 200 K is still very discernible despite the effect of thermal quenching. (b)  $\mu$ PL spectra of a comparable MDE QD at 5 and 190 K, without intensity normalisation. 190 K is the highest temperature at which the QD peak can still be distinguished from the background.

between 480 and 520 nm, while the MDE QD is emitting at 454 nm and its underlying fQW between 450 and 490 nm. A greater loss of indium occurs during the annealing stage of the MDE routine, increasing the energy of emission and causing a sample-wide shift in wavelength towards the bluer end of the spectrum. This can also be observed in the statistical comparisons presented in previous sections, such as in Figure 4.5. Similar to Figure 4.1 and 4.6, the Q2T QD has a smaller dot-to-background ratio as expected. With a similar QD integrated intensity, the difference in dot-to-background ratio is caused by the stronger QW emission in the Q2T sample. An estimation of the QW integrated intensity yields  $6.1 \times 10^4$  (Q2T) and  $2.5 \times 10^4$  cts/s (MDE) respectively. It is important to note that the identification a strictly comparable pair of QDs with every parameter held constant is not feasible, if not impossible, in a self-assembled system. Nonetheless, the pair of QDs in Figure 4.9 are similar in the most important aspects of low-temperature integrated intensity and linewidth, and should thus provide useful results in the investigation of temperature stability.

The PID temperature controller of the system is increased at 10 K intervals until 200 K for the Q2T QD and 190 K for the MDE one. As explained in the introduction, current commercial Peltier cooling technologies are able to reach  $\sim 190$  K. This comparison thus sheds light on the emission properties of the QDs in potential on-chip thermal conditions. The results presented in Figure 4.9(a) and (b) first confirmed that QDs fabricated via either routine can operate at Peltier-cooled temperatures. Between these two QDs, the Q2T one has a better temperature stability, as evident by the relatively stronger emission even at 200 K. On the other hand, 190 K is the highest temperature at which emission from the studied MDE QD can still be observed. A redshift is also observed in both Q2T and MDE QDs, the extents of which are very similar.

### 4.5.2 Integrated intensity and linewidth

In order to understand the process of thermal quenching in both QDs better, the  $\mu$ PL spectra at all studied temperatures have been fitted with Gaussian profiles, yielding integrated intensities presented in Figure 4.10(a). At 200 K, the brightness of the Q2T QD is still 12.2% of that at 5 K. Based on the trend of quenching, the studied Q2T QD should

be emitting at even higher temperatures. However, the QD was unfortunately lost during further temperature increases and no data at higher temperatures were recorded. The temperature stability of the Q2T QD can also be seen at  $T \leq 60$  K, where the integrated intensity presents no significant change and stays nearly constant. In contrast, the MDE QD begins to lose intensity as soon as the temperature is increased beyond 10 K. With a much greater rate of decrease, the integrated intensity at 190 K for the studied MDE QD is 0.8% of that at 5 K. As such, the studied Q2T QD has more than an order of magnitude slower quenching of brightness at elevated temperatures.

The reasons for the distinction between the temperature performance of the studied Q2T and MDE QDs could be 3-fold. Firstly and most importantly, the greater likelihood in creating potential minima in the vicinity of the MDE QD is a direct consequence of the annealing of the underlying QW epilayer. These fluctuations in the energy profile of the fQW tend to act as carrier trapping sites, and have been identified as the main reason for greater amounts of slow-timescale spectral diffusion and QD exciton oscillator strength reduction in the previous two sections. With larger thermal energy at higher temperatures, carriers in the QD not only possess sufficient energies to surmount the potential barrier of these trapping sites, but also gain greater mobility to escape into these non-radiative recombination pathways [27]. Based on the  $\mu$ PL spectra presented in Figure 4.9, the dot-to-background ratio of the studied Q2T QD changes from 2.25 at 5 K to 0.53 at 200 K. On the other hand, this ratio for the studied MDE QD changes from 9.01 at 5 K to 0.46 at 190 K. The temperature evolution of dot-to-background ratio is an indication of the change in the proportion of QD and QW emission intensities. The faster decrease of the MDE QD's dot-to-background ratio is an indication that the QD's intensity is decreasing more rapidly than the underlying QW, signifying a potentially much greater amount of carrier escape into the surrounding QWs containing more carrier traps.

Another possible reason for the slower intensity quenching of the studied Q2T QD is stronger quantum confinement. This is also evident in Figure 2.2(a) in Chapter 2, where a population of much smaller Q2T QDs are present compared to MDE ones. Furthermore, the deeper confinement could also be implied by the longer emission wavelength of the Q2T QD. With higher indium contents and lower emission energy, the InGaN/GaN band offset

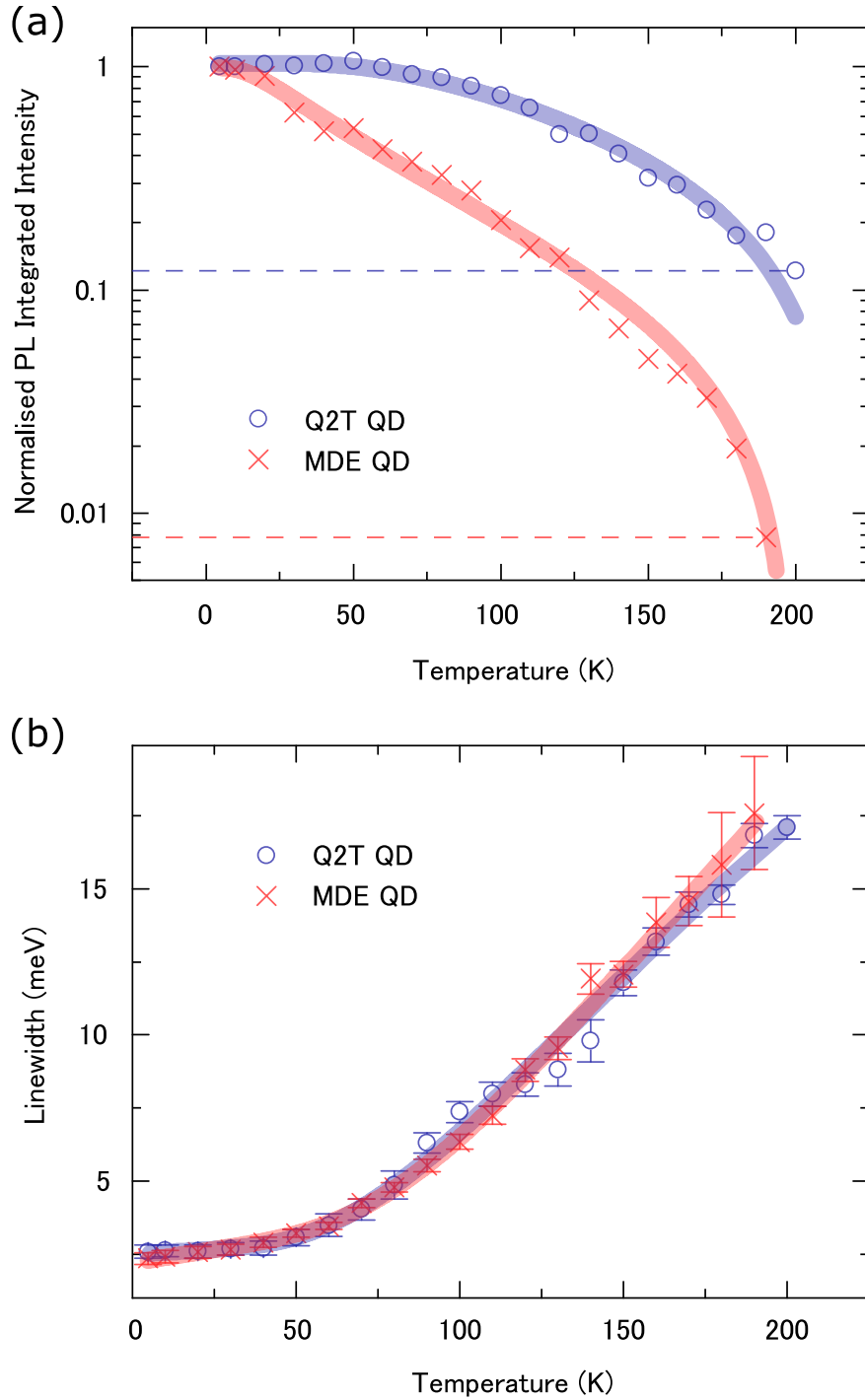


**Figure 4.10: Comparison of the temperature evolution of brightness and linewidth of a comparable pair of Q2T and MDE  $a$ -plane InGaN QDs.** (a) Normalised integrated intensity at each temperature for both QDs. The intensities at their highest recorded temperatures are highlighted, indicating an order of magnitude difference. (b) Linewidth values at each temperature for both QDs. No clear difference can be observed. The fitted lines in both (a) and (b) are included as guides to the eye.

becomes greater and thus the exciton is confined more deeply. However, it is important to note that carriers from the QD mainly escape into the local QW (with similarly high indium compositions), rather than the barrier material. A strong confinement would result in greater brightness at low temperatures, but not always necessarily at higher temperatures due to the QD-QW non-radiative decay pathways. Therefore, this reason does not fully explain the current observations.

Finally, thermally assisted interactions with acoustic phonons increase the probability of inelastic phonon scattering, which is a source of non-radiative recombination for both QDs. In order to assess whether there could be a different degree of phonon interaction, the linewidths at each temperature are extracted from the parameters of the Gaussian best fits and displayed in Figure 4.10(b). At this stage, it is worth mentioning that thermally induced broadening processes can be highly complex for the current QD platform, and not completely well understood. Nonetheless, coupling with acoustic phonons is a main source of broadening and contributes significantly to the linewidth at high temperatures [25, 99]. A more detailed investigation of temperature-dependent optical properties will be presented in the next chapter. For the both datasets, the linewidth evolution with temperature follows very similar trends. The linewidths at the highest temperature of the Q2T (200 K) and MDE (190 K) QDs are  $16.8 \pm 0.4$  and  $17.6 \pm 1.9$  meV respectively. With a slightly smaller starting linewidth and lower final temperature, the linewidth of the MDE QD broadens marginally faster than the Q2T one. However, most of the data are within the errors of each other, and their difference are much less drastic than the case of intensity decay. As such, the extent of phonon interactions is similar in both Q2T and MDE QDs, and should not cause a large difference in inelastic phonon scattering. This finding is not completely unexpected, as the coupling strength to acoustic phonons is more related to the intrinsic symmetry of the material rather than the local environment of a QD [27]. For example, the acoustic phonon coupling strength of *c*-plane InGaN QDs is much larger than that of *a*-plane ones, due to potentially stronger associations of the built-in piezoelectric fields with transverse acoustic phonons [192].

All in all, similar to the reduction of radiative lifetime and slow-timescale spectral diffusion, the much smaller number of carrier traps in Q2T samples form fewer non-radiative decay

pathways in the QWs, thereby decreasing the amount of carrier escape from the QDs and increasing their temperature stability. However, this does not immediately mean that current Q2T samples are better than MDE ones in the pursuit of temperature-dependent studies. As explained previously, the overall average emission intensity and dot density of the Q2T QDs are still lower than typical MDE ones. Under comparable situations, such as the pair of QDs in Figure 4.9, a Q2T QD might perform better at higher temperatures. In reality, a QD with  $\sim 1000$  cts/s in a Q2T sample is as rare as an MDE one with  $\sim 5000$  cts/s, and is extremely hard to come by during the scanning of QDs in a  $\mu$ PL experiment. On the other hand, the identification of an MDE QD with  $\sim 1000$  cts/s is relatively straightforward in a good sample. Furthermore, the temperature performance difference between MDE and Q2T QDs is only evaluated with one pair of comparable QDs. Larger statistics are needed to ascertain this difference with greater confidence and to quantify it with higher precision, but are currently not feasible due to time constraints of such experiments. Therefore, MDE QDs with a larger integrated intensity and potentially stronger confinement could result in equally stable temperature operation as that shown for the Q2T one in Figure 4.10(a). Coupled with much larger dot-to-background ratios, strongly emitting MDE QDs should still be the primary candidate for the investigation of high-temperature single-photon emission. Although unsuitable for HBT experiments, Q2T QDs with potentially greater thermal stability would be useful in the study of other optical properties at higher temperatures, and effectively compliment MDE QDs in the elucidation of their high-temperature photophysics.

## 4.6 Chapter summary

The development of the Q2T method as an improved MOCVD growth technique for *a*-plane InGaN QDs introduces significant changes in the resultant underlying InGaN epilayers. On the one hand, the absence of an annealing process allows much fewer disruptions in the InGaN QW, resulting in a marked reduction in potential minima, carrier traps, and non-radiative decay sites. On the other hand, the formation of dots is more reliant on the underlying InGaN layer, whose structural integrity increases the strength of the QW emission. Due to these changes, improvements in the rate of radiative recombination

lifetime, slow-timescale spectral diffusion, and temperature stability have been seen, while a decrease of sing-photon purity has also been observed. The linewidth, fast-timescale spectral diffusion, and optical polarisation properties remain unaffected.

The development of the Q2T method is not meant to be an end, but an intermediate stage that paves the way for better *a*-plane InGaN QD samples and devices in the future. Although pure single-photon emission cannot be achieved with Q2T QDs, their relative insensitivity to high thermal energies and small spectral Stark drifts could facilitate the study of the high-temperature photophysics of nitride QDs up to the regime of on-chip Peltier cooling. With the identification of excessively high QW emission intensities, the direction of further development is also clear. Initial results already demonstrate Q2T QDs with high dot-to-background ratios. At the moment, QDs grown with Q2T and MDE have different advantages and disadvantages, and one does not supplant the other. Both methods are also under intense development to tackle their specific areas of weakness. As such, Q2T QDs should be used to study temperature-related properties where single-photon emission is not required, but a minimised emission energy fluctuation is needed, such as fine-structure splitting. Moreover, Q2T QDs could also be used for structures where carrier population is important, such as the development of lasing platforms. For current single-photon studies at both low and high temperatures, MDE should still be used. In the next chapter, the temperature evolution of optical properties for the *a*-plane InGaN QD platform will be examined with a combined use of both MDE and Q2T QDs

# 5

## Ultrafast polarised single-photon sources beyond 200 K

### 5.1 Chapter introduction

Most of the discussion so far has been focused on the optical properties of *a*-plane InGaN QDs at cryogenic temperatures. However, one of the most important incentives for the development of a wide band gap QD platform is to achieve high-temperature operation. In particular, the emission of polarised single photons at 200 K and above would make QD operation possible in on-chip, Peltier-cooled thermal conditions. At the same time, due to the very limited number of literature reports in the high-temperature operation of nitride QDs [87, 99, 191], the evolution of their optical properties and related thermally activated processes have not been clarified. Owing to their inability to operate at elevated temperatures, such investigations are also scarcely conducted in mature arsenide platforms. However, the final section in Chapter 4 has demonstrated the ability of both MDE and Q2T *a*-plane QDs to emit at  $\sim 200$  K, thereby opening up the possibility for further investigation into these lesser known topics.

In this chapter, the ability of these QDs to emit single photons at 200 K and higher will be examined, while elucidating the changes in their optical characteristics with temperatures. According to the conclusion of Chapter 4, although Q2T QDs could have the potential to emit at higher temperatures with slower intensity quenching than MDE ones, the current

absolute Q2T intensities at 4.7 K are still lower. More importantly, for the demonstration of single-photon emission at higher temperatures, the much lower intensity of underlying QWs in the MDE samples would make the observation of  $g^{(2)}(0)$  of  $< 0.5$  more likely.

For elucidation of the underexplored area of high-temperature photophysics of nitride and other semiconductor QDs, a study of the temperature dependence of most optical properties, such as the thermal quenching of brightness, broadening of linewidth, and changes in radiative recombination, will be explained in detail. Furthermore, contributions from excited states become gradually prominent as temperatures increase beyond cryogenic conditions, with added Coulomb interactions between the hole ground state and the less polarised excited states. These could be part of the reasons for which no other semiconductor QD systems have reported polarisation at elevated temperatures. Since optical polarisation properties are one of the most important advantages of this platform compared to other nitride ones, their temperature evolution will be examined with both theoretical foundations and statistically significant experimental results up to 200 K.

## 5.2 Observation of QD emission up to 250 K

In order to investigate the temperature evolution of the optical properties of *a*-plane InGaN QDs potentially emitting at temperatures beyond 200 K, the identification of suitable QD candidates was first carried out at 4.7 K. Based on discussions in the previous two chapters, these potential QDs should exhibit very high emission intensities at 4.7 K, which signify strong quantum confinements and greater possibilities of high-temperature operation. At the same time, a large dot-to-background ratio is also desired for the purity of emitted single photons.

From a number of QDs identified, the MDE QD shown in Figure 5.1 has the best combination of high emission intensity and large dot-to-background ratio. Five 1 s  $\mu$ PL spectra have been recorded at 4.7 K. The intensity per second at each CCD pixel has been averaged with its standard deviation displayed as error bars in the figure. A Gaussian fitting has been performed on these data, and a very close fit is obtained. Some of the data points at the lower energy tail of the QD cannot be fitted within the Gaussian, as they originate

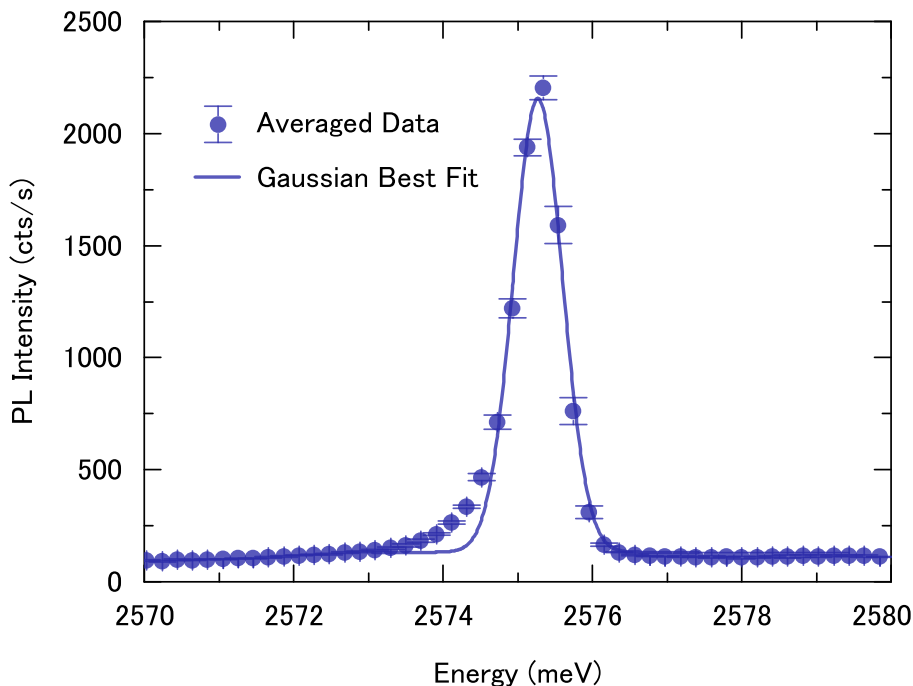


**Figure 5.1:**  $\mu$ PL spectrum of an MDE QD for the potential investigation of high-temperature single-photon emission. Raw spectroscopy data with an acquisition period of 1 s were recorded 5 times at 4.7 K. The mean and standard deviation at each CCD pixel have been calculated, and the results within a 10 meV window containing the QD signal are shown. A Gaussian best fit has been performed on the averaged data and displayed above.

from the interaction with phonons [99, 193]. Although the strength of this interaction increases with temperature, it still has a non-zero magnitude at cryogenic temperatures. As the temperature is still higher than absolute zero, such a phonon sideband can be observed in the PL of most strongly emitting QD.

The optimised parameters of the Gaussian indicate an exciton transition linewidth of  $712 \pm 68 \mu\text{eV}$ , lower than the mean MDE linewidth of  $932 \mu\text{eV}$  measured in Section 4.3.1. Coupled with the high peak emission intensity of  $> 2000$  counts/s, the small linewidth is a possible indication of a QD with small physical dimensions and strong quantum confinement [97]. As such, the studied QD could be predicted to operate at high temperatures. The magnitude of the linewidth is still much larger than the Fourier-limited linewidth ( $\sim \mu\text{eV}$ ), owing to the presence of fast-timescale spectral diffusion from itinerant carriers in the nearby QWs. This is evident in the  $\sim 132$  cts/s non-zero peak background rate obtained from the Gaussian fitting. With these data, a dot-to-background peak intensity

ratio is  $> 15 : 1$ , which is very rare in current  $a$ -plane QDs that are also emitting with a  $> 1000$  counts/s peak intensity. Lastly, the emission energy of the QD in Figure 5.1 is 2575.3 meV (481.4 nm), which is at the centre of the range of  $a$ -plane QDs' typical emission energies. Based on all the optical properties explained above, the studied QD should be an ideal candidate for the investigation of high-temperature single-photon generation.

In order to maximise the possibility of observing QD emission at elevated temperatures, an excitation power of 90 mW immediately out of the fibre (estimated  $\sim 25$  mW onto the sample) is used to saturate the QD emission. Again, achieving higher emission intensity is chosen over a potential decrease in single-photon emission purity. This power is kept constant throughout the course of the temperature evolution study. For accurate analysis of its optical properties, the spectrometer has been set to operate at its maximum 12001/mm grating blazed at 500 nm, with a slit of 100  $\mu\text{m}$  wide. A smaller slit (e.g. 25  $\mu\text{m}$ ) could be used for even higher resolution, but could potentially cause greater uncertainties in the optical polarisation measurements as the polariser and half-wave plate are rotated (see Section 2.3.3). Given that the linewidth of the nitride QD is much larger than the resolution of the spectrometer, the current slit size should be sufficient and is thus kept at 100  $\mu\text{m}$  throughout the experiment.

The temperature of the sample is then gradually increased with the PID controller of the *attocube* closed-cycle cryostat. Spectra have been recorded at 4.7 K, from 6 to 16 K at 1 K intervals, at 18 K, from 20 to 220 K at 5 K intervals, and from 230 to 250 K at 10 K intervals. At each step, the temperature is allowed to stabilise before any measurements are made. The spectra at 1 K steps at temperatures  $< 20$  K were taken to identify the time at which optical properties of the QD, such as exciton transition linewidth, start to change more significantly. A selection of these  $\mu\text{PL}$  spectra from low to high temperatures are shown in Figure 5.2. The quenching of QD intensity starts as soon as the temperature is increased. At higher temperatures, the rate of quenching also increases significantly. As such, for a more visual comparison of the temperature evolution of other optical properties, the peak intensity of every spectrum from 40 to 250 K has been normalised to that at 4.7 K. From Figure 5.2, it is clear that there is an accelerated redshift of emission energy and broadening of exciton linewidth, as the temperature gradually increases to 250 K. It is

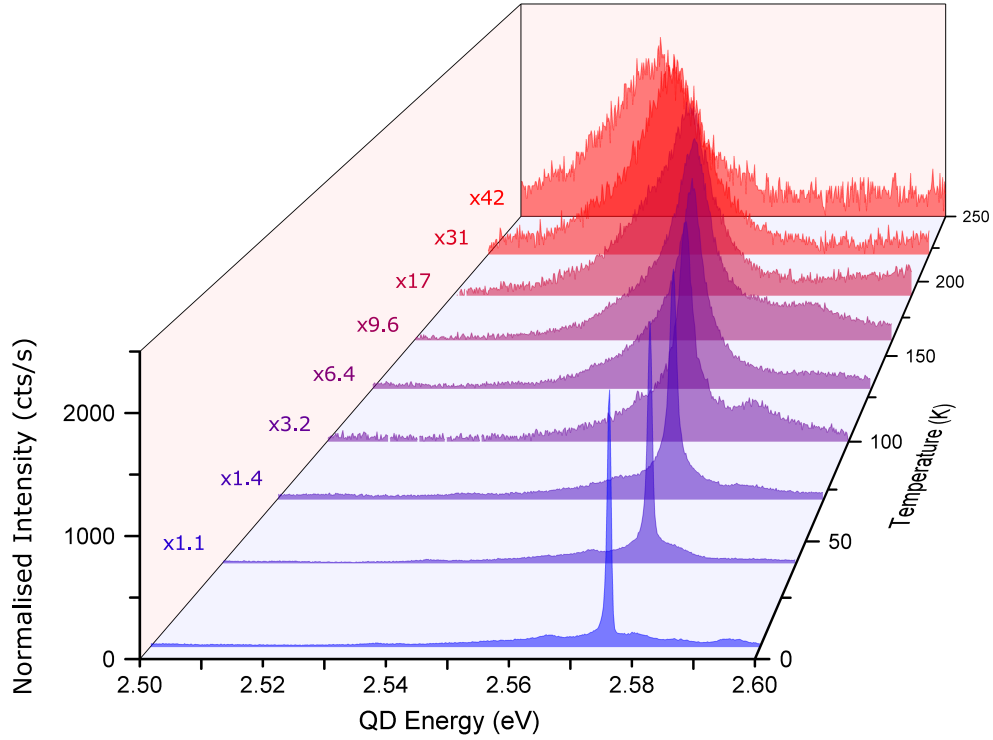


**Figure 5.2: Temperature evolution of  $\mu$ PL of the studied QD.** A selection of recorded spectra with an acquisition period of 1 s are shown at 4.7 K, and from 40 to 250 K at 30 K intervals. The excitation power of the laser was kept constant throughout the temperature changes. The peak intensities of each higher temperature has been normalised to that at 4.7 K, with normalisation factors displayed next to their respective spectra.

unfortunate that due to the significant position drift induced by high thermal energies, the location of the QD was lost at  $> 250$  K even with assistance from the position optimisation programme, and could not be recovered. As such, a more complete set of data until the thermally quenched QD emission is comparable to the fluctuation noise of the CCD was not obtained. Nonetheless, the current dataset should be sufficient for the investigation of a number of its optical properties, which will be examined in detail in the following sections.

## 5.3 Quenching of emission intensity

### 5.3.1 Non-radiative decay pathways

An electron-hole pair generated in a light-emitting semiconductor either recombines radiatively and emit a photon, or non-radiatively via a number of possible mechanisms [194] specific to the material, nanostructure, and local environment of the emitter. These non-radiative decay pathways can be gradually activated with the increase of thermal energy. The effect of these pathways in decreasing the radiative recombination efficiency  $\eta_{\text{RE}}$  can be expressed by an Arrhenius model [25, 65, 112, 195, 196],

$$\eta_{\text{RE}} = \frac{1}{1 + \sum_i^m A_i \exp(-E_{a,i}/k_B T)}. \quad (5.1)$$

Here, each term in the summation of the denominator represents a thermally activated non-radiative decay route, where  $E_{a,i}$  is the activation energy and  $A_i$  is the coupling strength. In a self-assembled QD system, it is non-trivial to gain direct knowledge of the precise number of non-radiative recombination pathways or their nature. As such,  $m$  can be set to 1, in which case  $A$  and  $E_a$  would denote the average coupling strength and activation energy for the emitter's intensity quenching processes. Equation 5.1 thus reduces to the form of

$$\eta_{\text{RE}} = \frac{1}{1 + A \exp(-E_a/k_B T)}, \quad (5.2)$$

and has been commonly used in the literature for the investigation of thermally induced intensity quenching of nanostructures [25, 65, 112, 195, 196]. However, in cases where the quantum emitters have significantly different coupling strengths to pathways with distinct activation energies, the use of a single-channel Arrhenius model provides a less accurate description of the experimental data. An alternative method is to set  $m = 2$  in Equation 5.1, so that two different Boltzmann terms can more precisely model the behaviour of quenching. In literature studies of InAs [197], CdTe [198], and InGaN [199] structures, the following two-channel decay form has also been used to produce more accurate descriptions of the experimental data.

$$\eta_{\text{RE}} = \frac{1}{1 + A_1 \exp(-E_{a,1}/k_B T) + A_2 \exp(-E_{a,2}/k_B T)} \quad (5.3)$$

However, it is important to note that with an increased number of parameters, a more accurate fitting to the experimental data can always be obtained. The key in these models should be the identification of the physical meaning of parameters, and the use of fitting results to gain more insights into the properties of the materials. The difficulty in assigning known physical processes and non-radiative mechanisms to more Boltzmann fitting terms makes the use of  $m \geq 2$  cases of Equation 5.1 less than meaningful. Therefore, only Equation 5.2 is used for the following analysis of intensity quenching for the QD shown in Figure 5.1 and 5.2.

#### 5.3.2 Temperature evolution of emission intensity

The  $\mu\text{PL}$  spectrum taken at each temperature as described in 5.2 have been fitted with Gaussian profiles to determine their integrated intensity. These data are shown in Figure 5.3 and fitted with Equation 5.2. With increasing temperatures, recombination through non-radiative pathways gradually dominate over radiative recombination, as manifested by the decrease of integrated intensity. It is worth noting that although the peak intensity decreased by a factor of 42 as indicated by Figure 5.2, the rate of integrated intensity quenching is relatively slower. This is due to the significantly broadened exciton transition linewidth and thus increased area under the Gaussian profile of the QD. In reality, the integrated intensity is a true measure of the number of photons radiatively emitted by the nanostructure. As such, unlike the evaluation of optical polarisation degrees where all experiments are performed at the same temperature, peak intensities should not be used in place of integrated intensity in temperature-dependent studies. At the highest recorded temperature of 250 K, 6% of the intensity at 4.7 K remains, indicating that 94% of the original excitons have undergone processes of non-radiative recombination.

The single-channel Arrhenius intensity quenching model produces a good description of the behaviour of intensity decay. The close fit of a standard semiconductor model to the experimental data also implies that the emission should arise from a solid-state QD, instead of a defect [112]. The processes for the emission from a defect can be more complicated, and

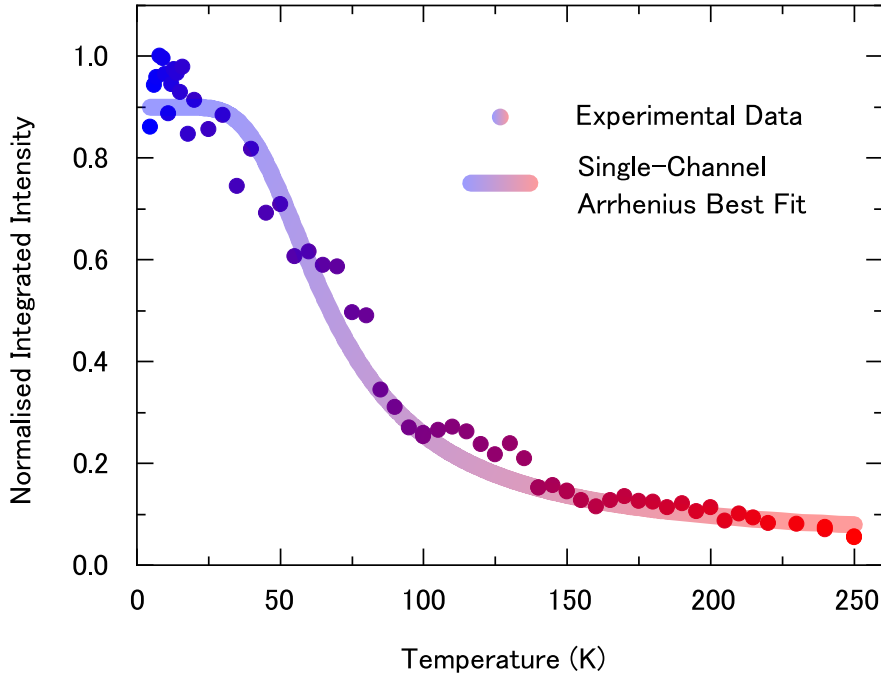


**Figure 5.3: Temperature evolution of integrated intensity of the studied QD.** All intensity calculations were performed by fitting Gaussian profiles on the QD PL spectra at each temperature, and evaluating the area of under the fitted curves. These intensity data were then fitted with Equation 5.2, where the average carrier escape via non-radiative decay pathways is represented by a single-channel Arrhenius quenching model.

could increase with greater thermal energies at certain temperature ranges. For instance, optical injected carriers in the InGaN QW could have a greater probability of escape into a point defect, thereby increasing its likelihood of radiative recombination due to a higher carrier density. However, with more thermal energy, the carrier population would increase further, making processes such as Auger non-radiative recombination [69, 200] more likely and reducing the radiative intensity. The lack of such behaviour is an indication that the emission is of semiconductor origin. For the studied QD, an activation energy of  $19.2 \pm 1.0$  meV is obtained with the fitting, which agrees very well with analysis from other nitride platforms published in the literature [201]. As such, it could be estimated that the average depth of a local non-radiative recombination path for the studied QD is  $\sim 20$  meV.

Although the remaining 6% intensity implies fast quenching, it is important to point out that the brightness decrease is very slow compared to arsenide systems. With typical

single InGaAs QDs, the intensity would drop well below 1% before the temperature is increased to 100 K. Furthermore, it is not possible to make a direct comparison between InGaN QD platforms, due to a lack of literature reports. The only report of a different InGaN system with single-photon emission above 200 K [191] does not specify the degree of quenching. However, in comparison to state-of-the-art dot-in-nanowire GaN systems [97, 99], the temperature stability is indeed worse. The strong quantum confinement in the GaN/AlN platform allows the intensity to stay almost constant up to 250 K. Nonetheless, as the first evidence of operation above 200 K in this platform, and one of the only two InGaN systems [25, 191] with this degree of temperature stability, the current *a*-plane InGaN QD is emitting strongly enough for the investigation of its optical properties and high-temperature photophysics beyond the thermoelectric cooling barrier with sufficient accuracy.

## 5.4 Redshift of emission energy

### 5.4.1 Temperature dependence of band gap

In a simplified picture, the stronger atomic vibrations at elevated temperatures weaken the bond energies in a semiconductor, resulting in a decreased amount of required energy to promote an electron from the valence band to the conduction band, i.e. a smaller band gap. This effect was first quantified by Varshni in 1967 by the well-known Varshni equation [202],

$$E_g(T) = E_g(0) - \frac{\alpha T^2}{T + \beta}, \quad (5.4)$$

where  $E_g(T)$  is the temperature-dependent band gap,  $\alpha$  and  $\beta$  are fitting parameters specific to the semiconductor material. However, it is important to note that Equation 5.4 is proposed as an empirical model, without a theoretical foundation. There have been observations of discrepancy between the model and experimental results [196, 203]. Since its introduction, alternative formulations [194, 203] have been attempted to improve upon the model. A more accurate description could be achieved by considering electron-phonon

interactions at higher temperatures. Firstly, as bosons, the average phonon number at a given temperature,  $\bar{n}_{\text{phonon}}(T)$ , can be expressed according to Bose-Einstein statistics,

$$\bar{n}_{\text{phonon}}(T) = \frac{1}{\exp \langle \hbar\omega \rangle / k_{\text{B}}T - 1}. \quad (5.5)$$

In Equation 5.5,  $\langle \hbar\omega \rangle$  is the average phonon energy of the semiconductor. The amount of redshift is then proportional to the total phonon energy, i.e.

$$\delta E \propto \langle \hbar\omega \rangle \bar{n}_{\text{phonon}}(T) = \frac{\langle \hbar\omega \rangle}{\exp \langle \hbar\omega \rangle / k_{\text{B}}T - 1}. \quad (5.6)$$

By introducing the Huang-Rhys factor [204],  $S$ , as a constant of proportionality that measures the strength of electron-phonon coupling, the following equation can be obtained.

$$E_{\text{g}}(T) = E_{\text{g}}(0) - S \langle \hbar\omega \rangle (\coth \langle \hbar\omega \rangle / 2k_{\text{B}}T - 1) \quad (5.7)$$

This is the O'Donnell-Chen band gap model [203] proposed to replace the original Varshni equation, as a more accurate description of the behaviour of temperature-dependent peak emission energy shift of semiconductors. In the analysis of data collected from the  $a$ -plane InGaN QD platform, the O'Donnell-Chen model has indeed been able to produce much more accurate fittings compared to the Varshni model, which often fails to converge and yields unphysical fitting parameters.

#### 5.4.2 Temperature evolution of emission energy

The Gaussian fitting at each temperature of the studied QDs emission profile also produces respective central emission energies, which are shown in Figure 5.4. The rate of redshift increases with higher temperatures. From 4.7 to 50 K, the emission energy decrease is  $< 1.5$  meV. On the other hand, the amount of redshift is  $> 15$  meV when the temperature is increased from 200 to 250 K. This is expected due to the accelerated increase of phonon interactions at elevated temperatures. The data has been fitted with Equation 5.7, yielding a very close fit with a reduced  $R^2$  value greater than 0.992. The close agreement with an established solid-state model further shows that the data has a semiconductor origin,

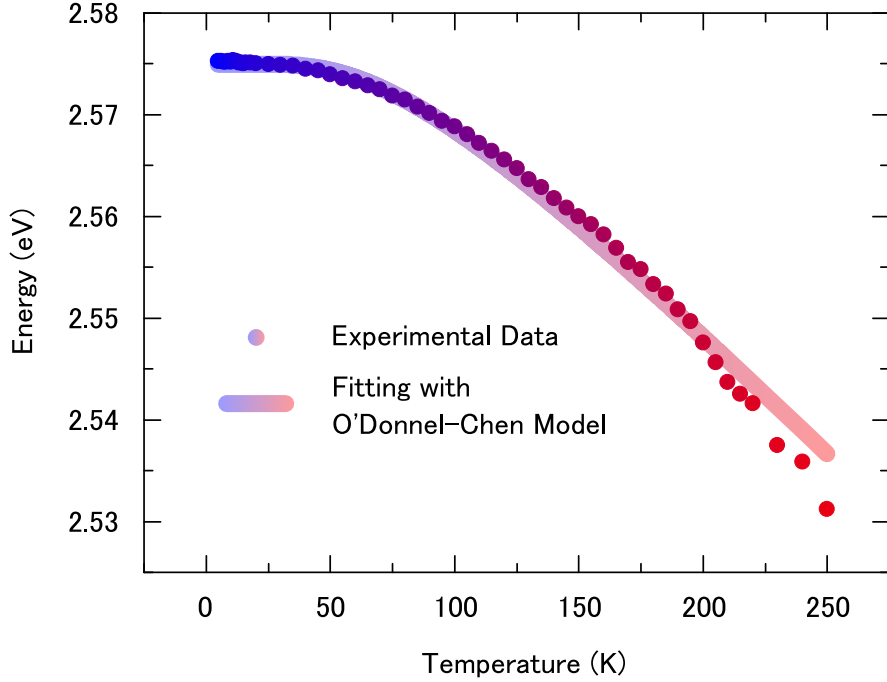


**Figure 5.4: Temperature evolution of peak emission energy of the studied QD.** All QD data points were obtained from the fitted parameters of Gaussian profiles at each temperature. Also shown is a non-linear curve fit performed with Equation 5.7. This phonon-based O’Donnell-Chen model describes the data well with a reduced  $R^2$  value  $> 0.992$ , compared to the previous phenomenological Varshni model, the fitting with which does not converge.

and should be from a QD rather than a defect where such agreement cannot be observed. The resultant fitting parameters are  $E_g(0) = 2574.98 \pm 0.07$  meV,  $S = 1.45 \pm 0.04$ , and  $\langle \hbar\omega \rangle = 19.6 \pm 0.5$  meV. The average phonon energy and dimensionless Huang-Rhys factor are comparable with results obtained in the nitride literature [112]. The temperature evolution of emission energy could be used as a tool for the tuning of emission energy for coupling with cavities or other two-level systems. However, the prospect of this type of coupling is still significantly limited by the relatively large linewidth and emission energy uncertainty of the platform, which will be evaluated in the following section.

## 5.5 Broadening of emission linewidth

### 5.5.1 Linewidth and Heisenberg's uncertainty principle

In Section 2.3.3, the mechanism of spectral diffusion in the broadening of exciton transition linewidth has been explained. The extent of fast- and slow-timescale spectral diffusion has also been investigated in Sections 4.3.1 and 4.3.2. Even without any spectral diffusion, the exciton transition linewidth should also be broadened by the uncertainty of its transition rate. According to Heisenberg's uncertainty principle,

$$\Gamma \cdot \tau = \sigma E \cdot \sigma t \geq \frac{\hbar}{2}, \quad (5.8)$$

the true linewidth  $\Gamma$  and lifetime  $\tau$  are uncertainties in the transition energy and time of the exciton, and their product is limited by  $\hbar/2$ . Since transition rate  $W$  is the reciprocal of  $\tau$ , the transition linewidth  $\Gamma$  can be re-written as aggregate of transition rates caused by all processes that perturb the radiative recombination of the exciton, i.e.  $\sum_i W_i$ , and expressed as

$$\Gamma \geq \frac{\hbar}{2} W = \frac{\hbar}{2} (W_{\text{rad}} + \sum_i W_i). \quad (5.9)$$

These processes could possibly include the thermally assisted interaction with acoustic phonons, coupling with optical phonons, and scattering to impurities and other localised carrier trapping sites [194, 205]. As temperature increases, most of these processes happen more frequently, thereby increasing the uncertainty of the total transition rate of the exciton and broadening its linewidth. By quantifying the contribution of each transition rate component, assuming temperature independence of  $W_{\text{rad}}$ , and incorporating the effects of spectral diffusion and other sources of inhomogeneous broadening, the inequality becomes the temperature-dependent linewidth relation [194, 201, 205, 206, 207, 208] with the form of

$$\Gamma(T) = \Gamma_0 + \kappa T + \Gamma_1 \exp(-E_a/k_B T). \quad (5.10)$$

In this equation,  $\Gamma_0$  is the sum of all inhomogeneous broadening, which includes the effect of size, shape, material composition, and slow-timescale spectral diffusion at low temperatures. The contribution of acoustic phonon scattering is expressed as  $\kappa T$ , where  $\kappa$  is the coupling strength [209, 210]. The last term in the equation represents a higher order broadening term, which is only activated at more elevated temperatures. The exact nature of this term is under intense debate, especially in the nitride community [25, 99]. Nonetheless, it is understood that the  $\Gamma_1$  term only affects the linewidth significantly at  $T > 100$  K. Otherwise, the inclusion of the acoustic phonon coupling component is an accurate linear approximation for describing the linewidth evolution with energy [211]. In my relevant publications [25, 26, 27, 28] and this thesis, I interpret the term as the average of all processes dominating the exciton transition rate at high temperatures. These processes could include temperature-dependent spectral diffusion, scattering with impurities, coupling to localised trapped carriers, and other unknown high-temperature mechanisms (such as a significant increase in the thermal release of holes). Since it is currently not possible to quantify the effect of each of these mechanisms, the phenomenological Boltzmann term should serve as a reasonable approximation. This is especially so, as these processes only become dominant when the temperature is high enough, e.g. comparable to  $E_a$ .

### 5.5.2 Slow broadening of linewidth

The linewidth values obtained from Gaussian fits for the spectrum at each temperature are shown in Figure 5.5. A fitting in accordance with Equation 5.10 is performed on the data, producing a close agreement. As shown in the inset of Figure 5.5, the linewidth broadening stays nearly constant at  $T < 20$  K, indicating negligible contribution from either of the temperature-dependent broadening components. The fluctuation of linewidth between 700 and 750  $\mu\text{eV}$  could be attributed to the presence of slow-timescale spectral diffusion. As the spectra were taken with 1 s acquisitions, these emission energy drifts could obscure the measurement of linewidth, resulting in the fluctuation shown in the figure inset.

The optimised fitting parameters yield  $\kappa = 9.98 \pm 1.07 \mu\text{eV K}^{-1}$ , which is in good agreement with acoustic phonon coupling strengths reported in the nitride literature [112]. From Figure 5.5, it can be observed that the interaction with acoustic phonons and its resultant

## 5.5. BROADENING OF EMISSION LINEWIDTH

---

linear increase in linewidth dominate at  $T < 90$  K. As the temperature is increased further, a much faster non-linear component sets in. The fitting also produces an activation energy of  $E_a = 39.6 \pm 1.3$  meV for this thermally assisted non-linear process. The large activation energy hence indicates that the broadening effect of this process is indeed only noticeable at  $T > 100$  K, as discussed in the last section. It is a common misconception that the  $E_a$  should be the same value as that obtained in the analysis of intensity quenching—a measure of the average depth of local carrier traps. However, the mechanisms for the non-radiative decay and exciton interaction with the local environment are not necessarily the same. In fact, they should be very different in the case of QDs. When electrons and holes undergo non-radiative recombination pathways, they do not emit photons and thus decrease the emission intensity. On the other hand, the interaction of exciton with phonons or carriers trapped locally does not necessarily forbid radiative recombination, as the interaction might not have sufficient energy to free the carriers from the QD. Instead, the photon is emitted with a larger uncertainty of energy due to the said interaction with the environment. Therefore, the two values of  $E_a$  obtained from intensity quenching and linewidth broadening are not directly comparable and should not be used interchangeably. Similar inequalities of  $E_a$  values have been observed in the analyses of other *a*-plane InGaN QDs.

As explained in the previous section, the nature of this non-linear broadening process cannot be ascertained with the current set of data. Nonetheless, a likely cause could be greater degrees of slow-timescale spectral diffusion. It has been reported that the extent of spectral diffusion of this type is likely to increase with higher temperatures [183]. The decomposition of the InGaN epilayer causes a number of local carrier traps near the studied MDE QD. With a greater influx of thermal energy, carriers have higher probabilities to fill the states of these potential minima, thereby increasing the strength of interaction between the exciton and these trapped carriers. These interactions cause greater slow-timescale spectral diffusion, and increase the uncertainty of the QD emission energy. The increased spectral diffusion can also be observed by the fluctuating data at  $T > 150$  K, where greater uncertainties are associated with the analyses of the results. This also explains the 2-fold larger activation energy of  $\sim 40$  meV for the non-linear broadening mechanism, as there

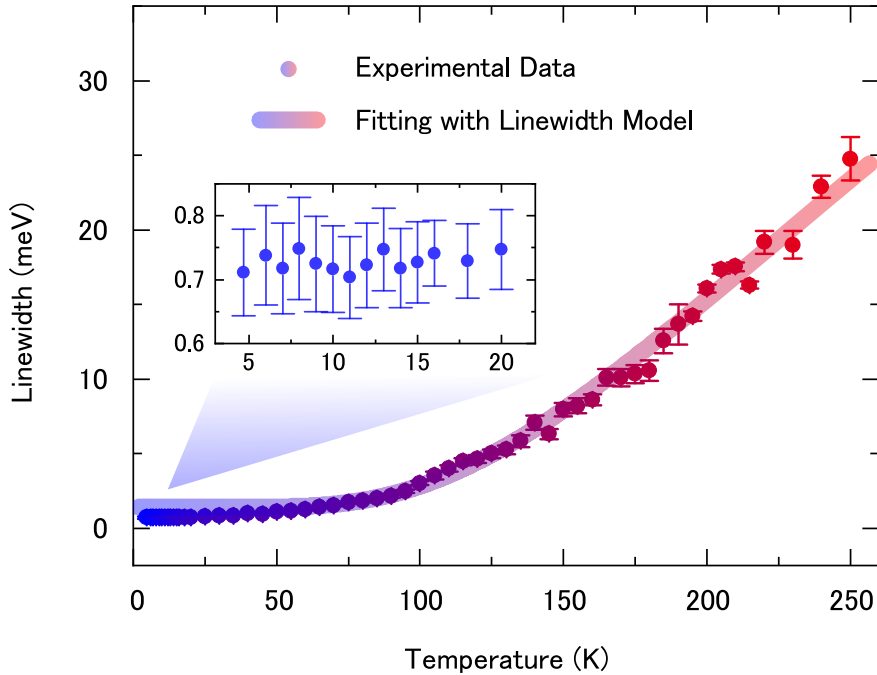


**Figure 5.5: Temperature evolution of exciton transition linewidth of the studied QD.** All linewidth values were obtained from the optimised parameters of Gaussian fits performed on the QD PL spectra at each temperature. These linewidth data are fitted with the linewidth relation introduced in Equation 5.10. Inset: a closer examination of the linewidth variation at  $T \leq 20$  K. The fluctuations could be caused by slow-timescale spectral diffusion.

needs to be sufficient carriers trapped in a large number of local potential minima before significant interaction with the QD exciton could occur. For brightness quenching, the number of emitted photons immediately decreases as long as there is sufficient energy to surmount the potential barrier of a small number of carrier escape routes, and thus the smaller activation energy of  $\sim 20$  meV.

In most non-nitride systems, an additional component governing the interaction with longitudinal optical (LO) phonons is also considered [194, 200, 212, 213]. However, the energy of nitride LO phonons is  $> 90$  meV [201]. The effect of LO phonons in the current material system would therefore require significantly higher temperatures than those under the current consideration ( $T \leq 250$  K). Hence, the contribution of LO phonons to the broadening of  $a$ -plane QDs is ignored in this analysis.

In polar  $c$ -plane QDs growth with similar methods, the linewidth could reach  $\sim 20$  meV

at around 120 K [192], in contrast to  $\sim 5$  meV for the studied  $a$ -plane QD at the same temperature. The reason for this has not been investigated thoroughly, but reports in the literature have found that the transverse acoustic phonon coupling to the built-in piezoelectric field has a significant contribution to the total acoustic phonon coupling strength [193]. Furthermore, the much stronger oscillator strength of the exciton also makes the perturbation of acoustic phonons less effective, resulting in a smaller contribution to the exciton transition rate and optical linewidth. As such, the development of the  $a$ -plane platform has made progress in the reduction of nitride emission energy uncertainties, particularly at temperatures close to the Peltier cooling barrier of 200 K.

It is also worth noting that the reduced phonon coupling at elevated temperatures also decreases the likelihood of inelastic phonon scattering, which is a possible source of non-radiative decay. Together with the fast radiative recombination rate, the probability of non-radiative recombination has been reduced, making operation at high temperatures more likely. This could be one of the key reasons why very few polar nitride systems have reported operation  $> 150$  K [87, 99, 191]. With a better understanding of intensity quenching and linewidth broadening in the  $a$ -plane QD platform, the next section will examine emission of single photons at these elevated temperatures.

## 5.6 Single-photon generation at 220 K

### 5.6.1 Filtered spectra and single-photon antibunching

The previous three sections have shown that the temperature evolutions of integrated intensity, peak energy, and exciton transition linewidth are all in very good agreement with established semiconductor theories, indicating that the emission does indeed have a semiconductor-based, rather than defect-based, origin. To further ascertain that the emitted photons are from a two-level system characteristic of a semiconductor QD, HBT autocorrelation measurements have been performed. Using the same method as that explained in Section 2.3.4, a pair of tuneable band pass filters were introduced in the optical collection path of the  $\mu$ PL system, in order to isolate the single-photon signals as far as possible. The filtered spectrum for the studied QD at 4.7 K is shown in Figure

5.6(a). Again, it is worth noting that although most of the QW emission at  $< 2.57$  eV and  $> 2.58$  eV has been cut off by the filters, the remainder in the spectrum cannot be further reduced. This is due to the non-perfect nature of the boxcar filter profiles, especially at the lower energy side. Coupled with the QW signals across the spectral range of the QD emission, the QD-to-total-intensity ratio  $\rho$  is estimated at  $\sim 68\%$  using the method described in Section 3.4.2.

The filtered signal was then passed through the HBT setup for photon statistics recording. The resultant normalised data are shown in Figure 5.6(b). A raw  $g^{(2)}(0)$  of 0.37 without any form of background correction has been obtained, confirming the single-photon nature of the emission. This raw  $g^{(2)}(0)$  is lower than that (0.47) obtained in Section 3.4, mainly due to the larger dot intensity ratio (68% vs 54%). After background correction analysis with the previously developed Equation 3.9, a  $g_{\text{cor}}^{(2)}(0)$  of 0.18 can be obtained, which is very similar to the  $g_{\text{cor}}^{(2)}(0)$  of 0.17 for the dot studied in Section 3.4. This is expected, as both the QD studied here and the one investigated in Section 3.4 are from similar  $a$ -plane samples, and a similar excitation power has been used to saturate the QD emission. The repopulation and re-emission from dot-related continuum states are again the likely reason for the non-zero  $g_{\text{cor}}^{(2)}(0)$  results, which can only be minimised with a combination of optical pumping wavelength closer to resonant conditions and lower excitation power [127]. It is also worth noting that a  $g_{\text{cor}}^{(2)}(0)$  of  $-0.38$  is obtained with the traditional background correction technique, further confirming the greater accuracy produced by the proposed Equation 3.9 in ascertaining the true single-photon purity.

As the temperature of the system was increased, HBT experiments were conducted at several temperatures  $> 100$  K. As explained in Section 5.3, the thermal activation of non-radiative decay routes gradually becomes dominant, quenching the QD emission brightness. At the same time, the intensity quenching of the underlying QWs happens at a slower rate, resulting in an increased dot-to-background ratio at higher temperatures. Hence, the measured raw  $g^{(2)}(0)$  values also gradually increase. The highest temperature at which the recorded raw  $g^{(2)}(0)$  is still  $< 0.5$  is at 220 K. The filtered spectrum and the HBT histograms at this temperature are shown in Figure 5.6(b). With the same estimation

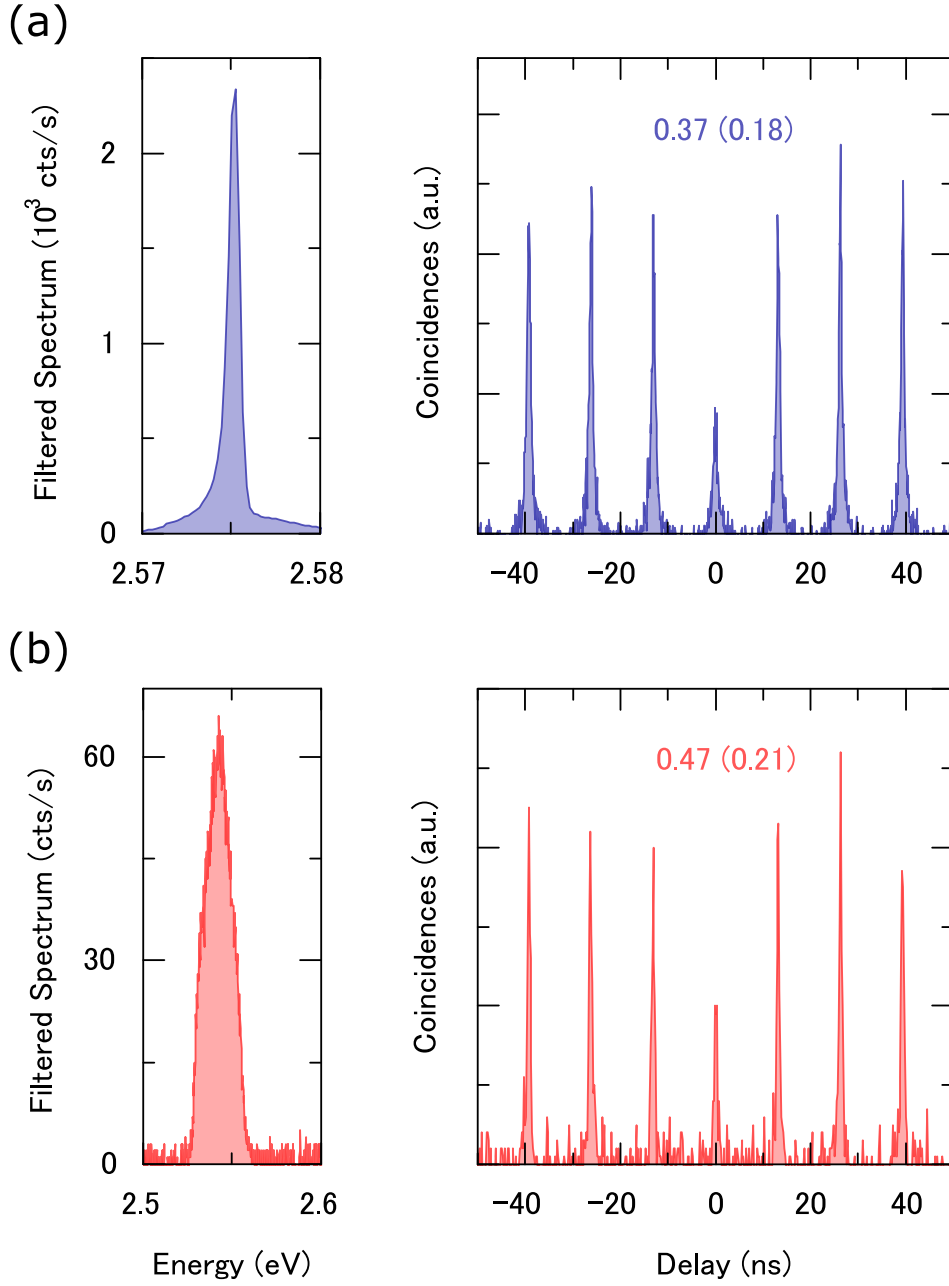


**Figure 5.6: Evidence of low- and high-temperature single-photon generation from the studied QD.** (a) Spectrum at 4.7 K restricted by a pair of tuneable band pass filters for isolation of the QD signal, which produced antibunching behaviour with a dip of 0.37 at time zero. The  $g^{(2)}(0)$  becomes 0.18 after correction of background QW emission. (b) The filtered spectrum of the studied QD at 220 K, the highest temperature at which a  $g^{(2)}(0)$  of  $< 0.5$  can still be observed. The parenthesised value is again the background-corrected result using Equation 3.9.

technique, the dot intensity ratio  $\rho$  has decreased from 68% at 4.7 K to 58% at 220 K. As a result, the uncorrected raw  $g^{(2)}(0)$  is recorded at 0.47.

At this stage, it is worth noting that the development of the  $a$ -plane QD platform has indeed met one of its initial goals—the generation of single photons at temperatures above the thermoelectric cooling barrier of 200 K. Amongst currently reported polar and non-polar InGaN QD systems, this is the second one along with Deshpande *et al*'s work (280 K) [191] that achieved  $> 200$  K single-photon emission. Within all nitride developments, there is only a third work based on GaN/AlN dot-in-nanowire (350 K) [99] that reported similar high-temperature single-photon generation.

With a  $\rho$  of 58% and Equation 3.9, a  $g_{\text{cor}}^{(2)}(0)$  value of 0.21 can be obtained. The reason for it not being closer to 0 has already been explained previously. The slight discrepancy from the  $g_{\text{cor}}^{(2)}(0)$  value of 0.18 at 4.7 K is most likely caused by the greater difficulty in obtaining accurate background signal estimations. As shown in Figure 5.2, the contribution of the phonon sideband becomes gradually significant as the temperature is increased from 4.7 to 250 K. Furthermore, with greater number of carriers escaping to carrier trapping sites at higher temperatures, the degree of slow-timescale spectral diffusion also increases. As a result, it becomes harder to differentiate the contribution from the Gaussian QD, its phonon sideband, and the underlying QW emission, during the first Gaussian fitting to determine the unfiltered background level (method explained in Section 3.4.2). Therefore, the high-temperature  $g_{\text{cor}}^{(2)}(0)$  value should be treated as a rough estimation, instead of an accurate determination, of the true single-photon performance. The uncorrected raw  $g^{(2)}(0)$  should still be the most important benchmark. At 220 K, the raw value of 0.47 is a relatively small increase from 0.37 at 4.7 K, which could be attributed to the strong quantum confinement and fast radiative recombination of excitons. Similarly, fast radiative lifetimes can already be seen from the slope of the HBT plots. In order to quantify the radiative recombination rates at different temperatures, temperature-dependent time-resolved  $\mu$ PL measurements were performed.

### 5.6.2 Rate of single-photon emission

Using the same method as that in Sections 3.3 and 4.4, TCSPC data have been first recorded at 4.7 K, and shown in Figure 5.7(a). A convolved Gaussian described by Equation 3.6 was used to fit the data, again due to the similarity between the expected radiative lifetime ( $\sim 300$  ps) to the IRF width of the PMT ( $\sim 140$  ps). The fitted parameters give a decay time constant of  $480 \pm 20$  ps, which is within the range of MDE QD lifetimes (200 to 600 ps) detailed in Section 3.3.2.

As temperature increases, the radiative lifetime of the studied QD fluctuates slightly, and sees a small trend of decrease. At 220 K, the data from the time-resolved studies yield a decay time of  $357 \pm 20$  ps. The decrease is due to the activation of non-radiative recombination pathways [25, 97]. The number of photons for each histogram column (at each smallest step on the time scale) becomes smaller at a faster rate, because at higher temperatures a photon has a higher probability of undergo non-radiative recombination after each incremental amount of time. Since the PMT can only directly record incident photons, i.e. radiative recombination, the measured lifetime would appear slightly shorter. This phenomenon is also noted by other researchers in the nitride [25, 97] and selenide [214] QD literature in their characterisation of exciton radiative recombination lifetimes. It is worth noting that this effect is very small, and only causes a  $\sim 25\%$  difference in the measured radiative lifetime with a  $> 200$  K increase in temperature. The results in Figure 5.7(b) thus show that the single-photon emission is accompanied by an ultrafast GHz repetition rate at 220 K.

In the other InGaN QD work in the literature that reports  $> 200$  K single-photon emission, a radiative lifetime of  $\sim 700$  ps is measured [143]. Even with the small nanowire structures for stronger confinement, the radiative lifetime of the polar InGaN QD is just below 1 ns. On the other hand, the use of non-polar *a*-plane indeed minimises the built-in nitride fields and produces exciton recombination lifetimes that are twice faster than the other InGaN platform above 200 K, without the need of smaller nanostructures to enhance its radiative recombination rate. It is important to remember that the studied QD is an MDE one. According to the investigation in Section 4.4, Q2T QDs are able to produce even faster radiative lifetimes, but at the expense of dot intensity ratios and single-photon purity. At

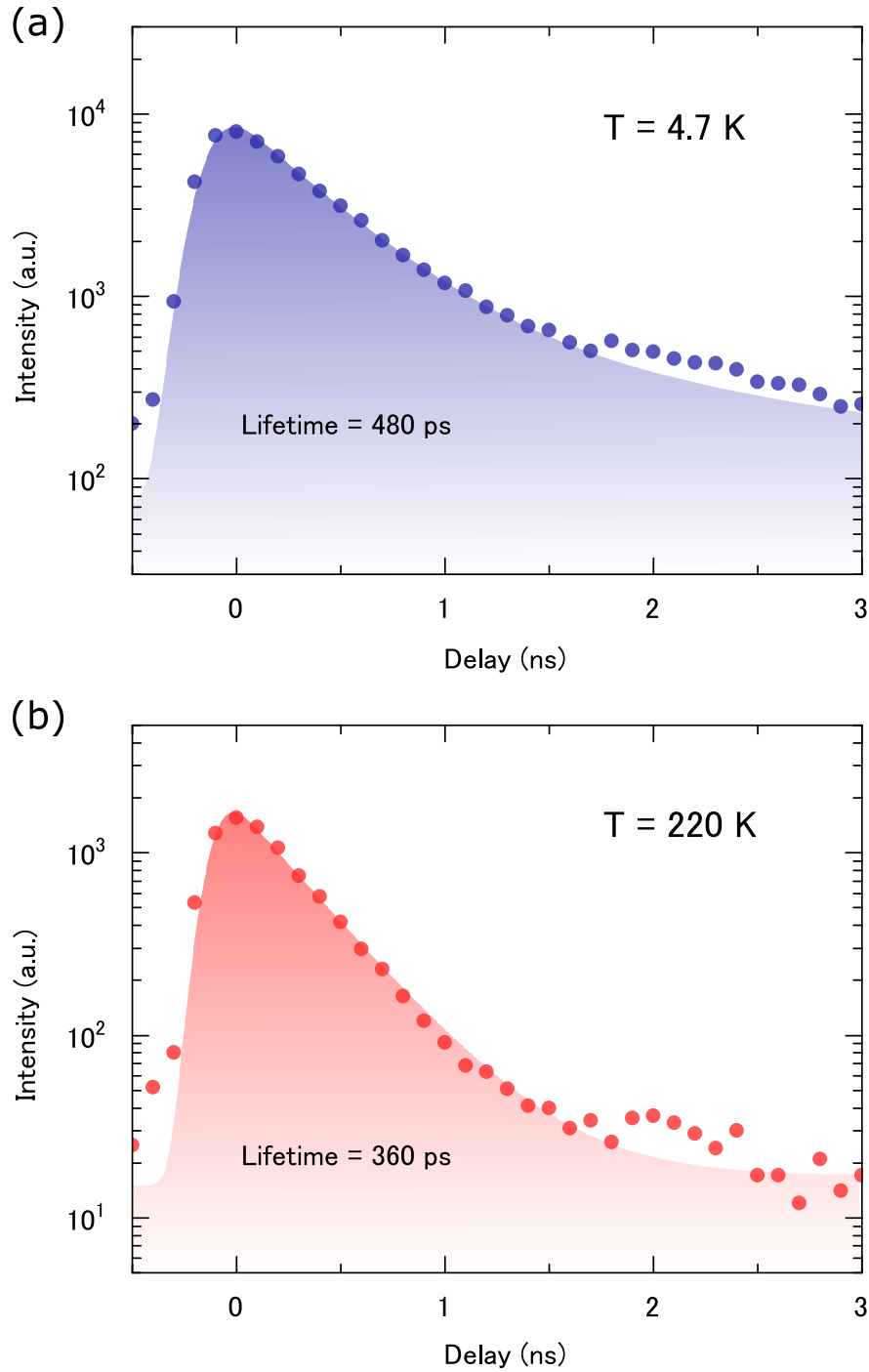


**Figure 5.7: Ultrafast repetition rate of single-photon generation from the studied QD.** (a) TCSPC data recorded at 4.7 K, and fitted with Equation 3.6. A time constant of  $480 \pm 20$  ps has been obtained. (b) Same measurement performed at 220 K, yielding a radiative recombination lifetime of  $360 \pm 20$  ps, signifying GHz single-photon generation rate above the Peltier cooling threshold.

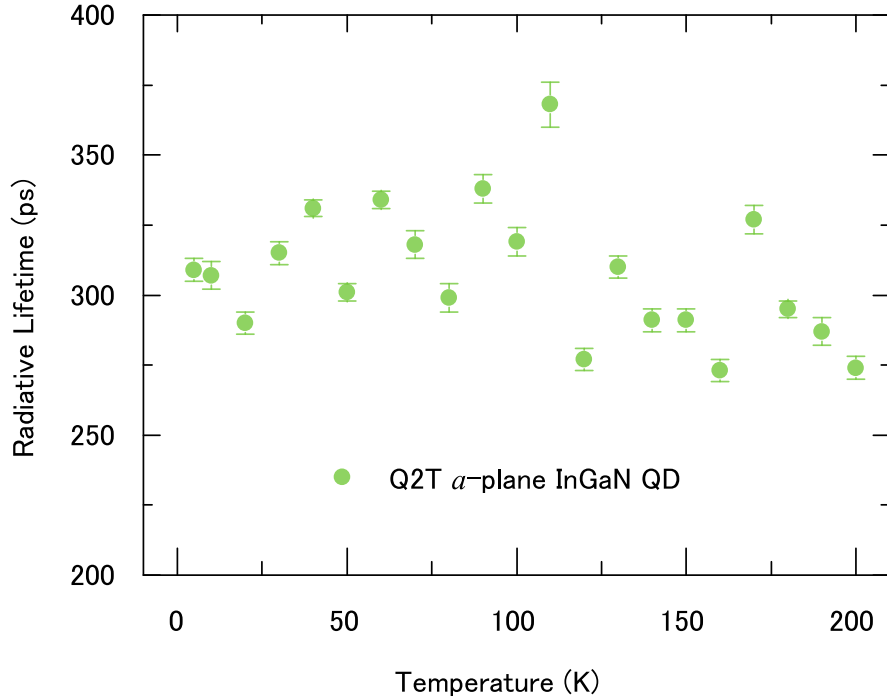


**Figure 5.8: Temperature-dependent radiative recombination lifetime of another  $a$ -plane InGaN QD.** Lifetime measured at 4.7 K, and from 10 to 200 K at 10 K intervals for a Q2T QD. According to conclusions in Section 4.5, it is easier to achieve higher temperature stability with a strongly emitting Q2T QD. A sub-300 ps radiative lifetime at 200 K has been recorded.

the moment, only the studied MDE QD has achieved single-photon generation up to 220 K with a  $< 0.5$  raw  $g^{(2)}(0)$  and a radiative recombination lifetime of 360 ps. However, without considering the requirement for single-photon purity, the better temperature stability and faster recombination rate of Q2T QDs could potentially allow for even faster radiative lifetimes at  $> 200$  K.

One such set of temperature-dependent radiative lifetime measurement has been performed on a Q2T QD, and the results are shown in Figure 5.8. The studied QD has a lifetime of  $309 \pm 4$  ps at 4.7 K, which is in agreement with findings in Section 4.4. Despite fluctuations, there is a weak trend of decrease in the measured lifetime, again attributed to the stronger effect of non-radiative recombination explained above. At 200 K, the measured lifetime becomes  $274 \pm 4$  ps. The smaller decrease (11%) compared to that of the studied single-photon emitting MDE QD (25%) could be caused by the slower brightness quenching and reduced non-radiative recombination pathways, as set forth in Section 4.5. This Q2T test

also serves as further confirmation that the non-polar  $a$ -plane QD platform does indeed have ultrafast photon emission rate at temperatures in the Peltier-cooled regime.

### 5.6.3 Non-classical light emission at 250 K

Sections 5.2–5.5 have detailed optical properties of the studied (MDE) QD up to 250 K ( $-23^\circ\text{C}$ ), the highest temperature at which PL was recorded. However, as explained previously, the rate of QD quenching increases at higher temperatures. At 250 K, the integrated intensity of the QD is  $> 50\%$  lower than that at 220 K. Due to the relatively slower quenching of the background QW emission, the dot intensity ratio has dropped significantly. Autocorrelation studies at this temperature yields an uncorrected raw  $g^{(2)}(0)$  of 0.73, as shown in Figure 5.9(a). This value is now  $> 0.5$  and insufficient to demonstrate a higher probability of single, instead of multiple, photon generation from the system. Nonetheless, it does still demonstrate non-classical antibunching, with the QD itself emitting single photons in the presence of a stronger background QW light source. While the result in Figure 5.9(a) is the highest temperature at which antibunching has been observed in the  $a$ -plane InGaN QD platform, it does pose another challenge in achieving purer single-photon emission at temperatures closer to ambient conditions. With a thermally accelerated decrease of the QD intensity, the  $g^{(2)}(0)$  will inevitably be higher. In particular, the challenge becomes the achievement of even higher temperature operation with a further reduced degree of non-radiative recombination, together with a minimised background QW emission. While parts of this challenge have been addressed independently, e.g. the greater temperature stability introduced by the new Q2T method, a solution to tackle the challenge in its entirety will be the next phase of the future development of this single-photon platform. Notwithstanding, it is important to recognise that at this initial stage, the increase of raw  $g^{(2)}(0)$  with temperature is already slower than other materials such as CdSe [69], demonstrating the potential of the  $a$ -plane nitride material in realising stable high-temperature operation.

In Figure 5.9(b), time-resolved analysis at 250 K has produced a radiative lifetime of  $285 \pm 11$  ps, showing strong exciton oscillator strength up to the highest operation temperature. The measurement result indicates a 20% decrease from that at 220 K (357 ps). The speed

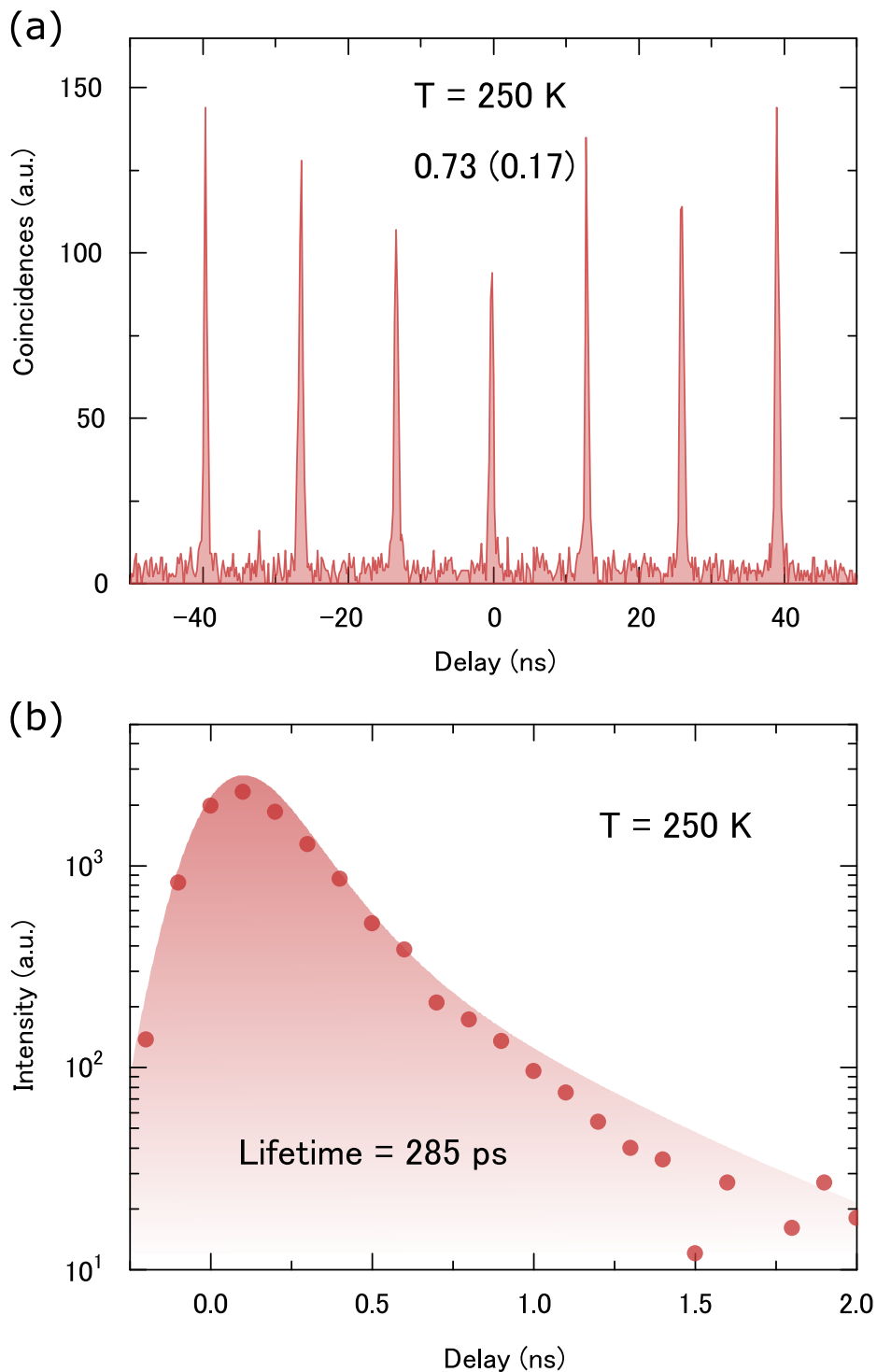


**Figure 5.9: Evidence of ultrafast antibunching of the studied (MDE) QD at 250 K.** (a) HBT autocorrelation histogram demonstrating a raw  $g^{(2)}(0)$  of 0.73, which can be corrected to 0.17 after the removal of QW backgrounds. (b) Time-resolved TCSPC data recorded at 250 K, and fitted with Equation 3.6. A time constant of  $285 \pm 11$  ps has been obtained.

of decrease is much faster over the last 30 K compared to that over the first 200 K (25%), owing to the accelerated exciton decay into non-radiative pathways.

### 5.7 Stability of polarisation properties

#### 5.7.1 Single-photon emission with polarisation control

Up to now, the ability of *a*-plane InGaN QDs to emit ultrafast single photons up to 220 K and ultrafast antibunched photons up to 250 K has been demonstrated. However, these features alone are not exclusive to the system, and have been achieved by several other semiconductor QD platforms [69, 99, 191]. Section 3.2 has analysed the unique polarisation properties of *a*-plane InGaN QDs, and shown a statistically high polarisation degree with deterministic polarisation axes. Here, temperature-dependent polarisation-resolved  $\mu$ PL is performed on the studied single-photon emitting QD, and the results are shown in Figure 5.10.

At 4.7 K, it can be seen that the normalised intensities at each polariser angle vary in a sinusoidal fashion, and fit well with Malus's law of Equation 3.2. Based on the maximum and minimum intensities, the DOLP  $P$  of the studied QD is evaluated to be  $0.83 \pm 0.01$ . This value is within the range of 0.6 to 1.0 recorded in Section 3.2, but lower than the statistical average of 0.90. In this set of experiments, the  $0^\circ$  marking of the polariser is aligned to the crystal *m*-direction for simplicity, as we already know and expect this polarisation anisotropy. From Figure 5.10(a), it can be seen that the fast axis of the polarised emission is indeed aligned to  $0^\circ$ , corresponding to a predefined and deterministic polarisation direction.

The same measurements have been performed when the temperature of the sample reached 220 K. The intensity results become noisier due to greater intensity fluctuations at this temperature. Nonetheless, a close fitting with Equation 3.2 can be obtained, and a  $P$  of  $0.80 \pm 0.13$  is calculated. The angle of polarisation also stays constant along the crystal *m*-direction, as indicated by Figure 5.10(b).

This result is of great importance for the *a*-plane InGaN QD platform, as it is the first report [25] of the observation of polarised single-photon emission above 200 K in semicon-

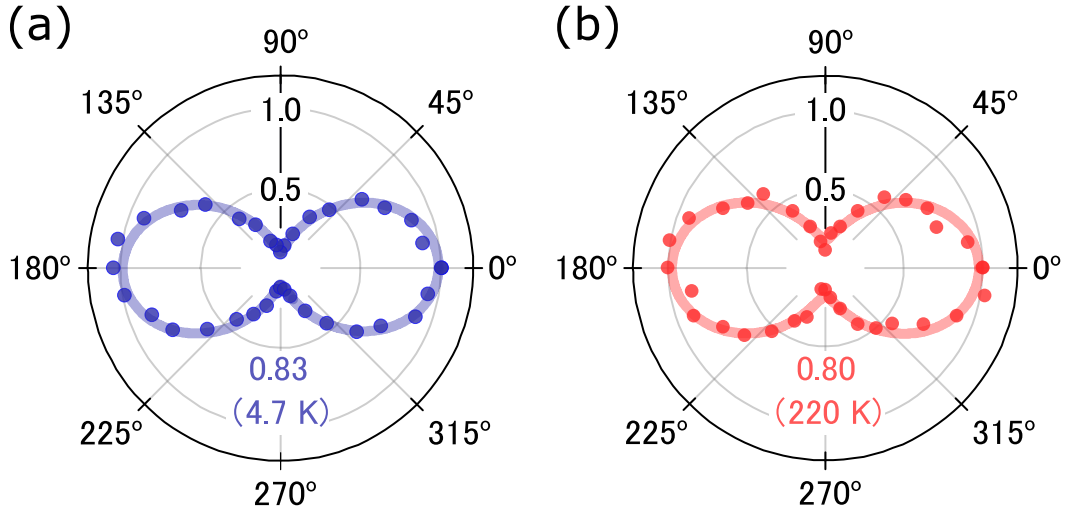


**Figure 5.10: Evidence of polarised photon generation with a deterministic axis from the studied single-photon emitting QD up to 220 K ( $-53\text{ }^{\circ}\text{C}$ ).** (a) Normalised intensities of the studied QD as the polariser is varied between  $0^{\circ}$  and  $360^{\circ}$  at  $10^{\circ}$  intervals at 4.7 K. The data points have been fitted with Equation 3.2, demonstrating their agreement with Malus's law of polarisation. The alignment of the polarisation axis with  $0^{\circ}$  of the polariser indicates a deterministic polarisation direction along the crystal  $m$ -axis. (b) Results of the same measurement performed at 220 K, showing linearly polarised emission with a fixed polarisation axis for the studied QD.

ductor QDs. In fact, there has been no report of linearly polarised emission from a QD at any temperatures above cryogenic conditions yet. Coupled with the HBT and lifetime measurement results in the previous section, this  $a$ -plane platform has now demonstrated ultrafast single-photon emission with deterministic polarisation properties at temperatures well above the thermoelectric cooling threshold (up to  $-53\text{ }^{\circ}\text{C}$ ). There are of course many other factors that still limit the external quantum efficiency of this system significantly. But looking at the aspect of polarisation alone and referring to the definition of DOLP in Equation 3.1, the theoretical maximum external quantum efficiency of this  $a$ -plane InGaN QD is increased to 90% ( $P = 0.80$ ), from the 50% ( $P = 0$ ) of an unpolarised semiconductor QD system.

### 5.7.2 Confirmation of high-temperature polarisation

In order to confirm that the emission of linearly polarised photons at 200 K is not an isolated case, another set of temperature-dependent polarisation measurements have been made with a QD from a different  $a$ -plane sample. As single-photon generation is not the focus of this investigation, a Q2T sample is again used in order to leverage on its high-temperature stability and obtain the desired polarisation results effectively. The chosen Q2T QD has an emission energy of  $\sim 2.54$  eV ( $\sim 488$  nm) at 4.7 K, as shown in Figure 5.11(a). This QD energy is representative of the  $a$ -plane platform, as the experimentally observed low-temperature energies are within the range of 2.3 to 2.8 eV. The relatively stronger background QW intensity compared to the MDE QD studied in the previous sections is characteristic of a Q2T QD, owing to the less disrupted epilayer as explained throughout Chapter 4. The linewidth of this Q2T QD is  $3.39 \pm 0.87$  meV, which is one of the highest observed in the system. The large linewidth could be attributed to strong interactions with phonons, which is evident by the relatively large phonon sideband at the lower energy end of the QD spectrum in Figure 5.11(a). As the polariser is turned  $90^\circ$ , the PL intensity of the QD is almost completely suppressed, indicating a very weak component along the crystal  $c$ -axis. The intensity variations at each  $10^\circ$  polariser angle agrees very well with Equation 3.2, as shown in the inset of Figure 5.11(a). A high polarisation degree of 0.93 can be obtained for the QD. There is a small angle offset of  $-10^\circ$  from the  $0^\circ$  ( $m$ -axis) mark, caused by the error in manual placement of the sample into the cryostat.

When the temperature is increased to 200 K (Figure 5.11(b)), the energy of the QD has redshifted to  $\sim 2.51$  meV, and the linewidth of the exciton transition has broadened to  $20.02 \pm 1.23$  meV, both of which are caused by the stronger thermally assisted interaction with phonons explained previously. The  $c$ -component of emission is relatively stronger at this temperature, indicating a reduction in the polarisation degree. The inset in Figure 5.11(b) displays the slightly noisier intensity variation with polariser angle, which still fits well with Equation 3.2. The reduced DOLP of the QD is calculated to be 0.85, with the same polarisation axis as that at 5 K. Therefore, the ability of  $a$ -plane InGaN QDs to emit highly polarised photons above the thermoelectric cooling barrier has been confirmed.

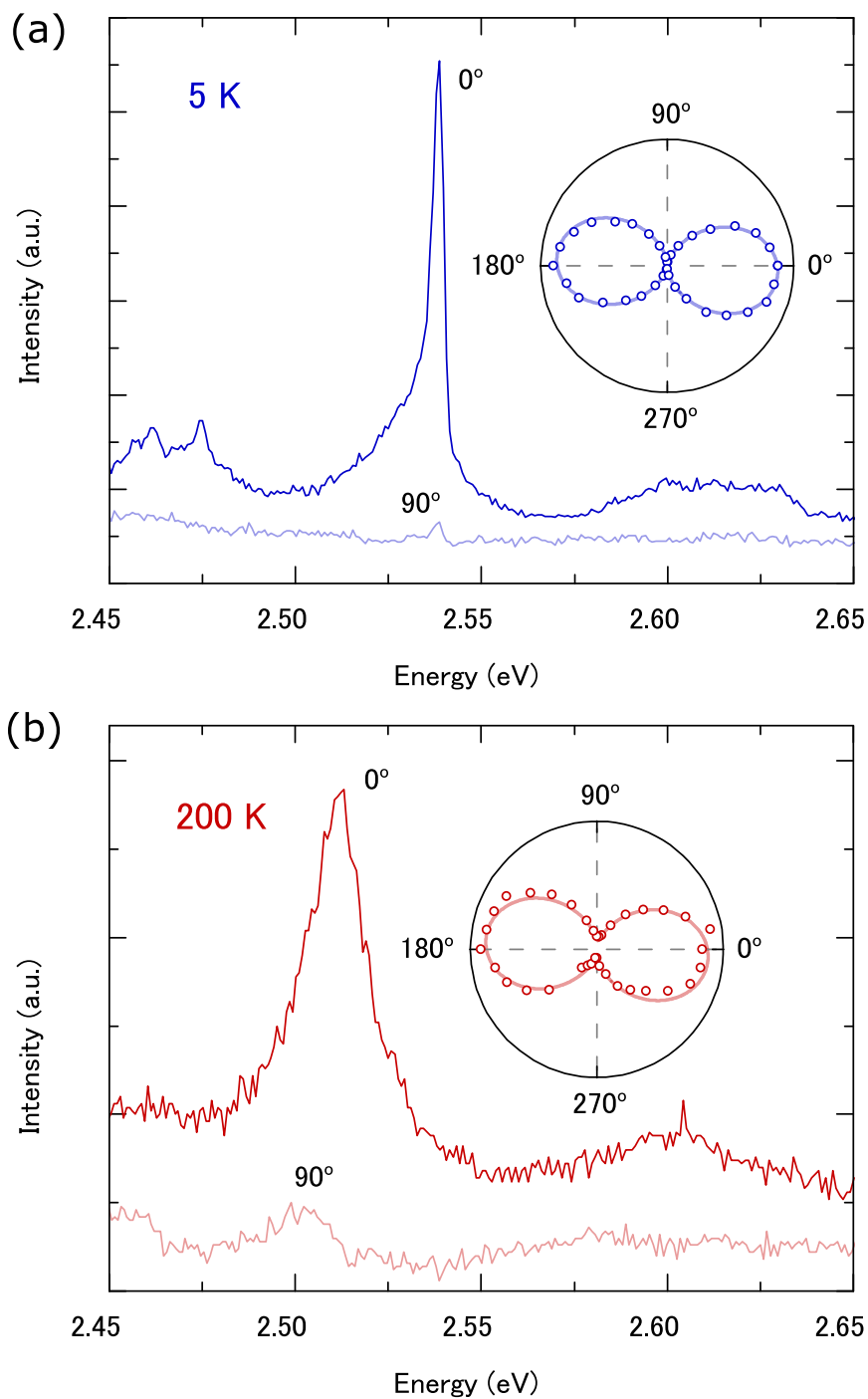


**Figure 5.11: Evidence of high-temperature polarised emission from a different *a*-plane InGaN QD up to 200 K.** (a) Cross-polarised PL of the QD at 5 K, with inset demonstrating the intensity variation with polariser angle and agreement with Malus's law. (b) The same measurements performed at 200 K, with linearly polarised emission, a slightly reduced polarisation degree, and an unchanged polarisation axis.

## 5.7. STABILITY OF POLARISATION PROPERTIES

---

During the temperature changes, the intensities corresponding to emission along the  $m$ - and  $c$ -axis of the sample have also been recorded at steps of 20 K. The DOLPs at each of these temperatures are calculated and shown in Figure 5.12(a). In order to ensure accurate polarisation measurements, data were only taken after the temperatures have stabilised to within 1 K of the targeted value. Firstly, no change in the polarisation axis ( $m$ -axis) has been seen, signifying the reliability of the predefined and deterministic nature of polarisation angle up to high temperatures. Looking at the changes in polarisation degree more closely, the behaviour can be split into two segments. For  $T < 100$  K, the DOLP stays nearly constant and above 0.9 with minimal fluctuations. As the temperature is increased beyond 100 K, the DOLP decreases gradually till 0.85 at 200 K. The reason for this decrease could be attributed to excited states, and will be explained in the following section. It is important to note that the DOLP decrease of 0.08 over a temperature range of 200 K is a small one, indicating the temperature insensitivity of polarisation properties for  $a$ -plane InGaN QDs.

Due to the difference of polarisation degrees between the two studied QDs, it would be useful to understand the range of attainable DOLPs at each temperature. As such, the statistical analysis of Section 3.2.4 is extended to higher temperatures, with reduced sample sizes due to feasibility. A total of  $\sim 200$  QDs have been studied, in which 40 were at 5 K, 20 at 20–120 K (20 K step), and 10 at 140–200 K (20 K step). These data are shown in Figure 5.12(b). There are identical DOLP values at higher temperatures, which result in overlapping data points. At each studied temperature, selection bias has been minimised in order to investigate the general behaviour of polarisation. The decreasing number of studied QDs at higher temperatures is due to the difficulty in identifying ones with sufficient intensity for accurate polarisation measurements. With increasing temperatures, the brightness of the emitters drops significantly as studied previously. Therefore, only QDs with very strong confinement survives at temperatures closer to 200 K. Out of these QDs, only a few of them still have a count rate high enough for accurate discrimination between maximum and minimum polarisation intensities. The average polarisation degree with their respective standard error has also been calculated at each temperature step and shown in Figure 5.12(b). Similar to the single dot studied in Figure 5.12(a), the average

## 5.7. STABILITY OF POLARISATION PROPERTIES

---

value stays nearly constantly up to 120 K and remains above 0.85. For all the data points collected at  $T \leq 100$  K, about half of them have a polarisation degree of 0.9 or above.

Across the entire temperature range, a few of the QDs have a DOLP of 1, with several others very close to unity. The  $\sim 100\%$  external polarisation efficiency make these QDs very useful for quantum information applications. On the other hand, there are indeed some QDs with DOLPs lower than the two single QDs studied above. Based on the work set forth in Section 3.2, it is not unlikely that a large (aspect ratio of  $\sim 2$ ) shape anisotropy exists, with an elongation along the  $c$ -axis. A theoretical quantitative treatment will be presented in the next section to address this effect at higher temperatures. For this investigation, QDs with a polarisation axis along the crystal  $c$ -direction have not been included. This is due to their small probability of occurrence, which makes it less feasible for statistical investigation at higher temperatures. Nonetheless, several of these QDs have been identified at various temperatures, and no anomalous results of DOLP have been seen.

Looking at the average polarisation degrees at each temperature, there are no values below 0.77, which confirms the ability of  $a$ -plane InGaN QDs to act as polarised photon emitters up to 200 K. However, while the spread of the DOLP values is relatively small for temperatures below 120 K, this range becomes much greater at  $T > 120$  K. In fact, all studied QDs ( $\sim 150$ ) at  $T \leq 120$  K have a DOLP of 0.75 or higher, except for 3 outliers with polarisation degrees of around 0.65. As the temperature is increased beyond 120 K, the range of DOLPs expands to between 0.5 and 1. The presence of QDs with lower DOLPs at high temperatures suggests two possibilities: (1) The contribution of excited states becomes more significant with greater thermal energies, and (2) the anisotropy of QDs could have a stronger effect on their DOLPs at higher temperatures. In order to shed light on these questions and better understand the ability of  $a$ -plane InGaN QDs to generate highly polarised photons at elevated temperatures, theoretical studies are required.

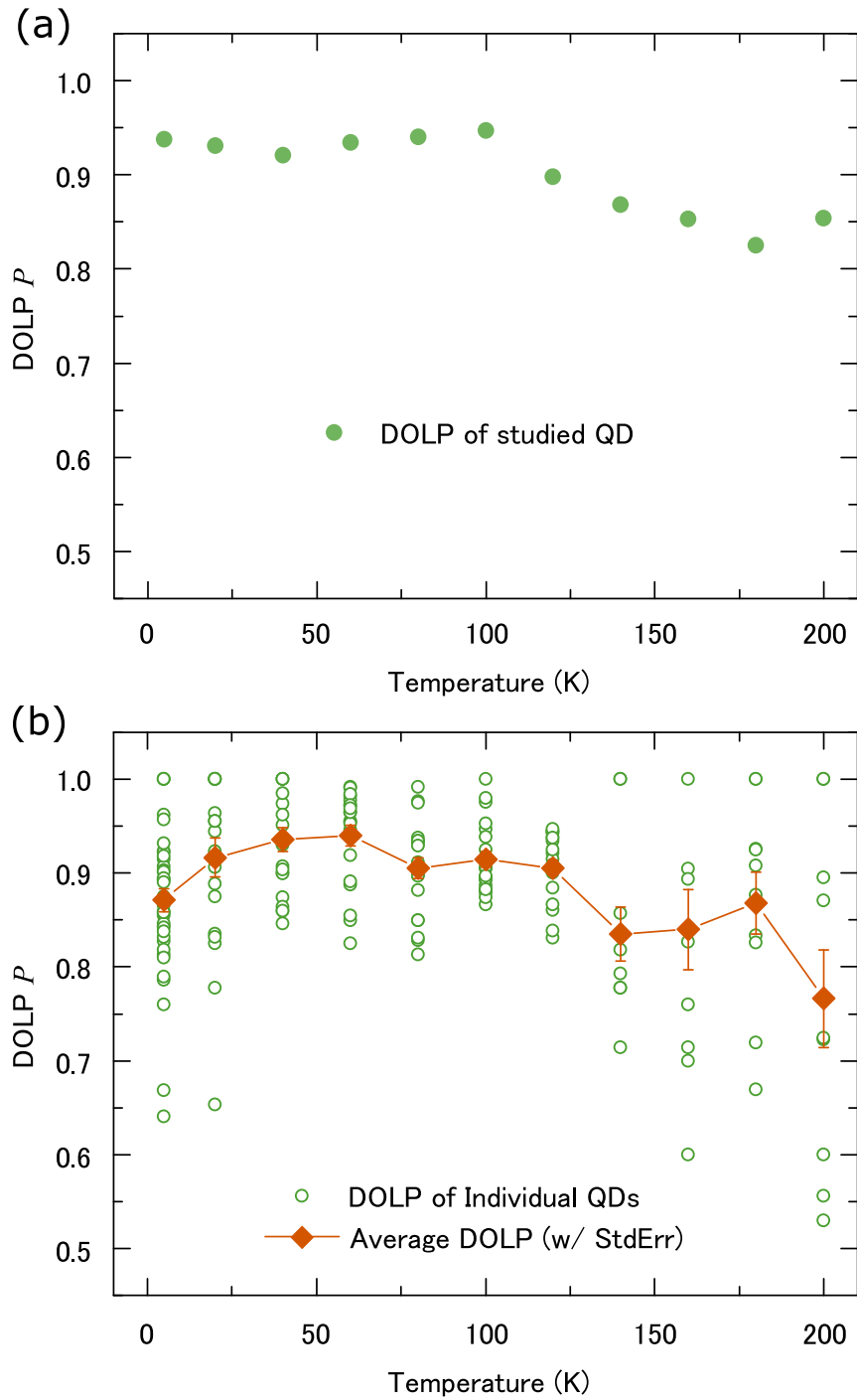


**Figure 5.12: Temperature evolution of polarisation degree for *a*-plane InGaN QDs.**

(a) DOLP of the single Q2T QD investigated in Figure 5.11 at 5 K, and from 20 to 200 K at 20 K intervals. (b) Statistical DOLP distribution of  $\sim 200$  QDs at the same temperature steps up to 200 K, with mean and standard error. All data points are  $> 0.5$ , while all mean DOLPs are  $> 0.75$ .

### 5.7.3 Theoretical support

Our collaborators in Tyndall modified the  $\mathbf{k}\cdot\mathbf{p}$  model used in Section 3.2 to take Fermi-Dirac statistics [215] into account, and investigated high temperature polarisation properties of these QDs from a theoretical perspective. More details of the theoretical framework can be found in our joint publication [26]. The final results of this collaborative work are presented in Figure 5.13 in support of the discussions in this section.

Three lens-shaped QD models with different geometries have been included. In Figure 5.13, QD-sym has a symmetrical circular base, while QD- $c$  and QD- $m$  have elliptical bases with elongations along the crystal  $c$ - and  $m$ -directions respectively. All data in Figure 5.13 are DOLP results computed at each temperature for these three QDs. Looking at QD-sym with a circular base, the polarisation degree is very high ( $> 0.95$ ) at low temperatures  $T \leq 20$  K. This is in line with the results obtained in Section 3.2, where the hole ground states have been confirmed with a  $|m\rangle$ -dominance. This high DOLP remains relatively constant till  $\sim 80$  K, indicating much higher spontaneous emission rates along the crystal  $m$ -direction. As the temperature is increased further, contributions from the  $|c\rangle$ -like states gradually become significant, reducing (increasing) the spontaneous emission rate along the crystal  $m(c)$ -direction. Therefore, the in-plane polarisation degree would slowly decrease at  $T > 80$  K. Till 200 K, the DOLP of QD-sym has dropped to 0.82, which is in agreement with both of the experimentally studied single QDs discussed in previous subsections. The theoretical simulation also includes the scenarios in which the temperature is increased to ambient conditions. At a temperature of 300 K, the calculated DOLP for QD-sym is 0.71.

However, as explained in Section 3.2, the stochastic self-assembly process cannot be expected to produce all QDs with circular bases. QD- $c$  and QD- $m$  with a two-fold anisotropy along the  $c$ - and  $m$ -directions are crucial in modelling the behaviour of the current  $a$ -plane InGaN QD platform. In particular, the degree of band mixing effects involving  $|m\rangle$ - and  $|c\rangle$ -like states become different, owing to changes in confinement effect along the  $m$ - and  $c$ -axes, which have been addressed in Section 3.2. As discussed in the case of QD-sym, the amount of mixing between  $|m\rangle$ - and  $|c\rangle$ -orbital characteristics increases at higher temperatures. Therefore, this effect will also be expected to increase with an elongation

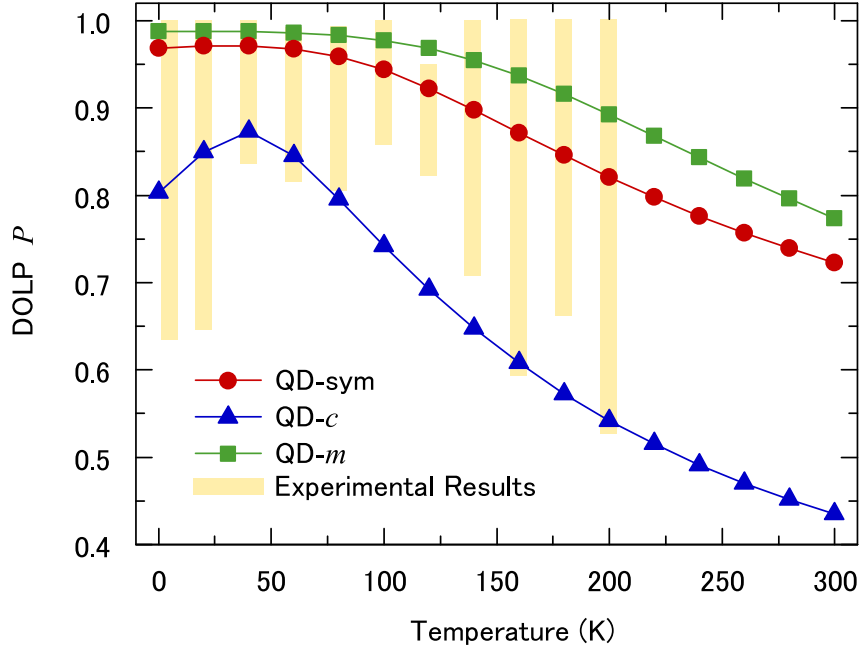


**Figure 5.13: Theoretical study of temperature-dependent polarisation degree of  $a$ -plane InGaN QDs.** Three lens-shaped QDs with different base geometry were included in the  $\mathbf{k}\cdot\mathbf{p}$  simulation, taking Fermi-Dirac statistics into consideration. Together, QD-sym (symmetrical circular base), QD- $c$  (2 : 1 elongation along  $c$ -axis), and QD- $m$  (2 : 1 elongation along  $m$ -axis) explain the experimental findings shown in Figure 5.12(b) well. The final results of this theoretical study were obtained by our collaborators in Tyndall National Institute.

(compression) along the crystal  $c$ -direction, resulting in an earlier (later) onset of DOLP reduction as the temperature rises.

This behaviour is indeed observed for both QD- $c$  and QD- $m$  in Figure 5.13. At  $T \leq 20$  K, the lower and higher DOLP of QD- $c$  and QD- $m$  respectively are in agreement with the low-temperature results obtained in Section 3.2. When the temperature is increased to above 40 K, the DOLP of QD- $c$  begins to drop significantly, reaching a value of 0.54 at 200 K. This result corresponds to and provides an explanation for the experimental findings in Figure 5.12(b), where DOLP results between 0.5 and 0.6 are present at very high temperatures. In the case of QD- $m$ , the reduced degree of band mixing is evident because DOLPs at all temperatures are higher than QD-sym. In fact, the DOLP of QD- $m$  remains nearly unchanged at  $\sim 0.98$  till 100 K, and only sees a small reduction to 0.9 at 200 K. When the temperature is increased to 300 K, the polarisation degree of QD- $m$  is still as high as 0.77.

As shown in Figure 5.13, the behaviours of QD-sym, QD-*c*, and QD-*m* have a very close agreement with the experimental ranges (also presented in Figure 5.12(b), and provide an explanation for the increasing spread of DOLP values at higher temperatures.

## 5.8 Temperature-dependent fine-structure splitting

### 5.8.1 Probing exchange interactions in nitrides

Due to the exchange symmetry between electrons and holes, there are two ground state transitions associated with orthogonally polarised photons. The small energy difference between these two transitions is the fine-structure splitting of the emitter [28]. The strength of the exchange interaction is much weaker compared to exciton transition energy itself, and is measured to be  $\sim 0.5$  meV in the context of nitride QDs [28, 105, 114, 182, 216]. Due to its diminutive nature, the dimension, geometry, material composition, and Coulomb environment (e.g. locally trapped carriers, phonon interactions) of the nanostructure could all affect the spatial part of the electron and hole wavefunction significantly, resulting in differences in FSS of each studied QD.

In polarisation-resolved  $\mu$ PL, it is in principle possible to resolve this small energy difference between the cross-polarised PL components. In practice, it proves to be a difficult measurement, especially because of its closeness to the extent of both fast- ( $\sim 1$  meV) and slow-timescale spectral diffusion ( $\sim 0.5$  meV). Nonetheless, with longer periods of signal acquisition and data averaging, such measurements have been made in InGaN QDs under cryogenic conditions [105, 114, 182]. However, it has not been possible to study the behaviour of FSS at elevated temperatures, mainly due to the inability to measure high-temperature polarised emission in the first place. With latest developments of *a*-plane InGaN QDs, this is now possible thanks to three key advantages:

1. The fast radiative recombination efficiency allows higher probability of radiative, instead of non-radiative, emission at high temperatures, thereby increasing the brightness and temperature stability. This is especially so with Q2T QDs, the details of which have been extensively covered in Chapter 4.

## 5.8. TEMPERATURE-DEPENDENT FINE-STRUCTURE SPLITTING

2. The predefined and deterministic polarisation properties built-in to the non-polar nitride material allow the observation of high-temperature polarised emission up to 200 K, as demonstrated in the last section.
3. The significantly reduced spectral diffusion, especially with Q2T QDs, is now an order of magnitude smaller than the expected FSS energy, allowing for more accurate and efficient measurement of FSS.

### 5.8.2 Constancy and change of FSS with temperature

In order to study FSS accurately, very specific choices of QDs need to be made. In particular, the ability to resolve the weak fine-structure component, especially at higher temperatures, is crucial for resolving the energy splitting. As such, only QDs that are polarised, but with a DOLP of  $< 0.80$ , can be used. Given the highly polarised nature of the platform, this already limits the number of viable candidates tremendously. Furthermore, with the intent of studying FSS up to 200 K, strongly emitting QDs that imply good quantum confinement are also required. Therefore, it poses a very experimentally challenging task to identify suitable QDs for this investigation, and only several QDs have been studied over a manageable timeframe.

The polarisation-resolved PL spectra of one such QD at 5 K is shown in Figure 5.14(a). The DOLP of this QD is 0.79, and its  $c$ -component is normalised with a factor of 8.34. Analyses yield central energies of  $2535.00 \pm 0.01$  and  $2534.55 \pm 0.02$  meV, for the strong and weak fine-structure components respectively. The FSS can hence be defined as  $|E_m - E_c|$ , where  $E_m$  and  $E_c$  are the transition energies of the fine-structure components along the crystal  $m$ - and  $c$ -directions. Hence, the FSS of this QD is evaluated to be  $450 \pm 22 \mu\text{eV}$ , and is in very good agreement with literature findings in both polar [182] and non-polar [105, 114] nitride QDs.

The temperature of the sample is then gradually increased, and the same measurements have been performed at a number of temperatures. At 200 K, both of the fine-structure components have undergone significant thermal quenching, but still remain resolvable. Data for even higher temperatures are not recorded for this particular QD, as the weaker component becomes too noisy for FSS evaluation. Despite the significantly broadened

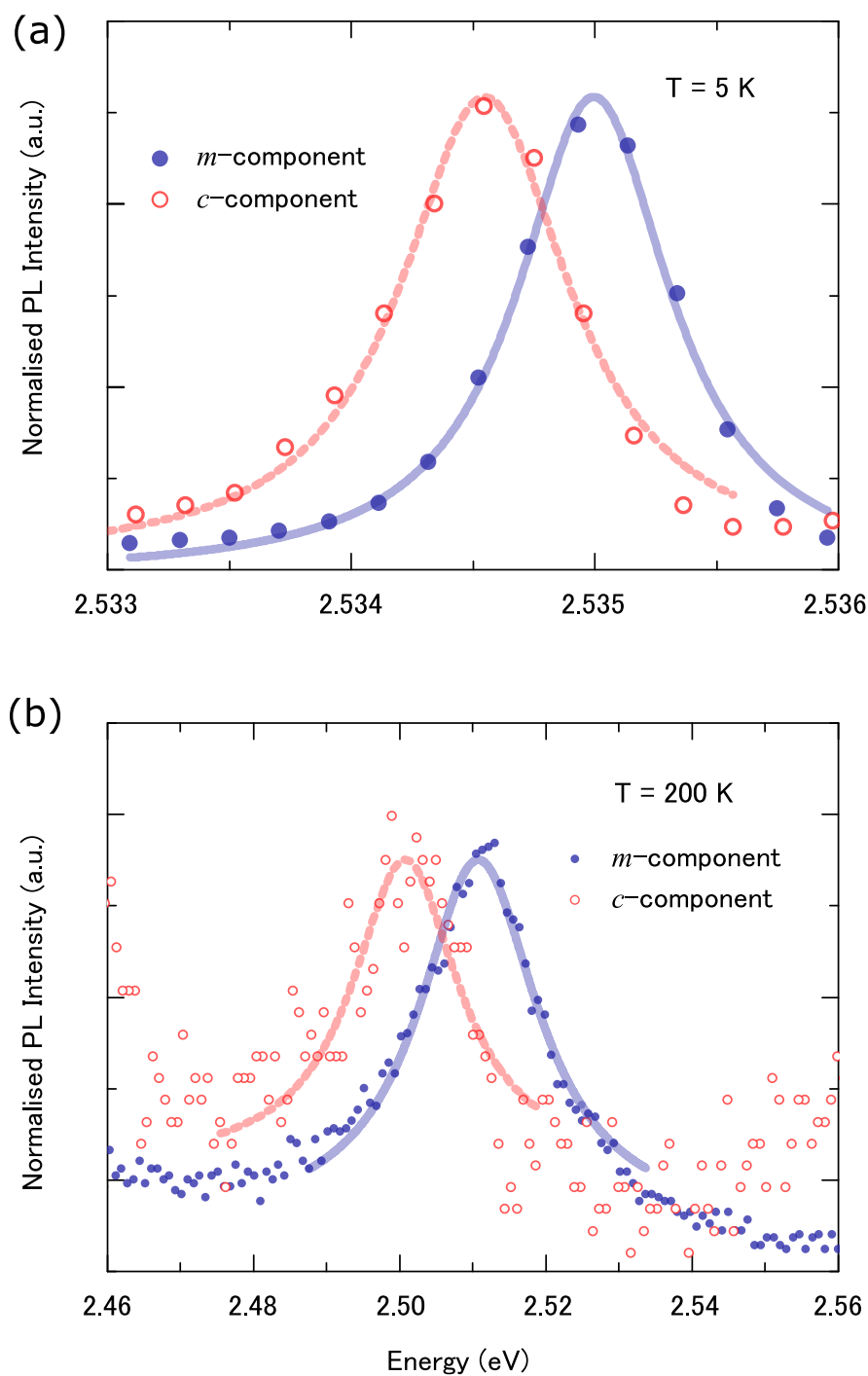


**Figure 5.14: Measurement of FSS at low and high temperatures for a Q2T  $a$ -plane InGaN QD.** (a) Cross-polarised components of the studied single QD at 5 K. The weaker component has been normalised by a factor of 8.34. (b). The same measurements and spectra at 200 K, displayed with a much larger horizontal energy scale. The weaker component has been normalised by 5.97.

## 5.8. TEMPERATURE-DEPENDENT FINE-STRUCTURE SPLITTING

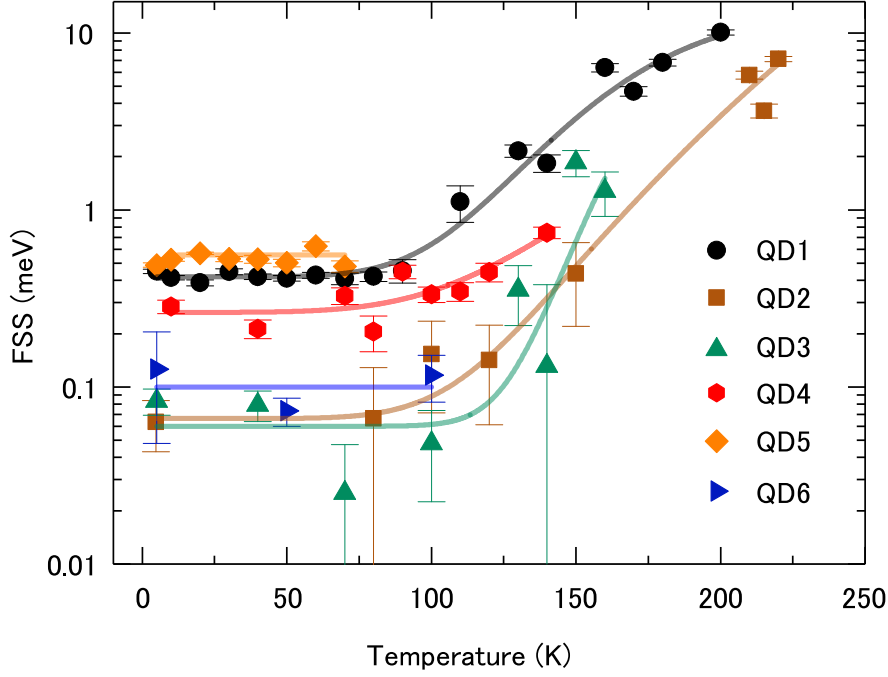


**Figure 5.15: Temperature-dependent FSS of *a*-plane InGaN QDs.** A total of 6 individual single QDs studied up to the highest temperature at which FSS can still be resolved. QD1 is the same as that shown in Figure 5.14. All 6 QDs show that the FSS remain constant at  $T < 100$  K. QD1–4 demonstrate quasi-linearly increasing FSS with temperature at  $T > 100$  K.

emission, it is possible to visually observe the decrease of the main component and rise of the weaker counterpart at a separate spectral location on the spectrometer interface, as the polariser is turned away from  $0^\circ$ . The polarisation degree has decreased from 0.79 to 0.71, as expected due to the stronger band mixing at higher temperatures explained in the last section. The peak emission energies of the *m*- and *c*-component have redshifted to  $2510.7 \pm 0.2$  and  $2500.7 \pm 0.6$  meV respectively. Due to the faster (slower) redshift of the *c*(*m*)-component, the FSS has been drastically increased to  $10.0 \pm 0.6$  meV. This FSS value at 200 K is the first such measurement of a semiconductor QD, and is an order of magnitude higher than the result obtained at 5 K.

Apart from this QD, similar behaviours have also been observed for a few other QDs studied. In order to examine the process of FSS increase, the splitting energies for these QDs at several temperature steps have been recorded and shown in Figure 5.15, where QD1 is the same QD studied in Figure 5.14. For all QDs, the FSS is recorded as far as the weaker fine-structure emission can still be accurately resolved. For QD1–6, the

## 5.8. TEMPERATURE-DEPENDENT FINE-STRUCTURE SPLITTING

highest FSS temperatures are 200, 220, 160, 140, 70 and 100 K respectively. Generally, it is observed that the FSS does not change significantly up to  $\sim 100$  K, but increases at temperatures higher than 100 K. The rate of increase is close to a linear one, and is different for each QD. In the case of QD1, this quasi-linear rate is  $150 \mu\text{eV}/\text{K}$ . The constancy of FSS at  $T < 100$  K is confirmed in all 6 QDs, and the increase at  $T > 100$  K is also confirmed by QD1–4. It is important to note that the large FSS is not simply increased slow-timescale spectral diffusion—the two cross-polarised peaks can indeed be observed at different spectral positions in real time as mentioned previously.

### 5.8.3 Statistical significance and phonon scattering

For greater statistical confirmation of this behaviour, multiple single QDs at each temperature has been studied and their FSS calculated. A total of 81 QDs were investigated at 5 K, and their results displayed in Figure 5.16(a). All FSS energies are found to lie within the range of  $100\text{--}900 \mu\text{eV}$ , again in agreement with findings in the literature [28, 105, 114, 182, 216]. A mean and standard deviation of  $443 \pm 132 \mu\text{eV}$  can be evaluated. The larger spread of values is attributed to the random differences in dimension, geometry and material composition in this self-assembled platform. Their impact on the spatial part of the exchange symmetry alters the FSS energies. Compared to arsenide systems [217, 218, 219, 220], these values are an order of magnitude greater, and exhibit no wavelength dependence. This missing correlation could be attributed to the greater complexity in the aforementioned nanostructure parameters of current *a*-plane InGaN QDs, all of which could contribute to the emission energy to different extents. Therefore, a correlation with FSS cannot be observed in the current system.

At 200 K, a total of 16 QDs have been studied and shown in Figure 5.16(b). The decreasing sample size is caused by significantly quenched emission of nanostructures, and a lack of suitable QD candidates at this temperature. The range of FSS is between 2 and 12 meV, confirming the previous finding that FSS energies at 200 K is an order of magnitude higher than those at 5 K. Similar to the situation at 5 K, no correlation with the exciton transition energy can be observed. One interesting observation is that these low-DOLP QDs are largely emitting below 2.6 eV, whereas the experimental upper limit in the 5 K case is

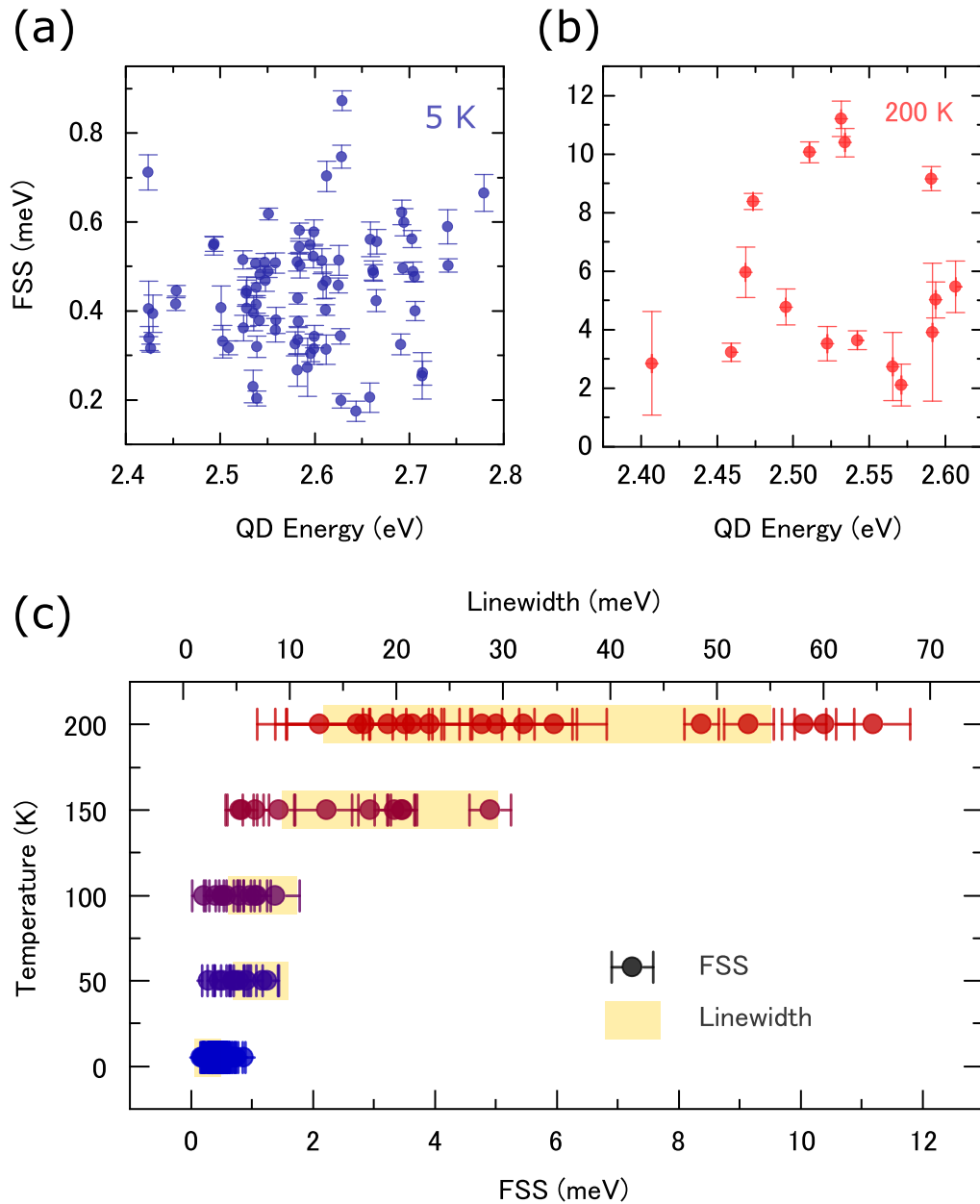


**Figure 5.16: Statistically significant temperature-dependent FSS measurement of *a*-plane InGaN QDs.** (a) FSS energies evaluated at 5 K for 81 individual QDs. No selection bias is present except ensuring resolvability of the weaker fine-structure component. No correlation with the exciton transition energy is found. (b) The same measurement at 200 K with 16 QDs. A global order-of-magnitude increase of FSS has been observed. (c) FSS of 10 additional QDs each at 50, 100, and 150 K. Also shown is the range of linewidths evaluated for the studied QDs. A qualitative correlation between phonon scattering strength and FSS can be established.

2.8 eV. A possible explanation is the presence of higher indium contents, *ceteris paribus*, which results in larger band offsets and greater quantum confinement, allowing for emission at conditions with higher thermal energy.

While the large FSS at 200 K has been confirmed experimentally, it is non-trivial to identify a theoretical foundation. Based on theoretical works [221] and recent studies in AlN nanostructures [222], it is possible that exciton-phonon interactions might affect the extent of exchange interactions. Hence, a scenario in which greater phonon interactions at higher temperatures alter the FSS of QDs is not unlikely. To accurately model the origin of these FSS differences and changes with temperature, theoretical studies involving configuration interaction, Fermi-Dirac statistics, QD geometry anisotropies, and phonon coupling would be required. Such a theoretical study is not currently feasible and well beyond the scope of this thesis. Notwithstanding, it is possible to experimentally verify the presence of a correlation between phonon scattering strength and FSS qualitatively.

Since the broadening of exciton transition linewidth is a measure of the degree of phonon coupling, their statistics can be compared against that of FSS at each temperature. 10 more QDs each at 50, 100, and 150 K have been investigated, and their results shown together with the statistics at 5 and 200 K in Figure 5.16(c). From the graph, it can be seen that the ranges of FSS are very close for  $T < 100$  K, but expand drastically at higher temperatures. This result confirms the finding in Figure 5.15. The ranges of linewidths for all the studied QDs at each temperature have also been evaluated and shown on top of the range of FSS energies. The ranges of linewidth and FSS overlap very well with each other, suggesting that a relationship between phonon interactions and FSS indeed exists in *a*-plane InGaN QDs.

## 5.9 Chapter summary

The contents of this chapter are arguably the most important milestones in the development of the *a*-plane InGaN QD platform. The key motivation for the initiation of this area of research is to explore possibilities in higher temperature regimes, thereby enabling future on-chip single-photon applications and fundamental semiconductor QD research that cannot be realised by other systems.

The concept of polarisation-controlled ultrafast single-photon generation has been demonstrated experimentally, with a  $g^{(2)}(0)$  of 0.47, radiative recombination lifetime of 357 ps, and a polarisation degree of 0.80 aligned to the crystal  $m$ -direction. The high-temperature polarisation properties are the key differentiating factor compared to other competing single-photon emitting systems, and have been confirmed with statistically significant results up to 200 K. These properties at high temperatures have also been investigated theoretically with our collaborators in Tyndall National Institute, concluding in a clear pathway forward in the development of nanostructures for realising robust and highly polarised room-temperature photon emitters.

Thanks to the temperature stability of  $a$ -plane InGaN QDs, it is now possible to investigate high-temperature photophysics of semiconductor QDs. The acoustic phonon scattering strength, as well as the depth of typical local carriers trapping sites, has been evaluated. Fine-structure splitting energies have been found to increase by an order of magnitude at 200 K. The onset of increase itself only happens at  $T > 100$  K, implying the presence of an unknown thermally activated process at this temperature. This is the first experimental observation of the temperature dependence of the FSS of semiconductor QDs. Experimental studies have found that this process has a positive correlation with the extent of phonon scattering, which increases at an accelerated pace at higher temperatures.

## 6

# Concluding remarks and outlook

The over-reliance on material defects and cryogenic temperatures has motivated the development of nitride-based wide band gap semiconductor quantum dots. In order to tackle current challenges in both reducing intrinsic nitride built-in fields and realising polarisation control, non-polar *a*-plane InGaN/GaN QDs can be employed using two of the available fabrication methods—MDE and Q2T. With a complete set of micro-photoluminescence studies of their optical properties, ultrafast polarisation-controlled single-photon generation has been demonstrated for the first time at 220 K ( $-53^\circ\text{C}$ ) in not only InGaN systems, but semiconductor QDs in general.

Although this is an initial development, several optical properties of *a*-plane InGaN/GaN QDs have been demonstrated with statistical significance and clarified with rigorous theoretical foundations, including the radiative recombination lifetime and optical polarisation at both low and high temperatures. Some of emission characteristics have now reached or exceeded state-of-the-art nitride developments. In particular, the radiative lifetimes of *a*-plane InGaN QDs have an average of  $< 200$  ps, and are faster than both ultra-small dot-in-nanowire GaN systems [97] and *m*-plane platforms [112] with theoretically weaker residual fields. The reduced average slow-timescale spectral diffusion of  $\sim 30 \mu\text{eV}$  is also amongst the smallest in the literature reports [189], making further investigations of linewidth, fine-structure splitting, and other related optical studies easier, more accurate and reliable.

The ability to observe optical properties in conditions with greater thermal energies

---

opens up the area of high-temperature photophysics for semiconductor QDs. Unexpected temperature-dependent behaviours, such as temperature-dependent FSS, need to be investigated for not only fundamental interests, but also the development of future on-chip quantum information applications. For instance, the accelerated increase of exciton transition linewidth poses greater challenges in realising applications in quantum computation. The large linewidth of all current nitride systems at both low and high temperatures, including the *a*-plane one detailed in this thesis, is one of the key limiting factors to conducting Hong-Ou-Mandel experiments [45] and achieving the emission of indistinguishable photons [46]. Overcoming this intrinsic material challenge is as crucial as achieving high-purity single-photon emission in paving the way for applications in nitride-based quantum information sciences.

Progress has been made in this area, where a characteristic spectral diffusion rate of  $\sim 20 \text{ ns}^{-1}$  has been found in GaN systems [135]. Although there are yet no effective methods to suppress the fast-timescale spectral diffusion, such measurements provides a better understanding of the nature of the scientific challenge. For this *a*-plane platform, identifying methods to further improve the sample quality is crucial, so that similar measurements can be attempted. At the same time, the minimisation of slow-timescale spectral diffusion, as pioneered by the *a*-plane system, has indeed moved the nitride platform a step closer to the generation of indistinguishable photons.

For single-photon purity, all successful ( $< 0.50$ ) HBT results have raw  $g^{(2)}(0)$  values  $> 0.3$ . A statistically significant study similar to those conducted for optical polarisation and radiative recombination lifetime is not yet possible, due to the much lower rate of successful HBT measurement. However, such statistics would be very important to gain more insights into the photophysics of single-photon emitting QDs, as well as directions to further advance this unique system. These will be possible with improved fabrication and ideally higher quality samples in the next phase of development. With the average brightness of QDs increased, it would also become possible to use excitation powers much lower than the QDs' saturation powers, thereby decreasing the relative QW intensity further. The small percentage of QDs polarised along the *c*-direction have the unique advantage of suppressed background QW emission, which is polarised orthogonal to the

---

QDs themselves. With further development to improve their emission properties and to control their growth, as well as the use of resonant excitation, these QDs could also be the key to achieving purer single-photon generation, a most crucial challenge in advancing the *a*-plane QD platform in the future.

In the case of intrinsic polarisation control, the *a*-plane system still has many areas of improvement. Based on the results presented in the thesis, an elongation along the *m*-direction would increase the DOLP until it reaches 1. With further forms of nanostructure engineering, such as masked etching to create *m*-elongated cuboids, there is potential to consistently produce DOLPs of 1 with minimal deviations, thus truly forgoing the need for external polarisers and bringing the external polarisation efficiency closer to 100%. Furthermore, such a design could also result in much better temperature stability of the polarisation properties. At the current stage, direct control of the QD geometry is not yet possible. However, it is worth noting that such concepts have already been proven in both asymmetric quantum dash formations [50] and polar nitride low-temperature single-photon emitters [150]. If the intrinsic polarisation properties of the *a*-plane material is combined with a desirable engineered anisotropy based on the findings in this thesis, it would be possible to achieve DOLPs close to unity at room temperature.

Indeed, the *a*-plane QD platform is still in its infancy, with planar epitaxial self-assembled samples and relatively poor emission characteristics compared to more mature nitride and non-nitride developments. Nonetheless, just like strongly emitting blue LEDs in the presence of significant threading dislocations, the optical properties of this “lucky” semiconductor are already rivalling more established systems. At the moment, electrically pumped single-photon sources with polarisation control has already been achieved with *a*-plane InGaN/GaN QDs [211], proving the advantage of device fabrication of a semiconductor QD platform. Combined with the ongoing progress in realising larger scale site-controlled samples, more sophisticated devices with electrical contacts on pillars, and the aforementioned nanostructure engineering, non-polar *a*-plane InGaN/GaN QDs have tremendous potential in leading the development of on-chip quantum information sciences.

# Bibliography

- [1] I. Aharonovich, D. Englund, and M. Toth, “Solid-state single-photon emitters,” *Nature Photonics* **10**, 631–641 (2016). 1
- [2] A. J. Shields, “Semiconductor quantum light sources,” *Nature Photonics* **1**, 215–223 (2007). 1, 4
- [3] B. Lounis and M. Orrit, “Single-photon sources,” *Reports on Progress in Physics* **68**, 1129–1179 (2005). 1, 4
- [4] N. Mizuochi, T. Makino, H. Kato, D. Takeuchi, M. Ogura, H. Okushi, M. Nothaft, P. Neumann, A. Gali, F. Jelezko, J. Wrachtrup, and S. Yamasaki, “Electrically driven single-photon source at room temperature in diamond,” *Nature Photonics* **6**, 299–303 (2012). 1, 7
- [5] X. He, N. F. Hartmann, X. Ma, Y. Kim, R. Ihly, J. L. Blackburn, W. Gao, J. Kono, Y. Yomogida, A. Hirano, T. Tanaka, H. Kataura, H. Htoon, and S. K. Doorn, “Tunable room-temperature single-photon emission at telecom wavelengths from sp<sup>3</sup> defects in carbon nanotubes,” *Nature Photonics* **11**, 577–582 (2017). 1, 7
- [6] T. T. Tran, K. Bray, M. J. Ford, M. Toth, and I. Aharonovich, “Quantum emission from hexagonal boron nitride monolayers,” *Nature Nanotechnology* **11**, 37–41 (2016). 1, 8
- [7] S. Castelletto, B. C. Johnson, V. Ivády, N. Stavrias, T. Umeda, A. Gali, and T. Ohshima, “A silicon carbide room-temperature single-photon source,” *Nature Materials* **13**, 151–156 (2013). 1, 7

- [8] A. M. Berhane, K.-Y. Jeong, Z. Bodrog, S. Fiedler, T. Schröder, N. V. Triviño, T. Palacios, A. Gali, M. Toth, D. Englund, and I. Aharonovich, “Bright Room-Temperature Single Photon Emission from Defects in Gallium Nitride,” *Advanced Materials* **29**, 1605092 (2017). 1, 8
- [9] S. Choi and I. Aharonovich, “Zinc Oxide Nanophotonics,” *Nanophotonics* **4**, 437–458 (2015). 1, 7
- [10] S. Buckley, K. Rivoire, and J. Vučković, “Engineered quantum dot single-photon sources,” *Reports on Progress in Physics* **75**, 126503 (2012). 1, 4, 6, 8
- [11] C. Santori, M. Pelton, G. Solomon, Y. Dale, and Y. Yamamoto, “Triggered Single Photons from a Quantum Dot,” *Physical Review Letters* **86**, 1502 (2001). 1
- [12] P. Michler, A. Kiraz, C. Becher, W. V. Schoenfeld, P. M. Petroff, L. Zhang, E. Hu, and A. Imamolu, “A Quantum Dot Single-Photon Turnstile Device,” *Science* **290**, 2282–2285 (2000). 1
- [13] N. Somaschi, V. Giesz, L. De Santis, J. C. Loredó, M. P. Almeida, G. Hornecker, S. L. Portalupi, T. Grange, C. Antón, J. Demory, C. Gómez, I. Sagnes, N. D. Lanzillotti-Kimura, A. Lemaître, A. Auffeves, A. G. White, L. Lanco, and P. Senellart, “Near-optimal single-photon sources in the solid state,” *Nature Photonics* **10**, 340–345 (2016). 1
- [14] X. Ding, Y. He, Z.-C. Duan, N. Gregersen, M.-C. Chen, S. Unsleber, S. Maier, C. Schneider, M. Kamp, S. Höfling, C.-Y. Lu, and J.-W. Pan, “On-Demand Single Photons with High Extraction Efficiency and Near-Unity Indistinguishability from a Resonantly Driven Quantum Dot in a Micropillar,” *Physical Review Letters* **116**, 020401 (2016). 1
- [15] M. Gschrey, A. Thoma, P. Schnauber, M. Seifried, R. Schmidt, B. Wohlfeil, L. Krüger, J.-H. Schulze, T. Heindel, S. Burger, F. Schmidt, A. Strittmatter, S. Rodt, and S. Reitzenstein, “Highly indistinguishable photons from deterministic quantum-dot microlenses utilizing three-dimensional in situ electron-beam lithography.” *Nature communications* **6**, 7662 (2015). 1

- 
- [16] Y.-J. Wei, Y.-M. He, M.-C. Chen, Y.-N. Hu, Y. He, D. Wu, C. Schneider, M. Kamp, S. Höfling, C.-Y. Lu, and J.-W. Pan, “Deterministic and Robust Generation of Single Photons from a Single Quantum Dot with 99.5% Indistinguishability Using Rapid Adiabatic Passage,” *Nano Letters* **14**, 6515–6519 (2014). 1
- [17] K. H. Madsen, S. Ates, J. Liu, A. Javadi, S. M. Albrecht, I. Yeo, S. Stobbe, and P. Lodahl, “Efficient out-coupling of high-purity single photons from a coherent quantum dot in a photonic-crystal cavity,” *Physical Review B* **90**, 155303 (2014). 1
- [18] O. Gazzano, S. Michaelis de Vasconcellos, C. Arnold, A. Nowak, E. Galopin, I. Sagnes, L. Lanco, A. Lemaître, and P. Senellart, “Bright solid-state sources of indistinguishable single photons,” *Nature communications* **4**, 1425 (2013). 1
- [19] Y.-M. He, Y. He, Y.-J. Wei, D. Wu, M. Atatüre, C. Schneider, S. Höfling, M. Kamp, C.-Y. Lu, and J.-W. Pan, “On-demand semiconductor single-photon source with near-unity indistinguishability,” *Nature Nanotechnology* **8**, 213–217 (2013). 1
- [20] J. Claudon, J. Bleuse, N. S. Malik, M. Bazin, P. Jaffrennou, N. Gregersen, C. Sauvan, P. Lalanne, and J.-M. Gérard, “A highly efficient single-photon source based on a quantum dot in a photonic nanowire,” *Nature Photonics* **4**, 174–177 (2010). 1
- [21] R. Hafenbrak, S. M. Ulrich, P. Michler, L. Wang, A. Rastelli, and O. G. Schmidt, “Triggered polarization-entangled photon pairs from a single quantum dot up to 30 K,” *New Journal of Physics* **9**, 315 (2007). 1
- [22] T. Zhu, F. Oehler, B. P. L. Reid, R. M. Emery, R. A. Taylor, M. J. Kappers, and R. A. Oliver, “Non-polar (11-20) InGaN quantum dots with short exciton lifetimes grown by metalorganic vapor phase epitaxy,” *Applied Physics Letters* **102**, 251905 (2013). 1, 2, 9, 13, 14, 16, 17, 20, 39, 55
- [23] Q. Guo and A. Yoshida, “Temperature Dependence of Band Gap Change in InN and AlN,” *Japanese Journal of Applied Physics* **33**, 2453–2456 (1994). 1, 9
- [24] T. Wang, T. J. Puchtler, S. K. Patra, T. Zhu, M. Ali, T. J. Badcock, T. Ding, R. A. Oliver, S. Schulz, and R. A. Taylor, “Direct generation of linearly polarized single

- photons with a deterministic axis in quantum dots,” *Nanophotonics* **6**, 1175–1183 (2017). 2, 12, 14, 21, 39, 42
- [25] T. Wang, T. J. Puchtler, T. Zhu, J. C. Jarman, L. P. Nuttall, R. A. Oliver, and R. A. Taylor, “Polarisation-controlled single photon emission at high temperatures from InGaN quantum dots,” *Nanoscale* **9**, 9421–9427 (2017). 2, 3, 28, 39, 70, 92, 98, 106, 109, 113, 120, 125
- [26] T. Wang, T. J. Puchtler, S. K. Patra, T. Zhu, J. C. Jarman, R. A. Oliver, S. Schulz, and R. A. Taylor, “Deterministic optical polarisation in nitride quantum dots at thermoelectrically cooled temperatures,” *Scientific Reports* **7**, 12067 (2017). 2, 3, 12, 14, 39, 113, 132
- [27] T. Wang, T. J. Puchtler, T. Zhu, J. C. Jarman, R. A. Oliver, and R. A. Taylor, “High-temperature performance of non-polar (11-20) InGaN quantum dots grown by a quasi-two-temperature method,” *Physica Status Solidi B* **254**, 1600724 (2017). 2, 10, 16, 17, 18, 39, 96, 98, 113
- [28] T. Wang, T. J. Puchtler, T. Zhu, J. C. Jarman, C. C. Kocher, R. A. Oliver, and R. A. Taylor, “Temperature-dependent fine structure splitting in InGaN quantum dots,” *Applied Physics Letters* **111**, 053101 (2017). 2, 3, 39, 81, 113, 134, 138
- [29] A. F. Jarjour, R. A. Oliver, and R. A. Taylor, “Nitride-based quantum dots for single photon source applications,” *Physica Status Solidi A* **206**, 2510–2523 (2009). 4
- [30] M. Fox, *Quantum Optics: An Introduction* (Oxford University Press, 2006), 1st ed. 4, 5
- [31] R. Hanbury Brown and R. Q. Twiss, “Correlation between Photons in two Coherent Beams of Light,” *Nature* **177**, 27–29 (1956). 4
- [32] A. Beveratos, R. Brouri, T. Gacoin, A. Villing, J.-P. Poizat, and P. Grangier, “Single Photon Quantum Cryptography,” *Physical Review Letters* **89**, 187901 (2002). 6
- [33] G. Brassard, D. Chaum, and C. Crépeau, “Minimum Disclosure Proofs of Knowledge,” *Journal of Computer and System Sciences* **37**, 156–189 (1988). 6

- [34] A. Muller, J. Breguet, and N. Gisin, “Experimental Demonstration of Quantum Cryptography Using Polarized Photons in Optical Fiber over More than 1 km,” *Europhys. Lett.* **23**, 383–388 (1993). 6
- [35] C. Kurtsiefer, P. Zarda, M. Halder, H. Weinfurter, P. M. Gorman, P. R. Tapster, and J. G. Rarity, “Quantum cryptography: A step towards global key distribution.” *Nature* **419**, 450 (2002). 6
- [36] C.-Z. Peng, T. Yang, X.-H. Bao, J. Zhang, X.-M. Jin, F.-Y. Feng, B. Yang, J. Yang, J. Yin, Q. Zhang, N. Li, B.-L. Tian, and J.-W. Pan, “Experimental Free-Space Distribution of Entangled Photon Pairs Over 13 km: Towards Satellite-Based Global Quantum Communication,” *Physical Review Letters* **94**, 150501 (2005). 6
- [37] A. Ourjoumtsev, R. Tualle-Brouri, J. Laurat, and P. Grangier, “Generating Optical Schrödinger Kittens for Quantum Information Processing,” *Science* **312**, 83–86 (2006). 6
- [38] H. Takesue, S. W. Nam, Q. Zhang, R. H. Hadfield, T. Honjo, K. Tamaki, and Y. Yamamoto, “Quantum key distribution over a 40-dB channel loss using superconducting single-photon detectors,” *Nature Photonics* **1**, 343–348 (2007). 6
- [39] S.-K. Liao, H.-L. Yong, C. Liu, G.-L. Shentu, D.-D. Li, J. Lin, H. Dai, S.-Q. Zhao, B. Li, J.-Y. Guan, W. Chen, Y.-H. Gong, Y. Li, Z.-H. Lin, G.-S. Pan, J. S. Pelc, M. M. Fejer, W.-Z. Zhang, W.-Y. Liu, J. Yin, J.-G. Ren, X.-B. Wang, Q. Zhang, C.-Z. Peng, and J.-W. Pan, “Long-distance free-space quantum key distribution in daylight towards inter-satellite communication,” *Nature Photonics* **11**, 509–514 (2017). 6
- [40] D. Loss and D. P. DiVincenzo, “Quantum computation with quantum dots,” *Physical Review A* **57**, 120 (1998). 7
- [41] C. H. Bennett and D. P. DiVincenzo, “Quantum Information and Computation,” *Nature* **404**, 247–255 (2000). 7

- 
- [42] S. Chen, Y.-A. Chen, T. Strassel, Z.-S. Yuan, B. Zhao, J. Schmiedmayer, and J.-W. Pan, “Deterministic and Storable Single-Photon Source Based on a Quantum Memory,” *Physical Review Letters* **97**, 173004 (2006). 7
- [43] J. L. O’Brien, “Optical Quantum Computing,” *Science* **318**, 1567–1570 (2007). 7
- [44] H. Wang, Y. He, Y.-H. Li, Z.-E. Su, B. Li, H.-L. Huang, X. Ding, M.-C. Chen, C. Liu, J. Qin, J.-P. Li, Y.-M. He, C. Schneider, M. Kamp, C.-Z. Peng, S. Höfling, C.-Y. Lu, and J.-W. Pan, “High-efficiency multiphoton boson sampling,” *Nature Photonics* **11**, 361–365 (2017). 7
- [45] C. K. Hong, Z. Y. Ou, and L. Mandel, “Measurement of Subpicosecond Time Intervals between Two Photons by Interference,” *Physical Review Letters* **59**, 2044 (1987). 7, 143
- [46] C. Santori, D. Fattal, J. Vučković, G. S. Solomon, and Y. Yamamoto, “Indistinguishable photons from a single-photon device.” *Nature* **419**, 594–597 (2002). 7, 143
- [47] M. J. Stevens, R. H. Hadfield, R. E. Schwall, S. W. Nam, and R. P. Mirin, “Quantum Dot Single Photon Sources Studied with Superconducting Single Photon Detectors,” *IEEE Journal of Selected Topics in Quantum Electronics* **12**, 1255–1268 (2006). 7
- [48] S. Strauf, N. G. Stoltz, M. T. Rakher, L. A. Coldren, P. M. Petroff, and D. Bouwmeester, “High-frequency single-photon source with polarization control,” *Nature Photonics* **1**, 704–708 (2007). 7, 40
- [49] D. C. Unitt, A. J. Bennett, P. Atkinson, D. A. Ritchie, and A. J. Shields, “Polarization control of quantum dot single-photon sources via a dipole-dependent Purcell effect,” *Physical Review B* **72**, 033318 (2005). 7, 40
- [50] F. Besahraoui, M. Bouslama, F. Saidi, L. Bouzaiene, M. H. Hadj Alouane, H. Maaref, N. Chauvin, M. Gendry, Z. Lounis, and M. Ghaffour, “Optical investigation of InAs quantum dashes grown on InP(001) vicinal substrate,” *Superlattices and Microstructures* **65**, 264–270 (2014). 7, 40, 144

- [51] I. Favero, G. Cassabois, A. Jankovic, R. Ferreira, D. Darson, C. Voisin, C. Delalande, P. Roussignol, A. Badolato, P. M. Petroff, and J. M. Gérard, “Giant optical anisotropy in a single InAs quantum dot in a very dilute quantum-dot ensemble,” *Applied Physics Letters* **86**, 041904 (2005). 7, 40
- [52] M. Munsch, J. Claudon, J. Bleuse, N. S. Malik, E. Dupuy, J.-M. Gérard, Y. Chen, N. Gregersen, and J. Mørk, “Linearly Polarized, Single-Mode Spontaneous Emission in a Photonic Nanowire,” *Physical Review Letters* **108**, 077405 (2012). 7, 40
- [53] P. Mrowiński, K. Tarnowski, J. Olszewski, A. Somers, M. Kamp, J. P. Reithmaier, W. Urbanczyk, J. Misiewicz, P. Machnikowski, and G. Sęk, “Tailoring the photoluminescence polarization anisotropy of a single InAs quantum dash by a post-growth modification of its dielectric environment,” *Journal of Applied Physics* **120**, 074303 (2016). 7, 40
- [54] R. Brouri, A. Beveratos, J.-P. Poizat, and P. Grangier, “Photon antibunching in the fluorescence of individual color centers in diamond,” *Optics Letters* **25**, 1294 (2000). 7, 66, 67
- [55] I. Aharonovich and E. Neu, “Diamond Nanophotonics,” *Advanced Optical Materials* **2**, 911–928 (2014). 7
- [56] T. M. Babinec, B. J. M. Hausmann, M. Khan, Y. Zhang, J. R. Maze, P. R. Hemmer, and M. Lončar, “A diamond nanowire single-photon source,” *Nature nanotechnology* **5**, 195–199 (2010). 7
- [57] A. Lohrmann, N. Iwamoto, Z. Bodrog, S. Castelletto, T. Ohshima, T. J. Karle, A. Gali, S. Praver, J. C. McCallum, and B. C. Johnson, “Single-photon emitting diode in silicon carbide,” *Nature Communications* **6**, 7783 (2015). 7
- [58] A. J. Morfa, B. C. Gibson, M. Karg, T. J. Karle, A. D. Greentree, P. Mulvaney, and S. Tomljenovic-Hanic, “Single-Photon Emission and Quantum Characterization of Zinc Oxide Defects,” *Nano Letters* **12**, 949–954 (2012). 7

- 
- [59] V. A. Fonoberov and A. A. Balandin, “Origin of ultraviolet photoluminescence in ZnO quantum dots: Confined excitons versus surface-bound impurity exciton complexes,” *Applied Physics Letters* **85**, 5971 (2004). 7
- [60] X. Ma, N. F. Hartmann, J. K. S. Baldwin, S. K. Doorn, and H. Htoon, “Room-temperature single-photon generation from solitary dopants of carbon nanotubes,” *Nature Nanotechnology* **10**, 671–675 (2015). 7
- [61] Y.-S. Park, S. Guo, N. S. Makarov, and V. I. Klimov, “Room Temperature Single-Photon Emission from Individual Perovskite Quantum Dots,” *ACS Nano* **9**, 10386–10393 (2015). 8
- [62] A. M. Berhane, C. Bradac, and I. Aharonovich, “Photo-induced blinking in a solid state quantum system,” *Physical Review B* **96**, 041203 (2017). 8, 25
- [63] Y. Zhou, Z. Wang, A. Rasmita, S. Kim, A. Berhane, Z. Bodrog, G. Adamo, A. Gali, I. Aharonovich, and W.-B. Gao, “Room temperature solid-state quantum emitters in the telecom range,” *Sci. Adv* **4**, eaar3580 (2018). 8
- [64] M. Kianinia, B. Regan, S. A. Tawfik, T. T. Tran, M. J. Ford, I. Aharonovich, and M. Toth, “Robust Solid-State Quantum System Operating at 800 K,” *ACS Photonics* **4**, 768–773 (2017). 8
- [65] M. Bommer, W.-M. Schulz, R. Roßbach, M. Jetter, P. Michler, T. Thomay, A. Leitnerstorfer, and R. Bratschitsch, “Triggered single-photon emission in the red spectral range from optically excited InP/(Al,Ga)InP quantum dots embedded in micropillars up to 100 K,” *Journal of Applied Physics* **110**, 063108 (2011). 8, 106
- [66] T. Braun, S. Unsleber, V. Baumann, M. Gschrey, S. Rodt, S. Reitzenstein, C. Schneider, S. Höfling, and M. Kamp, “Cascaded emission of linearly polarized single photons from positioned InP/GaInP quantum dots,” *Applied Physics Letters* **103**, 191113 (2013). 8
- [67] M. E. Reimer, G. Bulgarini, N. Akopian, M. Hocevar, M. B. Bavinck, M. A. Verheijen, E. P. A. M. Bakkers, L. P. Kouwenhoven, and V. Zwiller, “Bright single-photon sources in bottom-up tailored nanowires,” *Nature Commun.* **3**, 737 (2012). 8

- 
- [68] M. H. M. van Weert, N. Akopian, F. Kelkensberg, U. Perinetti, M. P. van Kouwen, J. G. Rivas, M. T. Borgström, R. E. Algra, M. A. Verheijen, E. P. A. M. Bakkers, L. P. Kouwenhoven, and V. Zwiller, “Orientation-Dependent Optical-Polarization Properties of Single Quantum Dots in Nanowires,” *Small* **5**, 2134–2138 (2009). 8
- [69] S. Bounouar, M. Elouneg-Jamroz, M. den Hertog, C. Morchutt, E. Bellet-Amalric, R. André, C. Bougerol, Y. Genuist, J.-P. Poizat, S. Tatarenko, and K. Kheng, “Ultrafast Room Temperature Single-Photon Source from Nanowire-Quantum Dots,” *Nano Letters* **12**, 2977–2981 (2012). 8, 108, 123, 125
- [70] O. Fedorych, C. Kruse, A. Ruban, D. Hommel, G. Bacher, and T. Kummell, “Room temperature single photon emission from an epitaxially grown quantum dot,” *Applied Physics Letters* **100**, 061114 (2012). 8
- [71] A. Tribu, G. Sallen, T. Aichele, R. André, J.-P. Poizat, C. Bougerol, S. Tatarenko, and K. Kheng, “A High-Temperature Single-Photon Source from Nanowire Quantum Dots,” *Nano Letters* **8**, 4326–4329 (2008). 8
- [72] M. J. Holmes, M. Arita, and Y. Arakawa, “III-nitride quantum dots as single photon emitters,” *Semiconductor Science and Technology* **34**, 033001 (2019). 8, 9
- [73] T. Zhu and R. A. Oliver, “Nitride quantum light sources,” *EPL* **113**, 38001 (2016). 8, 11
- [74] A. F. Jarjour, R. A. Oliver, and R. A. Taylor, “Progress in the optical studies of single InGaN/GaN quantum dots,” *Philosophical Magazine* **87**, 2077–2093 (2007). 8, 9
- [75] Y. Arakawa and S. Kako, “Advances in growth and optical properties of GaN-based quantum dots,” *Physica Status Solidi A* **203**, 3512–3522 (2006). 8, 9
- [76] H. J. Kimble, M. Dagenais, and L. Mandel, “Photon Antibunching in Resonance Fluorescence,” *Physical Review Letters* **39**, 691 (1977). 8
- [77] A. Kuhn, M. Hennrich, T. Bondo, and G. Rempe, “Controlled generation of single photons from a strongly coupled atom-cavity system,” *Applied Physics B* **69**, 373–377 (1999). 8

- [78] A. Kuhn, M. Hennrich, and G. Rempe, “Deterministic Single-Photon Source for Distributed Quantum Networking,” *Physical review letters* **89**, 067901 (2002). 8
- [79] B. Lounis and W. E. Moerner, “Single photons on demand from a single molecule at room temperature,” *Nature* **407**, 491–493 (2000). 8
- [80] B. Monemar, “Fundamental energy gap of GaN from photoluminescence excitation spectra,” *Physical Review B* **10**, 676–681 (1974). 9
- [81] K. Reimann, M. Steube, D. Fröhlich, and S. J. Clarke, “Exciton binding energies and band gaps in GaN bulk crystals,” *Journal of Crystal Growth* **189-190**, 652–655 (1998). 9
- [82] I. Vurgaftman and J. R. Meyer, “Band parameters for nitrogen-containing semiconductors,” *Journal of Applied Physics* **94**, 3675 (2003). 9
- [83] S. Nakamura, T. Mukai, and M. Senoh, “Candela-class high-brightness In-GaN/AlGaIn double-heterostructure blue-light-emitting diodes,” *Applied Physics Letters* **64**, 1687–1689 (1994). 9
- [84] S. Amloy, E. S. Moskalenko, M. Eriksson, K. F. Karlsson, Y. T. Chen, K. H. Chen, H. C. Hsu, C. L. Hsiao, L. C. Chen, and P. O. Holtz, “Dynamic characteristics of the exciton and the biexciton in a single InGaIn quantum dot,” *Applied Physics Letters* **101**, 061910 (2012). 9
- [85] O. Moriwaki, T. Someya, K. Tachibana, S. Ishida, and Y. Arakawa, “Narrow photoluminescence peaks from localized states in InGaIn quantum dot structures,” *Applied Physics Letters* **76**, 2361–2363 (2000). 9
- [86] A. F. Jarjour, R. A. Taylor, R. A. Oliver, M. J. Kappers, C. J. Humphreys, and A. Tahraoui, “Cavity-enhanced blue single-photon emission from a single In-GaN/GaN quantum dot,” *Applied Physics Letters* **91**, 052101 (2007). 9
- [87] S. Kako, C. Santori, K. Hoshino, S. Götzinger, Y. Yamamoto, and Y. Arakawa, “A gallium nitride single-photon source operating at 200 K,” *Nature materials* **5**, 887–892 (2006). 9, 92, 101, 116

- 
- [88] R. Arians, A. Gust, T. KÜmmell, C. Kruse, S. Zaitsev, G. Bacher, and D. Hommel, “Electrically driven single quantum dot emitter operating at room temperature,” *Applied Physics Letters* **93**, 173506 (2008). 9
- [89] B. Daudin, “Polar and nonpolar GaN quantum dots,” *Journal of Physics: Condensed Matter* **20**, 473201 (2008). 9, 13
- [90] F. Rol, B. Gayral, S. Founta, B. Daudin, J. Eymery, J.-M. Gérard, H. Mariette, L. S. Dang, and D. Peyrade, “Optical properties of single non-polar GaN quantum dots,” *Physica Status Solidi (B) Basic Research* **243**, 1652–1656 (2006). 9
- [91] P. Bhattacharya, S. Deshpande, T. Frost, and A. Hazari, “III-Nitride high temperature single-photon sources,” *Proc. SPIE* **9382**, 938207 (2015). 9
- [92] J.-H. Kim, Y.-H. Ko, S.-H. Gong, S.-M. Ko, and Y.-H. Cho, “Ultrafast single photon emitting quantum photonic structures based on a nano-obelisk.” *Scientific Reports* **3**, 2150 (2013). 9
- [93] E. Chernysheva, Ž. Gačević, N. García-Lepetit, H. P. van der Meulen, M. Müller, F. Bertram, P. Veit, A. Torres-Pardo, J. M. González Calbet, J. Christen, E. Calleja, J. M. Calleja, and S. Lazić, “Blue-to-green single photons from InGaN/GaN dot-in-a-nanowire ordered arrays,” *EPL* **111**, 24001 (2015). 9
- [94] S.-H. Gong, J.-H. Kim, Y.-H. Ko, C. Rodriguez, J. Shin, Y.-H. Lee, L. S. Dang, X. Zhang, and Y.-H. Cho, “Self-aligned deterministic coupling of single quantum emitter to nanofocused plasmonic modes,” *PNAS* **112**, 5280–5285 (2015). 9
- [95] J.-H. Cho, Y. M. Kim, S.-H. Lim, H.-S. Yeo, S. Kim, S. Gong, and Y.-H. Cho, “Strongly coherent single photon emission from site-controlled InGaN quantum dots embedded in GaN nano-pyramids,” *ACS Photonics* **5**, 439–444 (2017). 9
- [96] L. Zhang, C.-H. Teng, P.-C. Ku, and H. Deng, “Site-controlled InGaN/GaN single-photon-emitting diode,” *Applied Physics Letters* **108**, 153102 (2016). 9, 37
- [97] M. J. Holmes, K. Choi, S. Kako, M. Arita, and Y. Arakawa, “Room-Temperature Triggered Single Photon Emission from a III-Nitride Site-Controlled Nanowire Quantum Dot,” *Nano Letters* **14**, 982–986 (2014). 9, 23, 70, 91, 103, 109, 120, 142

- 
- [98] M. J. Holmes, S. Kako, K. Choi, P. Podemski, M. Arita, and Y. Arakawa, “Probing the Excitonic States of Site-Controlled GaN Nanowire Quantum Dots,” *Nano Letters* **15**, 1047–1051 (2015). 9
- [99] M. J. Holmes, S. Kako, K. Choi, M. Arita, and Y. Arakawa, “Single Photons from a Hot Solid-State Emitter at 350 K,” *ACS Photonics* **3**, 543–546 (2016). 9, 23, 66, 67, 92, 98, 101, 103, 109, 113, 116, 119, 125
- [100] R. H. Hadfield, “Single-photon detectors for optical quantum information applications,” *Nature Photonics* **3**, 696–705 (2009). 10, 33
- [101] V. A. Fonoberov and A. A. Balandin, “Excitonic properties of strained wurtzite and zinc-blende GaN/Al<sub>x</sub>Ga<sub>1-x</sub>N quantum dots,” *Journal of Applied Physics* **94**, 7178 (2003). 10
- [102] S. Sergent, S. Kako, M. Bürger, T. Schupp, D. J. As, and Y. Arakawa, “Polarization properties of single zinc-blende GaN/AlN quantum dots,” *Physical Review B* **90**, 235312 (2014). 10
- [103] S. Kako, M. Holmes, S. Sergent, M. Bürger, D. J. As, and Y. Arakawa, “Single-photon emission from cubic GaN quantum dots,” *Applied Physics Letters* **104**, 011101 (2014). 10, 13, 55
- [104] A. F. Jarjour, R. A. Oliver, A. Tahraoui, M. J. Kappers, C. J. Humphreys, and R. A. Taylor, “Control of the Oscillator Strength of the Exciton in a Single InGaN-GaN Quantum Dot,” *Physical Review Letters* **99**, 197403 (2007). 11, 52, 53
- [105] B. P. L. Reid, “Towards cavity quantum electrodynamics and coherent control with single InGaN/GaN quantum dots,” Ph.D. thesis (2013). 12, 25, 52, 134, 135, 138
- [106] I. A. Ostapenko, G. Hönig, C. Kindel, S. Rodt, A. Strittmatter, A. Hoffmann, and D. Bimberg, “Large internal dipole moment in InGaN/GaN quantum dots,” *Applied Physics Letters* **97**, 063103 (2010). 12
- [107] J. W. Robinson, J. H. Rice, K. H. Lee, J. H. Na, R. A. Taylor, D. G. Hasko, R. A. Oliver, M. J. Kappers, C. J. Humphreys, and G. A. D. Briggs, “Quantum-confined

- Stark effect in a single InGaN quantum dot under a lateral electric field,” *Applied Physics Letters* **86**, 213103 (2005). 12
- [108] J.-J. Shi and Z. Z. Gan, “Effects of piezoelectricity and spontaneous polarization on localized excitons in self-formed InGaN quantum dots,” *Journal of Applied Physics* **94**, 407 (2003). 12
- [109] M. Winkelkemper, R. Seguin, S. Rodt, A. Schliwa, L. Reißmann, A. Strittmatter, A. Hoffmann, and D. Bimberg, “Polarized emission lines from A- and B-type excitonic complexes in single InGaN/GaN quantum dots,” *Journal of Applied Physics* **101**, 113708 (2007). 12
- [110] R. M. Emery, T. Zhu, F. Oehler, B. Reid, R. A. Taylor, M. J. Kappers, and R. A. Oliver, “Non-polar (11-20) InGaN quantum dots with short exciton lifetimes grown by metal-organic vapour phase epitaxy,” *Physica Status Solidi C* **11**, 698–701 (2014). 13, 14, 16, 17
- [111] S. Founta, F. Rol, E. Bellet-Amalric, E. Sarigiannidou, B. Gayral, C. Moisson, H. Mariette, and B. Daudin, “Growth of GaN quantum dots on nonpolar *a*-plane SiC by molecular-beam epitaxy,” *Physica Status Solidi B* **243**, 3968–3971 (2006). 13
- [112] T. J. Puchtler, T. Wang, C. X. Ren, F. Tang, R. A. Oliver, R. A. Taylor, and T. Zhu, “Ultrafast, Polarized, Single-Photon Emission from *m*-plane InGaN Quantum Dots on GaN Nanowires,” *Nano Letters* **16**, 7779–7785 (2016). 13, 14, 37, 38, 46, 55, 66, 67, 70, 91, 106, 107, 111, 113, 142
- [113] Ž. Gačević, M. Holmes, E. Chernysheva, M. Müller, A. Torres-Pardo, P. Veit, F. Bertram, J. Christen, J. M. González Calbet, Y. Arakawa, E. Calleja, and S. Lazić, “Emission of Linearly Polarized Single Photons from Quantum Dots Contained in Nonpolar, Semipolar and Polar Sections of Pencil-Like InGaN/GaN Nanowires,” *ACS Photonics* **4**, 657–664 (2017). 13, 37, 38, 66, 67

- 
- [114] B. P. L. Reid, C. Kocher, T. Zhu, F. Oehler, C. C. S. Chan, R. A. Oliver, and R. A. Taylor, “Non-polar InGaN quantum dot emission with crystal-axis oriented linear polarization,” *Applied Physics Letters* **106**, 171108 (2015). 14, 39, 134, 135, 138
- [115] S. Schulz, D. P. Tanner, E. P. O’Reilly, M. A. Caro, T. L. Martin, P. A. J. Bagot, M. P. Moody, F. Tang, J. T. Griffiths, F. Oehler, M. J. Kappers, R. A. Oliver, C. J. Humphreys, D. Sutherland, M. J. Davies, and P. Dawson, “Structural, electronic, and optical properties of *m*-plane InGaN/GaN quantum wells: Insights from experiment and atomistic theory,” *Physical Review B* **92**, 235419 (2015). 14, 38
- [116] D. Kundys, D. Sutherland, M. J. Davies, F. Oehler, J. Griffiths, P. Dawson, M. J. Kappers, C. J. Humphreys, S. Schulz, F. Tang, and R. A. Oliver, “A study of the optical and polarisation properties of InGaN/GaN multiple quantum wells grown on *a*-plane and *m*-plane GaN substrates,” *Science and Technology of Advanced Materials* **17**, 736–743 (2016). 14, 38, 50
- [117] Y. Yu, X.-M. Dou, B. Wei, G.-W. Zha, X.-J. Shang, L. Wang, D. Su, J.-X. Xu, H.-Y. Wang, H.-Q. Ni, B.-Q. Sun, Y. Ji, X.-D. Han, and Z.-C. Niu, “Self-Assembled Quantum Dot Structures in a Hexagonal Nanowire for Quantum Photonics,” *Advanced Materials* **26**, 2710–2717 (2014). 14
- [118] R. A. Oliver, G. A. D. Briggs, M. J. Kappers, C. J. Humphreys, S. Yasin, J. H. Rice, J. D. Smith, and R. A. Taylor, “InGaN quantum dots grown by metalorganic vapor phase epitaxy employing a post-growth nitrogen anneal,” *Applied Physics Letters* **83**, 755–757 (2003). 17, 19
- [119] T. Zhu, H. A. R. El-Ella, B. Reid, M. J. Holmes, R. A. Taylor, M. J. Kappers, and R. A. Oliver, “Growth and optical characterisation of multilayers of InGaN quantum dots,” *Journal of Crystal Growth* **338**, 262–266 (2012). 17
- [120] R. A. Oliver, H. A. R. El-Ella, D. P. Collins, B. Reid, Y. Zhang, F. Christie, M. J. Kappers, and R. A. Taylor, “Growth of InGaN quantum dots with AlGaIn barrier layers via modified droplet epitaxy,” *Materials Science and Engineering B* **178**, 1390–1394 (2013). 17

- 
- [121] J. T. Griffiths, T. Zhu, F. Oehler, R. M. Emery, W. Y. Fu, B. P. L. Reid, R. A. Taylor, M. J. Kappers, C. J. Humphreys, and R. A. Oliver, “Growth of non-polar (11-20) InGaN quantum dots by metal organic vapour phase epitaxy using a two temperature method,” *APL Materials* **2**, 126101 (2014). 17, 74
- [122] F. Ferdos, S. Wang, Y. Wei, A. Larsson, M. Sadeghi, and Q. Zhao, “Influence of a thin GaAs cap layer on structural and optical properties of InAs quantum dots,” *Applied Physics Letters* **81**, 1195 (2002). 20
- [123] S. Hammersley, M. J. Kappers, F. C.-P. Massabuau, S.-L. Sahonta, P. Dawson, R. A. Oliver, and C. J. Humphreys, “Effects of quantum well growth temperature on the recombination efficiency of InGaN/GaN multiple quantum wells that emit in the green and blue spectral regions,” *Applied Physics Letters* **107**, 132106 (2015). 20
- [124] T. Zhu, T. Ding, F. Tang, Y. Han, M. Ali, T. Badcock, M. J. Kappers, A. J. Shields, S. K. Smoukov, and R. A. Oliver, “Self-assembled Multilayers of Silica Nanospheres for Defect Reduction in Non- and Semipolar Gallium Nitride Epitaxial Layers,” *Crystal Growth and Design* **16**, 1010–1016 (2016). 21
- [125] T. Zhu, J. T. Griffiths, W. Y. Fu, A. Howkins, I. W. Boyd, M. J. Kappers, and R. A. Oliver, “Growth of non-polar InGaN quantum dots with an underlying AlN/GaN distributed Bragg reflector by metal-organic vapour phase epitaxy,” *Superlattices and Microstructures* **88**, 480–488 (2015). 23
- [126] T. Zhu, Y. Liu, T. Ding, W. Y. Fu, J. Jarman, C. X. Ren, R. V. Kumar, and R. A. Oliver, “Wafer-scale Fabrication of Non-Polar Mesoporous GaN Distributed Bragg Reflectors via Electrochemical Porosification,” *Scientific Reports* **7**, 45344 (2017). 23
- [127] H. P. Springbett, K. Gao, J. Jarman, T. Zhu, M. Holmes, Y. Arakawa, and R. A. Oliver, “Improvement of single photon emission from InGaN QDs embedded in porous micropillars,” *Applied Physics Letters* **113**, 101107 (2018). 23, 70, 79, 117
- [128] J. P. Reithmaier, G. Şek, A. Löffler, C. Hofmann, S. Kuhn, S. Reitzenstein, L. V. Keldysh, V. D. Kulakovskii, T. L. Reinecke, and A. Forchel, “Strong coupling in

- a single quantum dot-semiconductor microcavity system.” *Nature* **432**, 197–200 (2004). 23
- [129] F. S. F. Brossard, B. P. L. Reid, C. C. S. Chan, X. L. Xu, J. P. Griffiths, D. A. Williams, R. Murray, and R. A. Taylor, “Confocal microphotoluminescence mapping of coupled and detuned states in photonic molecules,” *Optics Express* **21**, 016934 (2013). 23
- [130] M. J. Holmes, S. Kako, K. Choi, M. Arita, and Y. Arakawa, “Linearly polarized single photons from small site-controlled GaN nanowire quantum dots,” *Proc. SPIE* **9748**, 97481E (2016). 23, 37
- [131] A. V. Fedorov, A. V. Baranov, and K. Inoue, “Two-photon transitions in systems with semiconductor quantum dots,” *Physical Review B* **54**, 8627 (1996). 25
- [132] A. F. Jarjour, T. J. Parker, R. A. Taylor, R. W. Martin, and I. M. Watson, “Two-photon absorption in single site-controlled InGaN/GaN quantum dots,” *Physica Status Solidi C* **2**, 3843–3846 (2005). 25
- [133] A. F. Jarjour, A. M. Green, T. J. Parker, R. A. Taylor, R. A. Oliver, G. Andrew D. Briggs, M. J. Kappers, C. J. Humphreys, R. W. Martin, and I. M. Watson, “Two-photon absorption from single InGaN/GaN quantum dots,” *Physica E* **32**, 119–122 (2006). 25
- [134] B. P. L. Reid, T. Zhu, T. J. Puchtler, L. J. Fletcher, C. C. S. Chan, R. A. Oliver, and R. A. Taylor, “Origins of Spectral Diffusion in the Micro-Photoluminescence of Single InGaN Quantum Dots,” *Japanese Journal of Applied Physics* **52**, 08JE01 (2013). 29, 39, 81, 84, 87
- [135] K. Gao, I. Solovev, M. Holmes, M. Arita, and Y. Arakawa, “Nanosecond-scale spectral diffusion in the single photon emission of a GaN quantum dot Nanosecond-scale spectral diffusion in the single photon emission of a GaN quantum dot,” *AIP Advances* **7**, 125216 (2017). 29, 84, 143

- 
- [136] M. Holmes, S. Kako, K. Choi, M. Arita, and Y. Arakawa, “Spectral diffusion and its influence on the emission linewidths of site-controlled GaN nanowire quantum dots,” *Physical Review B* **92**, 115447 (2015). 30, 81
- [137] N. Baer, S. Schulz, P. Gartner, S. Schumacher, G. Czycholl, and F. Jahnke, “Influence of symmetry and Coulomb correlation effects on the optical properties of nitride quantum dots,” *Physical Review B* **76**, 075310 (2007). 37
- [138] S. Amloy, K. F. Karlsson, and P. O. Holtz, “III-nitride based quantum dots for photon emission with controlled polarization switching,” arXiv, DOI: [arxiv.org/abs/1311.5731v1](https://arxiv.org/abs/1311.5731v1) (2013). 37, 40
- [139] R. Bardoux, T. Guillet, B. Gil, P. Lefebvre, T. Bretagnon, T. Taliercio, S. Rousset, and F. Semond, “Polarized emission from GaN/AlN quantum dots: Single-dot spectroscopy and symmetry-based theory,” *Physical Review B* **77**, 235315 (2008). 37, 40
- [140] A. Lundskog, C.-W. Hsu, K. F. Karlsson, S. Amloy, D. Nilsson, U. Forsberg, P. O. Holtz, and E. Janzén, “Direct generation of linearly polarized photon emission with designated orientations from site-controlled InGaN quantum dots,” *Light: Science & Applications* **3**, e139 (2014). 37, 38, 50
- [141] C. H. Bennett and G. Brassard, “Quantum cryptography: Public key distribution and coin tossing,” in “Proceedings of IEEE International Conference on Computers, Systems, and Signal Processing,” (1984), pp. 175–179. 37
- [142] P. W. Shor and J. Preskill, “Simple Proof of Security of the BB84 Quantum Key Distribution Protocol,” *Physical Review Letters* **85**, 441 (2000). 37
- [143] S. Deshpande, J. Heo, A. Das, and P. Bhattacharya, “Electrically driven polarized single-photon emission from an InGaN quantum dot in a GaN nanowire,” *Nature Commun.* **4**, 1675 (2013). 37, 52, 120
- [144] S. Deshpande, A. Das, and P. Bhattacharya, “Blue single photon emission up to 200 K from an InGaN quantum dot in AlGaIn nanowire,” *Applied Physics Letters* **102**, 161114 (2013). 37, 92

- [145] Y.-J. Lu, J. Kim, H.-Y. Chen, C. Wu, N. Dabidian, C. E. Sanders, C.-Y. Wang, M.-Y. Lu, B.-H. Li, X. Qiu, W.-H. Chang, L.-J. Chen, G. Shvets, C.-K. Shih, and S. Gwo, “Plasmonic Nanolaser Using Epitaxially Grown Silver Film,” *Science* **337**, 450–453 (2012). 37
- [146] T. Yamamoto, M. Maekawa, Y. Imanishi, S. Ishizawa, T. Nakaoka, and K. Kishino, “Photon correlation study of background suppressed single InGaN nanocolumns,” *Japanese Journal of Applied Physics* **55**, 04EK03 (2016). 37
- [147] T. Jemsson, H. Machhadani, K. F. Karlsson, C.-W. Hsu, and P.-O. Holtz, “Linearly polarized single photon antibunching from a site-controlled InGaN quantum dot,” *Applied Physics Letters* **105**, 081901 (2014). 38
- [148] T. Jemsson, H. Machhadani, P.-O. Holtz, and K. F. Karlsson, “Polarized single photon emission and photon bunching from an InGaN quantum dot on a GaN micro pyramid,” *Nanotechnology* **26**, 065702 (2015). 38
- [149] S. Kim, S.-H. Gong, J.-H. Cho, and Y.-H. Cho, “Unidirectional Emission of a Site-Controlled Single Quantum Dot from a Pyramidal Structure,” *Nano Letters* **16**, 6117–6123 (2016). 38
- [150] C.-H. Teng, L. Zhang, T. A. Hill, B. Demory, H. Deng, and P.-C. Ku, “Elliptical quantum dots as on-demand single photons sources with deterministic polarization states,” *Applied Physics Letters* **107**, 191105 (2015). 38, 50, 144
- [151] C.-H. Teng, L. Zhang, T. Hill, B. Demory, H. Deng, and P. C. Ku, “Semiconductor Single-Photon Emitters with Tunable Polarization Output,” in “CLEO: 2014,” (2014), p. JTu4A.97. 38
- [152] T. J. Badcock, M. Ali, T. Zhu, M. Pristovsek, R. A. Oliver, and A. J. Shields, “Radiative recombination mechanisms in polar and non-polar InGaN/GaN quantum well LED structures,” *Applied Physics Letters* **109**, 151110 (2016). 38
- [153] C. Mounir, U. T. Schwarz, I. L. Koslow, M. Kneissl, T. Wernicke, T. Schimpke, and M. Strassburg, “Impact of inhomogeneous broadening on optical polarization of

- high-inclination semipolar and nonpolar  $\text{In}_x\text{Ga}_{1-x}\text{N}/\text{GaN}$  quantum wells,” *Physical Review B* **93**, 235314 (2016). 38, 50
- [154] E. Matioli, S. Brinkley, K. M. Kelchner, Y.-L. Hu, S. Nakamura, S. DenBaars, J. Speck, and C. Weisbuch, “High-brightness polarized light-emitting diodes,” *Light: Science & Applications* **1**, e22 (2012). 38, 50
- [155] S. Schulz, T. J. Badcock, M. A. Moram, P. Dawson, M. J. Kappers, C. J. Humphreys, and E. P. O’Reilly, “Electronic and optical properties of nonpolar  $a$ -plane GaN quantum wells,” *Physical Review B* **82**, 125318 (2010). 38
- [156] T. J. Badcock, P. Dawson, M. J. Kappers, C. McAleese, J. L. Hollander, C. F. Johnston, D. V. Sridhara Rao, A. M. Sanchez, and C. J. Humphreys, “Optical polarization anisotropy of  $a$ -plane GaN/AlGaIn multiple quantum well structures grown on  $r$ -plane sapphire substrates,” *Journal of Applied Physics* **105**, 123112 (2009). 38
- [157] C. H. Chiu, S. Y. Kuo, M. H. Lo, C. C. Ke, T. C. Wang, Y. T. Lee, H. C. Kuo, T. C. Lu, and S. C. Wang, “Optical properties of  $a$ -plane InGaIn/GaN multiple quantum wells on  $r$ -plane sapphire substrates with different indium compositions,” *Journal of Applied Physics* **105**, 063105 (2009). 38
- [158] Y. J. Sun, O. Brandt, M. Ramsteiner, H. T. Grahn, and K. H. Ploog, “Polarization anisotropy of the photoluminescence of  $m$ -plane (In,Ga)N/GaN multiple quantum wells,” *Applied Physics Letters* **82**, 3850 (2003). 38
- [159] S. L. Chuang and C. S. Chang, “ $\mathbf{k}\cdot\mathbf{p}$  method for strained wurtzite semiconductors,” *Physical Review B* **54**, 2491–2504 (1996). 39
- [160] O. Stier, M. Grundmann, and D. Bimberg, “Electronic and optical properties of strained quantum dots modeled by 8-band  $\mathbf{k}\cdot\mathbf{p}$  theory,” *Physical Review B* **59**, 5688 (1999). 39
- [161] O. Marquardt, S. Schulz, C. Freysoldt, S. Boeck, T. Hickel, E. P. O’Reilly, and J. Neugebauer, “A flexible, plane-wave based multiband  $\mathbf{k}\cdot\mathbf{p}$  model,” *Optical and Quantum Electronics* **44**, 183–188 (2012). 39

- 
- [162] O. Marquardt, S. Boeck, C. Freysoldt, T. Hickel, S. Schulz, J. Neugebauer, and E. P. O'Reilly, "A generalized plane-wave formulation of  $\mathbf{k}\cdot\mathbf{p}$  formalism and continuum-elasticity approach to elastic and electronic properties of semiconductor nanostructures," *Computational Materials Science* **95**, 280–287 (2014). 39
- [163] K. Schuh, S. Barthel, O. Marquardt, T. Hickel, J. Neugebauer, G. Czycholl, and F. Jahnke, "Strong dipole coupling in nonpolar nitride quantum dots due to Coulomb effects," *Applied Physics Letters* **100**, 092103 (2012). 39, 60
- [164] S. Barthel, K. Schuh, O. Marquardt, T. Hickel, J. Neugebauer, F. Jahnke, and G. Czycholl, "Interplay between Coulomb interaction and quantum-confined Stark-effect in polar and nonpolar wurtzite InN/GaN quantum dots," *European Physical Journal B* **86**, 449 (2013). 39, 60
- [165] B. P. L. Reid, C. Kocher, T. Zhu, F. Oehler, R. Emery, C. C. S. Chan, R. A. Oliver, and R. A. Taylor, "Observations of Rabi oscillations in a non-polar InGaN quantum dot," *Applied Physics Letters* **104**, 263108 (2014). 39, 55
- [166] S. Kremling, C. Tessarek, H. Dartsch, S. Figge, S. Höfling, L. Worschech, C. Kruse, D. Hommel, and A. Forchel, "Single photon emission from InGaN/GaN quantum dots up to 50 K," *Applied Physics Letters* **100**, 061115 (2012). 46
- [167] S. Lazić, E. Chernysheva, Ž. Gačević, N. García-Lepetit, H. P. van der Meulen, M. Müller, F. Bertram, P. Veit, J. Christen, A. Torres-Pardo, J. M. González Calbet, E. Calleja, and J. M. Calleja, "Ordered arrays of InGaN/GaN dot-in-a-wire nanostructures as single photon emitters," *Proc. SPIE* **9363**, 93630U (2015). 46
- [168] L. Zhang, C.-H. Teng, T. A. Hill, L.-K. Lee, P.-C. Ku, and H. Deng, "Single photon emission from site-controlled InGaN/GaN quantum dots," *Applied Physics Letters* **103**, 192114 (2013). 46
- [169] N. Jeon, B. Loitsch, S. Morkoetter, G. Abstreiter, J. Finley, H. J. Krenner, G. Koblmüller, and L. J. Lauhon, "Alloy Fluctuations Act as Quantum Dot-like Emitters in GaAs-AlGaAs Core-Shell Nanowires," *ACS Nano* **9**, 8335–8343 (2015).

- 
- [170] G. W. Hooft, W. A. J. A. van der Poel, L. W. Molenkamp, and C. T. Foxon, “Giant oscillator strength of free excitons in GaAs,” *Physical Review B* **35**, 8281 (1987). 53
- [171] M. Winkelnkemper, M. Dworzak, T. P. Battel, A. Strittmatter, A. Hoffmann, and D. Bimberg, “Origin of the broad lifetime distribution of localized excitons in InGaN/GaN quantum dots,” *Physica Status Solidi B* **245**, 2766–2770 (2008). 53
- [172] P. G. Eliseev, P. Perlin, J. Lee, and M. Osinski, “Blue temperature-induced shift and band-tail emission in InGaN-based light sources,” *Applied Physics Letters* **71**, 569 (1997). 53
- [173] S. K. Patra, T. Wang, T. J. Puchtler, T. Zhu, R. A. Oliver, R. A. Taylor, and S. Schulz, “Theoretical and experimental analysis of radiative recombination lifetimes in nonpolar InGaN/GaN quantum dots,” *Physica Status Solidi B* **254**, 1600675 (2017). 53, 60
- [174] J. A. Peter and C. W. Lee, “Binding energy and radiative lifetime of an exciton in a type-II quantum well,” *Physica Scripta* **85**, 015704 (2012). 53
- [175] S. Kako, M. Miyamura, K. Tachibana, K. Hoshino, and Y. Arakawa, “Size-dependent radiative decay time of excitons in GaN/AlN self-assembled quantum dots,” *Applied Physics Letters* **83**, 984 (2003). 53
- [176] K. Choi, S. Kako, M. J. Holmes, M. Arita, and Y. Arakawa, “Strong exciton confinement in site-controlled GaN quantum dots embedded in nanowires,” *Applied Physics Letters* **103**, 171907 (2013). 53
- [177] A. F. Jarjour, R. A. Oliver, A. Tahraoui, M. J. Kappers, R. A. Taylor, and C. J. Humphreys, “Experimental and theoretical study of the quantum-confined Stark effect in a single InGaN/GaN quantum dot under applied vertical electric field,” *Superlattices and Microstructures* **43**, 431–435 (2008). 53
- [178] R. Ivanov, S. Marcinkevičius, Y. Zhao, D. L. Becerra, S. Nakamura, S. P. DenBaars, and J. S. Speck, “Impact of carrier localization on radiative recombination times in semipolar (20-21) plane InGaN/GaN quantum wells,” *Applied Physics Letters* **107**, 211109 (2015). 55

- [179] Y. Koito, G. J. Rees, J. V. Hanna, M. M. J. Li, Y.-K. Peng, T. Puchtler, R. Taylor, T. Wang, H. Kobayashi, I. F. Teixeira, M. A. Khan, H. T. Kreissl, and S. C. E. Tsang, “StructureActivity Correlations for Brønsted Acid, Lewis Acid, and Photocatalyzed Reactions of Exfoliated Crystalline Niobium Oxides,” *ChemCatChem* **9**, 144–154 (2017). 57
- [180] C. K. Sun, S. Keller, G. Wang, M. S. Minsky, J. E. Bowers, and S. P. DenBaars, “Radiative recombination lifetime measurements of InGaN single quantum well,” *Applied Physics Letters* **69**, 1936 (1996). 57
- [181] S. W. Feng, Y. C. Cheng, Y. Y. Chung, C. C. Yang, Y. S. Lin, C. Hsu, K. J. Ma, and J. I. Chyi, “Impact of localized states on the recombination dynamics in InGaN/GaN quantum well structures,” *Journal of Applied Physics* **92**, 4441 (2002). 57
- [182] S. Amloy, Y. T. Chen, K. F. Karlsson, K. H. Chen, H. C. Hsu, C. L. Hsiao, L. C. Chen, and P. O. Holtz, “Polarization-resolved fine-structure splitting of zero-dimensional  $\text{In}_x\text{Ga}_{1-x}\text{N}$  excitons,” *Physical Review B* **83**, 201307 (2011). 81, 134, 135, 138
- [183] S. A. Empedocles and M. G. Bawendi, “Influence of spectral diffusion on the line shapes of single CdSe nanocrystallite quantum dots,” *J. Phys. Chem. B* **103**, 1826–1830 (1999). 81, 114
- [184] C. Kindel, G. Callsen, S. Kako, T. Kawano, H. Oishi, G. Hönig, A. Schliwa, A. Hoffmann, and Y. Arakawa, “Spectral diffusion in nitride quantum dots: Emission energy dependent linewidths broadening via giant built-in dipole moments,” *Physica Status Solidi RRL* **8**, 408–413 (2014). 81
- [185] G. Sallen, A. Tribu, T. Aichele, R. André, L. Besombes, C. Bougerol, M. Richard, S. Tatarenko, K. Kheng, and J.-P. Poizat, “Subnanosecond spectral diffusion measurement using photon correlation,” *Nature Photonics* **4**, 696–699 (2010). 84
- [186] G. Sallen, A. Tribu, T. Aichele, R. André, L. Besombes, C. Bougerol, M. Richard, S. Tatarenko, K. Kheng, and J.-P. Poizat, “Subnanosecond spectral diffusion of a single quantum dot in a nanowire,” *Physical Review B* **84**, 041405 (2011). 84

- 
- [187] S. Bounouar, A. Trichet, M. Elouneq-Jamroz, R. André, E. Bellet-Amalric, C. Bougerol, M. Den Hertog, K. Kheng, S. Tatarenko, and J. P. Poizat, “Extraction of the homogeneous linewidth of the spectrally diffusing line of a CdSe/ZnSe quantum dot embedded in a nanowire,” *Physical Review B* **86**, 085325 (2012). 84
- [188] H. Ibuki, T. Ihara, and Y. Kanemitsu, “Spectral Diffusion of Emissions of Excitons and Trions in Single CdSe/ZnS Nanocrystals: Charge Fluctuations in and around Nanocrystals,” *Journal of Physical Chemistry C* **120**, 23772–23779 (2016). 84
- [189] M. Arita, F. Le Roux, M. J. Holmes, S. Kako, and Y. Arakawa, “Ultraclean Single Photon Emission from a GaN Quantum Dot,” *Nano Letters* **17**, 2902–2907 (2017). 87, 142
- [190] F. Rol, S. Founta, H. Mariette, B. Daudin, L. S. Dang, J. Bleuse, D. Peyrade, J.-M. Gérard, and B. Gayral, “Probing exciton localization in nonpolar GaN/AlN quantum dots by single-dot optical spectroscopy,” *Physical Review B* **75**, 125306 (2007). 91
- [191] S. Deshpande, T. Frost, A. Hazari, and P. Bhattacharya, “Electrically pumped single-photon emission at room temperature from a single InGaN/GaN quantum dot,” *Applied Physics Letters* **105**, 141109 (2014). 92, 101, 109, 116, 119, 125
- [192] B. P. L. Reid, T. Zhu, C. C. S. Chan, C. Kocher, F. Oehler, R. Emery, M. J. Kappers, R. A. Oliver, and R. A. Taylor, “High temperature stability in non-polar (11-20) InGaN quantum dots: Exciton and biexciton dynamics,” *Physica Status Solidi C* **11**, 702–705 (2014). 98, 116
- [193] I. A. Ostapenko, G. Hönig, S. Rodt, A. Schliwa, A. Hoffmann, D. Bimberg, M. R. Dachner, M. Richter, A. Knorr, S. Kako, and Y. Arakawa, “Exciton acoustic-phonon coupling in single GaN/AlN quantum dots,” *Physical Review B* **85**, 081303 (2012). 103, 116
- [194] A. M. Jagtap, J. Khatei, and K. S. Koteswara Rao, “Exciton-phonon scattering and nonradiative relaxation of excited carriers in hydrothermally synthesized CdTe quantum dots,” *Phys. Chem. Chem. Phys.* **17**, 27579 (2015). 106, 109, 112, 115

- 
- [195] Q. Ding, X. Zhang, L. Li, X. Lou, J. Xu, P. Zhou, and M. Yan, “Temperature dependent photoluminescence of composition tunable  $\text{Zn}_x\text{AgInSe}$  quantum dots and temperature sensor application,” *Optics Express* **25**, 19065 (2017). 106
- [196] Z. Gacevic, A. Das, J. Teubert, Y. Kotsar, P. K. Kandaswamy, T. Kehagias, T. Koukoulou, P. Komninou, and E. Monroy, “Internal quantum efficiency of III-nitride quantum dot superlattices grown by plasma-assisted molecular-beam epitaxy,” *Journal of Applied Physics* **109**, 103501 (2011). 106, 109
- [197] T. Braun, C. Schneider, S. Maier, R. Igusa, S. Iwamoto, A. Forchel, S. Höfling, Y. Arakawa, and M. Kamp, “Temperature dependency of the emission properties from positioned  $\text{In}(\text{Ga})\text{As}/\text{GaAs}$  quantum dots,” *AIP Advances* **4**, 097128 (2014). 106
- [198] J. Krustok, H. Collan, and K. Hjelt, “Does the low-temperature Arrhenius plot of the photoluminescence intensity in  $\text{CdTe}$  point towards an erroneous activation energy?” *Journal of Applied Physics* **81**, 1442 (1997). 106
- [199] T. Lu, Z. Ma, C. Du, Y. Fang, H. Wu, Y. Jiang, L. Wang, L. Dai, H. Jia, W. Liu, and H. Chen, “Temperature-dependent photoluminescence in light-emitting diodes,” *Scientific Reports* **4**, 6131 (2014). 106
- [200] D. Valerini, A. Cretí, M. Lomascolo, L. Manna, R. Cingolani, and M. Anni, “Temperature dependence of the photoluminescence properties of colloidal  $\text{CdSeZnS}$  core/shell quantum dots embedded in a polystyrene matrix,” *Physical Review B* **71**, 235409 (2005). 108, 115
- [201] R. Seguin, S. Rodt, A. Strittmatter, L. Reißmann, T. Bartel, A. Hoffmann, D. Bimberg, E. Hahn, and D. Gerthsen, “Multi-excitonic complexes in single  $\text{InGaN}$  quantum dots,” *Applied Physics Letters* **84**, 4023 (2004). 108, 112, 115
- [202] Y. P. Varshni, “Temperature dependence of the energy gap in semiconductors,” *Physica* **34**, 149–154 (1967). 109
- [203] K. P. O’Donnell and X. Chen, “Temperature dependence of semiconductor band gaps,” *Applied Physics Letters* **58**, 2924 (1991). 109, 110

- [204] K. Huang and A. Rhys, “Theory of light absorption and non-radiative transitions in F-centres,” in “Proceedings of the Royal Society of London A,” , vol. 204 (1950), vol. 204, pp. 406–423. 110
- [205] J. Lee, E. S. Koteles, and M. O. Vassell, “Luminescence linewidths of excitons in GaAs quantum wells below 150 K,” *Physical Review B* **33**, 5512 (1986). 112
- [206] D. Gammon, S. Rudin, T. L. Reinecke, D. S. Katzer, and C. S. Kyono, “Phonon broadening of excitons in GaAs/Al<sub>x</sub>Ga<sub>1-x</sub>As quantum wells,” *Physical Review B* **51**, 16785 (1995). 112
- [207] K. Sebald, H. Lohmeyer, J. Gutowski, T. Yamaguchi, and D. Hommel, “Micro-photoluminescence studies of InGaN/GaN quantum dots up to 150 K,” *Physica Status Solidi B* **243**, 1661–1664 (2006). 112
- [208] X.-M. Dou, B.-Q. Sun, Y.-H. Xiong, S.-S. Huang, H.-Q. Ni, and Z.-C. Niu, “Temperature Dependence of Photoluminescence from Single and Ensemble InAs/GaAs Quantum Dots,” *Chin. Phys. Lett.* **25**, 3440 (2008). 112
- [209] X.-Q. Li and Y. Arakawa, “Optical linewidths in an individual quantum dot,” *Physical Review B* **60**, 1915 (1999). 113
- [210] I. Favero, A. Berthelot, G. Cassabois, C. Voisin, C. Delalande, P. Roussignol, R. Ferreira, and J. M. Gérard, “Temperature dependence of the zero-phonon linewidth in quantum dots: An effect of the fluctuating environment,” *Physical Review B* **75**, 073308 (2007). 113
- [211] C. C. Kocher, T. J. Puchtler, J. C. Jarman, T. Zhu, T. Wang, L. Nuttall, R. A. Oliver, and R. A. Taylor, “Highly polarized electrically driven single-photon emission from a non-polar InGaN quantum dot,” *Applied Physics Letters* **111**, 251108 (2017). 113, 144
- [212] M. T. Man and H. S. Lee, “Discrete states and carrier-phonon scattering in quantum dot population dynamics,” *Scientific Reports* **5**, 8267 (2015). 115

- [213] P. Jing, J. Zheng, M. Ikezawa, X. Liu, S. Lv, X. Kong, J. Zhao, and Y. Masumoto, “Temperature-Dependent Photoluminescence of CdSe-Core CdS/CdZnS/ZnS-Multishell Quantum Dots,” *J. Phys. Chem. C* **113**, 13545–13550 (2009). 115
- [214] C. d. M. Donegá, M. Bode, and A. Meijerink, “Size- and temperature-dependence of exciton lifetimes in CdSe quantum dots,” *Physical Review B* **74**, 085320 (2006). 120
- [215] Y.-R. Wu, Y.-Y. Lin, H.-H. Huang, and J. Singh, “Electronic and optical properties of InGaN quantum dot based light emitters for solid state lighting,” *Journal Of Applied Physics* **105**, 013117 (2009). 132
- [216] L. Zhang, C.-H. Teng, P.-C. Ku, and H. Deng, “Charge-tunable indium gallium nitride quantum dots,” *Physical Review B* **93**, 085301 (2016). 134, 138
- [217] M. Bayer, G. Ortner, O. Stern, A. Kuther, A. A. Gorbunov, A. Forchel, P. Hawrylak, S. Fafard, K. Hinzer, T. L. Reinecke, S. N. Walck, J. P. Reithmaier, F. Klopff, and F. Schäfer, “Fine structure of neutral and charged excitons in self-assembled In(Ga)As/(Al)GaAs quantum dots,” *Physical Review B* **65**, 195315 (2002). 138
- [218] S. Phillipov, Y. Puttison, Y. Huang, I. A. Buyanova, S. Suraprapapich, C. W. Tu, and W. M. Chen, “Exciton Fine-Structure Splitting in Self-Assembled Lateral InAs/GaAs Quantum-Dot Molecular Structures,” *ACS Nano* **9**, 5741–5749 (2015). 138
- [219] R. Seguin, A. Schliwa, S. Rodt, K. Pötschke, U. W. Pohl, and D. Bimberg, “Size-Dependent Fine-Structure Splitting in Self-Organized InAs/GaAs Quantum Dots,” *Physical Review Letters* **95**, 257402 (2005). 138
- [220] S. Seidl, B. D. Gerardot, P. A. Dalgarno, K. Kowalik, A. W. Holleitner, P. M. Petroff, K. Karrai, and R. J. Warburton, “Statistics of quantum dot exciton fine structure splittings and their polarization orientations,” *Physica E* **40**, 2153–2155 (2008). 138
- [221] H. Ajiki, “Exciton-Phonon Interaction in a Spherical Quantum Dot: Effect of Electron-Hole Exchange Interaction,” *Physica Status Solidi B* **224**, 633–637 (2001). 140

- [222] R. Ishii, M. Funato, and Y. Kawakami, “Effects of strong electron-hole exchange and exciton-phonon interactions on the exciton binding energy of aluminum nitride,” *Japanese Journal of Applied Physics* **53**, 091001 (2014). 140